Scalable Nanophotonic Light Management Design for Solar Cells

Thesis by
Colton Robert Bukowsky

In Partial Fulfillment of the Requirements for the
Degree of
Doctor of Philosophy in Material Science

CALIFORNIA INSTITUTE OF TECHNOLOGY
Pasadena, California

2019
Defended April 16, 2019

Colton Robert Bukowsky
ORCID: 0000-0003-3577-8050

ACKNOWLEDGEMENTS

My advisor, Harry Atwater, has deeply impacted my skills, perspectives, and thought processes in positive ways that are impossible to sum up in words. My years under his guidance have been the most formative period in my lifetime thus far. Harry's willingness to consider new ideas allowed my creativity to thrive. For better or for worse, I cannot remember a time Harry discouraged me with a "No," yet often remember him saying "Let's try that" or "That would be interesting". Harry's mentorship grew my primary passion of science into a deeper and more profound curiosity, as I became the scientist I am today. He has afforded so many students incredible opportunity and I consider myself lucky to have been one of them. Harry's enthusiasm, energy, and optimism, his support, patience, and understanding, his ethics, his resourcefulness and abundant creativity will continue to inspire me throughout my lifetime.

My mother Bobbie, has been my biggest supporter during my time at Caltech. I could not have done this without her selflessness and love. She has been my anchor in stormy seas, and my biggest fan at every success. Nothing has been too much to ask of her. She only asks her children be happy in what they do, and she has taken every opportunity to make this happen for me. My father Clifton, was the first to ignite curiosity and excitement for the mechanisms of the world around me. I undoubtedly inherited his penchant to ask "Why," "How," and "What if?". These questions are responsible for my studies, research, and a multitude of D.I.Y. projects. I appreciate our thoughtful discussions that have inspired the creativity in me. My brother Clif has never paused to think of himself before helping me. He has been a lighthouse in foggy weather and a strong sounding board. I am incredibly thankful for all he has done. Our differences are a perfect compliment to keep me well balanced. I also want to thank, my sister-in-law Liz, for her astounding help. She is the perfect addition to our family and I know Clif and Liz will create a wonderful family of their own. My step-father Al has made several sacrifices to help me get to this point. He was the first to predict that I would end up studying wave mechanics, and I thank him for his encouragement. Al has exemplified character I admire and strive towards. My step-mother Claire has been a great support to me in times when there was no one else I could turn to. She has taught me things textbooks could not. My sister Lexie, has kept me young and grounded. I appreciate the short but quality times we have enjoyed together when I didn't know how much I needed to just relax.

To my brother Cody, I am proud of the man he's become. He has encouraged me to keep going when things got really tough. Thank you to my aunts, uncles, cousins, and relatives whom have always been ready to help; your interest in the enigma of my science has always made me feel special. It is with much love I give thanks to my grandparents Maria Magdalena, Humberto, and Christine for leading the families that have brought me this far.

Kate Fountaine deserves special gratitude. I owe much of my success and growth to her. She gave so much of her time to teach and guide me academically. More than that, she has been a wonderful friend; one that will never be replaced as we part ways after Caltech. I will look back with fondness and joy at the amazingly fun times and adventures we spent together. I also am thankful for our wonderful fur-ball Napa and the times of immense support and joy he brought me since our first day together.

I also give thanks to the countless people who have made a difference in my time at graduate school. Thank you to my elder colleagues, especially Jonathan Grandidier, Ray Weitekamp, Ana Brown, Ragip Pala, Jim Fakonas, Giulia Tagliabu, Muhammad Alam, Mike Kelzenberg, Pilar Espinet, Krishnan Thayagarjan, Ruzan Sokhoyan, Artur Davoyan, Benji Vest and so many others. Dr. Rebecca Saive you were a great mentor and friend. I know I could not have done this without my close Atwater friends and cohort: Nick Batara, Kelly Mauser, Yulia Tolstova, Dennis Callahan, Kelsey Horowitz, John Llyod, Cris Flowers, Hal Emmer, Sunita Darbe, Stefan Olmelchenko, Hung-Jung Hsu, Sisir Yalamanchili, Michelle Sherrott, Will Whitney, and in no small part Thomas Russell. Dagny Fleischman gets a special thanks for being a friend that I almost missed having in my life, but I am fortunate our paths converged. Thank you to those who are next in line, you've been invaluable to my success: Rebecca Glaudel, Phillip Jahelka, Sophia Cheng, Haley Bauser, Megan Phelan, and David Needell with whom I was lucky to have closely worked. I owe great thanks to my original emotional and logistical support team Tinnifer, Tiffany Kimoto, Jennifer Blankenship, who made this possible as much as anyone, if not more. I want to recognize the backing of the KNI staff especially Melissa Melendez and Matthew Sullivan.

To my non-Caltech friends, your kindness and friendships have kept me on the right track, providing clarity, support, and fun whenever I've needed or wanted it. Thank you Erik Zinn, Ben Rosen, Dan and Jan, Kelly Guinan, Brian Lakin, Samantha Crow, Jessica Linares, Alex Pena, Jon Galamay, and Amanda Stephens. To all of

my friends, thank you for the wonderful times that have inspired and energized me.

I believe that no player has a small role. Thank you to all who have come in and out of my life during this time. There is no doubt that you have impacted my personal life and research career in positive ways. I want to thank everyone with whom I have crossed paths and been able to share laughs and smiles along the way.

ABSTRACT

The current trend in wide adoption of solar energy is encouraging in the context of current projections of increasing energy consumption and the dire need to decrease carbon emissions. The solar industry has expanded due to scientific advances in the power conversion efficiency of solar modules. In order maintain a rapid pace of adoption and further decrease electricity costs, converting each photon becomes increasingly important. This work focuses on nanophotonic approaches to increasing the power conversion efficiency of different solar photovoltaic designs. The projects voluntarily impose certain design constraints in order to be compatible with the large scale manufacturing needed by the solar industry. A focus was given to designs that can leverage the promising technology of nanoimprint lithography. Amorphous silicon tandem cells with embedded nanophotonic patterning attempted to increase absorption while minimizing materials and time costs. Simulated designs of Copper Indium Gallium Diselenide absorbers showed that the management of excited carriers is equally as important as light management in decreasingly thin absorber layers. Near perfect anti-reflection structures were given a detailed physical analysis to better describe the fundamental physics of near zero reflection due to nanocones printed on solar cell encapsulation glass. Experimental results agreed with the theoretical analysis, and showed that these nanostructures further increased absorbed photocurrent by trapping light in the encapsulation glass. Finally, a unique device in the form of a tandem luminescent solar concentrator/silicon solar module was proposed and analyzed as a low cost and adaptable technology for increased solar power conversion efficiency. Key to this design was discovery of new, near-perfect components for light management. Exciting and innovative designs are proposed to control the light-matter interaction within these devices. Study of a photonic luminescent solar concentrator predicted that luminescence can be trapped in photonic crystal slab waveguides with near zero loss. Rigorous experimental efforts to characterize a multitude of near-perfect samples help guide these designs toward their final goals.

PUBLISHED CONTENT AND CONTRIBUTIONS

Bukowsky, C. R. et al. (2019a). "Optical Modes of Near Perfect Transmittance in Printed Nanocone Arrays". In Preparation.
C.R.B. performed majority of simulation, analysis, design, measurements and wrote the manuscript of this work.

Bukowsky, Colton R et al. (2019b). "Photonic Crystal Slab Waveguides for Luminescent Solar Concentrators". In Preparation.
C.R.B. performed simulation, analysis, design and wrote the manuscript of this work.

Fleischman, Dagny et al. (2019). "High Spectral Resolution Plasmonic Color Filters with Subwavelength Dimensions". In: DOI: http://dx.doi.org/10.1021/acsphotonics.8b01634.
C.R.B. participated in the fabrication method design and performed characterization of this work. C.R.B provided manuscript revisions.

Needell, David R et al. (2019). "Spectrally Matched Quantum Dot Photoluminescence in GaAs-Si Tandem Luminescent Solar Concentrators". In: *IEEE Journal of Photovoltaics* PP. DOI: http://dx.doi.org/10.1109/JPHOTOV.2019.2892075.
C.R.B. participated in the formulation, mathematical derivation, design of experiment, and analysis of this work. C.R.B provided manuscript revisions.

Needell, David R. et al. (2018). "Design Criteria for Micro-Optical Tandem Luminescent Solar Concentrators". In: *IEEE Journal of Photovoltaics* 8.6, pp. 1560–1567. DOI: 10.1109/JPHOTOV.2018.2861751. arXiv: 1710.00034. URL: https://ieeexplore.ieee.org/document/8432067/.

Bukowsky, Colton R., Dennis M. Callahan, and Harry A. Atwater (2017). "Photon and Carrier Management Design for Non-planar Thin-film Copper Indium Gallium Diselenide Photovoltaics". US9825193B2. California Institute of Technology.

Bukowsky, Colton R. et al. (2017a). "Absorption enhancing and passivating nonplanar thin-film device architectures for copper indium gallium selenide photovoltaics". In: *2017 IEEE 44th Photovoltaic Specialist Conference (PVSC)*. Vol. 2016-Novem. IEEE, pp. 1–5. DOI: 10.1109/PVSC.2017.8366487.

Bukowsky, Colton R et al. (2017b). "Photon and carrier management design for nonplanar thin-film copper indium gallium selenide photovoltaics". In: *Solar Energy Materials and Solar Cells* 161.November 2016, pp. 149–156. DOI: http://dx.doi.org/10.1016/j.solmat.2016.11.008.
C.R.B. performed all simulation, analysis, design and wrote the manuscript of this work.

Saive, Rebecca, Colton R. Bukowsky, and Harry A. Atwater (2017). "Three-dimensional nanoimprint lithography using two-photon lithography master samples". In: pp. 1–4. arXiv: 1702.04012. URL: http://arxiv.org/abs/1702.04012.
C.R.B. assisted in and carried out new fabrication methods of this work. C.R.B provided manuscript revisions.

Saive, Rebecca et al. (2017). "Silicon heterojunction solar cells with effectively transparent front contacts". In: *Sustainable Energy & Fuels* 1.3, pp. 593–598. DOI: http://dx.doi.org/10.1039/C7SE00096K.
C.R.B. assisted in design and formulation of fabrication methods for this work. C.R.B provided manuscript revisions.

Atwater, H. A. et al. (2016). "Solar Cells and Methods of Manufacturing Solar Cells Incorporating Effectively Transparent 3D Contacts". US20160322514A1. California Institute of Technology.

Fountaine, Katherine T. et al. (2016). "Near-Unity Unselective Absorption in Sparse InP Nanowire Arrays". In: *ACS Photonics* 3.10, pp. 1826–1832. DOI: 10.1021/acsphotonics.6b00341.

TABLE OF CONTENTS

ACRONYMS AND SHORTHANDS

α absorption/extinction coefficient 23, 59, 116

μc-Si0$_x$ micro-crystalline Silicon Oxide 53, 54, 67, 70

μc-Si:H hydrogenated micro-crystalline Silicon 68

***n*-PrOH** *n*-propyl alcohol 45–48

a-Si$_{1-x}$Ge$_x$:H hydrogenated amorphous Silicon Germanium 3, 4, 19, 52–54, 56, 61–63, 65–68, 70

a-Si:H hydrogenated amorphous Silicon 3, 19, 51–54, 56, 61–63, 65, 67, 68, 70

a-SiC:H hydrogenated amorphous Silicon Carbide 53, 67, 70, 134

AFM atomic force microscopy 55, 61

AM1.5G ASTM Air Mass 1.5 Global 62, 65, 67, 69, 114

AOI angle of incidence 94, 95, 99–101, 103, 104, 108, 109, 111, 124, 128, 129, 144

ASB aluminum-tri-sec-butoxide 45–49

AZO aluminum doped zinc oxide 54, 64, 67, 69, 70

BEEA 2-(2-n-Butoxyethoxy)-ethylacetate 41–43, 45–47

CAD computer-assisted design 29, 55, 70, 139

CIGS Copper Indium Gallium Diselenide 4, 19, 22, 23, 25, 44, 145

CL Cody-Lorentz 59–62

CPV concentrating photovoltaics 110, 113

DI deionized 30, 41, 45–47, 49

EAA ethyl-acetoacetate 45, 46, 48, 49

EBL electron-beam lithography 3, 28–30, 32, 37, 63, 133

EQE external quantum efficiency 24, 25, 61, 62, 65–69, 101, 103, 116, 117, 121, 122, 178

FDTD Finite Difference Time Domain 53, 55, 57, 58, 61, 69, 98, 104, 106, 138, 139

FF fill factor 24, 68, 69, 115, 117, 122

FTO Fluorine doped Tin Oxide 53–56, 64

GG geometric gain 128, 135

ICP-RIE inductively coupled plasma reactive ion etching 3, 28–30, 38, 39, 49, 64, 67, 144

IPA isopropyl alcohol 28, 30, 31, 42, 45–49

IQE internal quantum efficiency 23, 24, 62, 67

IRL Intermediate Relfection Layer 53, 54

ITO Indium doped Tin Oxide 53–55, 67

J_{SC} short-circuit current density 23–25, 52, 61, 69, 115, 117, 122

JV current-voltage 23, 24, 65, 68, 70

LDOS local density of optical states 12, 16, 19, 132, 133, 136, 138

LED Light Emitting Diode 24, 65, 132

LSC luminescent solar concentrator 5, 110–114, 116–118, 120, 122, 126, 128, 130–133, 135, 138–140, 143, 146, 147

NIL nano-imprint lithography 3, 5, 27, 28, 38–41, 43–46, 49, 50, 53, 63, 64, 68, 78, 80, 91, 94, 109, 132, 134, 144

NIR near infrared 53, 61, 66, 69, 93

OTFCS (tridecafluoro-1,1,2,2-tetrahydrooctyl)-trichlorosilane 32, 50

P_f Purcell factor 132, 134, 136–138, 140–144

p-i-n p-type/intrinsic/n-type 52–54

PC photonic crystal 134, 135, 139–144

PDMS poly-dimethyl siloxane 31, 33–38, 40, 43

PECVD plasma enhance chemical vapor deposition 51–53

PL photoluminescence 110, 112, 116–118, 120–122, 124–126, 129, 130, 132, 135, 138–143

PLMA polylauryl-methacrylite 111, 112, 121, 124–127, 136, 138

PLQY photoluminescent quantum yield 116, 117, 119–121, 132, 134, 136–138, 143, 144

PMMA polymethyl-methacrylite 28, 30, 98

PV photovoltaic 1–4, 19–22, 25, 49–53, 91, 96, 101, 108–110, 112, 133, 145

QD quantum dot 5, 111, 112, 117, 120–122, 125, 129, 132–135, 137, 139–141, 143

RCWA Rigorous Coupled Wave Analysis 91, 93, 94, 96–98, 104

SEM scanning electron microscope 39, 44, 48, 49, 56, 64, 68

TCO transparent conducting oxide 51, 54, 64

TE transverse electric field 90, 92, 96, 99, 100, 103, 112, 138

TEM transmission electron microscope 56, 67–69

TIR total internal reflection 13, 14, 111, 112, 122, 125, 132, 134, 135, 139–144

TL Tauc-Lorentz 59–62

TM transverse magnetic field 90, 92, 94, 96, 100, 103, 112, 113, 138, 142

TMOS tetra-methoxy-silane 41, 42

TMTS methyl-trimethoxy-silane 41, 42, 48

V_{OC} open circuit voltage 24, 25, 65, 68, 69, 115, 117, 122

XPDMS hardened poly-dimethyl siloxane 33–36, 47

Chapter 1

INTRODUCTION: PHOTOVOLTAIC SOLAR ENERGY PRODUCTION AT THE NANOSCALE

1.1 Introduction and Scope

Awareness and attention to the status of the world's energy production has come to the forefront of our scientific community, local communities and organizations, governments, political leaders, and our global culture at large. The anthropogenic production of carbon dioxide has been extensively linked to rises in global temperatures.[4, 103, 114, 127, 150] Perhaps the most recent milestone is *The Paris Agreement* of 2015 signed in consensus at the 21st Conference of Parties. It to keep global temperatures 2 °C by drastically reducing carbon dioxide production; this came at a veritable tipping point in history. The need for technological options in terms of energy generation free of carbon dioxide emissions is clear. Figure 1.1 depicts the vastness of our available carbon-free solar energy resource.[72, 120] This to scale image clarifies the sheer magnitude of this resource on a per year basis compared to total known reserves of non-renewable energy resources. A special emphasis to the United States shows that only one quarter percent of available land-area is needed to produce the U.S.'s entire electricity demand. A motivation for developing solar energy technologies is immediate. This work adds fundamental investigation, exploration, and demonstration of options in the field of nanophotonic solar photovoltaic (PV) technology.

Nanophotonics as a field provides a vast variety of great opportunity communications, characterization and metrology, research methodology, computing, and many other applications. In the past decades, research in nanophotonics and the field of solar energy have intersected in a highly promising fashion. Solar PV is fundamentally concerned with the management of light to convert photons to energetic electrons, i.e. electricity. This same concept of light management is innate to nanophotonics. Thus combining these two fields provides new methods and strategies to best utilize the solar energy resource through a deep understanding of physical processes and mechanisms present in both arenas. Approaching the study and design of PV devices with this paradigm, that photonic properties and electronic performance are intrinsically coupled, leads to insights and conclusions poised to change the solar

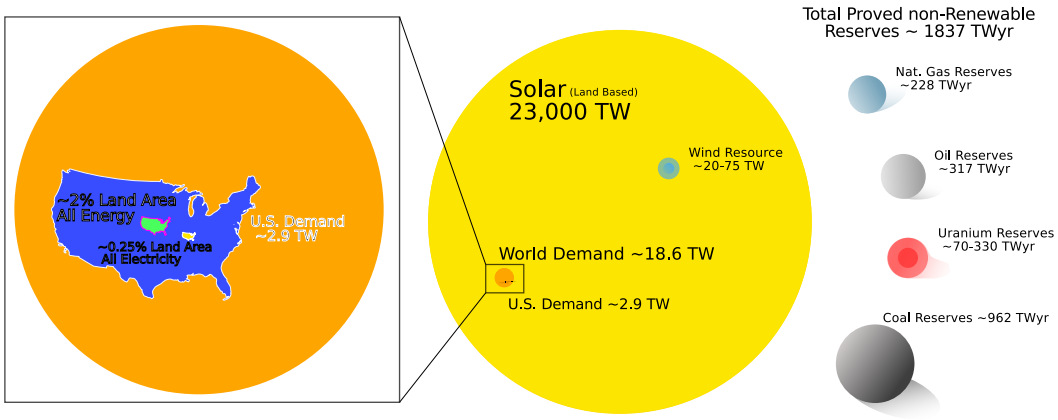

Figure 1.1: An update of a popular figure by Perez, R. depicting, to scale by area, the amount of solar power that impinges upon the earth over the course of one year. This is compared to the total proven energy reserves of non-renewable sources.The amount of energy used globally in 2018 is shown in orange. The inset shows the United States's 2018 power demand in blue. Within that inset is the land area needed for solar power generation to meet the U.S.'s entire yearly energy needs and all U.S. electricity needs (assuming 10% power conversion efficiency and a 25% capacity factor). This amounts to 2% and 0.25% of the U.S. total land area, respectively. Between 5-10% of the U.S. land area is urban environment and already provides ample opportunity for solar deplyoment on existing structures.

industry. In the nascent stages of PV research, crucial work forged understanding of materials properties, synthesis, and high quality materials production that has brought about a solar revolution. Today, combining that foundational PV materials research with a critical focus on how materials interact with light is providing opportunity to reach the next levels of affordable clean energy. Novel PV use cases and power conversion efficiencies are approaching the theoretical thermodynamic limits of solar PV systems.

Yet high performance nanophotonic designs and the needed terawatt scale solar energy generation are separated in length scale by by 22-28 orders of magnitude. Meeting this energy demand requires thousands of square kilometers of solar panels to be manufactured. The semiconductor chip and display manufacturing industries are the only examples of nanoscale manufacturing approaching this level of production. Still, many of the proven nano-fabrication methods in those industries will need drastic a cost decrease to facilitate scaling to the levels needed by solar energy. Significant progress in massively scalable nano-manufacturing is needed. This work sees this need and participates in the progress.

Here, new designs and experimental demonstrations addressing the solar PV scala-

bility requirement are presented. The technology of nano-imprint lithography (NIL) is a promising manufacturing technique towards this goal. NIL is used successfully in experiments, and NIL compatibility is a requirement for the majority of the work's design research. Each chapter discusses either fundamental nanophotonic principles in novel PV designs, experimental realization of these designs, or both.

Scope of this Thesis

Chapter 2 provides intimate and low-level knowledge of different methods developed for producing nanophotonic structures by NIL. Proven integrated-circuit nanofabrication tools and techniques are leveraged to advance in-laboratory scaling of silica sol-gel printed nanostructures. This chapter can serve as a guide for reproduction and extension of this work on scales of cm^2+. Fabricating nanostructures on this length-scale is considered proof-of-concept and ready for development towards standard solar cell areas. Mastery of this fabrication technique has and will benefit many other laboratory members' research work. Silicon master mold production details are presented starting from electron-beam lithography (EBL), to resist development, inductively coupled plasma reactive ion etching (ICP-RIE) etching of structures, and finally surface treatment of the molds. A reliable surface treatment procedure was a key development. Detailed instructions regarding bilayer soft-stamp fabrication also drastically improved process reliability. Novel efforts in soft-stamp scaling by "quilting" many stamp copies into a fused monolith are presented, demonstrating how a small, sub-cm^2 area can be multiplied. A robust procedure for silica sol-gel resist synthesis, modified and adapted from Reference [170], is described. Additionally, the first ever exploration of aluminum oxide sol-gel resit printing is cataloged. Various casting and printing strategies are given to overcome unique challenges faced by different feature designs.

Chapter 3 concerns simulation design and experimental efforts to modify hydrogenated amorphous Silicon (a-Si:H)/hydrogenated amorphous Silicon Germanium (a-$Si_{1-x}Ge_x$:H) tandem thin-film solar cells with printed nanophotonic structures. It was proposed and demonstrated that a combination of the tradition randomized texture in these devices can be combined with an ordered nanophotonic structure to increase light absorption. This is accomplished by increasing internal mode coupling via the scattering. Furthermore, the nanostructure can be designed to re-distribute the amount of light in each sub-cell to satisfy current matching requirements. Difficulties in scaling nanophotonic structures were overcome through the development of many strategies presented in Chapter 2. Extremely detailed characterization of

materials' optical properties, device structure, and iterative simulation-guided experiment led to a near perfect agreement between optical models and experiment. Experimental enhancement beyond the capabilities of randomized texture was seen in the a-$Si_{1-x}Ge_x$:H bottom cell.

Chapter 4 sought to clarify recent exciting developments randomly textured Copper Indium Gallium Diselenide (CIGS) manufacturing that led to novel light trapping properties in these devices. Coupled opto-electronic simulation methods showed that the texturing created scattered light with multiple photon absorption opportunities, and isolated low quality resonances, which enhanced performance compared to traditionally thick planar CIGS devices. The randomized texture can be employed in new CIGS devices with 60% materials savings, promising to increase in manufacturing throughput and reduce unit cost. The randomized texture was critically compared to the traditional planar geometry and to new nanophotonic strategies for light trapping. A 9% and 5% improvement for ordered structures and random texture, respectively, over planar devices of the same 700 nm thickness was found. The addition of a patented nanophotonic back-spacer layer increased the performance of all devices by reducing the main source of minority carrier surface recombination at the back contact. All geometries showed a greater than 20% improvement by adding this dielectric spacer. The randomly textured geometry reaching an ultimate power conversion efficiency of 19.7%, approaching record performance. Future work implementing these novel designs could ultimately surpass the record.

Chapter 5 is an in depth analysis of the light materials interaction of nanocone structures on solar cell cover glass showing near perfectly-zero reflection losses. The work presents a novel physical paradigm to explain this phenomenon. To this author's knowledge, the concept of dispersive cylindrical waveguide modes had never before been used to describe the effective index gradient function of nanocone-induced coupling to substrate glass. This paradigm can describe the zeroth order propagating wave where the often used Maxwell-Garnett continuous index approximation breaks down. It offers new physical insight into the origins of the near-perfect and angle independent anti-reflection response. Removing this glass reflection provides an immediate 5% power conversion improvement in PV cells. Also, more than 10% additional light is absorbed from trapping light in cover glass by diffractive modes, further improving upon zero reflection. A significant experimental demonstration of 0.37% glass reflection was enabled by extensive efforts to create a laser beamline with rare high-precision capabilities to 0.001%

reflection.

Finally, Chapter 6 and Chapter 7 are concerned with new solar cell designs in luminescent solar concentrator (LSC)s. LSCs offer significant advantages in cost and real-world deployment in typically non optimal locations for solar panels. These advantages result from their reduced semiconductor materials use and high diffuse light collecting capabilities. Variations of the LSC have existed for many decades, but have suffered from poor power conversion efficiencies. In LSCs, solar radiation is absorbed by a luminophore, such as CdS/CdSe quantum dot (QD)s, and then re-emitted as red-shifted luminescence, and travels through a waveguide to a solar cell millimeters to centimeters away. The escape of luminescence has limited previous LSCs' performance. An original analytical model for the travel of this luminescence is developed to aid rapid design development. Simulation based optimization of multilayer Bragg-stack notch filters produced designs for omni-directional luminescence trapping to eliminate the escape cone loss. These types of filters are employed in a unique silicon tandem module design. The same precise techniques used to characterize nanocones proved these filters have 99.99% reflectance in the target QD luminescence band.

Chapter 7 focuses on applying nanophotonic light trapping principles in a fashion not attempted before. Designs leverage a unique opportunity for luminescence manipulation from within photonic crystal array: the fact that luminescence trapping is decoupled from solar photon in-coupling. By placing luminophores directly into these nanostructures, photons are influenced to preferentially emit into lateral guided modes of photonic crystal slabs, which are thinner than most LSC waveguides by an order of magnitude. The luminescence can thus be guided to photon collectors at a distance. Simulation based analysis and optimization found near 100% light trapping is theoretically possible. Additionally, this optical environment has a high local density of optical states and increased Purcell Factor which can boost luminescent quantum yield by factors of 10 or more. This may open future doors for previously non-viable luminophores. Finally, it is proposed that this photonic crystal slab is compatible with NIL methods. This offers a route to highly efficient LSCs via scalable and inexpensive production methods.

A number of collaborative efforts found in Published Content and Contributions have not been included in this thesis, but were made possible by much of the work undertaken during the course of this author's tenure. They are mentioned here to bring attention to their accomplishments. Critical to these was success in NIL and

the extensive efforts to perfect the high-precision optical laboratory characterization tool, SARP, described in Appendix A. These works first produced leading experimental publications of near unity broadband absorption of the solar spectrum in III-V semiconductor nanowires and nanocones, enabled by nanofabrication process expertise. Next, Effectively Transparent Contacts for applications in front-contact solar cells were first realized via the nanoimprint methods developed here. The work showed that printed triangle contacts could redirect nearly all angles of incident light into a solar cell. This eliminated the 1-4% shadowing loss of front contacted solar cells, while trapping light into longer path-lengths and increasing photocurrent absorption. Finally, the uncommon construction and use of a transmission confocal microscope allowed sub-percentage transmission measurements of the first hyper-spectral plasmonic slit filters. These were the first to demonstrate visible wavelength selection with full-width-half-max values as low as 15 nm and signal to noise ratios between 5-10 in sub-micron features.

The remainder of this chapter provides a basic introductory tutorial on the physics required to understand this thesis. It can serve as a quick reference or general primer to the electromagnetics, materials science, and solid state physics encountered in this text. Further conceptual depth is presented within each chapter. Readers are still encouraged to examine citations and other resources for physical origins, derivations, examples, and deeper understanding. First, Maxwell's equations are formulated into the wave description of light. This is followed by brief discussion of the consequences of the wave nature of light in periodic and non-periodic optical environments. Next, the basics of solar energy photovoltaics are reviewed. The following sections provide connections between the two fields to create a foundation for the later chapters.

1.2 Relevant Fundamentals of Nanophotonic Light Materials Interaction

Waves in Periodic Systems

Perhaps most fundamental to this work is an understanding Maxwell's equations in different environments. The behavior of light in a homogeneous versus inhomogeneous systems presents opportunity for selective management of electromagnetic energy. The ultimate goal in nanophotonic photovoltaics is to convert this energy into useful electricity. Understanding when different theoretical frameworks or approximations are most apt is required to optimize light-matter interactions to this end. For example, a main achievement of this work is providing a clearer distinction between multiple optical phenomenon is Chapter 5. Suggested texts for

further understanding include *Photonic Crystals: Molding the Flow of Light*[79], *Modern Electrodynamics*[194], *Introduction to Nanophotonics*[52], *Principles of Nano-Optics*[113], *Optics: Principles and Applications*[141], and *Introduction to Electrodynamics*[75]. A detailed development of the mathematical origins of electromagnetic waves is demonstrated to provide low-level connections to the high level wave parameters, such as wave vectors and frequency. This research exploits these wave properties to achieve light management opportunities that traditional geometrical/ray optics can miss.

Electromagnetic Waves

A derivation of the properties of electro-magnetic waves from first principles is shown in order to assist in understanding different conclusions in the context of allowable solutions to Maxwell's equation. Wave vector, $\vec{k}$, origins are developed, (and its relation to frequency, $\nu = 2\pi\omega$), to provide a fundamental understanding and intuition for the work of Chapter 5/Chapter 6, as well as many other parts in this work. The paradigm that solutions to Maxwell's equations can be examined as a linear decomposition of the overall solution to an optical system proves incredibly powerful.

To start, Maxwell's Equations in the absence of free charge and currents are given as:

$$\nabla \cdot \mathbf{D}(\vec{r}, t) = 0 \tag{1.1a}$$

$$\nabla \cdot \mathbf{B}(\vec{r}, t) = 0 \tag{1.1b}$$

$$\nabla \times \mathbf{E}(\vec{r}, t) = -\frac{\partial \mathbf{B}(\vec{r}, t)}{\partial t} \tag{1.1c}$$

$$\nabla \times \mathbf{H}(\vec{r}, t) = \frac{\partial \mathbf{D}(\vec{r}, t)}{\partial t} \tag{1.1d}$$

$$\tag{1.1e}$$

where $\mathbf{E}$ is the electric field, $\mathbf{H}$ the magnetic field, $\mathbf{D}$ the electric displacement, and $\mathbf{B}$ magnetic induction. These are position $\vec{r}$ and time t dependent functions field functions. The electric displacement $\mathbf{D}$ in the absence of free charge is related to the electric field $\mathbf{E}$ by

$$\mathbf{D}(\vec{r}, t) = \epsilon_0 \epsilon_r \mathbf{E}(\vec{r}, t) \tag{1.2}$$

and the magnetic induction $\mathbf{B}$ related to the magnetic field $\mathbf{H}$ by

$$\mathbf{H}(\vec{r}, t) = \frac{1}{\mu_0 \mu} \mathbf{B}(\vec{r}, t) \tag{1.3}$$

where ϵ_0 and μ_0 are the electric permittivity and magnetic permeability constants of free space. In a material, ϵ_r and μ_r are the relative permittivity and relative magnetic permeability of that material, and reduce to unity in free space. The relative magnetic permeability in non-magnetic materials is usually approximately equal to unity,$\mu = 1$. These are the materials of interest here. Material permittivity is usually also a function of position, $\epsilon_r(\vec{r})$. It is also appropriate to assume that the electric displacement $\mathbf{D}$ is linear such that $\epsilon_r(\vec{r})$ does not have any functional dependence on frequency.

These assumptions and substitutions of Equation (1.2) and Equation (1.3) into Maxwell's equations transform Equation (1.1) to

$$\nabla \cdot \epsilon_r(\vec{r})\mathbf{E}(\vec{r},t) = 0 \tag{1.4a}$$

$$\nabla \cdot \mathbf{H}(\vec{r},t) = 0 \tag{1.4b}$$

$$\nabla \times \mathbf{E}(\vec{r},t) = -\mu_0 \frac{\partial \mathbf{H}(\vec{r},t)}{\partial t} \tag{1.4c}$$

$$\nabla \times \mathbf{H}(\vec{r},t) = \epsilon_0 \epsilon_r(\vec{r}) \frac{\partial \mathbf{E}(\vec{r},t)}{\partial t} \tag{1.4d}$$

where the permittivity and permeability constants of Equation (1.4a) and Equation (1.4b) drop out due to the equation being equal to zero. Expressing Equation (1.4c) and Equation (1.4d) with only terms of either $\mathbf{E}$ or $\mathbf{H}$ allows the system of differential equations to be solved. Taking the curl of Equation (1.4c) (and similarly for Equation (1.4d)) gives:

$$\nabla \times (\nabla \times \mathbf{E}(\vec{r},t)) = \nabla \times \left(-\mu_0 \frac{\partial \mathbf{H}(\vec{r},t)}{\partial t} \right) \tag{1.5}$$

Using the definition of the vector Laplacian and the fact that the divergence of the electric field $\mathbf{E}$ (magnetic field $\mathbf{H}$) is zero, Equation (1.4a) (Equation (1.4b)) becomes an expression for $\mathbf{E}$ ($\mathbf{H}$) decoupled from $\mathbf{H}$ ($\mathbf{E}$):

$$\begin{aligned}
\nabla \left(\nabla \cdot \mathbf{E}(\vec{r},t) \right) - \nabla^2 \mathbf{E}(\vec{r},t) &= \nabla \times \left(-\mu_0 \frac{\partial \mathbf{H}(\vec{r},t)}{\partial t} \right) \\
\nabla^2 \mathbf{E}(\vec{r},t) &= \mu_0 \nabla \times \left(\frac{\partial \mathbf{H}(\vec{r},t)}{\partial t} \right) \\
\nabla^2 \mathbf{E}(\vec{r},t) &= \mu_0 \frac{\partial}{\partial t} \left(\nabla \times \mathbf{H}(\vec{r},t) \right) \\
\nabla^2 \mathbf{E}(\vec{r},t) &= \mu_0 \frac{\partial}{\partial t} \left(\epsilon_0 \epsilon_r(\vec{r}) \frac{\partial \mathbf{E}(\vec{r},t)}{\partial t} \right)
\end{aligned} \tag{1.6}$$

Finally, substitution of Equation (1.4d) (Equation (1.4d)) into the result of Equation (1.6) above obtains the decoupled second order differential equations

$$\nabla^2\mathbf{H}(\vec{r},t) = \mu_0\epsilon_0\epsilon_r(\vec{r})\frac{\partial^2\mathbf{H}(\vec{r},t)}{\partial t^2} \tag{1.7a}$$

$$\nabla^2\mathbf{E}(\vec{r},t) = \mu_0\epsilon_0\epsilon_r(\vec{r})\frac{\partial^2\mathbf{E}(\vec{r},t)}{\partial t^2} \tag{1.7b}$$

where Equation (1.7) are characteristic wave equations. These second order partial differential equations are *classical three dimensional wave equations*. In general, solutions take the form of some function $f(\vec{r},t) = g(\vec{r} - \mathrm{v}t)$. The constant v can be positively or negatively valued, and so another valid solution $f(\vec{r},t) = g(\vec{r} - \mathrm{v}t) + h(\vec{r} + \mathrm{v}t)$ can be found due to the linearity of the differential equations. Any sum of the functions g and h can be solutions to f. Here, f is the field of interest, either $\mathbf{H}$ or $\mathbf{E}$.

The most simple (and common) solution to $\mathbf{E}$ or $\mathbf{H}$ is the infinitely differentiable sine wave with amplitude E_0:

$$\mathbf{E}(\vec{r},t) = E_0(\vec{r})\cos(\vec{r} - \omega t) \tag{1.8}$$

The term E_0 is the maximum field amplitude, and the term ω is the wave's phase velocity. An electro-magnetic wave's phase velocity is given by the wave equation in Equation (1.7), $v = c = 1/\sqrt{\mu_0\epsilon_0\epsilon_r}$. This shows the speed of light derives directly from other physical constants of electro statics and the origin of light slowing in a medium with a relative permittivity ϵ_r.

Generalizing and expanding Equation (1.8) allows explicit expression of important components. The equation is briefly reduced to dependence in only one dimension z to demonstrate the significance of scalar values.

$$\mathbf{E}(z,t) = E_0\cos\left(\frac{2\pi}{\lambda}(z - v\lambda t) + \phi\right) = E_0\cos\left(\frac{2\pi z}{\lambda} - 2\pi v t + \phi\right) \tag{1.9}$$

Parameters useful to the context of discussing light waves become apparent in this dissected representation. The wavelength λ, frequency v, and phase offset ϕ are put into context. A factor of 2π does not affect the solution. These terms are transformed into the common form of the vectorial wave expression by substituting the appropriate vector generalizations, and an equivalent expression for the speed of

light follows.

$$z \rightarrow \vec{r} \tag{1.10a}$$

$$kz = \frac{2\pi z}{\lambda} \rightarrow \vec{k} \cdot \vec{r} \tag{1.10b}$$

$$\omega = 2\pi\nu \tag{1.10c}$$

$$c = \omega\vec{k} \cdot \vec{r} = \frac{\omega k_0}{\sqrt{\epsilon_r}} = \frac{\omega k_0}{n} \tag{1.10d}$$

$$\mathbf{E}(\vec{r}, t) = E_0 \cos\left(\vec{k}\vec{r} - \omega t + \phi\right) \tag{1.11}$$

The sine solution becomes an expression of the *wave vector* $\vec{k}$ (also known as the *propagation vector*, or simply the k-vector) and the angular frequency ω. Equation (1.10d) shows the relationship of the wave vector in a homogeneous medium to the free space wave vector is the inverse square root of the relative permittivity. This constant factor is the *index of refraction*, $n = \sqrt{\epsilon_r}$. Another important implication is that the wave is traveling in the direction of $\vec{k}$, and is related to the wave's momentum by $\vec{p} = \hbar\vec{k}$. The conservation of momentum importantly indicates that $\vec{k}$ is also a conserved vector.

The wave solution expressed in terms of a sine function demonstrates the origin of many important scalars and vectors. An equally valid solution, yet more mathematically useful, is the complex infinitely differentiable exponential solution to the wave equation, provided by Euler's formula:

$$e^{i\left(\vec{k}\vec{r} - \omega t + \phi\right)} = \cos(\left(\vec{k}\vec{r} - \omega t + \phi\right)) + i\sin(\left(\vec{k}\vec{r} - \omega t + \phi\right)) \tag{1.12}$$

The physical parts of the solution, i.e. the electric $\mathbf{E}$ and magnetic $\mathbf{H}$ fields, are recovered by taking the real part of the complex solution. Mathematically, this solution is more useful when adding waves, it allows separation of spatial from time dependencies, and greater generalization to complex wave vector, frequency, permittivity as well as other flexibility when finding full field solutions and/or fundamental descriptions of different systems (especially when the assumptions made here do not hold). This form is given below, where the tilde denotes a complex vector function.

$$\begin{aligned}
\tilde{\mathbf{E}}(\vec{r}, t) &= E_0 e^{i\left(\vec{k}\vec{r} - \omega t + \phi\right)} \\
\tilde{\mathbf{E}}(\vec{r}, t) &= E_0 e^{i\phi} e^{i\left(\vec{k}\vec{r} - \omega t\right)} \\
\tilde{\mathbf{E}}(\vec{r}, t) &= \tilde{\mathbf{E}_0} e^{\left(i\vec{k}\vec{r} - i\omega t\right)}
\end{aligned} \tag{1.13}$$

$$\begin{aligned}\tilde{\mathbf{E}}(\vec{r},t) &= \tilde{\mathbf{E}}_{\mathbf{0}}(\vec{r})e^{-i\omega t} \\ \tilde{\mathbf{H}}(\vec{r},t) &= \tilde{\mathbf{H}}_{\mathbf{0}}(\vec{r})e^{-i\omega t}\end{aligned} \tag{1.14}$$

Due to linearity, a sum of these solutions can be used to represent any full solution to an electro magnetic wave problem in a medium with a spatial dielectric function $\epsilon(\vec{r})$, also know as a mode of the optical system. This work is generally concerned with the spatial field dependence of the solutions, $\tilde{\mathbf{E}}_{\mathbf{0}}(\vec{r})$ and $\tilde{\mathbf{H}}_{\mathbf{0}}(\vec{r})$. This is because the work analyzes steady state systems through the examination of field distributions represented by either the Fourier transform of Equation (1.14) or the fundamental harmonic modes of such a solution. These harmonic modes are transverse as required by Equation (1.4a) and Equation (1.4b), $\vec{k} \cdot \hat{n}_{\tilde{\mathbf{E}}_{\mathbf{0}}}$.

It is a point of interest to display Maxwell's equations as an eigenvalue problem, called the *master equation* in Reference [79]. combining Equation (1.4c) and Equation (1.4d) with Equation (1.14) yields

$$\nabla \times \left(\nabla \times \frac{1}{\epsilon_r(\vec{r})} \tilde{\mathbf{H}}(\vec{r}) \right) = \left(\frac{\omega}{c}^2 \right) \tilde{\mathbf{H}}(\vec{r}) \tag{1.15}$$

This displays the spatial permittivity function as a linear operator on the eigenfunction $\tilde{\mathbf{H}}_{\mathbf{0}}(\vec{r})$ with eigenvalues of $\left(\frac{\omega}{c}\right)^2$ and eigenfunctions $\tilde{\mathbf{H}}(\vec{r})$, shown next to be readily described by corresponding k-vector, $\vec{k_m}$.

Plane Waves, Dispersion, and Local Density of Optical States

In a homogeneous environment, the time independent form of the fields is inferred from separating the time component of Equation (1.14). This function is the plane wave representation of the field. It has continuous translational symmetry in free space, meaning that any real wave vector is a valid solution.

$$\begin{aligned}\tilde{\mathbf{E}}(\vec{r}) &= \tilde{\mathbf{E}}_{\mathbf{0}} e^{i\vec{k}\cdot\vec{r}} \\ \tilde{\mathbf{H}}(\vec{r}) &= \tilde{\mathbf{H}}_{\mathbf{0}} e^{i\vec{k}\cdot\vec{r}}\end{aligned} \tag{1.16}$$

The plane wave is polarized in the direction of $\tilde{\mathbf{E}}_{\mathbf{0}}$ ($\tilde{\mathbf{H}}_{\mathbf{0}}$). Applying Equation (1.15) shows that the eigenvalues are of the form $\frac{\omega}{c^2} = \frac{\vec{k}|^2}{\epsilon}$. This gives the definition of the *dispersion relation*, $\omega = \frac{c|\vec{k}|}{\sqrt{\epsilon}} = \frac{c|\vec{k}|}{n}$ for a plane wave. In general, the dispersion relation of any wave function is the functional relation between ω and $|\vec{k}|$, $\omega(|\vec{k}|)$, and provides some relationship of the wave speed and the refractive index to the

wave vector. Terminologies such as *slow light* or *slow modes* refer to the fact that the wave has a large inverse coefficient modifying the speed of light in a vacuum for a given k-vector. More rigorously, the speed of a wave is given by the group velocity, defined as the gradient of ω with respect to $\vec{k}$:

$$v_g \equiv \vec{\nabla}_{\vec{k}} \cdot \omega \tag{1.17}$$

The scalar, or 1 dimensional, representation $v_g = \frac{d\omega}{dk}$ is also useful for qualitative understanding of wave speed. This is the origin of the terminology *effective index* or *mode index*, helping to connect the familiar propagation of a plane wave to that of some mode with a complicated field function.

The group velocity is inversely proportional to the *local density of optical states (LDOS)*, $LDOS \propto \frac{d\omega}{dk}^{-1}$. For each infinitesimal change in wave frequency, there is a corresponding change in the wave vector. The frequency is directly proportional to the electromagnetic energy by Planck's equation, $E = \hbar\omega$, thus another useful way of thinking about this relationship is the amount of change in energy for each change in $\vec{k}$. A decrease in this group velocity corresponds to a higher density of electromagnetic states, and the ability for a greater amount of energy to exist in an optical environment. In a simple homogeneous environment, this is proportional to the permittivity (n^2), but in a nano-structured environment, especially a periodic environment, opportunities exist to greatly decrease the group velocity at certain frequencies. Electromagnetic energy will concentrate into modes that have a high LDOS. Analogously, the LDOS is related to the traditional solid-state description of the Density of States equation in a periodic system by a factor of $|\vec{e}_l \cdot E_{n,\vec{k}}(\vec{r})|^2$. A rigorous representation is presented below for context in this work.(see Bloch's Theorem, Chapter 4 of Reference [81], and Reference [112]):

$$LDOS_l(\vec{r},\omega) = \frac{\epsilon(\vec{r})}{(2\pi)^d}\Sigma_n \int_V \delta[\omega - \omega_n(\vec{k})]|\vec{e}_l \cdot E_{n,\vec{k}}(\vec{r})|^2 d\vec{k} \tag{1.18}$$

where $|\vec{e}_l \cdot E_{n,\vec{k}}(\vec{r})|^2$ is the electric field magnitude in the direction of a dipole orientation $\vec{e}_l$ for mode number n and k-vector, V is some k-space volume of dimensionality d, and δ indicates the Dirac delta function. This form explicitly shows the important considerations that the LDOS is directly proportional to the positionally dependent electric field strength, and vice-versa. The dipole orientation dependence of the LDOS also has important implications for the last chapters of this work.

Total Internal Reflection

In a linear non-dispersive medium, such as a transparent material, plotting dispersion relation gives a straight line. The phenomenon of total internal reflection (TIR) is usually represented as a consequence of Snell's law for a ray of light incident in a refractive index of n_1 at some angle θ_1 from the normal of a surface that is refracted into another medium of index n_2 at an angle θ_2:

$$\frac{\sin(\theta_1)}{\sin(\theta_2)} = \frac{n_2}{n_1} \tag{1.19}$$

when $n_2 < n_1$ TIR occurs because the solution to Snell's law is imaginary, and light rays are considered *index guided* in that medium since they cannot escape and must travel with some direction component parallel to the surface. The angle at which this occurs is given by rearranging Equation (1.19).

$$\theta_1 = \arcsin\left(\frac{n_2}{n_1}\right) \tag{1.20}$$

This can also be derived from wave vector component conservation, providing a more general and useful paradigm for examining specific modes. The condition for index guiding is re-expressed in terms of the required wave-vectors for guided light in the plane of a high refractive index region, perpendicular to the normal. The wave vector is defined by Equation (1.10d) as the free space wave vector $\vec{k}_0$ modified by a refractive index n:

$$\begin{aligned} |\vec{k_0}| = \frac{2\pi}{\lambda_0} = \frac{\omega}{c} \quad , \quad |\vec{k_m}| = n\frac{2\pi}{\lambda_0} = \frac{\omega}{c} \\ n|\vec{k_0}| = |\vec{k_m}| = \frac{\omega}{c} \end{aligned} \tag{1.21}$$

where λ_0 is the wavelength in vacuum and λ is the wavelength in a dispersion-less medium of refractive index n of a plane wave with an angular frequency ω, and the speed of light c. $\vec{k}_m$ is the wave vector of some mode (wave) inside of a lossless medium, which differs from the free space by a factor of n. Again, the wave vector gives the propagation direction.[1]

By separating $\vec{k}_0$ $\vec{k}_m$ into their vector components, the perpendicular component to the structure and direction of the index guided mode is as $\vec{k_0 z}$ and $\vec{k_{mz}}$ respectively.

[1] Strictly, the wave propagation direction is given by the velocity vector. The wave vector and velocity vector directions are the same for familiar plane waves, but for modes of a complicated structure, such as a periodic permittivity functions, they can be more rigorously defined by solving Equation (1.17) as in Reference [79] page 40. However, the conditions for guided wave vectors are unchanged.

Similarly the in-plane components are given by $\vec{k_{0\|}}^2 = \vec{k_{0x}}^2 + \vec{k_{0y}}^2$ and $\vec{k_{m\|}}^2 = \vec{k_{mx}}^2 + \vec{k_{my}}^2$. The index guiding condition for a slab of material must satisfy:

$$\vec{k}_{\|}^2 = \vec{k}_x^2 + \vec{k}_y^2 \tag{1.22a}$$
$$n^2\vec{k}_0^2 = \vec{k}_{m\|}^2 + \vec{k}_{mz}^2 \tag{1.22b}$$
$$n^2\vec{k}_0^2 - \vec{k}_{mz}^2 = \vec{k}_{m\|}^2 \tag{1.22c}$$
$$\sqrt{n^2\vec{k}_0^2 - \vec{k}_{mz}^2} = \sqrt{\vec{k}_{m\|}^2} \tag{1.22d}$$

By Equation (1.22d), the wave $\vec{k}_m$ has enough magnitude in the $\vec{k}_z$ component to propagate through an interface of free space and material with refractive index n only when $n\vec{k}_0^2 > \vec{k}_{mz}^2$. There is enough magnitude in the z direction such that magnitude of the free space wave vector $\vec{k_0}$ is unchanged after refraction. This is the wave vector expression of Snell's law. Wave guiding (TIR) occurs when:

$$\begin{aligned} n^2\vec{k}_0^2 &< \vec{k_{mz}}^2 \\ n^2\vec{k}_0^2 - \vec{k}_{mz}^2 &< \vec{k}_{m\|}^2 \end{aligned} \tag{1.23}$$

and the root of Equation (1.22d) becomes purely imaginary, corresponding to an *evanescent wave* $\vec{k_0}$ that decays exponentially into free-space. Alternatively, waves from free-space cannot enter a medium into modes with k-vectors greater than that of free-space. In the classical picture, this is responsible for a maximum angle of refraction for light entering a high refractive index environment at an angle $\theta_{incident} \lessapprox 90\,\text{deg}$. This gives rise to the phenomenon of a *escape cone*, which provides intuition for the allowed directions that light can enter and exit a material with an interface to another material of differing refractive index. A schematic is found on the left of Figure 1.4. Yet another to state TIR is that the wave outside of the high index environment is must be phase matched to the wave inside. Implications of this are subtle. The decaying wave actually extends away from the interface, but does not propagate freely, and is bound to the high index environment. However, this also means that optical components in this near-field are close enough to interact with this decaying field, providing opportunities for light management design otherwise hidden by classical ray-paradigm optics.

Briefly, a third type of wave vector, a complex wave vector $\tilde{\vec{k}}$, can be found as a solution to the electromagnetic wave problem. There is no restriction disallowing a complex wave vector in the solution of Equation (1.14). A simple instance of

these waves is not readily shown here, but can be understood qualitatively in the context of purely real or purely imaginary wave vectors. Physically, these waves propagate in either free-space or within a lossless permittivity environment $\epsilon(\vec{r})$. They are characterized by a change in the field amplitude when entering or exiting the environment $\epsilon(\vec{r})$. The transitional decay happens over a short enough distance that $k_0/\vec{k}$ maintain appreciable amplitude in either environment. Thus these waves are not guided waves, nor are they purely plane waves, but valid modes of a structure. These waves are called *leaky modes* or *lossy modes* (not to be confused with purely imaginary waves which are lossy and evanescent). These types of waves are typically encountered in periodic $\epsilon(\vec{r})$ structures and can be important modes of different light management incoupling design.

Bloch's Theorem and Periodicity

An inhomogeneous environment with discrete periodicity can be characterized by a primitive lattice vector $\vec{a}$ such that $\epsilon_r(\vec{r}) = \epsilon_r(\vec{r} \pm m\vec{a})$ for any integer m. For a translation in position $\vec{b}$, the resulting wave vector shift must be a multiple of $\frac{2\pi}{a}$ to leave the wave function unchanged:

$$\tilde{\mathbf{E}}(\vec{r}) = \tilde{\mathbf{E}}_\mathbf{0} e^{i\vec{k}\cdot\vec{r}} = \tilde{\mathbf{E}}_\mathbf{0} e^{i\vec{k}\left(\vec{r}\pm m\vec{b}\right)} = \tilde{\mathbf{E}}_\mathbf{0} e^{\pm im\vec{k}\cdot\vec{b}} e^{i\vec{k}\cdot\vec{r}} = \tilde{\mathbf{E}}_\mathbf{0} e^{\pm im\vec{k}\cdot\frac{2\pi}{\vec{a}}} e^{i\vec{k}\cdot\vec{r}} \tag{1.24}$$

The vector $\vec{b}$ is the reciprocal lattice vector of the periodic environment. Combined with the fact that any solution of the wave equation can be represented as the sum of all modes with appropriate expansion coefficients results in eigenvector solutions $\tilde{\mathbf{E}}_k$

$$\tilde{\mathbf{E}}_k = \tilde{\mathbf{E}}_\mathbf{0} e^{\left(i\vec{k}\cdot\vec{r}\right)} \cdot \mathbf{u_k}(\vec{r}) \tag{1.25}$$

for some periodic function describing an infinitely periodic lattice $\mathbf{u_k}(\vec{r})$. The result is that each mode can be expressed as a plane wave solution multiplied by some periodic function. The Bloch theorem also has the implications that $\vec{k}$ is conserved under translations modulo $\vec{b}$. This allows the study of modes in a periodic permittivity function to be restricted to wave vectors $\frac{\vec{b}}{2} \leq \vec{k} \leq \frac{\vec{b}}{2}$ since wave vectors $\vec{k} \geq \frac{\vec{b}}{2}$ are equivalent to $\vec{k} + \frac{\vec{b}}{2}$. We can further restrict the area to only positive vectors $0 \leq \vec{k} \leq \frac{\vec{b}}{2}$ because $-\vec{k} + \frac{\vec{b}}{2} = \vec{k} - \frac{\vec{b}}{2}$ by symmetry. This concept is the study of the irreproducible Brillouin zone, where a certain range of unique wave vectors cannot be represented as a sum of reciprocal lattice vectors.

After a description of modes, periodicity, and wave vectors, Figure 1.2 demonstrates the variety of these modes for a photonic crystal from Chapter 7. Figure 1.2 is a

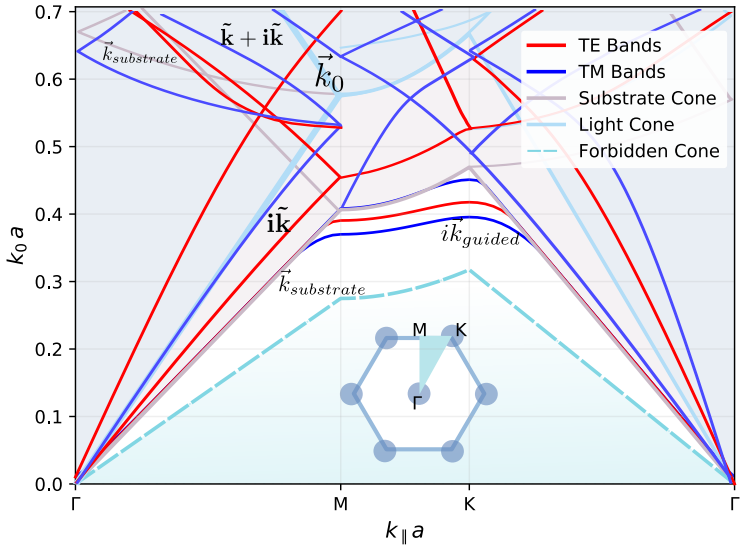

Figure 1.2: A folded band diagram for a hexagonal photonic crystal slab of refractive index 2.2 on a glass substrate. Light blue and gray bands are the light line and substrate line, respectively. A continuum of plane-wave occupy the shaded areas. Bands represent discrete modes at a given $\vec{k}_0$ and $\vec{k}_\parallel$. Beneath the light line and substrate light line, modes are purely complex and are guided in either the substrate (gray area) or the photonic crystal (white). Bands that cross the line are propagating complex wave vectors. No modes have enough momentum to exist beneath the cone formed by $n_{PC}\vec{k}$ (teal).

folded band diagram, plotting the in plane wave vector components $\vec{k}_\parallel$ along the reciprocal directions of the lattice's irreproducible Brillouin zone. Waves with momentum greater than these symmetry points fold back onto these symmetry vectors by Bloch's theorem. All the in-plane modes can be represented in these band diagrams.

Purely real waves occupy a continuum above the light line in the blue shaded area. Discrete modes solutions are represented by the various lines called bands. Bands can be complex $mathbf\vec{k} + i\vec{k}$, and thus can propagate in free space but also exist within the structure. They can also be purely imaginary, in that they are guided within the substrate (modes beneath the light line, gray shaded area) or photonic crystal (modes beneath substrate line in white shaded area). It is readily apparent that free space modes can be numerous, while photonic crystal slabs may have only a few guided modes. The inverse slope of each mode is proportional to the LDOS for each mode, as discussed previously. Specifically, the photonic crystal modes have slopes that are exactly zero at the Brillouin zone. Electromagnetic energy concentrates into these modes.

The Statistical Ray Optic limit

Ray optics develops a picture of light behavior that is independent of the wave nature of light. Light is still readily described by the wave vector $\vec{k}$, but focus is given on the *intensity* distribution, or a description of power per unit area. Intensity is proportional to the square of the electric field function, $I \propto |\tilde{\mathbf{E}}|^2$, removing phase considerations. The ray optics picture considers light to behave as a plane wave described by a ray in the same direction as $\vec{k}$. It is most valid in the limit that light interacts with materials and interfaces over long distances, propagating many wavelengths from one inhomogeneity before interacting with another. In this regime, wave vectors are scattered by roughness or other interface texturing. Scattering of intensity and $\vec{k}$ can be minimal to none for very large wavelengths relative to interface texturing, isotropic for texture on the same order of the wavelength, or a distribution in between. In many instances statistical approximations and models are very successful in quantifying different behaviors of light.

A particularly powerful description of the intensity distribution of light in one medium compared to that of free space is the *statistical ray optic limit* or the $4n^2$ *limit* developed by Yablonovitch in 1982.[181, 183] The formulation shows the thermodynamic limit of photon intensity inside a medium of refractive index n compared to free space, and is a popular figure of merit for solar cell light trapping. A common objective of nanophotonic light management is the possibility to surpass this thermodynamic limit by nano-structuring. This shifts density of optical states from certain frequency bands to target frequency bands. The classical density of optical modes is a constant value inside a homogeneous medium.

For a smooth slab of high refractive index material, with sufficiently small but real absorption, illuminated by isotropic black body radiation on all sides, light can only enter or exit the material as determined by Snell's law and the corresponding the escape cone. The average light intensity inside the slab will be equivalent to that of free-space since a significant portion of the available propagation directions are inaccessible. To access all wave-vectors, the surface needs to be structured or roughened to scatter into these restricted modes. The ray-optic limit of intensity is found by considering a textured planar sheet of homogeneous material with n greater than 1. Surrounded by black-body radiation on all sides, the electromagnetic energy density is

$$I \equiv U\frac{d\omega}{dk} = U v_{group} = \frac{\hbar\omega}{e^{\frac{\hbar\omega}{kT}}}\frac{d\Omega n^2 \omega c}{4\pi^3} \tag{1.26}$$

which is a modified Planck blackbody radiation intensity expression, with energy

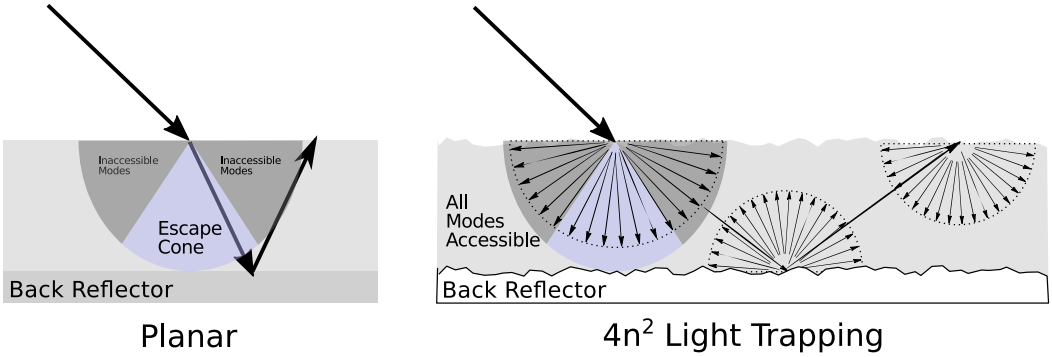

Figure 1.3: A planar versus Lambertian textured absorber. Light can only access the modes of the escape cone in a planar material. A textured material allows light to explore the entire slab, filling all of the available modes.

density U, group velocity, frequency ω, wave number k, and differential solid angle Ω. The intensity in the material differs by only a factor of n^2 relative to free-space. This intensity can be doubled by limiting the system to a single semi-infinite half-space. This is accomplished by placing a isotropically scattering, white *Lambertian* surface or a perfect mirror on one side of the slab. In the limit of perfectly isotropic scattering and Ergodic behavior, light is sufficiently scattered due to both the textured surface and the back-reflector such that light explores the entire high-index material. This leads to an increase of the internal intensity by a factor of $I_{internal} = 2n^2 I_{incident}$. This leads to a $4n^2$ ray-optic maximum absorption enhancement relative to the exponential Beer-Lambert frame-work.

Beer-Lambert absorption gives the relative intensity of incident light to intensity at some point along a linear direction in an absorbing medium. The absorption coefficient α determines how strongly the initial intensity decays along the travel direction, z, after some distance or thickness of a material t.

$$I(t) = 1 - I_0 e^{\int_0^t -\alpha dz} = 1 - I_0 e^{-\alpha t} \tag{1.27}$$

The volume absorption is given by

$$A_{vol} = \int \alpha \frac{I_{internal}}{2\pi} dV d\Omega = \alpha t I_{internal} A_{incident} \int_0^\pi sin(\theta) d\theta = 2\alpha t I_{internal} A_{incident} \tag{1.28}$$

where $A_{incident}$ is the area of incident radiation. A factor of 2π on the left hand side accounts for $I_{internal}$ being spread over a full sphere due to bi-directional scattering at the interfaces (see Reference [183], section 4). The differential volume element is accounted for by the thickness and incident area. From Equation (1.26),

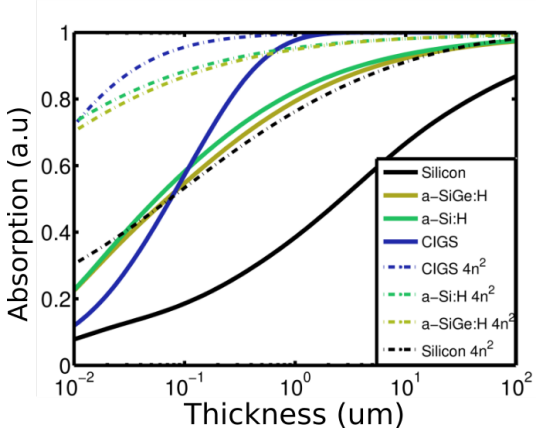

Figure 1.4: The $4n^2$ absorption limits with increasing thickness compared to the absorption from a single, un-scattered photon path.[161] Shown are curves for silicon, a-Si:H, a-$Si_{1-x}Ge_x$:H, and CIGS, materials that were studied in this work.

$I_{internal} = 2n^2 I_{incident}$, substitution into Equation (1.28) gives

$$2\alpha t I_{internal} A_{incident} = 4n^2 \alpha t I_{incident} A_{incident} \tag{1.29}$$

giving the maximum absorption enhancement factor of $4n^2$. For a high index semiconductor such as silicon, this factor provides an effective photon path length of near 50x. The consequence of occupying all available modes in the context of internal intensity and light absorption is that significantly less material can be used to absorb the incident radiation, important for decreasing costs of applications such as solar energy. Increasing the maximum value of $I_{internal}$ can lead to volumetric absorption enhancements beyond the classical limit within a certain range of frequencies.[17] Nanophotonic light trapping in photovoltaic devices manipulate the a device's LDOS such that no the above statistical formulation no longer holds at all frequencies.

1.3 Photovoltaics

Here, the photovoltaic conversion of photons is presented. Applying nanophotonic physics helps to couple more photons into a greater number of modes. Further, Chapter 3 and Chapter 4 demonstrate that the location of absorption within a device is equally important to photon incoupling. This can have large effects on both the current and voltage that a PV cell can realize, and thus its power output. Key to increasing solar power conversion efficiency is an understanding of the available photons and which of those need be better captured. Light should also be converted to electrons at optimum locations. An overview of the photovoltaic device and solar spectrum is given to inform which areas of a solar cell benefit light trapping. A

detailed understanding can be found in resources such as Reference [155], [178], [144], and [124].

Photovoltaic Device Energy Bands

A semiconductor device is characterized by the property of an electronic band-gap. Similar to the wave nature of light described above, the wave nature of electrons in a crystal lattice gives rise to certain modes and propagation vectors that are allowed, while others are disallowed. Bloch's theorem and the periodic solutions to Schrödinger's equation are responsible for this phenomenon. These modes are termed *energy states* or *electron states* in solid state physics. Large numbers of discrete electron energy states close enough in energy level that they result in continuous bands at the infinite periodicity limit. The semiconductor crystal in question has a finite number of electrons, and thus these states are occupied up to an energy level known as the valence band. A certain range of forbidden energies separates this valence band from the next highest energy band, the conduction band. This forbidden range is known as the *band gap*. Electricity flow requires energy states that are unoccupied, so electrons with energy equal to or above the conduction band are free to travel, but valence band electrons cannot.

At ambient room temperature, thermal energy promotes a certain amount of electrons to the conduction band, leaving behind an empty state called a hole. The energy level distribution of electron occupation is described by the *Fermi-Dirac distribution*. The *Fermi level* is the energy with a 0.5 probability of occupation by an electron; this distribution describes the chemical potential of the carrier. In an intrinsic semiconductor, this level lies at the middle of the band gap at 300 K. By introducing atoms which differ in atomic number, or *doping*, hole or electron states are introduced into the band-gap. These dopant states are close in energy to the band edges, on the order of $k_B T$, that thermal fluctuations promote carriers between these dopant energy levels and the valence/conduction bands. These close additional energy states will shift the Fermi energy towards those states. A p-type semiconductor will have added free states, and the Fermi level shifts towards the valence edge, while in an n-type semiconductor the opposite.

Perhaps the most common way to create a PV device is to physically mate an n-type and p-type semiconductor, forming a diode junction. Figure 1.5 shows a schematic of energy levels in a p-n diode and depicts subsequently covered phenomena. In the dark, the equilibrium Fermi level is flat through the device. Due to the dopant energy

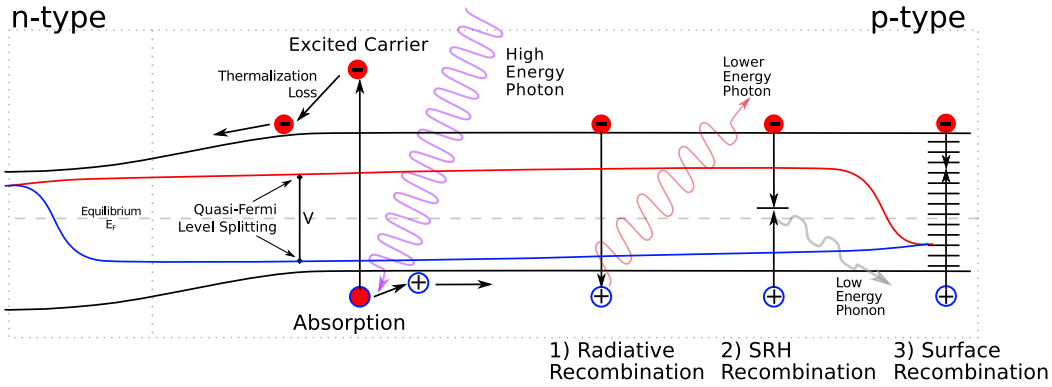

Figure 1.5: A schematic of some relevant charge carrier behavior in a p-n solar cell under steady illumination. High energy light is absorbed, some energy is lost to thermalization of the carrier. Excited carrier populations create potential energy gradients, which charge will diffuse down. The difference in the quasi-Fermi levels creates a voltage, V. Carriers are subject to mid-gap Shockley-Reed-Hall recombination and surface recombination.

level density the valence and conduction bands of each semiconductor away from each other as the Fermi level must be flat. Across the junction, a built in electric field results from the energy difference of these bands. Applied positive voltage results in an exponential flow of current in one direction. By raising the potential of majority carriers, voltage essentially moves conduction bands closer in energy. This reduces the built in electric field energy barrier and allows greater diffusion across the new potential energy gradient, creating current. Negative voltage pushes the conduction bands further apart, and current saturates in the reverse. A similar but spontaneous current results from external stimulus such as light. Photons with energy greater than the band gap will promote a valence electron by energy equivalent to the photon. This puts the electron into the conduction band and leaves *hole* in the valence band. Energy that raises an electron beyond the conduction band is lost to *thermalization* as the carrier falls to the band edge. Under a steady state of illumination, two Fermi-Dirac distributions termed the *quasi-Fermi levels* ϵ_{FC} and ϵ_{FV} describe the new populations of excited electrons and holes respectively. The difference between these two quasi-Fermi levels is the potential energy of these carriers, manifests as voltage across the device. Excited carriers diffuse down the chemical potential gradient towards the edges, where an electrical contact collects the current to do work in an external circuit.

Excited carriers do not always make it to the edge contacts in real devices. A number of defects create recombination pathways that impact the ability of PV devices to separate charges. Only three of many are presented here. First, radiative

recombination is the preferred method of recombination. When not connected to an external circuit, carriers must recombine or, an unphysical population of all electrons would build up in the conduction band. Thus radiative recombination does not "lose" any energy in the sense radiative recombination is the mechanism that balances the number of photons absorbed with the number that radiated, creating an equilibrium or steady-state. In fact photons re-emitted inside the device can be recycled by being reabsorbed before exiting completely. The second recombination pathway is *Shockley Reed Hall* recombination. A defect state with energy level near the center of band gap provides the largest free energy change for excited carriers, and is quickly filled. The energy emitted is lost as a low-energy phonon that cannot be re-absorbed and increases the device temperature. The third relevant recombination pathway is *surface recombination*. At a free surface, the periodic lattice is terminated, and a continuum of energy states exists in the band gap. This type of recombination is actually required for electrons that travel through an electrical circuit to recombine with a hole. However, when a minority carrier, such as the electrons on the right of Figure 1.5, diffuse to the wrong edge, they are lost to surface recombination. The occurs at all interfaces in the device to varying degrees. *Passivation* reduces the number of surface states and corresponding carrier loss. Chapter 4 addresses this type of recombination.

The Solar Spectrum

Key to solar PV operation and thus its overall power conversion efficiency is the incident solar photon flux. Figure 1.6 shows standard the ASTM AM1.5G solar irradiance spectrum, $S(\lambda)$, in dark blue and the equivalent photon spectrum, $PC(\lambda)$, in gray. The sun's solar radiation is well approximated by a black-body emitter at a temperature of 5800 K, but atmospheric elements absorb part of this spectrum, creating sharp dips in the flux that reaches the earth's surface. This work uses the AM1.5G spectrum when calculating total absorbed photons in simulated solar cells. The red shaded portion of this spectrum represents the spectral power that is converted by an ideal CIGS solar cell device with a band gap of 1.15 eV. The spectral power at each wavelength is less than the total available power due to thermalization of electrons, as displayed in Figure 1.5. This lost power is shown in light blue. Finally, there is a portion of solar power lost because the photon energy is too low to promote valence band electron (orange). This light is either reflected or absorbed as heat, but cannot be converted to electricity by the PV device.

The entire AM1.5G spectrum has an integrated photon-flux, often referred to here

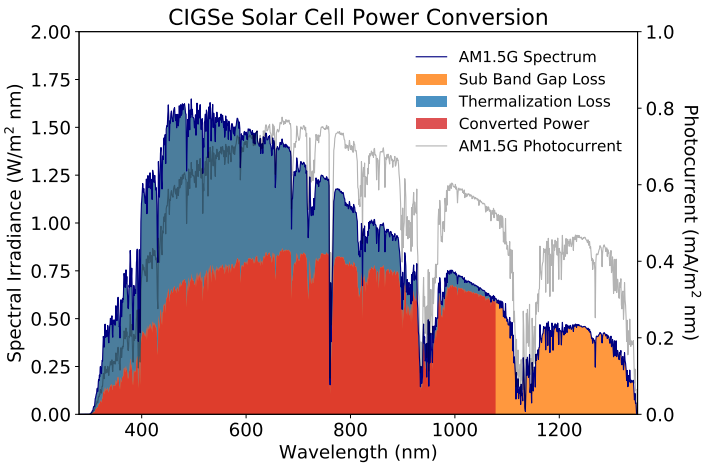

Figure 1.6: The AM1.5G spectrum represents the Sun's typical irradiance and photocurrent at Earth's surface. Power than can be converted by a CIGS solar cell is colored red. The photocurrent and power are related by photon energy, $E = \hbar\omega$.

as photocurrent, equivalent to 68.9 mA cm^{-2}. About 1/3 of this is usually not above the band gap energy of common semiconductor devices. Today's dominant solar cell technology is silicon based, with a band gap of 1.11 eV, has 43.94 mA cm^{-2} available for absorption.

Current-Voltage Relationship

The power per area of a solar cell depends on both the voltage and current output of the device, since electrical power is the product of the two, $P = VJ$. Figure 1.7 shows the characteristic exponential current-voltage (JV) relationship of a solar cell under illumination. When a solar cell's contacts are connected by a lossless wire, the cell is short circuited and outputs the maximum possible current density, the short-circuit current density (J_{SC}). The J_{SC} is the result of competing generation and recombination rates. Generation rate G is found by integrating all absorbed solar photons [178]:

$$G = J_{sc} - R_{non-rad} = -q \int_0^{\text{inf}} \alpha(\lambda) t S(\lambda)(\lambda) \tag{1.30}$$

where the Beer-Lambert absorption/extinction coefficient (α) gives wavelength dependent probability of photon absorption in a material of thickness t. q is the elementary charge. The generation rate is equivalent to the J_{SC} when the non-radiative recombination rate $R_{non-rad}$ is zero. A non-zero recombination rate introduces losses, and means a non-unity internal quantum efficiency (IQE) η_{Int}, or the efficiency with which each absorbed photon is converted to a collected electron.

The external quantum efficiency (EQE) combines the absorption with the IQE and reflection to give a useful equation to predict the J_{SC}.

$$\begin{aligned} J_{sc} = G - R_{non-rad} &= -q \int_0^{\text{inf}} \eta_{Int}(\lambda)\alpha(\lambda)tS(\lambda)(\lambda) \\ J_{sc} &= -q \int_0^{\text{inf}} \eta_{Ext}(\lambda)S(\lambda)(\lambda) \end{aligned} \tag{1.31}$$

The opposite of this condition is the open-circuit, where the cell produces the maximum voltage, open circuit voltage (V_{OC}). An ideal solar cell with only radiative recombination achieves a V_{OC} by the equations given below, where k_b is the Boltzmann constant, T is temperature, J_0 is the diode reverse saturation current, J_0^{rad} and $Jnon - rad_0$ are the radiative and non-radiative recombination contributions to J_0.[51, 124, 144, 178]

$$\begin{aligned} V_{OC} = \epsilon_{FC} - \epsilon_{FV} &= \frac{k_b T}{q} ln\left(1 - \frac{J_{SC}}{J_0}\right) \\ &\approx \frac{k_b T}{q} ln\left(\frac{J_{SC}}{J_0^{rad}}\right) + \frac{kT}{q} ln\left(\frac{J_0^{rad}}{J_0^{rad} + J_0^{non-rad}}\right) \\ &\approx \frac{k_b T}{q} ln\left(\frac{J_{SC}}{J_0^{rad}}\right) + \frac{kT}{q} ln(Q_{LED}) \end{aligned} \tag{1.32}$$

The V_{OC} of an ideal solar cell only experiences radiative recombination. Deviation from the ideal is determined by the fraction of radiative emission compared to the total recombination in the dark. The implication is that a solar cell with high radiative recombination is also a good Light Emitting Diode (LED), thus it can be described by an external LED efficiency, Q^{LED}.[51, 124] A last important detail of the V_{OC} is that it is defined as the difference in potential of the quasi-Fermi levels. Both depend on the volumetric concentration of excited carriers. Rather than only attempting to increase this value by adding more absorbed photons or reducing recombination, reducing the volume these populations exist in should increases the voltage. This effect is seen in nanophotonic thin-film solar cells, where physical dimensions affect both the J_{SC} and V_{OC}.

The product of the current with the voltage gives the power curve depicted. Maximum power output occurs near the exponential knee, represented by the shaded area in the plot. The ratio of maximum power to the J_{SC} and V_{OC} product defines a parameter called the fill factor (FF) that gives an intuition of the JV curve "squareness". Along with the J_{SC} and V_{OC}, the FF can be used to quickly compare the

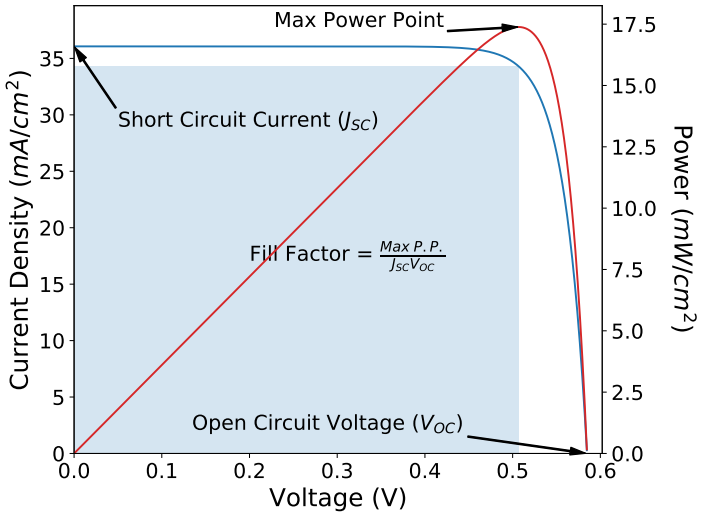

Figure 1.7: An example of CIGS single junction solar cell with realistic EQE=0.85 and Q_{LED}=10^{-6}
under AM1.5G illumination. The common solar cell performance parameters are labeled.

quality of a solar cells. For example, devices with high V_{OC} and high J_{SC} but a low fill factor exhibit losses from electrical resistance, or from shunting.

Finally, the power conversion efficiency, or often just efficiency, is the ratio of power from the cell relative to power incident upon the cell. The integrated power density from the AM1.5G spectrum of Figure 1.6 is 100.03 mW cm^{-2}. The power density output of the solar cell depicted in Figure 1.7 is 19.43 mW cm^{-2}, for a power conversion efficiency of 19.4%. This solar cell is non-ideal, with a EQE of 0.85 and Q_{LED} of 10^{-6}. This is contrasted to an ideal solar cell with a band gap tuned to the AM1.5G which has a maximum theoretical 33% solar power conversion efficiency.

Tandem Devices

This section covers one of the multitudes of solar cell and PV devices. This also work addresses tandem solar cells, in which two devices are are either monolithically or mechanically stacked on top of each other. A large band-gap device placed in front of a lower band gap device splits the solar spectrum between the two, converting more power and achieving an enhanced efficiency due to minimizing thermalization losses. Monolithic tandem devices only pass a single current value through the circuit, so the minimum current density produced by either cell becomes a limiting factor. Device design must take this into account and balance the absorbed photocurrent

in each sub-cell; the subject of Chapter 3 presents nanophotonic strategies to meet this goal. Alternatively, mechanically stacked tandem cells have four electrical terminals, relaxing this current matching requirement since the power from each is collected individually. A novel design of this type is studied in Chapter 6.

1.4 Summary

This chapter presented a compelling motivation for the study of solar energy technologies. The intersection of nanophotonics and photovoltaics provides unique opportunities to aid in the goal of clean solar energy generation. A summary of this work's scope is also provided. Finally, foundational principles required to gain context in the scope of this thesis were presented. This author encourages readers to explore the fascinating physics and materials science of solar cell devices and nanophotonics through referenced texts. A deeper knowledge will enable a fuller grasp and appreciation for each achievement presented here.

Chapter 2

SCALABLE NANOPHOTONIC FABRICATION BY NANOIMPRINT LITHOGRAPHY

2.1 Introduction

Among many potential routes to bridging the solar-nanophotonic length scale gap are molecular self-assembly, and innovative engineering efforts towards large-scale patterning and etching. Intriguingly, one of the few comparable industries, in terms of length scale disparity, is that of the paper printing industry, where over 120 million newspapers were produced annually at its peak in the 1990's.[6] We can estimate this to be in the thousands of kilometers annually, but is low enough cost to be affordable to average consumers. This examples provides motivation to focus on similar roll-to-roll processes such as rolling UV lithography masks, gravure printing, and the focus of this work – NIL. Whether described nominally as pressure-embossing, hot-embossing, substrate conformal imprint lithography, or nanoimprint lithography, these processes share the same principle of a physical transfer of a nanopattern from one substrate to another. NIL stands out for nanophotonic applications due being able to directly print dielectric materials properties and the potential for roll-to-roll scaling.

In this work, efforts are made to enable the promises of nanophotonic light management in solar PV devices by constraining designs to be NIL compatible designs possible. Experiments to fully fabricate devices with NIL were performed, and in some instances encouraging successes were realized. These designs and techniques build upon previous in-house and literature works to provide another step forward in scalable nanophotonic design for solar energy.

2.2 The Nanoimprint Lithography Process

Unsurprisingly this process begins at the bottom. The dimensions of interest are bounded by the single digit micrometer scale and typically decrease to the hundreds to tens of nanometers at the lower bounds. Fortunately, NIL excels in both these regimes and has even been shown effective at the length scale of single nanometers.[54, 170] The general process is shown in Figure 2.1. Upon the selection or design of a particular nanophotonic structure a first mold must be fabricated. The approach taken in this first step was utilizing the proven nanofabrication techniques

and tools, including with rare or new methods. The use of these tools is not a fundamental requirement of general NIL, but was effective for this work, and at times critical, for this work's achievements.

Figure 2.1A) shows how EBL was used to define a pattern in polymer resist cast upon a silicon or other semiconductor substrate. Silicon was most commonly used, though work was demonstrated in III-V semiconductors including InP. This substrate was turned into a master mold through ICP-RIE etching represented in Figure 2.1B), and is in the structure of the final intended nanoimprinted structure. This mold can be copied multiple times as in Figure 2.1 C)-D). These master molds should be able to be re-used hundreds or more times over. Finally, the stamp is pressed into a liquid resist, allowed to set, and removed as shown in Figure 2.1E)-F).[170] The final structure Figure 2.1G) was either an the active nanophotonic element, or served as an etch mask for further reproduction of the original pattern, skipping the bottleneck of EBL in Figure 2.1A).

Master Mold Fabrication

To prepare the master mold of nano-pillars or nano-holes, EBL and ICP-RIE techniques were used. First, a silicon wafer was cleaned via ultrasonication in acetone and then isopropyl alcohol (IPA), each for 5 minutes. Next a dip in buffered-HF acid was performed for between 15-30 seconds to hydrophilicize the surface by removing the native silicon dioxide layer. The resist was spun onto the wafer within 20 minutes of this cleaning. For negative tone patterns, MA-N2803 was spun coat onto the wafer at 4,000 rpm with a minimal ramp time for 45s. The wafer and resist was then baked on a hot plate at 90 °C for 60s. For positive tone patterns, ZEP-520a was spun coat at 500rpm for 5 second and then at 4,000 rpm for 45s and then baked on a hot-plate at 180 °C for 2 minutes.

Fabrication of nanocone structures requires different patterning steps as follows after the buffered HF cleaning. The wafer was rinsed in a petri dish with acetone for 2 min, followed by a rinse in a petri dish of methanol for 2 min. The wafer was dried with a nitrogen stream and placed on a hot plate at 180 °C for 2 min. The wafer was allowed to cool for 1 min. Immediately after, polymethyl-methacrylite (PMMA) 495-A4 was spun cast onto the wafer at 3500 rpm for 1 min and then placed back onto the hot plate to bake for 5 min at 180 °C. The wafer was allowed to cool for 1 min. Next, PMMA 950-A4 was spun cast on top of the previous PMMA layer at

[1]Image B modified from https://plasma.oxinst.com/campaigns/technology/icp-etching

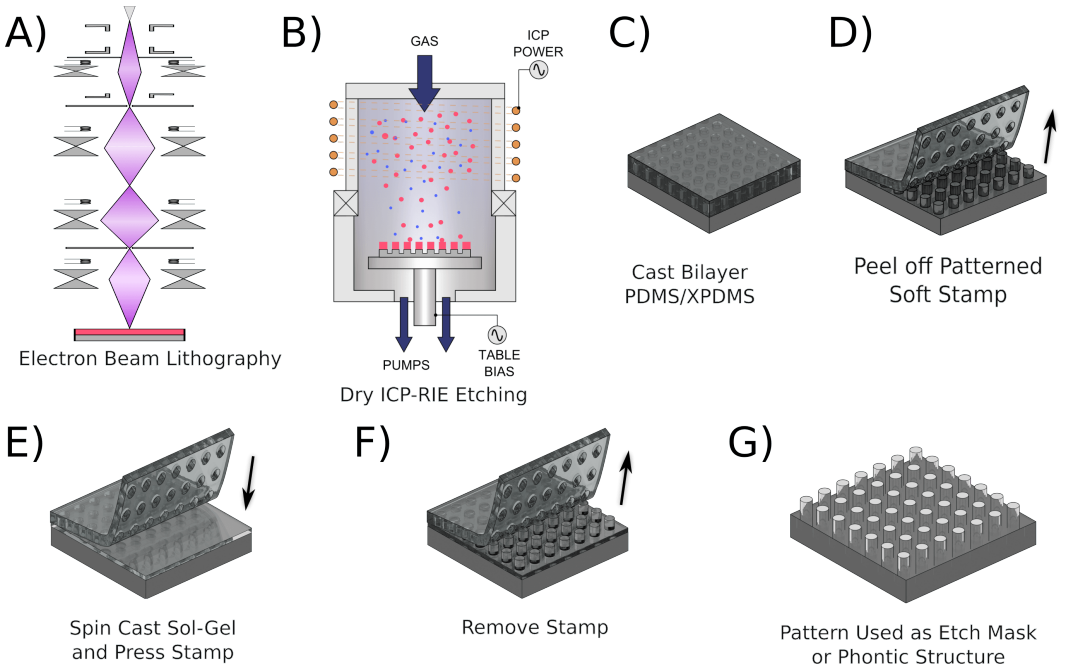

Figure 2.1: Schematic not to scale: Start to finished nanoimprinted silica nanopillars. A) EBL is used to define a pattern in resist on a substrate followed by B) etching in a ICP-RIE dry etch.[1] C) A bilayer PDMS soft-stamp is cast on the the nanostructure and cured. D) The negative of the pattern is reproduced in the soft-stamp and the stamp is peeled off the master. E) It is then pressed into a liquid layer of resist that is cast onto a new substrate. F) After the resist cures, the pattern of the master mold is revealed. G) Any resist that is left on the substrate in between the pattern can be dry-etched away or the pattern can be left as is, becoming the active nanophotonic structure, or it can be used as an etch mask for reproduction of the master, starting again at step B).

3500 rpm for 1 min. It was again placed back onto the hot plate to bake for 5 min at 180 °C and allowed to cool for 1 min.

The pattern was then prepared with the Layout Editor computer-assisted design (CAD) program and processed with the Genisys Layout BEAMER software. An important processing step was the addition of Proximity Effect Corrections in order to have a uniform pattern across the write area. A second crucial portion of the file processing was to fracture the pattern using Genisys's "sequencing" fracturing method with 10 nm resolution. This fracturing method gave both speed and pattern accuracy at resolutions and beam currents that are typically considered high for the features being created. The pattern was exposed using the Leica Vistec EPBG 5000 with 100 kV accelerating bias and a electron beam dose of around 415 $\mu C\,cm^{-1}$ (negative tone patterns) or about 280 $\mu C\,cm^{-1}$ (positive tone patterns) with a beam current of between 2 nA and 10 nA depending on the pattern, desired speed, and

desired accuracy. Typically a 5 nA beam current provided the best balance between accuracy and speed. Using parameters and file fracturing in this style allowed for large area pattern EBL writes to drastically decrease in time. Previous to these methods, EBL write times of a 1 cm area required 48 h of write time. After process optimization, an area of 20 cm could be written in a little over 14 h. However, this is an example of only one maximum in the speed of EBL writing. The write time depends largely depends on the pattern density and resolution. Followers of these methods are encouraged to experiment with arrays of small area patterns to determine the speed optimized parameters that meet the pattern resolution tolerances before attempting large area EBL writes.

The exposed pattern was either developed in MF-319 for 45 s and immediately rinsed in deionized (DI) water for 60 s for MA-N2803, or developed in ZED-N50 for 60 s followed by a 20 s rinse in IPA for ZEP-520a and dried with Nitrogen. For PMMA double layers, the resist was developed in 1:3 MIBK:IPA (volume ratio) for 2 min and then rinsed with DI water.

PMMA double layers were used for deposition of a hard oxide mask during the fabrication of nanocones. Alumina was deposited onto the developed wafer using electron beam evaporation. A target layer thickness of 20 nm was deposited, Layers up to 40 nm were also seen to be compatible with the lift off and etch process. After deposition of alumina, the wafer was placed in an ultra-sonication bath of IPA heated to 40 °C and left to sonicate until all visible traces of the alumina and resist were gone. Sonication beyond this point is encouraged to assure complete removal. This resist removal time varies based on the quality and thickness of the alumina evaporation layer, as in some instances the alumina would encapsulate the resist and would not lift off.

After resist development, the wafer was etched using the Oxford Plasmalab 100 ICP-RIE system. A pseudo-bosch recipe was used with etch recipe parameters as follows: stage temperature of 20 °C, a C_4F_8 flow of about 35 $cm^3\,min^{-1}$ and SF_6 flow of about 26 $cm^3\,min^{-1}$, RF forward power of 40 W and ICP forward power of 1200 W, a chamber pressure of 7.5 mTorr. The etch rate was about 120 $nm\,min^{-1}$ for silicon etching of nanopillars. The details of fabrication nanocones follows a similar etching process that is given in Reference [185]. . The remaining resist was removed with an oxygen plasma etch recipe, i.e. a standard oxygen ICP-RIE cleaning. Figure 2.3 and Figure 2.2 demonstrate examples of the silicon master mold and the soft-stamps resulting from a master mold that followed this process

for nanopillars.

Master Stamp Surface Treatment

Bonding of master molds to the soft-stamp copy can become an issue under certain conditions. A surface treatment is crucial to avoiding this setback. This was seen when using polymer and silicon master molds, but not typically with III-V semiconductor materials. The bonding is a product of poly-dimethyl siloxane (PDMS) components reacting at higher surface energy interfaces, and the surface energy of a master mold is directly proportional to its wettability. Non-passivated surfaces with a high degree of wettability usually indicate the presence of oxygen terminated surfaces, such as those found in epoxide polymers and the native surface oxide of silicon master molds. These oxygen atoms can form carbon-oxygen or silicon-oxygen bonds with the PDMS reactive sites, covalently bonding the soft-stamp to the master. This bonding also commonly occurred through Van-der Waals interaction when patterns had high aspect ratio and/or physically dense patterns.

Preparation of the master mold surface is a crucial first step for maximized surface passivation. A gaseous or liquid state surface treatment is used to react with the surface in a self-terminating monolayer of organic molecules and/or ligands. A deprecated surface treatment used a closed chamber with the master mold inside along with a few drops of triclhoro-methyl-silane (TMCS) in a nearby container. TMCS was allowed to evaporate and react for a minimum of 30 min. The reaction provided sufficient passivation for previous researchers working with micro-fluidic devices, but it failed to reliably release nanoimprint soft-stamps the master mold. It was discovered that the humidity in the room was not well enough controlled to guarantee repeatable surface treatments for many nanopatterns. This discovery led to the following preparation process. Though this method cannot be used for preparing polymer master molds, like those use in Reference [130], it is highly effective for silicon master molds. Full oxidation of the surface was required, to ensure a reactive surface. The silicon master mold was rinsed in acetone followed by IPA and finally an oxygen plasma treatment is performed for 10 minutes. The surface should have very high surface energy and be cleaned of any interfering chemicals. Next, the master mold surface needed to be fully terminated with hydroxyl (OH) groups. This is done by placing the master mold in a water rinse, followed by 30 min in a dessication chamber with a moisture source under constant vacuum. A wet cloth or similarly high surface area moisture source was effective to provide a sufficient amount of

water vapor in the desiccator. This is followed by replacing the moisture source with 3-5 drops of (tridecafluoro-1,1,2,2-tetrahydrooctyl)-trichlorosilane (OTFCS) in a small, open container. Both the master mold and drops of OTFCS are left in the desiccator for 30 min under constant vacuum. These two sources, water and OTFCS are cycled in 30 min intervals for a minimum of 3 cycles. Ideally, the master mold should finally be heated to between 50 °C to 120 °C for 4 h-12 h, though in many cases this was not required. OTFCS replaced TMCS because it is a long, fluorine saturated organic molecule. Similar to molecular Teflon, it provides the a significantly better anti-sticking surface treatment. This process ensured a strong covalent bond between the surface and the mono-layer, enabling multiple re-uses of the master mold without re-treatment. However, out of caution, re-treatment was often performed for master molds that were the result of significant EBL time investment.

This reaction above proceeds as follows. Atomic chlorine readily leaves the chlorosilane as HCl gas when exposed to moisture, and reactive Si-OH hydolyzable groups are formed, creating a silanol. These OH ends of the silanol adsorb to the surface OH terminations on the master mold via hydrogen bonds. The two OH groups will react when supplied the necessary energy, with H_2O acting as the leaving group, and an silicon-oxygen-silicon-carbon bond is formed. This passivates the surface oxygen reactive groups on the master mold. The constant vacuum ensures vaporization of the two reactants from their sources and also drives covalent bonding by driving the removal of water from the reaction. The final heating step accomplishes a similar water removal, solidifying the covalent bonds.

This reaction can also occur in the liquid phase of an alcohol with heat (a 4 weight percent mixture of silane to alcohol is sufficient), where the organic alcohol replaces the atomic chlorine as the leaving group. The alcohol is, theoretically, not as strong of a leaving group compared to OH, as electron density is drawn away from the oxygen atom. However, the benefit of a liquid state process is the combination of hydrolysis reactions and heating.

Once the chlorine is replaced by an OH element at the Si of the silane, the molecules can react with other hydrolyzed silanols to form short-chain silane oligomers in either the gaseous or liquid phase treatments. This is expected to happen to a greater degree in the liquid phase due to the greater molecular density, though no difference was detected. Depending on the structure, this may be desirable. For example, larger micro-scale structures may benefit from the increased physical

Product Code	Parts by Vol.	Specific Gravity	Volume (mL)	Mass (mg)
Mixture Part A				
VDT-731[1]	1	0.96	2.3	2.208
VQX-221[2]	0.8084	1.05	1.7	1.785
SIT 7900[3]	0.0411	0.998	0.091	0.09080
SIP 6831.2[4]	0.008	0.8852	0.02[6]	0.0177
Mixture Part B				
HMS-501[5]	0.9565	0.96	1.25	1.2
		Total:	6.311	6.213

[1] (7.0-8.0% vinylmethyl siloxane)- dimethylsiloxane copolymer, trimethylsiloxy terminated
[2] vinyl Q resin dispersion, 50% in xylene
[3] 2,4,6,8-tetramethyl-2,4,6,8- tetravinylcyclotetrasiloxane
[4] Platinum-divinyl tetramethyl disiloxane complex; 2% Pt in xylene
[5] (45-55% methylhydro siloxane)- dimethylsiloxane copolymer, trimethylsiloxane terminated
[6] This represents a typical value, which lower than the original formulation of Reference [170]. Values of 0.01-0.02 mL are typically used to give a longer pot-life, while 0.060 mL is used in Reference [170].

Table 2.1: XPDMS Formula used in this work. Constituents chemical components given in ratio parts to the whole mixture for arbitrary volume. Typical volume for coverage of 2-3 100 mm wafers shown.

barrier between pattern surface and soft-stamp without a loss of pattern fidelity. Decreasingly small nano-patterns could conceivably suffer from resolution loss if the oligomer barrier becomes thick. The trade-offs are pattern and situationally dependent. They are presented here to bring attention to the variety of ways that successful and convenient surface treatments can be applied.

Soft PDMS and XPDMS Double Layer Nanoimprint Stamps

Bi-layer soft-stamps formed with micrometer scale thin-film of hardened poly-dimethyl siloxane (XPDMS) and a thicker layer of PDMS copy the pattern of the master mold. Table 2.1 shows the constituents of the XPDMS, their amounts, and other details needed to scale the recipe. All components are purchased from the Gelest corporation. Part A was combined in a high-density polyethylene mixing cup and then mixed with a counter-rotating Thinky mixer for 1 minute and de-foamed for 1 minute. Part B was added and immediately after the entire mixture was mixed for 30s and de-foamed for 30s using the same mixing setup. The XPDMS had a pot-life between 5 and 15 minutes, so the liquid XPDMS was immediately be cast upon the master molds. This was done via spin coating with a 15s ramp, and held at 500rpm for 1 minute. For thicker XPDMS or taller structures, the spin speed was

be reduced. Thickness affected the properties of the XPDMS to different degrees. When this layer is too thin, it did not bind strongly with the soft PDMS second layer. When too thick micro cracks formed more readily in the XPDMS layer when handled. Thin layers cure faster and thus leave less time to covalently bond to the soft PDMS backing layer. Thicker layers maintain their high modulus of elasticity but lose the ability to withstand larger strains or compressions. [170]

The XPDMS was pre-cured for between 0.5-2 minutes at 80 °C. An XPDMS layer has usually pre-cured long enough when the layer is glassy. An good indicator of this is to lightly touch an area of the wafer away from the pattern. If the depression quickly returns to a smooth specular layer, more pre-curing time is needed as the XPDMS is still liquid and could intermix with the soft PDMS backing layer. If the contact results in a plastic deformation or the XPDMS layer returns to a planar layer over the period of seconds, the pre-cure has been performed for the correct amount of time. If the layer is hard to the touch, and or does not deform at all, the sample has been over-cured and there is a greater risk of the bilayer stamp de-laminating during use.

A 10:1 resin to curing-agent ratio of Momentive Products RTV-615A and RTV-615B was used PDMS recipe was prepared in parallel to the pre-cure to create the soft backing layer. This regular PDMS was cast upon the XPDMS/master mold combination after the pre-curing period in a petri-dish or similar that was lined with Al foil. The entire system was degassed in a vacuum desiccator for about 15-30 minutes. The entire stamp was cured in an 80 °C oven for periods between 1 hour and 24 hours. It was found that longer curing periods were not as crucial to stamp integrity or stamp performance as others have found.[170] Afterward, the entire monolithic PDMS was allowed to cool to room temperature. This assisted in avoiding XPDMS sticking to the master mold. It is hypothesized that this was due to isotropic strain relaxation of the stamp around the pattern. Foil was then be peeled away, and the master mold cut out of the PDMS. This is done by *gently* sliding a razor blade *around the edges*, only enough to create a shallow incision that frees the edges from the monolithic PDMS. Alternatively, for a smooth edged wafer (i.e. one that had not been previously scribed), tape was be wrapped around the circumference. By folding the edge of the tape under the wafer and leaving some width standing above the wafer, a "petri dish" was created. This created a level stamp that did not need to be cut from PDMS, but only removal of the taped edge. This was the preferred method when possible. The soft bilayer stamp was then

gently peeled from the master once the edges had been freed. A slow and shallow angle peel is recommended to avoid cracking of thick or over-hardened XPDMS.

The mixture given in Table 2.1 deviates from that of Reference [170] to give a longer pot-life and create a more time-stable mixture. Rapid solidification of the original recipe often occurred, so the Pt based catalyst was reduced to one-third of the original requirement. This gives a slightly longer pot-life and makes the resulting polymer more robust against changes in the room humidity, which can also affect the solidification time of the XPDMS. Also, Part B was doubled to soften the XPDMS some, which helped to reduce instances of the layer sticking to the Si master and cracking during in use. The modulus of this recipe was not directly measured but was able to faithfully reproduce the patterns of Si masters without exception. The modulus is estimated to be lower than the recipe for 65 MPa given in Reference [170] while still significantly higher than the modulus of typical 10:1 PDMS. For comparison, the volume ratio of each chemical component in the original formula, in order, is 1:0.8:0.045:0.0250:0.60 and was reported to give a modulus of 80 MPa. The recipe of Table 2.1 was still able to reliably achieve high fidelity reproduction of nano-scale structures.

Following the given procedures should lead to a high fidelity soft-stamps with no PDMS residuals on the master mold. Yet there are physical limitations that were observed related to the shape and aspect ratio of nanopatterned master molds. The XPDMS in its initial liquid state will infill all areas of the pattern as it can still wet the passivated master. The modulus of both the stamp and master will determine at which pattern aspect ratios are amenable to successful separation of soft-stamp and mold. Conceptually, the soft-stamp must be able to clear the features of the master with out the pattern breaking off into the stamp (negative tone, pattern out-of substrate), or without the stamp being retained by the master (positive tone, pattern into substrate). Perhaps obvious, a cone-like pattern will give more clearance as it is peeled off than a rod, while an inverted cone will likely never allow the soft-stamp to peel off without removing the inverted cone from the substrate. The same fundamental geometrical limitations will apply to PDMS that has infiltrated into deeply recessed patterns of the master mold. Lastly, the symmetry and orientation of the nanopatterns play a role; this was seen in development of Effectively Transparent Contacts with micro-scale dimensions in the two dimensions and macro-scale dimensions along the third dimension – a microscale triangular prism shape that was centimeters long.[130, 132, 133, 135].

Should any PDMS stick to the master mold, it is typically impossible to remove via physical methods. However, both XPDMS and PDMS formulas can be etched away without damage to a silicon master mold by soaking in a 1:1 volume ratio of tetra-*n*-butylammonium fluoride(TBAF) and a non-hydroxylic aprotic solvent such as dimethylformamide.[29, 87, 98, 99, 157] TBAF breaks down the Si-O bonds of the polymer while dimethylformamide allows the shortened chains to dissolve.[87] The duration of this etch depends on the amount of PDMS adhered to the master mold, and thus took anywhere from minutes to hours. Etch rates of different TBAF and solvent combinations can be found in reference [87].

Scaling: "Quilting" Small Area Stamps to Larger Areas

Though large progress was made is speeding up the write times of cm^2 areas, solar cells and their areas often exceeded that of the soft-stamp. Efforts to overcome this in a scalable fashion involved creating many copies of the same pattern, made possible by being able to re-use the master mold. By arraying multiple soft-stamp copies, nano pattern creation became parallelized.

Four or more soft-stamps were made sequentially according to the process described in 2.2. Each stamp was cut to the required shape in order to fit a larger desired shape, in a "quilted" fashion. The patterns were either be cut within the patterned area to approximate a continuous pattern between adjacent stamps or with a un-patterned border. Stitching errors were present when doing cutting within the pattern. This method was only used when large area periodic nano-arrays were needed, such that any stitching errors were inconsequential. This is typically the case for large area solar cells. These stitching interfaces were seen to be on the order of up to 100 µm. The stamp is placed patterned-side down onto a clean and flat Si wafer, such that intimate contact is made between the two. This ensures each pattern is coplanar with the others. Figure 2.2 shows example results of this process.

Initially, PDMS was cast onto the cutouts assembled on the Si wafer to glue them together into a monolithic stamp. The stamp seen in Figure 2.2 A was made via this process. This approach generally worked, but created some minor issues. First, during the curing of the PDMS at 80 °C, cutouts will expand before the liquid phase PDMS cures, and upon cooling, one side of the new monolith gains some curvature due to the strain mismatch created in heating. This was overcome by applying a small downward pressure during the stamping process.

Second, if patterns are meant to be in close contact (such that cuts are made through

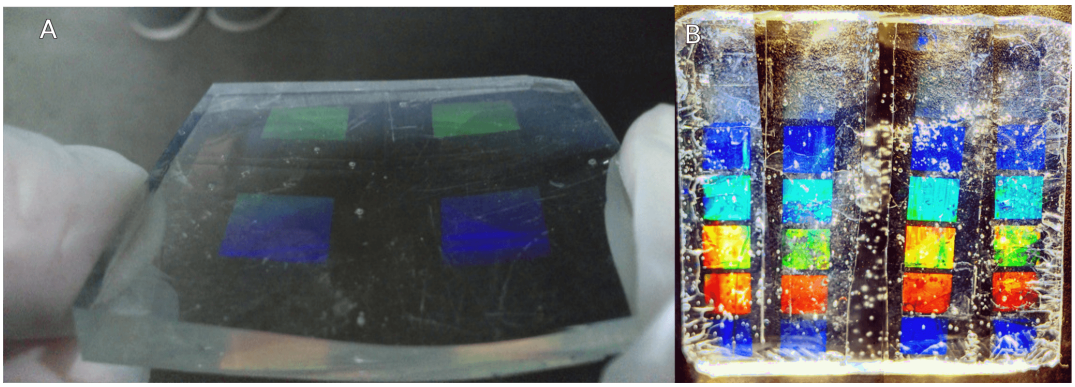

Figure 2.2: The diffraction from two quilted soft-stamps. A) a nanopatterned PDMS soft-stamp with a 1 cm^2 area that has been copied 4 times and quilted together. B) A 4 column stamp made from a master mold with 6 patterned areas of 6 mm^2. The white scattering areas are bubbles in the PDMS "glue" on the opposite side of the patterned area. The image in B) was enhanced emphasize the pattern diffraction. Both stamps were cut to the same size square size as the target substrate of 5 cm^2.

the patterned area itself), the liquid phase PDMS will be pulled into the nanopatterned area during the degassing phase. This was avoided in Figure 2.2A by leaving a margin around the patterns such that the intimate contact to the silicon surface did not allow liquid inflow. In Figure 2.2B, the process of Figure 2.2A was not used due to the allowable pattern margin of the experiment in Figure 2.2B. In this case, PDMS was mixed, degassed, pre-cured to a viscosity that would not underflow, and then spread onto the topside of the stamp cutouts. While spreading, many bubbles were introduced, which are seen in Figure 2.2B. These did not affect the patterned side since the PDMS only served as glue. In this case, curvature was exacerbated since the PDMS was applied to room temperature cutouts, and then placed into the curing oven. In the future, this might be avoidedby allowing the PDMS glue to cure at room temperature, or pre-heating the assembled stamp array. The increased curvature sometimes led to lower fidelity patterns near the monolith edge due to requiring greater stamping pressure. Using typical adhesives such as tape or glues does not work for combining stamps. In Figure 2.2B, stamps needed a specific spacing between adjacent stamps. When writing the master pattern in a Si wafer via EBL, additional macroscopic alignment markers were written to these dimensions (in this case 1 cmx5 cm). When copied into the soft-stamp, these were visual references aided cuts in the PDMS.

Last, it was discovered that using a solid glass backing helped to avoid mismatched strain and curvature issues., A typical laboratory microscope slide was used. The same PDMS gluing strategy was used to bind this rigid back layer either during the

initial stamp creation or after.

Scaling: Generational Master Stamps

A second approach to scaling master molds was to avoid "quilting" PDMS stamps altogether. Again, cutouts were made of multiple stamps. Sol-gel resist was spun coat onto a new Si wafer and then imprinted with each stamp as in Figure 2.1E)-G) by carefully placing each next to one another. Because this was a manual process, the alignment of each could not be guaranteed between imprints. To overcome this alignment issue, after the sol-gel structure solidified, this multiplied pattern was used as an etch mask as in Figure 2.1B) to permanently fix the alignment of patterns into a new silicon master mold. This is designated a "second generation" master mold. From this second generation master, new soft-stamps were made.

The limiting factors in doing this were two-fold. First, and fidelity errors the stamp process were permanently duplicated in the second generation master; this was minimized with careful control of environmental contaminants and meticulous stamp placement and removal. Second, the height/depth of the pattern is limited by the effectiveness of the imprinted-structure's material to serve as an etch mask. Etch selectivity of the typically used silicon dioxide sol-gel to Si is limited to less than 1:1 ratio when apply the ICP-RIE pseudo-Bosch parameters as in 2.2. This resulted in a second generation master with a etch depth less than that of the first generation master mold. This is not necessarily always a drawback to this approach, as the first generation master mold has a fixed depth, so creating second generation stamps provided a route to vary this parameter in experimental studies. Briefly, alternate Si ICP-RIE etch chemistries using HBr rather than SF_6 were explored and showed a higher 1:2 or better etch selectivity for sol-gel to Si, giving greater control over pattern morphology. The observed drawbacks of this etch chemistry were sloped sidewalls and a roughened Si surface. This etch was not explored in full detail due to other resolutions to the scaling problem. Third generation stamps were then created, but a decrease in pattern fidelity occurred due to accumulating contaminants, stamp replication, and other printing errors. A further reduction of the pattern's height/depth were observed. The feasibility of scaling nano-patterned areas in this fashion is not conclusively proven nor dis-proven here; rather the work demonstrates proofs of concepts in leveraging the multiple use principles of NIL for exponentially increasing the size of a small area pattern to much larger areas.

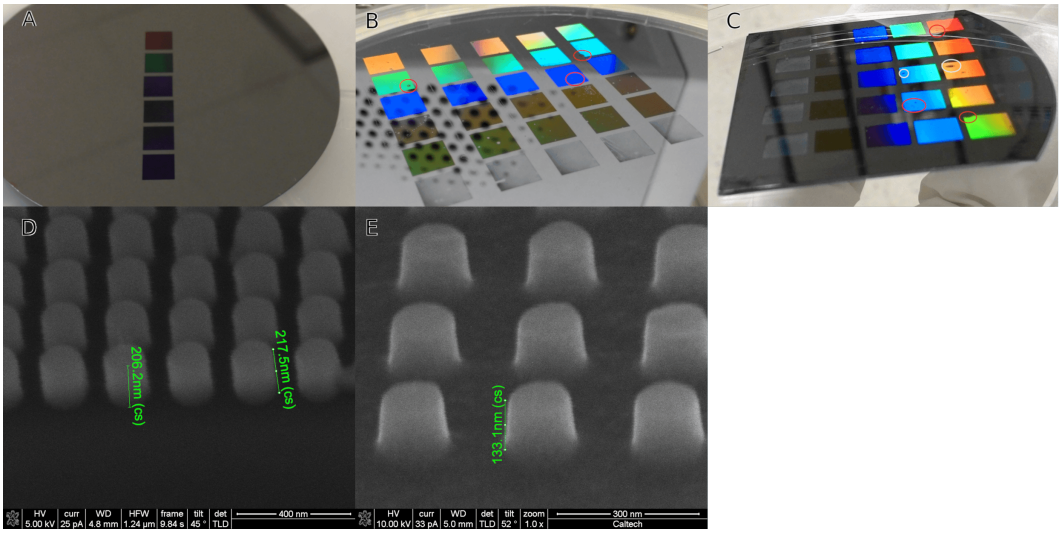

Figure 2.3: The diffraction from two quilted soft-stamps. A-C) First, Second, and Third generation Si master mold molds. B) was made from multiple copies of A) and then ICP-RIE. C) was made from a soft-stamp copy of B) and ICP-RIE. D-E) Scanning electron microscope (SEM) images of A) and B) respectively, show that the height of the pillar pattern decreased during the duplication. Red circles indicate fidelity loss copied from Second to Third generation masters, while white areas indicate errors introduced during creation of the Third generation only.

2.3 Sol-gel Imprint Resists

Multiple resists can be used in conjunction with NIL provided they can flow or be deformed to the negative-tone stamp features on the nanoscale. Many literature examples can be found wherein patterns are recreated in varied materials from commercial UV-curable polymers (AMONIL, Katiobond, et. al.) to oxides or metals (Au, Ag).[5, 37, 44, 77, 86, 90, 122, 132, 189] In this work, most imprinting was performed with oxide sol-gel resists such as silica [170, 186] and alumina, while some of the processes described here were also adapted to Ag inks. [131] The value prospects of directly printed nano-structures is their low cost, variable refractive indexes, lack of optical absorption, and reduction of processing steps such as etching. One of the drawbacks however is time based curing, rather than popular ultra-violet light curing. Additionally, when the stamp is placed, the sol-gel will take longer to cure based on stamp size and sol-gel amount. Last, this work found thicker layers were not possible from spin-coating due to the low viscosity of the alcohol solvent. The benefits of directly printed structures overcame these resolvable drawbacks.

Silica

Nanoparticles from an alkoxide precursor polymerization reaction in solution that form a solid in liquid is called a *sol*. A sol-gel is created when the colloidal suspension, loses its liquid phase through evaporation or other process and the nanoparticles are forced to branch and network. The sol particles will coalesce into a low solids-density gel structure, with a low amount of liquid still present. The cross-linking and branching reaction can be driven further with an elevated temperature annealing to increase the density, driving away any remaining liquid phase and finalize condensation reactions, creating stronger internal bonding between particles essentially sintering the particles. Shrinkage of any nano-structure will occurs during such a process, and so it was avoided in this work for better control over pattern dimensions. Heating was was not necessary to achieve robust solid nanostructures. The initial solidification occurs when a soft stamp is applied to sol-gel resist in NIL. The liquid phase must be able to escape in order for solidification to occur. Alcohol can diffuse into the PDMS stamp readily and is thus the solvent of choice. This process is shown schematically in Figure 2.1E-G.

The process for synthesizing silicon-dioxide based resist in this work is adapted from Reference [170]. This recipe provides a material with low refractive index of 1.42 in the visible wavelengths. A liquid phase, alcohol based sol is created in a first step, then diluted further to become more amenable to spin-coating thin-films on substrates. The full reaction is effectively halted mid-way by storage in a freezer, allowing the sol to be stored for greater than one year depending on the degree of sol particle growth. In fact, some sols were still effective after more than two years in storage. The chemical components are given in Table 2.2, along with helpful values that can be used to scale the reaction volume as desired. The exact reaction followed in this work is listed below, though custom component volumes calculated by using Table 2.2 can be substituted as needed for larger or smaller batches. Preparation

Chemical	Molar Ratio	Molar Volume (mmol/mL)	Unit Premix Batch Volume (mL)
TMOS	1	6.78	0.1475
TMTS	1	7.01	0.1427
Formic Acid	$36.2\text{x}10^{-6}$	1	$36.2\text{x}10^{-6}$
DI H_2O	17.69	55.34	0.320
n-propanol	35.54	13.36	2.660

Table 2.2: Required components for creating silica sol-gel NIL resist. This table provides necessary values for scaling batch of silica sol-gel resist premix. The molar ratio should be maintained in the final batch. An arbitrary batch size can be made by multiplying the right column by the final batch volume to get the required volumes of components in the right ratios. These values were calculated from the experimental procedure given.

1. Prepare a warm water bath at 50 °C
2. Prepare a 1 molar formic acid by (15 mL is made by first adding 5 mL DI H_2O followed by 0.857 mL of (88% HCCOOH) and finally 14.143 mL DI H_2O)

Silica Sol-gel Pre-mix Reaction

3. Add 7.66 mL TTMOS to new beaker
4. Add 7.35 mL TMTS
5. Dilute the mixture with *n*-propanol by adding 1.49% of the final volume (2.57 mL)
6. Mix with stirring bar until fully homogenized.
7. Add 1.88 mL 1 Molar Formic Acid
8. Place mixture into water bath and allow reaction for 10-120min.[1] Keep covered or use condenser to avoid evaporation.
9. Add 16.60 mL DI H_2O and the remaining *n*-propanol (135.602 mL)
10. Remove from heat and let reaction stand for 20 min.
11. Put into freezer with temperature less than −30 °C for 24 hrs before first use
12. Store premix in freezer when not in use.

Dilute for Typical Use

1. prepare a dilution mix of 98wt% (*n*-propanol) and 2wt% (2-(2-n-Butoxyethoxy)-ethylacetate (BEEA), 98%)
2. Mix 1 part premix from above and 1 part solvent mix

[1] 10 min was seen to be sufficient and kept in storage longer. This time should be increased for higher TMOS TMTS ratios.

When using the silica sol-gel for imprinting, the premix was diluted with a compatible high boiling-point solvent, in this case BEEA. This allowed for some extra time, between 5-10 min, for the stamp to be placed on the coated substrate before solidification. A typical amount was 2wt% in *n*-propanol. In cases where a large surface area was printed, or a large volume of the structure was open (and correspondingly needs to be filled with sol-gel) neat premix was used when spin casting, though the time to stamp drastically decreases. In some cases it was necessary to drop cast premix in excess directly onto the substrate; this is discussed further in Section 2.3.

Silanol Reaction

The silica sol-gel reaction is the result of hydrolysis-condensation reactions, and in silica is known as the Stöber process. In the first part, the methoxy groups of the TMOS and TMTS are lost as it is readily replaced with the added water in a condensation reaction. This hydroxide group can then react with a alcohol or hydroxyl group on another Si atom in a condensation reaction in which a water or alcohol molecule is lost and a strong Si-O-Si bond is formed. This process allows for disordered polymerization of Si-O networks, as each Si atom can form up to 4 bonds each. Reference [170] found the degree of cross-linking was key to 1:1 structure reproduction via nanoimprint. Either too high or too low cross-linking degree would give cracking and/or shrinkage. The introduction of TMTS added another degree of cross-linking control. Since one Si bonding site is taken by a highly stable methyl-silane bond, the cross-linking degree can be less than 4 by choosing an appropriate molar ratio of TMOS to TMTS. A molar ratio greater than 1:1 and a cross-linking degree of less than 3.5 gives reliable high fidelity nano-structure reproduction, and is used in this work.

Silica Sol-gel Printing

A substrate was cleaned with water, acetone, and finally IPA in a clean room. An oxygen-plasma cleaner was also be used for further rigorous cleaning, resist spreading, and adhesion of the sol-gel to a freshly oxidized surface. The soft-stamp was cleaned briefly with water followed by IPA. IPA sonication was sometimes used to ensure the stamp pattern was clear of all contaminants, especially if any sol-gel from a previous print has remained in the stamp from "rip-off" errors. A quick 1-2 minutes dip in buffered hydrofluoric acid was also highly effective at removing any previous rip-off residue without harming the stamp's nano-pattern. The stamp was

allowed to rest after application of any organic solvent to abate curvature due to swelling of the PDMS backing layer.

The silica sol-gel dilution was kept cool with ice-packs when in use outside of the freezer to maintain the halted reaction. The entire substrate was covered in the liquid sol-gel to ensure even coating. A spin-coater was used to cast the sol-gel in its liquid form in a multi-step spin coating recipe. A typical recipe is given in Table 2.3, though each pattern may require tweaking. Stamps were placed upon the substrate

Table 2.3: The spin coating recipe used for silica sol-gel spin-coating.

Step	Speed (rpm)	Ramp (rpm sec^{-1})	Time (s)	Lid Status
1	200	100	10	Open
2	500	1000	10	Closed
3	1000	2000	2	Closed
3	200	1000	5-30	Open

as quickly and carefully as possible to avoid contamination. Once the stamp was in-place it was not be moved again since the thin 100 nm thin film will begin to dry upon stamp contact, as any residual alcohol was quickly absorbed. The BEEA remained for at least 30 min. Next, pressure was applied for intimate stamp/substrate contact. A TexWipe or similar non-stick cover was placed over the area of the back of the soft-stamp; this cover ensured that the PDMS stamp did not stick to anything used to provide stamping pressure. Many options for printing pressure application were used, from a small weight, to a placing the entire stamp/substrate into a vacuum bag to apply iso-static pressure across the top and bottom of the stack. The vacuum bag method emulates many of the commercially available tools for NIL. Pressure was carefully removed to avoid disturbing the stamp prematurely. It was then gently peeled away using a razor blade or similar to start natural separation of substrate and stamp. Allowing a slow, natural loss of adhesion between the two was optimal compared to a forceful mechanical peeling.

As mentioned before, in some cases, a denser solids-by-volume sol-gel and/or thicker resist layer is needed to fill the stamp volume. A rough calculation should indicate if this is the case. For example, the nano-cone patterns of Chapter 5 require a large resist volume due to being a tall, close packed, spatial dense pattern. The volume per unit of one cone is roughly 2x greater than the 100 nm per cone area provided by the above spin-cast film. In this case, neat premix sol-gel was used to increase the resist layer thickness. The premix was drop cast onto the substrate and excess was removed by allowing flow off the edge by tilting at an angle. The stamp was

placed, but had a large amount of mobility due to the lubrication of the thick resist layer. In this case, best results were seen by using a weight rather than a vacuum bag. It is hypothesized that the higher pressure of the vacuum bag expelled too much resist from under the stamp during pressing. A large degree of swelling with large resist volumes was observed. An integrated glass stamp backing (see Section 2.2) alleviated this issue and provided an even pressure. Drying time was increased to 12-24 hours or longer. No pattern dimension irregularities in the print were detected from the stamp swelling when examined by SEM.

A successful stamp was achieved when the pattern was visually homogeneous, there were no visibly missing portions of the copied nanopattern, and the soft-stamp was visibly clear of rip-off error. The patterns with reproduced with high fidelity. A 20 nm residual layer will be left across the entire surface, below the pattern when using NIL. A fully cured stamp adhered strongly to the substrate such that rinsing with organic solvent did not remove the pattern. Often in the large volume nano-imprints, there were edge errors, so a larger than needed area was typically used. Sol-gel resist was be detected to have expired when nanoimprint patterns display widely varying film-thickness (manifesting as colored thin-film interference), printing fidelity loss, longer than expected curing time, or when a gentle solvent rinse erased the pattern. The poor adhesion of the pattern to a properly oxidized substrate supports the hypothesis that the condensation reaction has proceeded too far, while in storage. Again, the process requirements vary with pattern, and experimentation with the toolbox of methods described is encouraged.

Alumina Sol Gel

Chapter 4 explores the use of oxide sol-gels for passivation of solar cell semiconductor absorbers. Literature has shown that alumina is particular well suited to increasing the voltage in CIGS solar cells.[89, 165–168] To experimentally realize this an alumina sol-gel was created to investigate potential for the fabrication of nanophotonic patterned CIGS solar cell devices. Alumina also provides another option for an intermediate refractive index sol-gel around 1.6-1.7 compared to 1.42 for silica or 2.2 for titania. The potential of NIL with alumina resist has not, to this author's knowledge, been explored in depth. Other metal oxide sol-gels for nanoimprint have been explored in much greater detail.

Organo-aluminum precursors are more reactive than silane precursors. Evidence of this is given by the enthalpy of formations of alumina versus silica – they are

-1676 kJ mol^{-1} and -911 kJ mol^{-1} respectively. Also, aluminum alkoxide precursors are more sensitive to water both in the sol-gel reaction and in the ambient atmosphere. However, some precursors, specifically aluminum-tri-sec-butoxide (ASB), are stable in alcohol based sols like those compatible with large scale NIL production methods. Other aluminum alkoxide compounds were not fully explored due to their lack of alcohol solubility. The ultimate goal was to emulate the silica sol-gel properties of structure reproduction, pot-life stability, and thin-film cast-ability.

ASB was used because it is stable in its liquid phase. Different molar ratios of DI water for hydroylysis, ethyl-acetoacetate (EAA) as a stabilizer, IPA and isobutyl alcohol as a solvent were explored during the study. The same BEEA high boiling point solvent additive was used to provide time for stamping.

This sol-gel reaction was highly dependent upon the ratio of EAA that was added during the hydrolysis reaction. EAA serves to stabilize the highly reactive alumina via a chelation effect from its multiple polarized ketone groups.[110, 156, 197] Experiments started with molar ratios of ASB:*n*-propyl alcohol (*n*-PrOH):EAA:DI H_2O, as taken from Ref. [156] to be 1:10:1:4, where *n*-PrOH was used in place of IPA for its lower evaporation rate. To determine the optimum molar ratio of EAA to Al, the ratio was varied from 1:0.5-1.5. From these trials, imprint results were seen with the literature ratio of 1:1 ASB:EAA. Positive results were also see when the water molar ratio was increased to 1:17 ASB:DI H_2O in formulation 1 of Table 2.4. It is hypothesized that allowing the reaction to settle for an extended period allowed for a greater Al ion stabilization and the addition of an excess of H_2O was thus made possible only after 24 hours or longer. Also, promising imprints were seen with a doubled IPA:ASB ratio, given in Table 2.5. A post-reaction observation of an optically clear sol was a positive first indicator, and meant that large particle nucleation was not occurring in solution. A second positive indicator was the ability of the sol to spread on a substrate without instantly drying, critical to stamping. The EAA stabilization component was the key breakthrough for both of these results.

A typical reaction procedure is given below, corresponding to the sol-gel formulation of Table 2.4. A key point is that the dissolution of EAA into the chosen alcohol was performed first. Preparation

1. EAA and IPA, *n*-PrOH, *sec*-butanol, isobutyl alcohol, or *t*-butanol should be dried with molecular sieves prior to usage
2. A high precision scale was preferred to a calibrated micro-pipette due to the high viscosity of ASB

Table 2.4: Components for creating alumina sol-gel recipe 1 NIL resist and helpful values.

Chemical	Molar Ratio	Molar Volume ($mol\,mL^{-1}$)	Density ($g\,mL^{-1}$)	Mol. Weight ($mol\,g^{-1}$)
ASB	1	238.2	0.967	246.32
EAA	0.5-1.5	133.914	1.029	130.14
DI H_2O	17	18.01	1.0	18.01
n-PrOH (dried)	10	48.3	0.804	60.095
BEEA	2wt%[1]	199.76	0.978	204.26

[1] The weight percent of BEEA of the final solution is given. The premix was diluted with 2wt% IPA.

Table 2.5: Components for creating alumina sol-gel recipe 2 NIL resist and helpful values.

Chemical	Molar Ratio	Molar Volume ($mol\,mL^{-1}$)	Density ($g\,mL^{-1}$)	Mol. Weight ($mol\,g^{-1}$)
ASB	1	238.2	0.967	246.32
EAA	0.5	133.914	1.029	130.14
DI H_2O	0.5	18.01	1.0	18.01
IPA (dried)	10	47.234	0.786	60.095
BEEA	2wt%[1]	199.76	0.978	204.26

[1] The typical weight percent of BEEA of the final solution is given. The premix was diluted with 2wt% IPA. Values up to 10wt% worked, but without any obvious benefits compared to 2wt%.

3. (Encouraged) A reaction vessel was pre-cooled to -25 °C and an small ice bath prepared to slow the speed of the reaction. The ice bath was placed on a stir plate such that a stir-bar could be used. A stir-bar was set to a low speed 200-500 rpm
4. (Potential Improvement Opportunity) consider performing reaction in an inert atmosphere to control for humidity and condensation. This was not tried, but due to the reaction speed, this should provide more favorable conditions

Alumina Sol-gel Pre-mix Reaction (4.418 mL, 5 mg batch)

5. 2.302 mL (2.863 g) *n*-PrOH was added to the reaction vessel.
6. 0.638 mL (0.620 g) EAA was added to the reaction vessel.
7. This was thoroughly mixed at low temperature in an ice bath.
8. 1.135 mL (1.174 g) ASB was added to reaction vessel.
9. Components were mixed until the solution was fluid and appeared milky white

10. The solution was stored at -25 °C for 24 hours after which time it became a clear solution.
11. 1 mL (1 g) DI H_2O and 0.2 mg BEEA was added and stirred until clear.
12. The solution was stored in a freezer similar to silica sol gel when not in use.

Aulmina Sol-gel Printing

The solution was spin-cast upon a substrate after the addition of H_2O and then imprinted. Imprinting needed to occur as quickly as possible, since the film dried in less than 10-30 s. Reaction formulas need significant improvement in this area of drying time, as large area imprints were very difficult to realize due to this factor. A spin-coat recipe that showed moderate success in some trials is given in Table 2.6. The recipe emulates some steps of the silica sol-gel recipe in Table 2.3.

It was noted that rip-off was a more significant problem with alumina compared to silica. A similar surface passivation treatment applied to the stamp itself, as is done for master molds in Section 2.2, might be used to mitigate bonding between XPDMS and the alumina print.

Table 2.6: Spin coating recipes used with the most promising alumina sol-gel formulations given by Tables 2.4 and 2.5 respectively.

Step	Speed (rpm)	Ramp (rpm sec^{-1})	Time (s)	Lid Status
Alumina sol-gel 1 spin-coat recipe				
1	1000	2000	5	Open
2	750	1000	5	Open
3	1500	2000	2	Open
Alumina sol-gel 2 spin-coat recipe[1]				
1	1000	2000	5	Open

[1] Mild heating up to 50 °C was applied for 5 min after stamp placement. Film cracking and or rip-off error was seen around edges. This method worked best for a larger substrate.

Attempts to slow the thin-film reaction and drying time to allow more stamping time were perfomed using formula 2 from Table 2.5 by diluting the premix with higher boiling point alcohols to a molar ratio of 20 mol alcohol to 1 mol ASB with 0-2wt% BEEA. IPA, *n*-PrOH, *sec*-butanol, and isobutyl alcohol were all tried as a route to increase the stamping time window. The boiling point of these alcohols increase in this order. Following the silica sol-gel example, higher boiling point solvents were promising since silica sol-gel is diluted with the higher boiling point *n*-PrOH. This proved to be correct, as the dilution solvent choice did have a appreciable effect

on the stamping time window after spin-coating. While IPA was initially used, it only resulted in partial imprint patterns, and the time to dry was less than 10 s after spin-casting. Additionally, the small areas of patterned film were high fidelity. *sec*-butanol proved to be a better dilution solvent for stamping time, giving up to 30 s for imprinting. However, micro-cracks across the film were seen in SEM analysis as shown in Figure 2.4 B). *sec*-butanol dilution gave the best large area imprints, approaching silica sol-gel print quality. Freshly prepared sol-gel premixes, on the order of days old, followed by dilution with *sec*-butanol or other higher boiling point solvent printed best.

Conclusions and Future Direction

The choice of IPA versus another alcohol solvent is reported to be inconsequential to the reaction, since any shorter or equal length chain alcohol will readily replace the *t*-butanol groups of ASB in solution, but the resulting film density can be affected. For example, Ref. [156] reports IPA gives a denser gel than a premix reaction with ethanol solvent. This work's results from different alcohol solvents for both the premix and dilution support Reference [156]. The cause of micro-cracking is suspected to be an effect of a low solids-density in the diluted ink and/or the alumina density itself. Micro-cracking was more prevalent when the molecularly larger *n*-PrOH was used during the *premix reaction* compared to IPA. In regard to dilutions, only longer chain dilution alcohols were printable, potentially limiting ultimate film density control. Some investigation was performed into different ratios of dilution with IPA and larger alcohol molecules; some of the best prints were obtained when using IPA during the premix and *n*-PrOH for dilution, or a combination of IPA and larger alcohol for dilution.

Alternate causes for micro-cracking may be explained by comparison to Reference [170] regarding silica sol-gel. First, they found that a higher degree of cross-linking negatively affected a print's fidelity, while decreasing cross-linking with a second silane (TMTS) gave the intended fidelity. Here, the sol-gel is allowed to fully cross-link, meaning a denser solid-phase is likely formed upon the loss of solvent.

Finally, Figure 2.4 shows examples of the progress made in printing alumina sol-gel. Figure 2.4 A-C) SEMs show the micro-structure of the prints and corresponding photographs below, D-F). Good nano-fidelity was initially seen, when EAA was not being used, but small print areas. B-E) Shows that adding EAA and diluting with isobutyl alcohol allowed a longer print window, with higher long range fidelity,

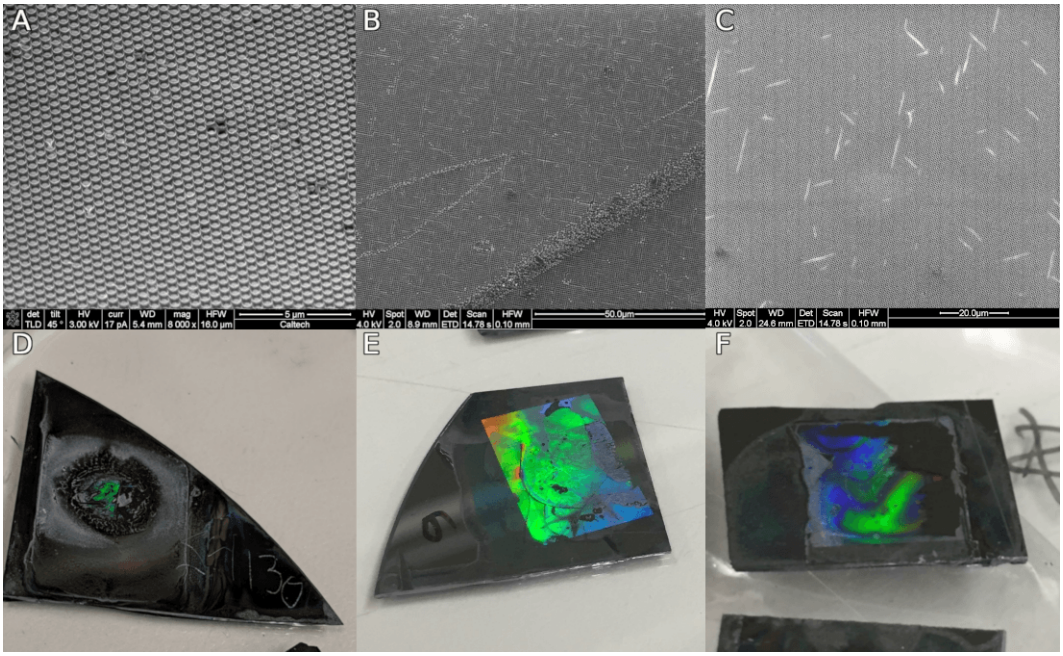

Figure 2.4: SEM images and photographs of various alumina sol-gel printings. All final dilution ratios are 20:2:1:1 alcohol:ASB:EAA:DI water. A-C) SEM images for different sol-gels. D-F) Photographs of the macro scale print corresponding to the SEM image above each. A,D) A tilted image shows IPA without EAA gave a good reproduction and no cracking on the micro-scale, but small 1 mm^2 area. B,E) Adding EAA and isobutyl alcohol shows 1 cmX1.5 cm prints were possible, but significant micro-scale cracks were found. C,F) Show using EAA and an IPA 1:1 dilution; large 1 cmX1.5 cm prints were printed and micro-cracking was minimized, but irregularities in the film thickness from the small print window prevented a full area print. F) was spin-cast at 750 rpm for 10 s.

but micro-cracking was significant. Finally, the best print observed is displayed in Figure 2.4 C,F) which was made with an IPA dilution, with similar results for *sec*-butanol (not imaged). Micro-cracks were still seen in these larger areas, but to lower degree.

Future directions for alumina sol-gel should involve more control over the reaction atmosphere by considering ambient humidity effects on the premix reaction and the final film. There is hope that high-throughput techniques may more effectively resolve issues of the stamping time window, micro-cracking, and sol stability. The parameter space was too broad for a full optimization here, but promising directions of study have been found. Further investigation should include strategies for etching alumina sol-gel resists. In order to place these nano-structures inside the stack of a PV device, holes around the structure in the residual layer must be open for current to pass through the device. Additionally, alumina sol-gel based masks could be among some of the most selective ICP-RIE etch masks achievable through NIL

compared to polymer resist or silica. This is supported by the high selectivity of vacuum deposited alumina masks used in high aspect ratio etching of silicon, making alumina etch masks important for not only PV applications, but also semiconductor processing. [184, 185]

Optical and materials characterization should also be performed. Initial characterizations reporting the optical constants of the sol-gel will inform its usefulness in optical design. Characterization of the alumina compound in terms of its composition and crystalline state should clarify other expected properties in terms of semiconductor passivation. A positive development in this area would be critical to further progress in Chapter 4. In Chapter 4 it is proposed that these types of sol-gel could benefit from doping of important chemical species such as sodium. Solubility of sodium species in this sort of alcohol-based sol-gel would need to be explored, but could yield great new patterning and manufacturing options in thin-film solar cells.

2.4 Summary

A detailed accounting for the NIL procedures developed and experience gained was presented. Nanofabrication optimization for large area patterns is described. New and process-critical methods such as stamp-quilting and OTFCS surface treatments were developed to further the scalability and reliability of laboratory scale sol-gel patterning. Large dense area sol gel patterns were produced for the first time by printing spatially dense nanocone arrays. First attempts at patterning alumina sol-gel showed promise but need further investigation. Alumina sol gel provide a unique opportunity for high selectivity etch masks and nanostructures with electronic-passivation properties for use in semiconductors.

In general, it was found that there is no singular method to NIL. Each pattern is unique and the conceptual understanding presented aided in resolving each obstacle encountered when printing new patterns. This work does show, however, that once a pattern printing procedure has been developed, it can faithfully and reliably produce large areas of nanopatterns. The experience and working knowledge shared here will aid future researchers in realizing successful NIL experiments.

Chapter 3

NANOPHOTONIC LIGHT TRAPPING STRUCTURES IN TANDEM a-Si:H/a-$Si_{1-x}Ge_x$:H THIN-FILM SOLAR CELLS

3.1 Tandem Amorphous Silicon Solar Cells

Previous work in studying the light interaction with thin-film solar cells has produced significant understanding of the ability for nanophotonic structural modifications to increase light trapping in diminishingly small volumes. This has been often and readily shown in the a-Si:H materials system.[7, 42, 94] a-Si:H provides an attractive optoelectronic system for studying nanophotonic light management due to its low-cost, quick, and relatively easy fabrication. These amorphous materials systems are also compatible with roll-to-roll nanoimprint production of superstrate/substrates, including flexible substrates. On these superstrates, the majority of the device is deposited via plasma enhance chemical vapor deposition (PECVD) from gas precursors. Absorbing layers are on the order of 100 nms, and can be deposited rather quickly at low temperatures below 300 °C. a-Si:H device's absorber layers are required to be thin, and require some sort of light trapping strategy for appreciable power conversion efficiency. Traditionally, a randomly textured transparent conducting oxide (TCO) superstrate has been the preferred method of light trapping in these devices. Their non-crystalline structure reduces the structural constraints of PV devices such as c-Si and GaAs devices. It is extremely difficult to nanostructure a crystalline absorber internally. To do so is generally only possible via a destructive etching process, leading to performance degradation. The thin-film deposition of a-Si:H opens up the possibility of greater control over light-absorber behavior. Coupling into internal guided modes of high refractive index absorbers such as a-Si:H, designs aim to reach or exceed the classical $4n^2$ absorption enhancement limit.

Amorphous silicon and its alloys are distinct from crystalline silicon or polycrystalline silicon due to their limited short-range order. The typical tetrahedral bonding between nearest neighbor silicon atoms is interrupted, and a random network of silicon atoms results. A significant portion of the valence electrons are left as dangling bonds and serve as deep-level free carriers traps. This results in low carrier mobilities, particularly of holes due to the excess of electrons in the network. These low mobilities impose a limit on the thickness of an a-Si:H PV device.[154]

The typical addition of 10at% hydrogen to the deposition process serves to passivate these dangling bonds.[62, 154] This returns a reasonable amount of semiconductor behavior, but devices are still electronically limited to 100 nms because of the high defect density, poor conductivity, weak internal electric fields, and susceptibility to light induced degradation by the Staebler-Wronski mechanism.[148, 154] These obstacles require an electric field through the length of the intrinsic absorber, created by sandwiching it with p-type and n-type layers on either side, creating a p-type/intrinsic/n-type (p-i-n) device. The p-type layer should always face incident light so that low-mobility holes travel less physical distance.[154]

The bandgap can be tuned in the range of about 1.7-1.9 eV. These amorphous materials are sometimes referred to as as direct bandgap semiconductors. However, they are better characterized in terms of their continuous density of available electronic defect states into the bandgap, which create mobility edges wider than the electronic bandgap below which carriers cannot move freely.[19, 50, 140] Thus, the electronic bandgap in these amorphous materials is wider than in its crystalline form. In terms of the optical bandgap, these materials exhibit an exponential decrease of absorption for decreasing photon energy known as the Urbach tail. This tail will give an optical bandgap smaller than the electronic gap as photons are absorbed by the defect states below the mobility gap. This exponential decrease in absorption and requirements of thin absorber layers for electronic performance work against each other in thin-film a-Si:H devices. This motivates low-cost nanophotonic light management solutions.

Amorphous silicon alloys and compatible dopant species are numerous, providing additional parameters for exploration. The ability to alloy Germanium into a-Si:H to create a lower band-gap a-$Si_{1-x}Ge_x$:H and deposit this within the same PECVD system is particularly important to this work. Combining a-Si:H solar cell followed by an a-$Si_{1-x}Ge_x$:H solar cell creates a tandem device which can use more of the solar spectrum, out to a wavelength of 900 nm.[62] These two PV cells are connected in electrical series and thus, the same amount of electrical current must flow through both cells during operation.[146] Ideally, both would produce the same current. Practically this is not always the case, and the excess current is lost to recombination in the cell that produces it. The challenge presented is to determine the effect of combining traditional texturing with periodic dielectric light trapping structures in an effort to balance the photocurrent absorbed in both cells to output the maximum J_{SC}. Concurrent work in single junction a-Si:H solar cells determined that an optimal balance of randomization and ordering should perform better than

either on their own,[8] as ordering will greatly enhance certain wavelengths while random texture aims to achieve the conditions of full $4n^2$ classical light trapping. (see Section 1.2).

3.2 Iterative Thin-film a-Si/a-SiGe Nanophotonic Simulation Based Design

Amorphous silicon PV cells were deposited onto a superstrate in a p-i-n layered structure. The first layer was a p-doped hole collector, followed by an in intrinsically doped absorber layer, and finally an n-doped electron collector. In this collaborative work, a series connected monolithically stacked tandem cell was the basis for exploration of improved light trapping by combining a traditional random texture with a NIL printed, periodically ordered 2D photonic crystal structure. The tandem cell layers were deposited onto the combined pattern for use in a superstrate fabrication.

The canonical/reference tandem cell studied is shown in Figure 3.1 and described here. A low iron content glass (Asahi U-Type) with randomly textured Fluorine doped Tin Oxide (FTO) was used as the superstrate for a near-completely PECVD based fabrication. The first semiconductor layer was a p-type layer that is Boron doped, p-hydrogenated amorphous Silicon Carbide (a-SiC:H), which provided a larger band-gap window for reduced parasitic loss,[154] followed by a intrinsic i-a-Si:H layer and n-type layer, Phosphorous doped n-a-Si:H. Next, an n-type micro-crystalline Silicon Oxide (μc-Si0$_x$) Intermediate Relfection Layer (IRL) served as a recombination layer and a low refractive index layer to help control the photocurrent balance between the top and bottom cells of the tandem.[14, 67, 69, 91] Next, the second p-i-n with a-Si$_{1-x}$Ge$_x$:H intrinsic layer was deposited, with the p(n)-layers being p(n)-a-Si:H. Last, the stack was removed from the PECVD chamber and an Indium doped Tin Oxide (ITO) buffer layer was sputter deposited followed by a thin Ag film which served as the back contact. Further details of the tandem cell fabrication can be found in References [67–69]. The randomly nano-textured FTO was modified via a conformal NIL print of square lattices of silica sol-gel pillars with varying diameters, heights, and pitch to enhance the absorption in the near infrared (NIR) of the bottom cell.

Rigorous Optical Modeling of Thin-film Tandem Solar Cells

CAD Geometric Model

A Finite Difference Time Domain (FDTD) model of the tandem cell was created in order to parametrically vary an inserted photonic crystal pattern before the top

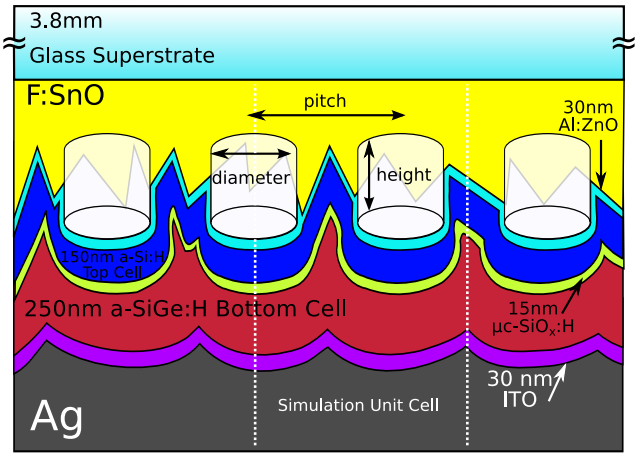

Figure 3.1: The typical a-Si:H/a-$Si_{1-x}Ge_x$:H studied here. The FTO was 750 nm on a 3.8 mm glass substrate. Three parameters that define the periodic lattice are shown as variables: the pillar diameter, pitch/period, and their height. These were coated in a thin aluminum doped zinc oxide (AZO) TCO for better electrical front contact. The first p-i-n cell had a total thickness of 150 nm, with each doped layer being 10 nm. The μc-$Si0_x$ IRL is 15 nm. The second p-i-n cell was a total of 250 nm, also with 10 nm thick doped a-Si:H layers. Finally a 30 nm ITO or μc-$Si0_x$, layer acted as a buffer between the Si layers and the 200 nm Ag back contact, which would have otherwise electrically poisoned the Si material.

cell, followed by a conformal deposition onto this pattern. Other optical models previously used geometric approximations of the conformal deposition[32, 42, 94, 95, 151], but it was found that this was not a sufficient approach in optimizing tandem a-Si:H/a-$Si_{1-x}Ge_x$:H devices. This model necessarily incorporated rigorous structural details of the device. Small input variations resulted in strong effects on the optical responses, especially with regard to portions of the spectrum where weak absorption tails in each materials are present. The real portion of refractive index was typically not problematic, but the current matching requirement correspondingly required accurate accounting of absorption in each layer, even when absorption was small valued. Mis-allocated photocurrent absorption would yield false results for the overall device performance predictions. Large shifts in photocurrent between the two cells was seen when adjusting pattern parameters to strike an optimal balance of photocurrent absorption between the two. The difference in absorbed photocurrent in the canonical, un-patterned tandem device was already small relative to the possible photocurrent absorption enhancements that could have been made with structuring, so careful control over the initial model's structural recreation was necessary to yield accurate results when simulating modified geometries. Last, a full 3-dimensional model was required to fully capture the complexity of the a-Si:H/a-$Si_{1-x}Ge_x$:H tandem device. Implementations of 2-dimensional models could not

match the necessary accuracy achieved with the full 3-dimensional model described here.

First, a detailed $10\,\mu m^2$ surface map of a textured FTO surface was measured via Atomic force microscopy (AFM) and imported into the model as the superstrate surface. Then, an ordered square array of pillars was built in the Lumerical FDTD CAD software. A first difficultly was estimating the effective height of such pillars, as the texture does not provide a clear reference plane to measure against. Here, the height was taken as an input, and an algorithm defines the reference plane as the mean height of the FTO layer at the center of the simulation volume and then offset the top of the pillar by the input height from that mean position. The pillar's base was then extended into the FTO layer, whereby a logical operation defined the material at each voxel to be either material, with the FTO have the highest priority. In this fashion, any FTO texture that is offset from the reference plane into the structuring (a peak) overrides the material of the pillar. Any area below the reference plane that was not FTO (a valley) was taken to be the pillar's material. This represents a true conformal printing, avoiding inclusions of free-space or removal of FTOtexture that may reside within a pillar. This can be seen through the semi-transparent representations of the pillars in Figure 3.1.

Next, measurements of the root-mean-square (RMS) roughness of the initial FTO surface and the final ITO surface were used to create a linear interpolation of the expected RMS roughness after each conformally deposited layer. The original FTO measurement data was iteratively smoothed until the target RMS roughness of each layer was reached within 10^{-4}.[53, 97] The new surface profiles were output to a file and used as an input into the CAD model to define the corresponding semiconductor layer. This smoothing is represented schematically in Figure 3.1. Again, to avoid free-space or spuriously incorrectly defined materials at each voxel, the layer was extended up through the FTO, with decreasing selection priority. This gave a rigorously detailed model of the device geometry due to the initial texture, and accounted for regions of each layer that are thicker than their nominal values due to accumulation in texture valleys. These details were important in being able to fit simulations to experimental results of canonical tandem devices using empirically measured values of layer thickness and corresponding deposition time. Using measured thickness values was more accurate than using the nominally targeted deposition thicknesses in modeling. This was due to layers being thicker than expected according to the deposition time-thickness calibration for structured

devices.

Ordered structuring was added by a geometrical approximation of the shape of a conformal layer around a pillar. The shape is usually seen in cross-sectional SEM and transmission electron microscope (TEM) images as a rounded layer, similar to a bump or dome (Figure 3.2 and Figure 3.7). In the model, this shape is approximated as a hemi-ellipsoidal cap on top of a pillar with appropriate radius on each axis.[43] Using SEM cross-sectional images of first iteration tandem cells that incorporated silica sol-gel pillars, each hemi-ellipsoidal object was modeled with linear fit of the increasing dome radius as a function of total material thickness. During the fabrication, it was observed that pillars would begin to smooth, and their tops would also have a hemi-ellipsoidal cap shape also, as seen in the cross-sectional SEM image in Figure 3.2. This was also accounted for by the model's geometric fitting.

An approximation that the surface texture, along with the array, is periodic was made such that capturing a small portion of the texturing was sufficient. This assumption was made as a trade-off between accuracy and computational intensity. The input pitch of the square pillar array only determined the periodic extent of the model unit cell indirectly, as the periodicity is more accurately defined by the coalescence of final curvatures in the Ag layer. Schematically, this is represented in Figure 3.1 by the vertical dashed lines indicating the simulation unit cell. 1.5 periods was used

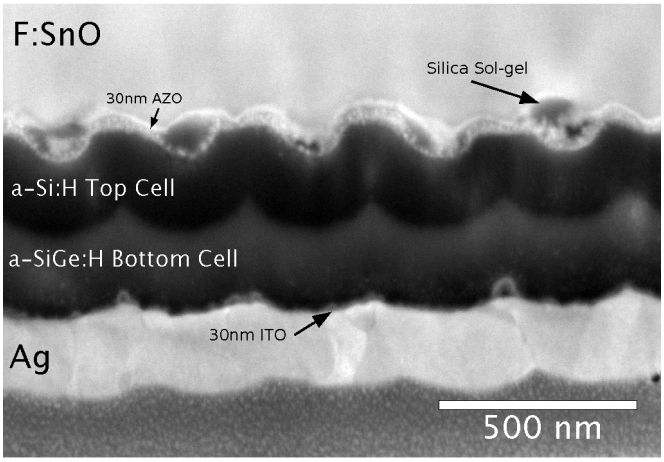

Figure 3.2: A cross-sectional SEM of a tandem a-Si:H/a-$Si_{1-x}Ge_x$:Hsolar cell with silica sol-gel pillars incorporated onto a textured FTO superstrate and the device layers conformally deposited.

in simulations to try to capture an appropriate amount of random texture to avoid repeating too small a sampling of the random texture. Thus, for a given input pitch in the model, the actual unit cell periodicity is defined by the propagation of the linearly increasing radii of the hemi-ellipsoidal cap in each layer. As an example, for very thin layers of absorber material, the final radius of the last hemi-ellipsoidal texture occurs close to the center of a pillar. For a pillar of the same diameter, but very thick layers, the final radius of the last hemi-ellipsoidal cap approaches a planar approximation and the actual periodic structure converges to pillar array's nominal value. Experimental pitches were selected according this final periodicity of the coalescing bumps. In experiment, the pitch of the cylinders directly controls this coalescence.

Non-standard FDTD Simulation Strategies

A discussion of important, proper FDTD usage strategies is appropriate. First, one of the strengths of the FDTD method is that many wavelengths can be measured during the same simulation. By virtue of injecting a short pulse into the simulation, the time-dependent nature of this pulse means it necessarily contains a broad spectrum of frequencies. This is a strength for simulation goals that are not as sensitive to erroneously allocated power absorption. However, this was a drawback when current balancing a tandem device in simulation. Here, dispersive materials were involved, and a continuous polynomial fit-function describing the optical properties would have been required for broadband data collection. The imperfect polynomial fitting leads to absorption errors, especially near or below the bandgap of our materials. Mathematically, this is because a polynomial fit cannot be exactly zero at each frequency below the optical band gap. Thus it was found to be more accurate to collect simulation results one wavelength/frequency at a time, as the refractive index fitting function is exact for a single wavelength. This was especially important when absorptive materials were being simulated below their band-gap. Single wavelength simulations also correct for errors when using "auto-shutoff" features in FDTD, which ends a simulation when a certain total remaining energy threshold is reached. Because lower frequencies contain less energy, and additionally are on the edge of the input Lorentzian frequency distribution, the higher energy frequencies dominate this metric. Low frequencies will not have decayed/converged to their final values as quickly as the higher frequencies. By evaluating only one frequency, the energy cut-off accurately calculates the energy of interest in the simulation. Last, In the Lumerical software, the *"optimize for short pulse"* should not be used as it will

broaden the input frequency spectrum. This option can also potentially risk not allowing enough time for scattered light to interact with resonances across larger distances in the simulation before the signal decays. This situation deviates from a steady state approximation. It is recommended to future researchers to perform careful convergence testing in these situations.

When using a single frequency in simulation, the input wave has a narrow, well defined frequency spectrum, meaning it adds a level of coherence that is not present in solar light or measurements. This led to resonant peaks that were sharper and stronger than seen in experiments. The *"partial spectral averaging"* feature was used to de-rate the response of a single frequency by analytically averaging the response of neighboring frequencies, generally increasing the agreement between simulation and experiment by an appreciable degree.[83, 84]

Last, because the simulation volume contains interfaces of absorbing and non-absorbing materials at any given frequency, an individual field component method of calculating the absorbed power was used. Due to the requirement to compute the curl of the electric and magnetic fields in FDTD, the fields are not co-located, but offset by one half of the side length of the Yee-cell voxel.[82] Each component is located either on the face center or middle of each edge, and the values are typically interpolated to a common voxel origin for computations. This is problematic when thin layers on the order of the voxel size, such as in this system. At lossy|dielectric interfaces, absorption from a neighboring layer can be interpolated into the wrong layer. To correct this, the individual electric field vector component absorption calculations were used. Absorbed power is computed by

$$P_{abs} = \frac{1}{2}\omega\epsilon''\left|\vec{E}\right|^2 \tag{3.1}$$

The above equation allows distribution of the scalar factors (where ω is the angular frequency and ϵ'' is the imaginary component of the dielectric constant) to each field component individually. This allowed application of the proper ϵ at each point in the simulation volume before interpolating the absorbed power, even if the actual location of the field component on the Yee-cell lies across the interface.[73] Alternatively, the locations of the Yee cell absorbed power locations were "masked" by their associated dielectric constant ϵ, and the proper ϵ'' values were applied to all components in the Yee-cell. This restricts the inclusion of electric field components which may be inflated due to considerably higher field values arising from nearby high permittivity materials within the same Yee-cell. These approximations are

required for accurate, yet computationally tractable simulations. A staircase mesh should be used with this technique. Similar techniques were used in Chapter 4.

Ellipsometry Characterization Fitting to Cody-Lorentz Model

Accurate optical constants were the second key input to the predictive optical model. Ellipsometry was used to fit measurement spectral reflection amplitude component Ψ and phase shift Δ, and spectral transmission to the Tauc-Lorentz (TL) and Cody-Lorentz (CL) parametric optical models. These parameters were fitted to models of thin-films with known the thicknesses to all the different constituent materials. During the first iteration of models and experiments, the TL parametric model was used to fit the data. The TL model was initially used due to it historically being a popular framework for the characterization of the band-gap of amorphous materials. Initially the band gap of the materials was determined by collaborators via the Tauc method. This method is a linear fit of the product of the photon energy and square root of α as a function of photon energy, where $\alpha = 4\pi k/\lambda$ where $k == \epsilon''$ is the imaginary part of the refractive index.[68, 69, 159] In the TL model, the optical bandgap is defined as the energy at which the fit line has a value of zero absorption, i.e. when it crosses the abscissa at zero ordinate. This Tauc optical band gap was used as an input into the TL model when fitting initial ellipsometric data.

Tauc gap determinations depend on measuring a suitable range of α in which the proper linear relation is seen. However the fitted energy range of the curve is often arbitrary. When optical measurements can not reliably obtain data in for low values of α near the optical gap edge, the true nature of the Tauc curve is subject to extrapolation. [25, 40] While this simpler approximation is useful in a variety of instances, here its value could vary by up to 0.5 eV between different measurement tools. This was especially true for very thin-films on the order of 50 nm, where the uncertainty of the film-thickness by profilometry used to calculate α was an additional limitation for the TL model. The CL optical constants model was used here to increase the accuracy of simulations.

An overview of the TL and CL optical constants models is given. Both expressions are Kramers-Kronig consistent, and the real part of the permittivity can be calculated from the imaginary part. Equation (3.2) gives the Lorentz oscillator function which is responsible for the dielectric properties for energies much greater than the band-gap, $E >> E_g$. Here, A is the resonant amplitude, B_r is a width/broadening parameter, and E_n is the resonant energy position. Equation (3.3) and Equation (3.4)

show the imaginary and real parts of the dielectric permittivity of the Tau-Lorentz formulation. The assumption that the imaginary part of the optical constant abruptly achiceves a zero value does not provide much flexibility to account for absorbing states below the Tauc bandgap E_t, where the Urbach tail transition begins. This can be accounted for in the CL equations. The second key difference between the two is in the expression $G_t(E)$ of the TL formulation, which assumes a constant momentum matrix and parabolic bands near the gap.[25, 40] The P of Equation (3.4) indicates the principle value integral and ϵ_∞ is the permittivity at infinite energy, which is usually unity.

$$L(E) = \frac{AE_nB_rE}{(E_n^2 - E^2)^2 + B_r^2E^2} \tag{3.2}$$

$$\epsilon_2(E) = \begin{cases} 0 & E < E_t \\ G_t(E)L(E) & E_t \leq E \end{cases}, \quad G_t(E) = \frac{(E - E_t)^2}{E^2} \tag{3.3}$$

$$\epsilon_1(E) = \epsilon_\infty + \frac{2}{\pi}P\int_{E_t}^{\infty} \frac{E'\epsilon_2(E')}{E'^2 - E^2}dE' \tag{3.4}$$

The analytical solution of the Cody-Lorentz model of Ferlauto in Equation (3.5) and Equation (3.6) improves upon the TL model by adding an expression for the imaginary part of the dielectric constant below the Tauc gap energy and assuming a quadratic energy relationship with a constant dipole matrix element.[40] The parameter E_u is the slope of the Urbach tail absorption below the optical bandgap and E_p is a second transition energy which demarcates the transition at $E_g + E_p$ from the stronger Lorentz-like absorption of higher energies. This adds flexibility to account for the change in carrier-excitation mechanism.

$$\epsilon_2(E) = \begin{cases} \frac{E_tG_c(E_t)L(E_t)}{E}e^{\frac{E-E_t}{E_u}} & E < E_t \\ G_c(E)L(E) & E_t \leq E \end{cases}, \quad G_c(E) = \frac{(E - E_g)^2}{(E - E_g)^2 + E_p^2} \tag{3.5}$$

$$\epsilon_1(E) = \epsilon_\infty + \frac{2}{\pi}P\int_{E_g}^{\infty} \frac{E'\epsilon_2(E')}{E'^2 - E^2}dE' \tag{3.6}$$

Each layer was individually characterized as a thin-film deposited on Eagle XG display glass measured with a J.A. Woollam UV-Vis ellipsometer and fit with the WVASE software to obtain the complex refractive index values from the fitted parameters. The first step to accurate fitting of each absorbing material was an accurate fit of the Eagle XG substrate by the TL model. Next, the X-ray rocking technique

was used to accurately determine the thickness of each film within ±2 nm. Each measured film was on the order of 50 nm so that the thickness was similar to that of the actual device to avoid any potential thickness dependent inaccuracies. Reflection measurements of Ψ and Δ were taken between the angles of 50° and 70°. These angles are specifically on either side of the substrate's Brewster's angle. Near this angle, Ψ and Δ are most sensitive to thin-film interference phenomena due to larger phase shifts and amplitude variations. Spectral transmission was also measured at normal incidence. These values were then fitted using a global parameter fit for each of the values in the TL and CL equations above, with optimization weights favoring the NIR wavelengths near the a-$Si_{1-x}Ge_x$:H band gap. This wavelength band was where previous design iterations indicated the most discrepancy between model and experiment. Finally, as a determination of the accuracy of the materials constants, a full 3D FDTD simulation over a large area 3 μm^2 of the AFM measured texture was performed and compared to the canonical experimental tandem.

Figure 3.3 shows the difference between the two models' optical constants for the most difficult to measure material, a-$Si_{1-x}Ge_x$:H. The TL model over estimated the real and imaginary parts of the refractive index at the wavelengths where the top a-Si:H cell begins to transmit light to the bottom a-$Si_{1-x}Ge_x$:H cell. These wavelengths required a high degree of accuracy to output proper photocurrent absorption predictions. The inset shows a logarithmically scaled zoom of the imaginary parts from 600 nm to 900 nm. The TL prediction shows a steep drop in this value as the E_t bandgap (near 900 nm) is approached compared to a smooth decline in the CL data. The knee in the CL model signifies an absorption mechanism transition to that of the Urbach tail. Results comparing the reference tandem cell device's experimentally measured EQE to the modeled response using CL optical constants are shown in the right-hand side plot of Figure 3.3. The predictions of each sub-cell very closely matched the EQE measurements. This was the closest agreement that was seen. An comparison of the model/experimental EQE curves for nano-structured tandem cells is shown in Figure 3.6B.

Rigorous Optical Model J_{SC} Prediction

Finally, after a rigorous iterative characterization effort to match model to canonical reference a-Si:H/a-$Si_{1-x}Ge_x$:H tandem cell measurements, the model was used to predict the EQE response of devices incorporating both ordered and rough textures into a device. The height and diameter parameters of a square pillar array indicated in Figure 3.1 were varied. The resulting possible J_{SC}, which is the integral of the

EQE weighted by the ASTM Air Mass 1.5 Global (AM1.5G) solar photocurrent spectrum, of each parameter combination of the top and bottom sub-cells is shown in Figure 3.4. The carrier collection efficiency, IQE, is assumed to be unity due to the very thin thickness of each sub-cell; the implications of this assumption are discussed in Section 3.4.[32, 42, 43]

Figure 3.4A shows that increasing the pillar height shifts absorption to the top cell. Available surface area for deposition increases with pillar height. Maintaining a constant layer thickness on the pillar means that more material is deposited overall. This realistically represented the constant experimental deposition time used in fabrication of the patterned and un-patterned devices. The top cell shows a band of enhancement starting around a diameter of 200 nm that follows the pillar diameter. This is due to coupling into guided modes of the device via diffraction which is a pitch dependent phenomenon. Figure 3.4B Shows a similar increase in collected photocurrent due to increasing height of pillars for the same reasons as that of the top-cell, with enhancement occurring along the boundary in the parameter space of where the top-cell current no-longer benefits from increased pillar height. A band around 200 nm for all heights in Figure 3.4B shows a relative decrease for heights between 125 nm to 175 nm, while this is a region of enhancement for the top cell. Finally, Figure 3.4C shows the maximum collectible current from the series connected device, which is the minimum of the absorbed photocurrent in either sub-

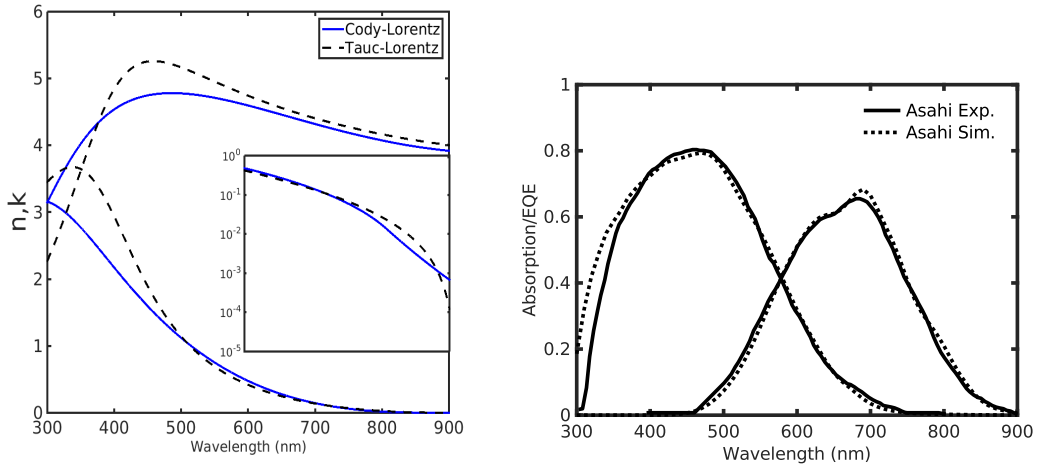

Figure 3.3: Left: A) The difference in the TL and CL optical models for a-$Si_{1-x}Ge_x$:H thin-films. The TL and CL models disagree at key spectral positions where the a-$Si_{1-x}Ge_x$:H material is optically/electronically responsive.**Right: B)** A comparison of the canonical reference a-Si:H/a-$Si_{1-x}Ge_x$:H tandem compared to the model predicted response using the CL optical constants for each layer.

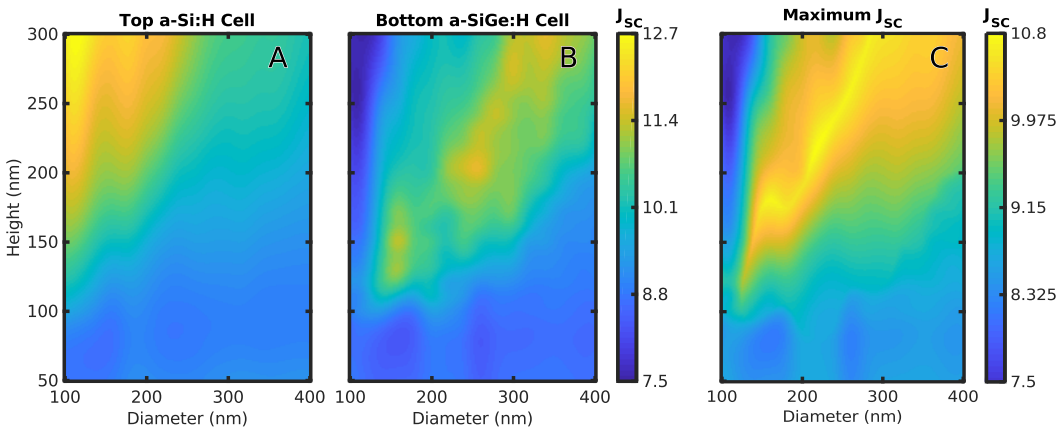

Figure 3.4: The rigorous 3D model was used to predict the devices potential current output due to various combinations of pillar height and diameter. The pitch is such that the conformal layer modeling is close-packed. **A)** The predicted integrated J_{SC} contribution of the top a-Si:H sub-cell. **B)** The predicted integrated current of the bottom a-$Si_{1-x}Ge_x$:H sub-cell. **C)** The minimum current of each sub-cell is taken to predict the output of the series connected tandem device.

cell. The region of maximum enhancement lies at the boundary between the two enhancement regions, with a maximum value at a height of 175 nm and a diameter of 150 nm. The enhancement regime appears to continue with increasing height, but beyond 300 nm, the pillars begin to become larger than the nominal total layer thickness. The enhancement that trends with height is likely due to the addition of increasing amounts of material arising from the conformal deposition coating the tall pillars.

3.3 Nanoimprinting Nanotextured Surfaces

Fabrication of nanophotonic pillar arrays was completed by use of conformal NIL. Procedures can be in Chapter 2. A pillar array with diameter of 150 nm was patterned with EBL on a silicon substrate and etched into this substrate to a final height of 250 nm, according to the predictions of Figure 3.4. Five different pitches (215 nm, 270 nm, 315 nm, 360 nm, and 405 nm) were written over 6 mm^2 in a column of 5 cm. Development of fast, large area EBL pattern writing was developed to scale the achievable area and reduce the required time to complete such patterns. The column was reproduced in soft-stamps multiple times, which were then combined into a quilted large stamp. This quilted stamp was designed to match the dimensions of the Asahi superstrates, 5 cmx5 cm. Quilting was developed to repeatably recreate the same layout as the shadow mask used for Ag back contact deposition.

During all nanoimprint stamping, a roughly 20 nm residual layer of sol-gel separates

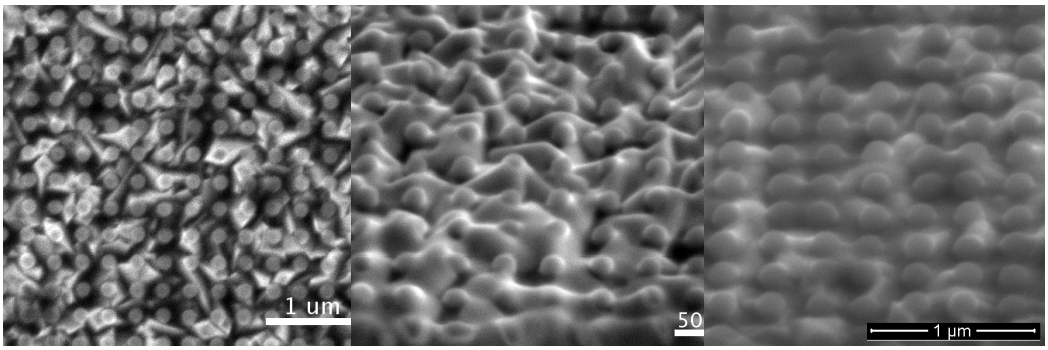

Figure 3.5: Left: A) A plan view of pre-etched conformal NIL sol-gel pillars on Asahi substrate shows successful transfer of a high fidelity pattern. **Middle: B)** A 52° SEM image of the pattern after etching shows pillars that have been smooth to rounded top bumps, which was taken into account in the optical model. **Right: C)** A 52° SEM image of the pattern after AZO deposition shows further smoothing.

the pattern from the substrate. This is discussed in Chapter 2 and seen in Figure 2.1F. This layer proved to be especially problematic on textured surfaces. Due to the initial liquid state of the sol-gel, the sol-gel would fill the valleys in the texture and planarize the surface. This created an electronically insulating barrier between the front contact and the tandem device. When stamping on flat substrates, a short approximately 10 s ICP-RIE silica etch can be used to remove this residual between pattern features. This was not sufficient to remove the material in-filling the texture. Etch times were increased to 50 s and 60 s. The results of these longer etches removed most but not all of the excess sol-gel. It also shortened and rounded the pillar shape. Final samples showed reduced heights from 250 nm to 200 nm for a 50 s etch and 125 nm for a 60 s etch. A height difference of nearly 75 nm over the extra 10 s was observed, indicating a non-linear etch rate. The resulting structures can be seen in the cross-section images of Figure 3.2, Figure 3.5 and Figure 3.7.

After etching, electrical contact was difficult to ensure, leading to low yield in deposited devices. The solution was to deposit a thin TCO layer, 30 nm AZO, onto the sol-gel pillar array to ensure electrical contact with the FTO front contact. The deposition was performed via sputter deposition, and calibrated to yield low resistivity. This was seen to be dependent on gas flow ratio during sputtering of the AZO target, with a decrease of over 3 orders of magnitude from 150 Ω cm for an Ar/O_2 flow ratio of 109 to 0.05 Ω cm for an Ar/O_2 ratio of 509, each with a constant AC deposition power of 100 W.

3.4 Results and Discussion: Experimental Results Explained by Model

The fabricated samples were exchanged with collaborators at the National Chiao Tung University in Taiwan for deposition of the a-Si:H/a-$Si_{1-x}Ge_x$:Htandem cells. Collaborators independently measured EQE with an LED based spectral illumination and AM1.5G spectrum filtered solar simulation to measure the JV performance. This author also performed independent EQE measurements. An example is shown in Figure 3.6B. The EQE was measured with the monochromated laser line described in Appendix A with a 2x microscope objective. EQE measurements of individual sub-cells require that the cell not being measured must have excess current so that the generated current of the measured sub-cell can pass through the device. This is known as light-biasing. To accomplish this, a 400 nm (when measuring the bottom-cell) or 850 nm (when measuring the top-cell) focused LED laser source was incident on the device from the side onto the same spot as the 2x focused beam. Due to the low mobility and relatively high power of the focused monochromated beam, the LED lasers were focused into a tight spot to minimally over-fill the monochromatic spot. Light biasing of either cell creates a V_{OC} in the light biased sub-cell. This must be compensated for in order for the entire device to be at 0 V. A Keithly voltage source was connected in series between the cell contact and the lock-in amplifier measurement to hold the entire circuit at 0 V.

Figure 3.3 shows the model matches experiment well for the simple canonical reference tandem cell in spectral EQE. Of the many patterned device trials, few returned positive results in terms of enhanced EQE. However, absorption was visibly improved, as can be seen in as can be seen in Figure 3.6A.

Figure 3.6B shows the experimentally measured EQE of a champion patterned tandem cell compared to the simulated EQE for approximately the same pattern dimensions. The model was able to predict new peaks due to enhanced coupling into new waveguide modes of the bottom a-$Si_{1-x}Ge_x$:H cell. The bottom cell was targeted because it was the current-limiting cell in the canonical device. Minor adjustment on the order of single nm's were made in the model to account for film thickness differences between patterning and the canonical device seen in Figure 3.3B. Due to the imprecise control of the interstitial sol-gel etch, the EQE was matched by sweeping various pillar heights. The best match to experiment was found to be 200 nm. An enhancement shoulder around 754 nm is slightly red-shifted in the model, while the peak at 806 nm agrees near perfectly, as well as another small enhancement peak near 850 nm.

Figure 3.6C and D show the electric field magnitude in the whole tandem device and the power absorption by the a-$Si_{1-x}Ge_x$:H bottom cell absorber at a wavelength of 806 nm. These correspond to the peak seen in Figure 3.6B. Figure 3.6C shows one of the waveguide modes created by the ordered structuring occurs near the bottom of the cell. Here, the bowl shaped Ag back contact concentrates field, leading to higher power absorption in the bottom cell. The absorption in the back-reflection layer and the Ag back contact are filtered out in Figure 3.6D. These layers also have an increase in power absorption, but the generated carriers are not collected. This

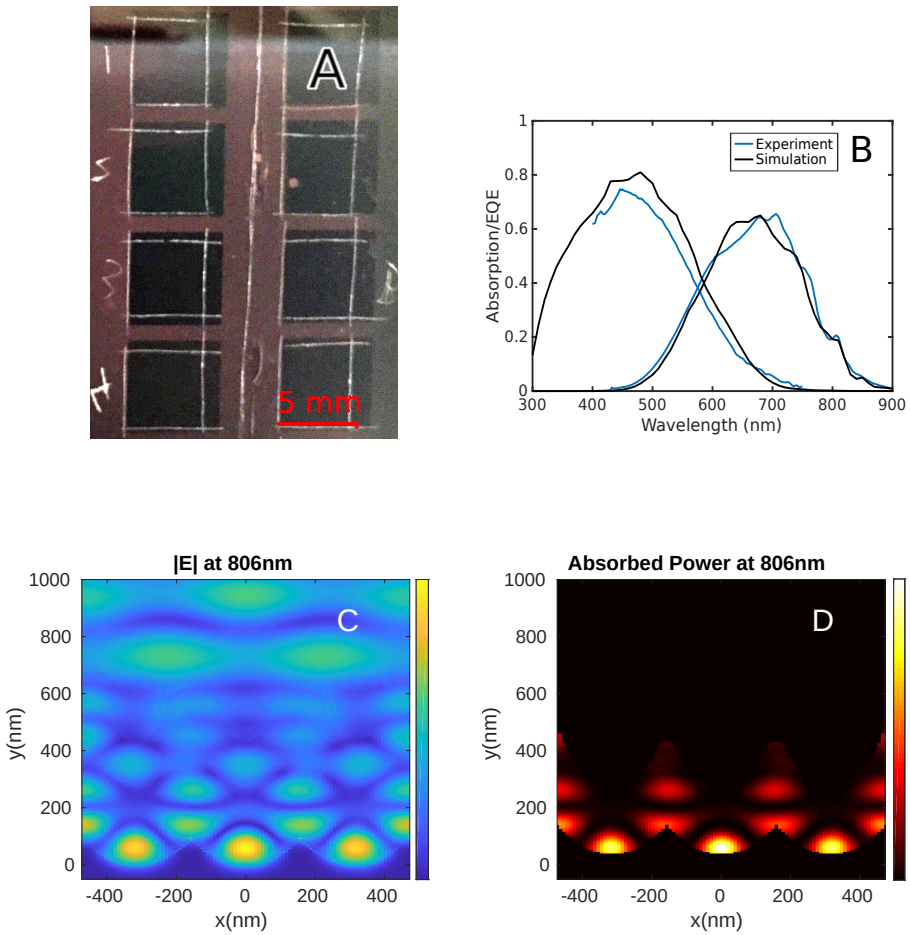

Figure 3.6: A) A photograph of the nanoimprinted solar cells. Layers are deposited over the entire textured superstrate. Scribe marks roughly outline device areas. Darker squares are patterned areas while the lighter areas outside these squares have only the Asahi texture. Each pattern has a pillar diameter of 150 nm. Each row is the same pattern, while the columns change the array pitch. From top to bottom, these were 270 nm, 315 nm, 360 nm, 405 nm. B) The best match between the model and experimental measurements of EQE. The model predicts new peaks due to light trapping in the NIR, but does not account for losses below 650 nm. C) A cross-section of the electric field magnitude of a resonant mode at 806 nm of the device in B). D) The absorbed power in the bottom a-$Si_{1-x}Ge_x$:H cell due to the field in C), which is proportional the carrier generation rate.

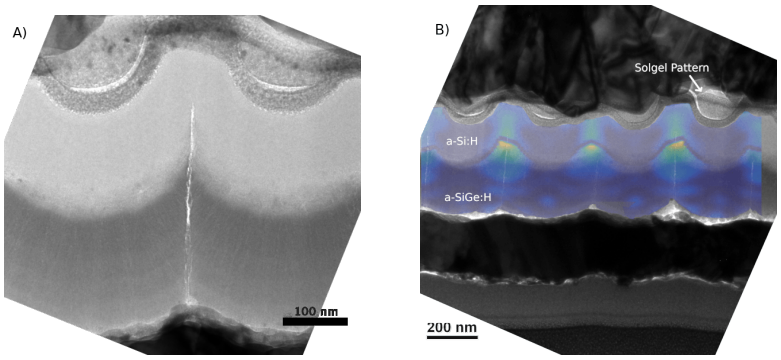

Figure 3.7: **A)** A high-resolution TEM cross-section image shows two periods of the patterned array. A line defect through the bottom a-$Si_{1-x}Ge_x$:H cell is clearly seen, as well as finer hairlike line defects extending radially from the center layer. **B)** A false-color map of the AM1.5G weighted optical generation rate for incident light between 550 nm to 650 nm obtained via the optical model is overlaid onto another TEM image. Optical generation is concentrated at defect lines, leading to loss in this wavelength range. Images were rotated from their original format for clarity.

provides an explanation of why the enhancement at this wavelength is modest.

Results from the model and experiment disagree in the visible spectrum between 400 nm to 700 nm. In Section 3.2 the assumption of unity IQE proved to be appropriate when modeling the reference tandem cell, as seen in Figure 3.3B. However, the disagreement indicated there must be unaccounted losses. Cross-sectional TEM imaging was used to examine the internal structure of the experimental cell with EQE depicted in Figure 3.6B. High resolution TEM images of the tandem cell are shown in Figure 3.7A and B. The different layers are more clearly visible in TEM. From the top of Figure 3.7A, two periods of the pattern can be seen with a shape conforming to the texture underneath. The smoothing due to the ICP-RIE etching is also apparent. Next, the AZO capping layer is visible. Fainter, but still detectable, is the first a-SiC:H p-layer, followed by the a-Si:H absorber, the μc-$Si0_x$ intermediate reflection layer, the a-$Si_{1-x}Ge_x$:H absorber, the ITO layer and finally the Ag near the bottom appears black.

The most glaring discrepancy between Figure 3.2 and Figure 3.7 are the bright vertical lines through the a-$Si_{1-x}Ge_x$:H layer. These are unintended defects arising from the nature of the conformal deposition. Rather than coalescing, physical boundaries were formed between pillars. Reference [7, 139] found similar degradation in performance for single junction a-Si:H solar cells, proposing that these

line defects may act as shunt pathways and current sinks, reducing the V_{OC} and FF. Reference [32] demonstrated in optoelectronic modeling that these defects are the location of greatest recombination rate. Key differences between those works with periodically structured a-Si:H solar cells and this work are that in Reference [32] a substrate periodic structure was used and in Reference [7], hydrogenated micro-crystalline Silicon (μc-Si:H) was used as the bottom cell. Figure 3.7B, shows an overlay of the simulated optical generation for wavelengths between 550 nm to 650 nm in the tandem cell. Carrier generation hot-spots are concentrated at the high recombination line defects in this wavelength region. This is distinctly different than the *substrate* patterned devices examined in Reference [32]. Generation in this area contrasts the regions of maximum carrier generation at the bottom of the cell in Figure 3.6D which led to enhancement at the longer wavelengths. The different locations of generation explain the losses in the visible wavelength compared to the enhancement in the near-infrared. The decrease in EQE of the top cell below 500 nm is less readily explained, but could also be due to these line defects extending into the top cell absorber layer but were not resolved in the TEM images.

Finally, the JV curves for two sets of tandem solar cells are presented in Figure 3.8. The two data sets represent a 50 s and 60 s etch time, giving pillar heights of approximately 200 nm and 125 nm, respectively, as estimated by etching rates and cross-sectional SEM. Of the 5 different pitches, 4 yielded measurable devices. The 215 nm pitch arrays never leading to working devices. The taller pillars perform worse in terms of FF and V_{OC} for all array pitches for the taller pillars. The formation

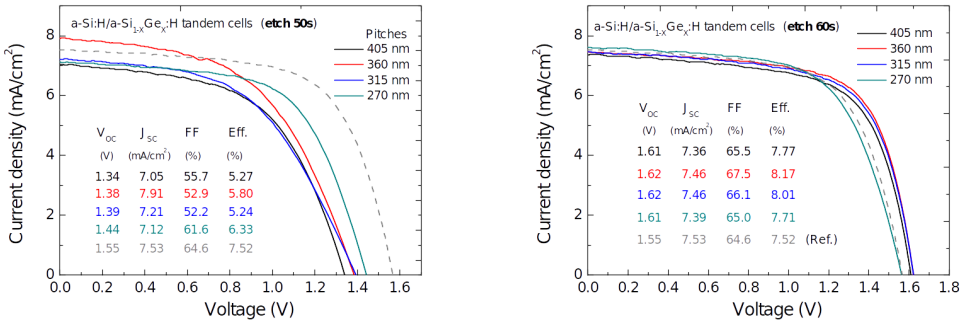

Figure 3.8: JV curves of tandem a-Si:H/a-$Si_{1-x}Ge_x$:Hsolar cells with 150 nm diameter NIL pillar arrays of various pitches that were applied to textured Asahi superstrates. The silica sol-gel pillars of **A**) and **B)** were etched to removed excess sol-gel for 50 s and 60 s respectively. Figure courtesy of H.J. Hsu.

of line defects in tall pillars is more likely. The loss of V_{OC} and FF in samples with taller pillars support the findings of Reference [7] and Reference [139]. Additionally, the J_{SC} is worse than the reference device for all but one pitch. The increased current in that sample resulted from shifting visible wavelength absorption from the bottom cell to the top cell.

The longer etch time and shorter pillars out-perform the reference cell in their efficiency, V_{OC}, and FF. The J_{SC} is either slightly less than, or equal to the reference cell. The EQE curves resulting by the optical model did not predict this result, as all model results showed greater AM1.5G integrated current than the modeled reference cell. The EQE curves (not depicted) also showed no enhancement modes in the bottom cell, as the pillars have been shortened significantly due to the extended etching. These results still have unknown origins, as many factors could be responsible for the differences in positive performance compared to the reference cell. Increased V_{OC} was observed when a control sample with the same AZO deposition was put through the same etching and fabrication processes. This provided some evidence of either decreased resistance at the front contact, or perhaps smoothing that may have mitigated any line defects from higher aspect ratio portions of the Asahi texture.

3.5 Conclusions

Unfortunately, the results in Figure 3.8 directly opposed the optical model's prediction of Figure 3.4 that taller pillars should better. Combining TEM evidence with the optical model showed that this was caused by a concentration of optical carrier generation at these line defects in the bottom cell. Though the optical FDTD model was extremely rigorous in terms of accurately recreating texture, conformal deposition shapes, thickness, and optical constants of each layer, it could not ultimately predict the observed electronic defects. The complexity of modeling this system was extreme, yet still some parameters were unaccounted for. Typically, simulation-driven-experiments can lead to successful greater experimental success. Unfortunately, this was not the case for this work. The optical model was successful, however, in helping to explain some of the decreased performance. The model helped elucidate the causes of peaks in the NIR wavelengths and loss due to the concentration of generation at defects.

Two different approaches could have been taken to drive a more successful line of experimentation. First, a full optoelectronic model similar to Reference [32]

could have helped to avoid some false-positive predictions by including electronic defects and full JV curve simulations. The drawbacks to this approach would be further expanding the necessary rigorous parameter space to include electronic properties such as mobilities, trap states, and defect densities etc. of each material. These parameters are well documented for only some of the materials such as a-Si:H and AZO, and were not as readily available for other materials such as μc-Si0$_x$, a-SiC:H, or a-Si$_{1-x}$Ge$_x$:H. Second, a traditional experimental parameter space exploration would have obviated the CAD model. This approach could have reduced the parameter space to that of pillar pitch, pillar diameter, and etching time as a proxy for pillar height. The monochromated laser beam line of Appendix A was upgraded to handled this sort of experimental optimization due to the demonstrated need, but only after the conclusion of the collaboration. No more samples could be made for experimental optimization at that point. The results of this work showed the importance of a full optoelectronic approach in device simulation, which was developed in Chapter 4.

Chapter 4

PHOTON AND CARRIER MANAGEMENT DESIGNS FOR NONPLANAR THIN-FILM $Cu(In_xGa_{1-x})Se_2$ PHOTOVOLTAICS

4.1 Introduction

Thin-film solar cells have been researched as alternatives to crystalline silicon solar cells for decades due to high efficiencies greater than 20% and the intrinsic benefits of thicknesses on the order of microns, such mechanical flexibility and a variety of substrate options. Typically, CIGS photovoltaic devices are between 1-3 μm thick, allowing the majority of incident sunlight to be absorbed. Reducing the thickness of devices below 1 3 μm is desirable to increase production throughput capacity while reducing the materials cost associated the rare-earth metal indium, which is also highly in demand for large area applications by the flat-panel display industry. Reducing thickness would also decrease the number of minority carriers lost to bulk recombination, thereby increasing the voltage of devices. [58] However sub-micron cells cannot absorb all incident photons in a traditional planar architecture, and the reduced bulk recombination are lost due to surface recombination at the back-contact. Here, we demonstrate that nanophotonic structures could address both of these issues, leading to efficiencies unattainable by planar devices with the same electronic qualities.

Light management by incorporation of randomly textured microstructures or nanostructures has been extensively investigated for crystalline silicon, amorphous silicon, and GaAs photovoltaics,[18, 33, 60, 85, 107, 183] but such approaches have not been as extensively applied to polycrystalline thin-film compound materials and devices, such as CIGS, CdTe, and Cu_2ZnSnS_4. [24, 93] Here, we explore the underlying mechanisms of unexpectedly high absorption in random textures that were seen experimentally by Heliovolt and compare them to other popular light trapping structures for thin-film photovoltaics. [95, 136, 168] Our simulation approach is uniquely able to extract differences between different structures by holding constituent materials parameters constant, such that performance differences are solely due to device geometry. By building on progress in other materials systems, we identify opportunities for improvement to both the short-circuit current density (J_{SC}) and open circuit voltage (V_{OC}) via coupled optoelectronic simulations.

Many studies of light management in photovoltaics and solar cell architectures have focused on increased light absorption as a design objective with important implications. [16, 43] As a first approximation, this type of analysis gives a qualitative indication of how light management can increase cell efficiency. However, coupled optoelectronic modeling in which both full-field electromagnetic simulation of light absorption and scattering is combined with detailed carrier generation, transport, and recombination models results in a more complete picture. [31, 100] Accurate modeling of the spatial distribution of generated carriers is important, in addition to increasing overall absorption because ultimately, the charge carrier collection efficiency directly affects photovoltaic efficiency. Only a full optoelectronic model can quantitatively relate optical absorption enhancement, electronic transport, and photocurrent density enhancement, and highlight electronic transport issues which can be overcome by improved optical design. For example, we observe that randomly textured CIGS absorbers can absorb the majority of the incident spectrum in a film of 700 nm planar equivalent thickness, but generated carriers are lost to parasitic recombination in near the back-contact interface. Strategies to overcome these issues are described as well other light trapping for CIGS devices grown via more conventional film synthesis processes. We identify possible CIGS device architectures that enable thinning of the CIGS absorber layer to an equivalent thickness of 700 nm while maintaining or improving the J_{SC} and/or the V_{OC} compared to those of thicker planar devices.

4.2 Methods

Optical Modeling of CIGS Absorbers

Randomly textured CIGS thin film photovoltaic absorbers exhibit a complex random film topography that results from a Cu and Se flux assisted re-crystallization process, leading to grain coalescence and coarsening as well as void formation via reactive mass transport. [136] These absorber layers were experimentally seen to have exceptional light trapping characteristics, motivating this numerical simulation study of the underlying light trapping mechanisms in comparison to other potential architectures. Experimental corroboration of the device performances predicted by the models herein was rendered impossible by the cessation of Heliovolt's research and development effort. However, the published experimental External Quantum Efficiency (EQE) measurements qualitatively match the results herein, leading to the conclusion that our representation is a reasonable approximation of these textured devices. [136]

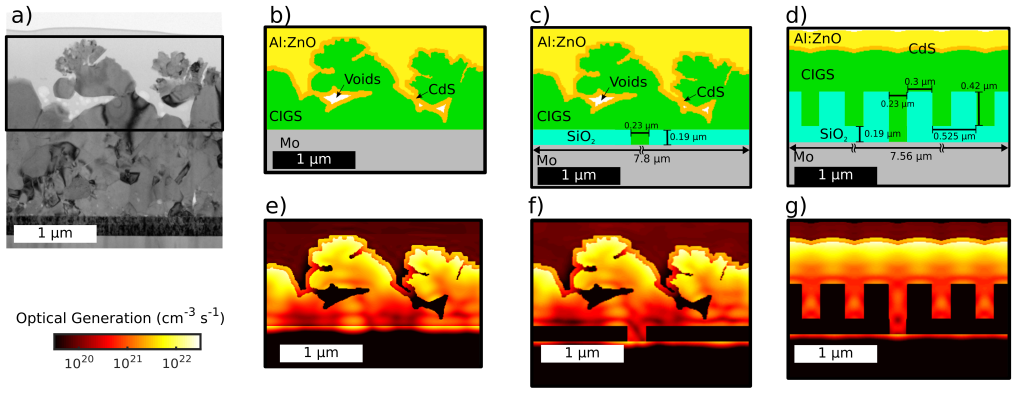

Figure 4.1: Simulated Cross-Sections a) A representative focused ion beam(FIB) cross section of randomly textured CIGS absorber films is used to define the photovoltaic model for a Mo back-contact device, shown in b). In c), a SiO_2 layer serves to increase reflection and define electrical line contacts, enhancing CIGS film passivation; d) shows a periodic CIGS photonic structure defined by deposition on a patterned SiO_2 layer with electrical line contacts. The optical generation profiles, weighted by the AM-1.5G solar spectrum, for devices simulated in b), c), and d) are shown in e), f), and g).

The provided cross-sectional scanning electron microscope (SEM) images of these absorber films were used to construct models for optoelectronic simulations aimed at identifying mechanisms of light trapping. A representative cross-sectional image can be seen in Figure 4.1a, which is a CIGS film with equivalent planar thickness of 1.7 µm. This cross section was contrast-thresholded and filtered with imaging software to create a digital representation of the film. [1]

The device schematic in Figure 4.1b illustrates a simulated device structure that utilizes this absorber film morphology. The device cross section in Figure 4.1b includes a 50 nm CdS conformal window layer, contacted to a CIGS absorber layer to simulate device structure resulting from conformal bath deposition. Voids which occur naturally during the recrystallization process are included in the model, and are consistent with the film morphologies observed in cross-sectional SEM micrographs. The CdS layer is coated with a 150 nm aluminum-doped zinc oxide (AZO) that fills the remainder of the volume and serves as a transparent front contact. The back-contact consists of a 500 nm molybdenum (Mo) planar thin film.

Representative devices cross sections, such as in Figure 4.1b, were rendered for full field electromagnetic simulations in two dimensions (2D) with periodic boundary conditions. [43] Electromagnetic simulations using the finite-difference time-domain (FDTD) method were performed with normally incident plane wave illumi-

nation; all optical quantities reported here were obtained as polarization averages of the transverse electric and transverse magnetic responses for the films. The absorbed fraction of the incident solar spectrum was constructed from a set of single wavelength electromagnetic simulations that were then power-weighted by the spectral irradiance of the ASTM -AM1.5G solar spectrum. The fractional gallium composition of absorbers in [136] is close to x=0.4, and refractive index data for this composition was used to construct the complex dielectric function for CIGS absorbers in electromagnetic simulations. [3] CdS optical constants are taken from [162], ZnO from [43], and Mo from the Sopra Materials Database[147].The power absorbed in each material can be calculated from the electric field magnitude and complex refractive index at each mesh point in the simulation. The optical generation rate, G_{opt}, is calculated by

$$G_{opt}(\lambda, \vec{r}) = \frac{\epsilon''(\lambda, \vec{r})|\mathbf{E}(\lambda, \vec{r})|^2}{2\hbar} \tag{4.1}$$

where ϵ'' is the imaginary part of the material's complex permittivity, $|\mathbf{E}|^2$ is the electric field magnitude, $\vec{r}$ is the position vector, λ is the wavelength, and $\hbar$ is the reduced Planck's constant. [31, 43] Spatial maps of charge carrier generation are then used as inputs of the device physics simulations described in the following section. [31, 46]

Electronic Modeling of CIGS absorbers

The optical generation profiles for all structures depicted in Figure 4.11 as well for planar films were input into carrier transport simulations to numerically calculate the steady state EQE and current density-voltage (J-V) characteristics of each device. We took advantage of previously reported transport parameters for CIGS photovoltaics,[57] except where explicitly stated herein. While the reader is referred to [57] for specific materials parameters, we explicitly point out two important parameters here. First, the CIGS|Mo surface recombination velocity is set to the thermal velocity, $10^7\,\mathrm{cm\,s^{-1}}$, and represents a worst-case scenario. Coupled with the Mo|CIGS Fermi-Valence Band offset of $-0.2\,\mathrm{eV}$, the valence band in the region close to the back-contact bends downward. Second, the defect density model used more rigorously represents non-uniform lifetimes in regions with strong illumination and depletion, giving a more accurate response than the Shockley-Read-Hall (SRH) recombination model. Still, an instructive estimate of the CIGS bulk minority(majority) carrier diffusion length, as determined by the Einstein relation for

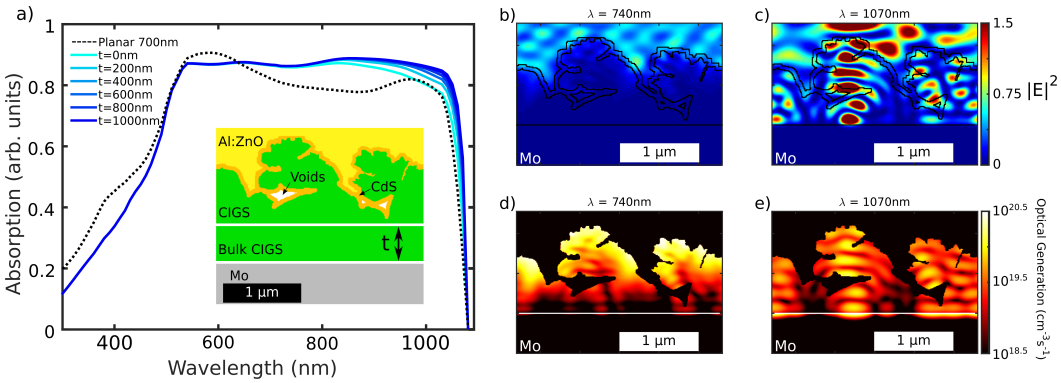

Figure 4.2: Randomly Textured Absorbers a) Absorption for CIGS device with a randomly textured absorber. Inset shows thickness, t, of planar CIGS film underlying randomly textured structure, which is varied between 0 μm (light blue) and 1 μm (dark blue). Absorption is nearly constant across the spectrum and weakly dependent on film thickness. In b) and c), magnitude of the polarization-averaged electric field intensity, $|\mathbf{E}|^2$, at λ=740 nm and λ=1070 nm respectively. In d) and e), optical generation rate; Mo back-contact interface indicated by horizontal white line.

diffusivity and the SRH equation of lifetime, is about ~700 nm (~8 μm) with the parameters used. Our planar device model quantitatively matches closely to Ref. [57]. The slightly lower short-circuit current densities, and correspondingly slightly lower open circuit voltages, between our model and that of Ref. [57] can be explained by the more rigorous treatment of light absorption and local photocarrier generation rate provided by FDTD simulations and the fact that the optical constants used in Ref. [57] were not reported.

This simulation method is general and can be used for any arbitrarily-shaped 2D device cross-section. Absorption in the randomly textured CIGS films was compared to planar thin films (not shown), CIGS films with dielectric separation layers (Figure 4.1c), and CIGS films deposited onto periodic dielectric structures (Figure 4.1d). Figure 4.1c and Figure 4.1d show only a subset of the larger structure periodicity defined by line contacts (the 2D approximation to point contacts), with contact periodicity of 7.8 μm and 7.56 μm respectively. Figure 4.1f and Figure 4.1g depict the total optical generation of those structures, respectively.

4.3 Results and Discussion

Optical Analysis

Absorption in Self-Assembled Randomly Textured CIGS Films

Looking at the generation map of Figure 4.1e immediately highlights two findings from full field electromagnetic simulation: (1) photocarrier generation hotspots in

the CIGS absorber, and (2) areas of parasitic absorption in surrounding layers. Areas of high carrier generation are generally close to the randomly textured CdS/CIGS film interface. The randomly textured CIGS surface layer absorbs most of the incident light, suggesting that the underlying 1 μm CIGS film beneath the surface topology in Figure 4.1a could be superfluous with respect to light absorption. Figure 4.2a shows results for a series of randomly textured CIGS structures with varying underlying bulk film thickness, t (inset), where lighter shades of blue correspond to thinner absorber layers. Typically, in CIGS photovoltaics, absorbing layer thicknesses are on the order of 2-3 μm. [126] The thickest film simulated in Figure 4.2a corresponds to addition of a 1 μm layer of underlying CIGS material, illustrated by the darkest blue curve, resulting in a CIGS device with a planar equivalent thickness of 1.7 μm, which is close to the typical absorber thickness for CIGS. The high absorption of the randomly textured CIGS device is a remarkably constant across the visible and near infrared spectrum above the CIGS bandgap, and qualitatively resembles experimentally measured EQE spectra of reference [136] in Figure 4.2a. As the underlying CIGS film thickness is varied from 1 μm to 0 μm, the reduction in absorbed photocurrent in CIGS less than 3%. This result indicates an exceptional ability of randomly textured CIGS film structures to efficiently scatter and/or absorb light that would be reflected or transmitted by a planar device with equivalent 700 nm CIGS thickness, represented as the black dashed curve in Figure 4.2a.

Figure 4.2b and Figure 4.2c show TE and TM averaged electric field intensity, $|\mathbf{E}|^2$, profiles at λ=740 nm and λ=1070, and Figure 4.2d and Figure 4.2e show the corresponding optical generation rates. These profiles indicate strong light scattering and absorption by the randomly textured CIGS films. Absorption in the planar device begins to decline at wavelengths beyond 600 nm due to increasing reflection, while absorption in the randomly textured CIGS absorbers does not decline until ~740 nm due to the longer optical path lengths and scattering promoted by the texture, as demonstrated in Figure 4.2b and Figure 4.2d. Beyond 740 nm, the randomly textured CIGS begins to transmit light, and a non-zero thickness for the underlying CIGS layer is required for full absorption. In regions of the spectrum where light reaches the Mo back-contact, it is parasitically dissipated in the metal. The significant absorption loss in the Mo is due to its refractive index being relatively well-matched to CIGS, leading to a low reflectivity interface. [24, 28] Typically, the metal back-contact in a solar cell should serve as a good back reflector to enable multi-pass absorption, in addition to its role as an electrical contact. However, in a CIGS solar cell, Mo is typically used to create a small to zero Schottky contact to

CIGS and for its Na^+ permeability, despite its undesirable optical properties.[115, 149]

Furthermore, Figure 4.2c and Figure 4.2e indicate field intensity enhancement in the lobes of the CIGS randomly textured structure; these lobes are characterized by their location above a void. The sharp refractive index contrast at the CIGS|CdS|void interface results in reflection back into the absorber material. Thus these lobes effectively act as monolithically integrated low Q resonators. These lobes are also areas of high electric potential, implying that a large fraction of the carriers generated in these regions are collected.

Figure 4.3a shows the spectral absorption of each material in the randomly textured CIGS structure with no underlying planar CIGS film (Figure 4.1b,Figure 4.1e), which aids the identification of opportunities for more efficient light management. The solid black curve overlaid onto the absorption spectra represents the simulated EQE, with the difference between absorption and EQE indicating device Internal QE. The most significant fraction of absorption occurs in the CIGS layer (blue). However, at wavelengths shorter than the AZO and CdS bandgaps, CIGS absorption is significantly diminished due to parasitic interband transitions in the CdS and AZO layers. The parasitic absorption at shorter wavelengths accounts for ~11% of the total incident photons above the CIGS bandgap ($4.4\,mA\,cm^{-2}$). We note that AZO parasitic absorption here is greater in the randomly textured structure than in a traditional planar design because of the increased total AZO material required to make a conformal front contact here. While light absorbed in the AZO is completely lost, the simulated EQE curve (solid black) shows that some carriers generated in the CdS window layer do contribute to the short circuit current. However, this collection from the CdS is inefficient due to the high defect concentration in the window layer. [57] Optically, a thin AZO layer would be ideal, but electronically, a thin AZO layer would incur increased resistive losses. Similarly, further thinning of the CdS could also be detrimental, causing pin holes and shunts among other transport-related issues. [26, 126] Use of wider band gap heterojunction window layer materials is a potential alternative to minimize photocurrent lost in CdS, and is currently under investigation. [109, 149]

Figure 4.3b shows the material parsed absorption for a textured CIGS device with t=1 μm. The absorption response in the blue wavelengths is the same because the device is not optically thin. Unsurprisingly, the major difference between the thick device and the thin device is a reduced portion of near infrared (NIR) portion of

the spectrum is absorbed by the Mo back-contact. The solid black curve overlay represents the simulated EQE of the thicker device, which has increased proportional to the reduced absorption in the Mo back-contact in the NIR. Additionally, the dashed black curves show the experimental EQE data from Ref. [136] for comparison. Optically, the 1-reflection (1-R) curve shows that the overall absorption is closely matched. More importantly, the experimental and simulated EQE curves display a reasonably similar behavior. Both EQE curves show a large, flat response across the solar spectrum into the NIR enabled by the strong scattering of longer wavelengths. The difference in the higher simulated EQE curve can be ascribed to using literature values for electronic properties of the material, but the agreement enables us to draw conclusions about the factors that are most important in structured devices.

The other optical loss mechanisms are reflection at the front surface interface and absorption by the Mo back-contact. Front surface reflection losses can be broadly addressed by applying at typical MgF_2 anti-reflection coating. The loss in the Mo can be mitigated by appropriate design of dielectric reflection layers to give high refractive index contrast along with promising electronic transport behavior,[168] as discussed below.

Thin Film and Patterned Dielectric Layers

Parasitic losses in the Mo are difficult to avoid for sub-micrometer absorber layer thicknesses. However, these losses can be reduced by increasing reflectance at the CIGS |Mo interface. A dielectric separation layer with Mo line contacts, as shown in Figure 4.1e and Figure 4.1f, has been proposed to increase reflectance at this interface. [165, 166, 168] To maximize the reflectance of this new dielectric interface, the dielectric layer should have a low index and its thickness should be designed for destructive interference at wavelengths near the band edge. As an example, low refractive index silica sol-gel (n=1.42) layers could be utilized and patterned via NIL. [169, 170] An optimum low refractive index layer thickness of $\sim$190 nm was found from electromagnetic simulations designed to maximize the absorbed photocurrent. This low refractive index layer thickness maximizes its reflectance at λ=1040 nm. Owing to the nonplanar film morphology studied here, we have optimized absorbed photocurrent using FDTD and partial spectral averaging for all device geometries. This more closely resembles experimental results due to the small, random thickness variations of real films. [84]

Figure 4.3c demonstrates the reduction of parasitic Mo absorption and correspond-

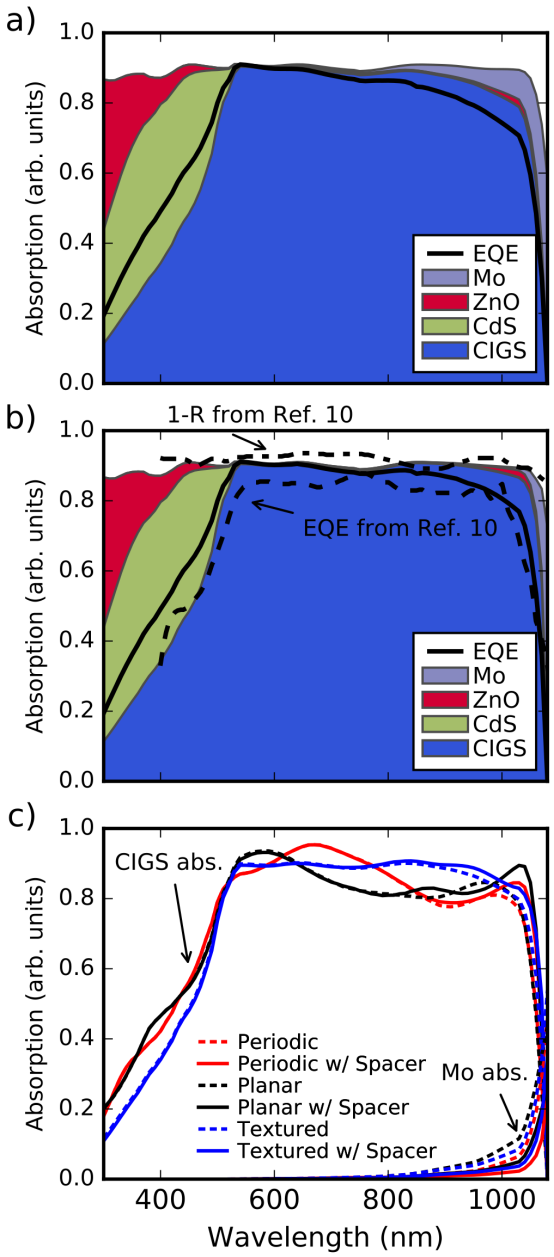

Figure 4.3: Absorption in Component Materials a) Absorption in a simulated randomly textured device with a planar equivalent of 700 nm, indicated in each layer, where t=0 nm. The black curve overlaid on the plot is the simulated device external quantum efficiency. b) The same as in a, but for t=1000 nm. The 1-R and experimental EQE from [136] are provided in dashed lines for direct comparison to the model here. In c), comparison of CIGS and Mo absorption for different device structures with and without dielectric layers between the absorber and back-contact.

ingly increased CIGS absorption due to enhanced CIGS back interface reflectance for the structures depicted in Figure 4.1 as well as a planar thin film. First, comparing the dashed black curve and the solid black curve, we see that insertion of the low index layer into the planar structure increases absorption in a planar film slightly at wavelengths where the CIGS is optically thin, beginning around 800 nm. The largest boost in absorption is near the band edge, where the dielectric layer is designed to reflect light back into the CIGS absorber via destructive interference.

Alternatively, periodically ordered structures, such as an array of pillars, can also improve absorption in the CIGS layer (Figure 4.1d,Figure 4.1g). A periodic structure with a period of 525 nm, a height of 420 nm, and feature width of 300 nm imparts a periodic structure to a conformably deposited CIGS absorber layer that has again been optimized for absorbed photocurrent. This strongly increases CIGS absorption between 600 nm and 800 nm, seen in the red dashed curve of Figure 4.3c, corresponding to the maximum of solar photon flux. This periodic structure has similar anti-reflection properties as the randomly textured absorbers, where the conformal and periodic surface texture preferentially scatters light into the absorber at these wavelengths, indicated by the generation profile in Figure 4.3g. [43, 92] Unlike the randomly textured absorber, a periodic structure can be controllably reproduced via methods such as NIL. Augmenting the periodically ordered structures with a 190 nm dielectric layer at the Mo interface gives an additional absorption increase close to the band-edge, exhibited by the solid red curve of Figure 4.3c. The overall absorption spectrum closely resembles a superposition of the effects from the two light trapping mechanisms, suggesting multiple strategies can be combined to achieve overall broadband enhancement. A $^1/_4$ wavelength MgF_2 anti-reflection coating tuned to λ ~900 nm is discussed in SI1.

Combining a dielectric reflection layer with randomly textured CIGS absorbers does not result in the same absorption enhancement as with the lithographically patterned and planar films, as seen when comparing the solid and dashed blue curves of Figure 4.3c. The reduced enhancement is attributed to the strong scattering of incident light, which inhibits the destructive interference condition within the dielectric layer. Nevertheless, a modest broadband increase in absorption is seen at longer wavelengths where the CIGS absorber is optically thin, beginning around λ=900 nm. This corresponds to the fraction of light that is reflected back into the absorber at the CIGS|SiO_2 interface, and can be inferred by comparing the Mo absorption curves of the three architectures without and with dielectric separation

layers (dashed versus solid) in Figure 4.3c. The dielectric layer clearly decreases the parasitic absorption near the band edge in all cases, verifying the enhanced back interface reflectance.

Anti-Reflection Coatings and Optimized Planar Device

Because it is commonly employed in experimental devices and in order to find an upper limit of device performance for the electrical parameters used, the optimum MgF_2 Anti-Reflection Coating (ARC) thickness was found by optimizing for photocurrent absorbed in the CIGS material. For planar and structured devices, the optimum thickness was 110 nm, while for the periodic device, the optimum was 166 nm. Figure 4.4a compares the 700 nm device with ARC (cp. Structured device with t=0 nm), the 1.7 µm device with ARC (cp. Structured device with t=1000 nm), and a 2.9 µm device with ARC. The 2.9 µm planar device with ARC was the optimal CIGS thickness found by parameterizing the CIGS thickness with the figure of merit being efficiency in order to compare to the devices studied. Figure 4.4b shows that when adding the dielectric spacer layer to devices with optimized ARC, the thin planar device out-performs the optimized planar device in the case of perfect CIGS|SiO_2 interface passivation. The decreased reflection in the planar 700 nm device increases the current, and therefore efficiency, compared to Figure 4. The same is true of the other devices. The randomly textured device performs best of the three. These curves show the added benefit of dielectric layers, but also recognize that if suffciently low interface SRVs cannot be acheived, the optimum device will

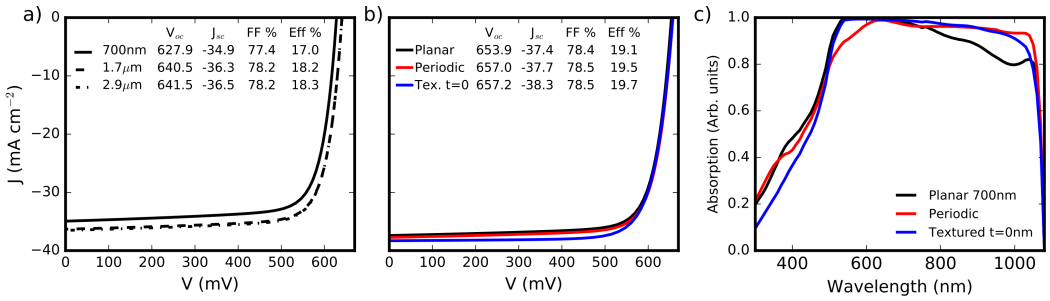

Figure 4.4: Devices with Anti-Reflection Coatings a) The JV curves of planar device with 110 nm Mg_2 ARC. The thicker optimized 2.9 µm device shows a minor improvement over the 1.7 µm device corresponding to the planar equivalent thickness of a textured device with t=1000 nm b) The planar, periodic, and textured devices with a 190 nm dielectric layer at the back-contact and ARC outperform even the optimized planar device. Inset of a) and b) show the J-V parameters of the devices. c) the CIGS absorption spectra for the ARC coated devices in b).

still be a thick planar device with ARC.

Figure 4.4c shows the CIGS absorption when the ARC is applied. Compared to Figure 3c, the optimum ARC for planar and structured devices maximizes absorption near the peak of the photocurrent flux in the solar spectrum between 600-800 nm, with the optimum ARC coating being 110 nm thick. The periodic device has an optimum ARC thickness of 166 nm. The periodic texture already enhances the absorption response between 600-800 nm significantly, leading to an ARC tuned to about 900 nm having the most additional effect. The large attenuation coeffecient of CIGS leads to decoupling of the multiple photon management strategies in this device, and enables the periodic pattern, the ARC, and the dielectric layer to be separately active in different parts of the spectrum. The absorption peak due to the periodic pattern centered around 700 nm is not significantly affected by the ARC (nor is the near band-edge enhancement of the dielectric layer) as one would expect if the two were resonantly coupled. A better optimization would co-optimize the periodic pattern, the ARC, and the dielectric layer simultaneously, since it is unclear whether or not the ARC or periodic texture is the more effective strategy between 600-800 nm. However, the absorption response in Figure 4.4c demonstrates how the enhancement effects can be superimposed as long as they are sufficiently decoupled.

Carrier Transport Analysis

Randomly Textured Absorbers

The absorbed photocurrent can be determined for optical structures with improved light management, such as the randomly textured CIGS absorbers described here, but the corresponding device transport and electrical performance cannot be predicted from optical models alone. Common assumptions in existing literature on optical modeling of photocurrent enhancement include unity or constant internal quantum efficiency, neglecting wavelength and/or spatially dependent collection probabilities. [35, 76, 116, 173] In some systems this assumption is well justified,[43, 187] while, in others, a fully coupled optoelectronic model is necessary for qualitatively and quantitatively accurate results. [46, 100] Here, a fully combined optical simulation and carrier transport analysis (c.f., red EQE curve in Figure 4.3a indicates that photons and electrons are more efficiently collected at shorter wavelengths than at longer wavelengths in the randomly textured device. All generated carriers are collected near 550 nm, while only about 80% of generated carriers are collected at 1040 nm, given by the ratio of the absorbed photons and the EQE curve. Minor-

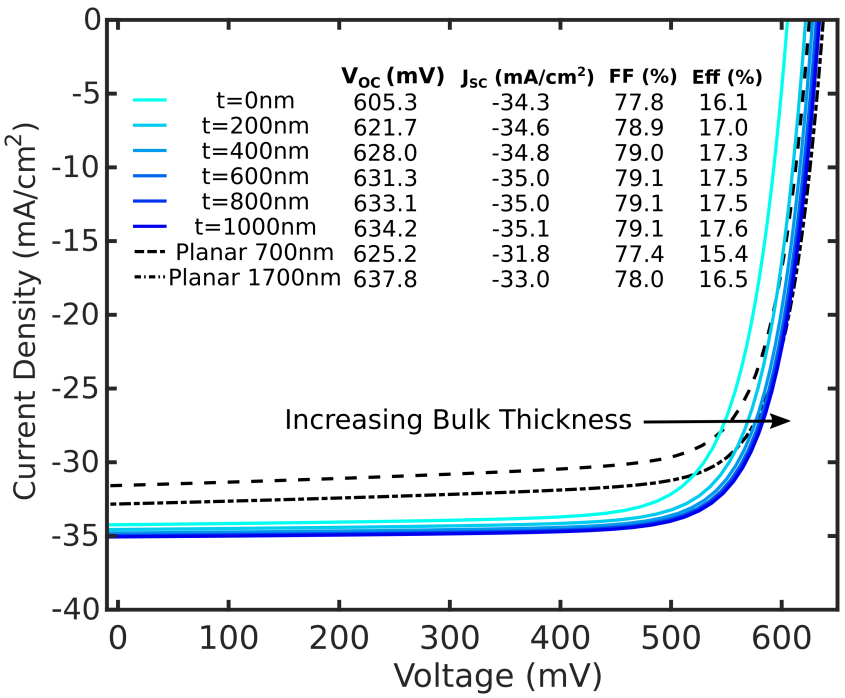

Figure 4.5: Randomly Textured CIGS Photovoltaic Response Simulated devices with varying CIGS bulk thickness, t, (c.f., inset of Figure 4.2a) compared with the simulated J-V curves of equivalent planar devices. Extracted J-V parameters are given by inset.

ity electrons generated near the CIGS|Mo interface are swept to the back-contact and recombine. This only occurs at longer wavelengths with correspondingly low absorption coefficients in the absorber.

The illuminated J-V curves for various underlying CIGS film thickness are shown in Figure 4.5. The change in J_{SC} between the t=700 nm and t=1700 nm devices is 0.8 mA cm^{-2}, and this increase is less than 3% as previously predicted by the optical analysis. In contrast the V_{OC} increases significantly, from 605.3 mV to a maximal value of 634.2 mV. The small increase in J_{SC} alone cannot account for the substantial increase of the V_{OC}. The observed V_{OC} gain is instead attributed to the spatial separation of carrier generation in thicker films from parasitic recombination at the back-contact, giving minority carriers generated at depth a greater chance of diffusing to the space charge region near the diode junction. [58] The minority carrier diffusion length is ~700 nm, and for sufficiently thick CIGS films, the majority of photogenerated carrier are at least this distance from the back-contact, so recombination is reduced and the V_{OC} approaches a maximal value.

Here, the V_{OC} of a randomly textured device with 1 µm of underlying CIGS shows a slightly diminished VOC compared to a planar device of the equivalent 1.7 µm

of material (634.2 mV and 637.8 mV respectively). This can be expected due to the increasing junction area, and therefore dark recombination. However, these simulations found the increase in current overcomes the loss in voltage when considering the overall efficiency, provided back-surface recombination is mitigated by sufficient underlying thickness. For these textured devices it is equally important that the surface recombination velocity (SRV) between at the CdS|CIGS interface is kept below 10^3 cm s^{-1} or the substantially increased interface area will quickly reduce device fill factor as the SRV at this interface increases (See SI2). These results encourage further investigation of this system into other potential limiting issues, including increased shunting, potentially high defect concentrations at sharp features, and the additional need to control the junction interface recombination.

Electronic Benefits of Thin Film Dielectric Layers

Thin film dielectric separation layers embedded between the CIGS absorber and Mo contact provide a barrier to minority carrier recombination if appropriate surface passivation can be achieved at CIGS|dielectric interfaces. SRVs in the range of 10^2-10^4 cm s^{-1} have been reported for alumina dielectric layers, and similar values could be expected with other oxides such as silica. [93, 165] Figure 4.6 shows light J-V parameters of the textured device in Figure 4.1c while parametrically varying the SRV at the CIGS|dielectric separation layer interfaces. The V_{OC} remains large until $\sim 10^3$ cm s^{-1} and then drops monotonically for larger surface recombination velocities; similar results are seen for the J_{SC} and efficiency. The periodically structured device suffers the most in terms of J_{SC} and fill factor with this increase in SRV due to its larger interface area. The planar device maintains the most stable V_{OC}, but loses J_{SC} must faster than the randomlyl textured device. If low SRVs can be achieved, a line/point contact scheme with a dielectric reflection layer would represent an attractive device design to increase both the J_{SC} and V_{OC} of any device architecture. [93, 165] The improvements when adding the dielectric layer are summarized in Table 4.1, along with the device performance when adding a MgF_2 ARC that has optimized for photocurrent absorbed by the CIGS (SI1).

The back-contact passivation by dielectric separation layers in sub-micron thickness CIGS films is only required when a band offset exists between the CIGS and the Mo contact. A thin layer of $MoSe_2$ is sometimes used to create an indirect ohmic contact to Mo, but this has been reported to cause delamination issues in cases when this layer is excessively thick. [149] Ga grading has also been proposed to avoid

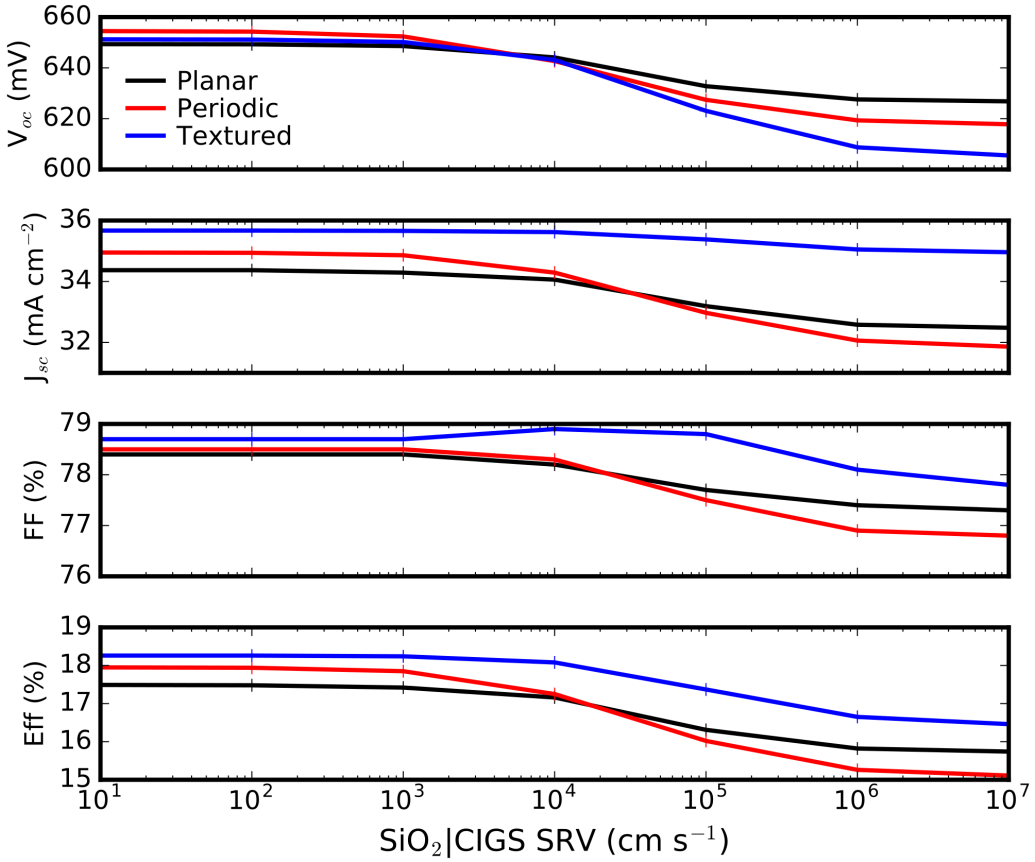

Figure 4.6: Effect of Dielectric Surface Recombination V_{OC}, J_{SC}, fill factor, and efficiency of simulated devices with dielectric layers (t=0 nm for the randomly textured device) that define line contacts for parametrically varied CIGS|SiO_2 interface surface recombination velocity.

minority carrier loss to the back-contact. [58] We examined the sensitivity of the randomly textured CIGS device to this offset in the Supplementary Information (SI3) and find that, electronically, adding dielectric reflection layers have a similar effect as making this offset more positive, but, optically, dielectric layers give more J_{SC} due to increased double pass absorption. Thus, sparsely arrayed line contacts are the preferred design to simultaneously minimize surface recombination and enable the required majority carrier transport while increasing double pass absorption.

Due to computational limitations, we were unable to simulate line contact with spacing of greater than 7.8 µm. Thus the ultimate potential of the dielectric layer line contact design was not fully optimized in this study. We note that majority carriers are collected at the back-contact in this scheme, so the period of the line contacts can be on the order of the majority carrier diffusion length. The line contacts were 230 nm in width for all devices as in Figure 4.1 and Figure 4.1d. We observed

Table 4.1: Summary of JV Parameters for Different Device Configurations

Simulated Device	V_{OC} (mV)	J_{SC} (mA cm^{-2})	FF (%)	Effciency (%)
Equivalent Thickness Planar	625.2	31.8	77.4	15.4
Periodic Structure[1]	641.0	33.6	78.5	16.9
Randomly Textured	605.3	34.3	77.9	16.1
Simulated Device with 190 nm Dielectric Layer[1]				
Equivalent Thickness Planar	648.6	34.3	78.4	17.4
Periodic Structure	652.4	34.9	78.5	17.9
Randomly Textured	654	35.2	78.4	18.1
Simulated Device with 190 nm Dielectric Layer and ARC[1]				
Equivalent Thickness Planar	653.1	37.4	78.4	19.1
Periodic Structure[2]	654.8	37.6	78.5	19.3
Randomly Textured	655.8	38.3	78.5	19.7

[1] The SRV at the CIGS|SiO_2 interface is 10^3 cm s^{-1}
[2] This ARC was 166 nm instead of 110 nm

that decreasing the contact opening could further enhance the passivation effect, indicating that recombination is not negligible even for this line contact spacing of 7.8 µm, but very small line contacts on the order of 150 nm began to limit the J_{SC}. Additionally, experimentally contacting the Mo may be difficult with excessively small vias. We also recognize the beneficial role of Na^+ ion diffusion through the Mo back-contact should not be ignored, but incorporation of sodium fluoride into dielectric reflection layer has been reported before. [165, 166, 168] It is proposed first here that direct incorporation of Na^+ into a sol-gel layer used in nanoimprint fabrication could be a scalable solution to controlled Na^+ incorporation.

Effect of Increased Junction Interfacial Area

There is justified concern that the increased junction interface would increase the junction recombination. A sensitivity analysis was performed for this parameter for the textured and planar CIGS devices. The increased junction does show the textured devices being more sensitive to the textured junction for increasing surface recombination velocity (SRV), as shown in Figure 4.7. For SRVs at the CIGS|CdS interface up to $\sim 10^3$ cm s^{-1}, the textured geometry outperforms the planar geometry due to its ability to collect significantly more photocurrent. The thinner and thicker devices show the same trends in both devices, and the efficiency becomes independent of thickness as surface recombination becomes the dominant recombination

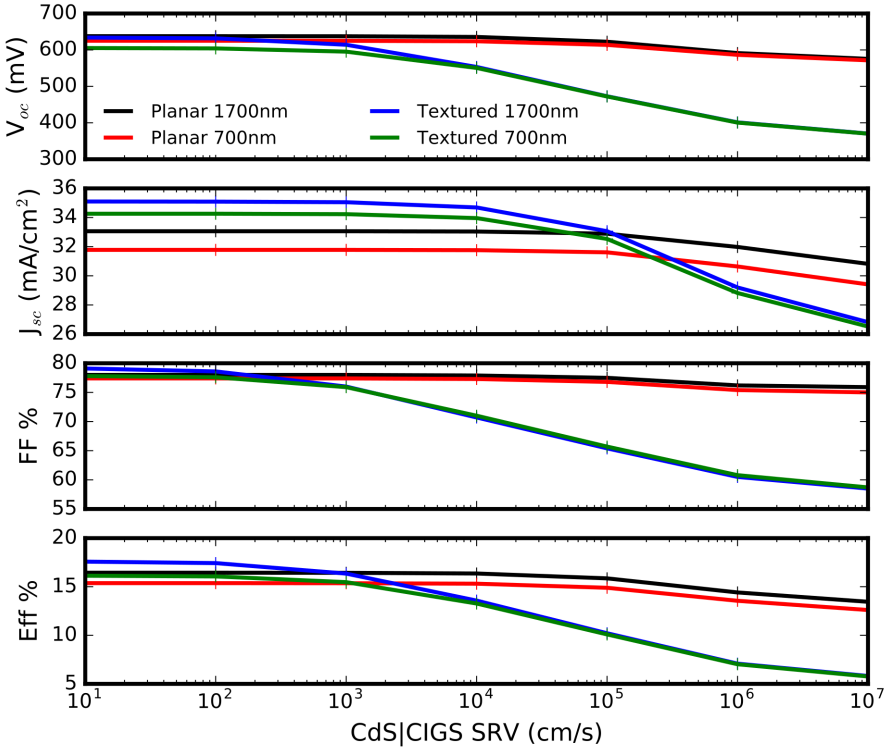

Figure 4.7: Recombination at Junction for Planar and Textured Devices Variation of the surface recombination velocity at the CIGS|CdS interface for different architectures and thicknesses reveal that the textured CIGS absorber outperforms a traditional planar geometry for moderate SRV values, but steeply declines in performance as the SRV begins to become the dominant recombination mechanism due to increased junction interfacial area.

mechanism for the textured devices. The fill factor and voltage are most affected by increases in junction recombination, with fill factor being the first parameter to show decline as charge carriers find recombination sites before being able to cross the junction. The patterned structure was not parametrically studied here, but its interfacial area is between that of the textured device and the lower limit of the planar device; the performance of such a device would be bounded by the results given here.

CIGS|Mo Band Offset

The back-contact passivation by dielectric separation layers in sub-micron thickness CIGS films is only required when a band offset exists between the CIGS and the Mo contact, which was -0.2 eV for all electronic results presented thus far.[57] A thin

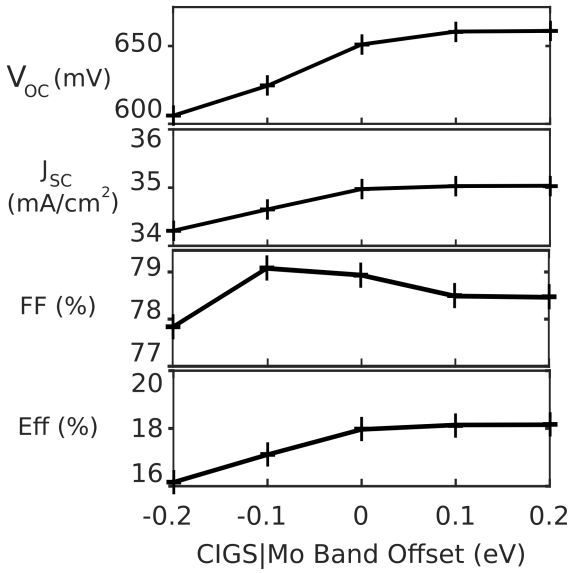

Figure 4.8: Sensitivity to Absorber|Back-contact Band Offset Randomly textured device (planar equivalent of 700nm, Figure 1b) sensitivity to the back-contact band offset. Minimizing the negative bending of the conduction band in CIGS allows more photogenerated minority carriers to reach the junction (J_{SC}) and enables a larger concentration of excited carriers to be maintained (V_{OC}).

layer of $MoSe_2$ is sometimes used to create an indirect Ohmic contact to Mo.[149] Gallium grading has also been proposed to avoid minority carrier loss to the back contact.[168] We examined the sensitivity of the randomly textured CIGS device with 700 nm planar equivalent thickness to this offset in Figure 4.8. A -0.2 eV offset corresponds to a ~50 mV loss in V_{OC} compared to a V_{OC} of 651 mV for zero band offset. A V_{OC}=660 mV is observed for more positive offsets, and a maximum efficiency of 18.1% is achievable in randomly textured CIGS devices studied. For a band offset of 0 V, the contact is mildly selective to majority carriers, and this effect further increases with positive offset. As the selectivity of the contact increases, the concentration of excited carriers does do, leading to larger quasi-fermi level splitting. The J_{SC} follows the open circuit voltage, as more carriers are can be collected at the junction. The fill factor remains relatively constant with varying band offset. Thus, creating Ohmic or selective contact is another viable route to reduction of minority carrier recombination in sub-micron CIGS absorbers, and again highlights the importance of the back-contact properties for very thin CIGS.

4.4 Conclusion of $Cu(In_xGa_{1-x})Se_2$ Simulation Based Analysis

We report coupled optoelectronic simulations for light trapping and surface passivation in CIGS photovoltaics, and indicate designs to match or exceed the performance

of thick planar absorbers. For randomly textured CIGS cells, the majority of light absorption occurs in the textured region near the junction. Long wavelength light is effectively scattered giving a flat, broadband absorption spectrum. Other light trapping strategies were examined, including dielectric separation layers located between the CIGS absorber and Mo back-contact. These layers can be designed to preferentially reflect near band-gap light back into the absorber to reduce parasitic Mo absorption. Periodic dielectric structures can also give enhancement by increasing scattering into the device. Employing various combinations of different light trapping strategies in these thin film devices demonstrates synergistic effects. For example, combining dielectric layers and periodic nanostructures gives absorption spectra characterized by superposition of these two different effects.

These optoelectronic models also addressed the other main challenge to sub-micron absorbers, namely, minority carrier recombination at the back-contact. Dielectric separation layers show the dual promises of surface passivation while enhancing double-pass absorption. Finally, we compared each device with the addition of a $^1/_4$ wavelength MgF_2 anti-reflection coating and found that a randomly textured absorber with t=0 nm (700 nm planar equivalent) with a 190 nm dielectric separation layer shows the largest potential efficiency. These efficiencies represent an upper bound to the CIGS architectures simulated here. Experimentally, planar devices may be easier to achieve due to the less stringent requirements on SRV of the CIGS|SiO_2 and CIGS|CdS interfaces. However, randomly or periodically structured CIGS devices with reasonably achievable CIGS|SiO_2 SRV values significantly out-performed the planar architectures. Devices utilizing this design approach could result in improved CIGS photovoltaic efficiency with a significant reduction in absorber layer thickness, and corresponding reduction in material consumption and cost.

Chapter 5

NEAR PERFECT ANTI-REFLECTION IN LOSSLESS DIELECTRIC NANOCONE STRUCTURES

5.1 Introduction

Whereas there has been much work in the area of absorbing nanocone arrays [2, 47–49, 184], less literature explores the physical mechanisms of non-absorbing dielectric nanocones. [21, 61, 63, 118, 164] The physical mechanisms active in these types of nano and micro cones are often portrayed as a gradual change in the refractive index of the interface, leading to broadband anti-reflection responses for incident light.[22, 71, 158, 160, 171] When the cone diameter is comparable to the wavelength, an effective-medium graded index is not the always most accurate description for the light-material interaction. The wave-optical paradigm is required to fully describe the optical behavior in dielectric cones. The taper is key to incoupling a broad spectrum of light from free space propagation into the cone, and subsequently the substrate, through cylindrical waveguide modes.[47, 49, 184]

At the scales comparable to the wavelengths studied herein, the only supported waveguide modes are the lowest order HE_{11} and secondarily HE_{12} cylindrical waveguide modes. The first and second subscripts represent the radial and angular mode orders, respectively. There is no non-zero field component along the cone axis in along the z-dimension propagation direction. When $|\vec{E}_z|^2$ is greater than $|\vec{H}_z|^2$, the mode is transverse electric field (TE) like and is called HE, with the opposite true of transverse magnetic field (TM) like, called EH. Figure 5.1 introduces the dispersion and characteristic $|\vec{E}_z|^2$ field profiles of these modes in cones. The top-left shows a schematic of nanocones on a glass substrate. The top-middle plot shows the analytic dispersion diagram for an infinitely long sol-gel cylinder of refractive index n=1.42, the cone studied in this work.[170] The free-space propagation constant $\vec{k}_0$ (where $\lambda = \frac{2\pi}{k}$) and axial propagation constant (k_z, perpendicular to the substrate) are normalized to the cylinder radius. These curves were used to calculate a z-dependent effective mode index function of a truncated nanocone (top right), which is proposed as a novel approximation of the effective index seen by light in nanocones at a particular wavelength. We assume the mode solution for a cone radius at z is reasonably approximated by the infinite cylinder over a short distance. This results in a smooth

effective index change over the entire cone, resembling a quintic polynomial, which has been analytically shown to provide strong anti-reflection performance.[121] The waveguide mode index function uniquely predicts an imperceptible index change at the truncated cone tip. The Maxwell-Garnett graded index function of z is also plotted for comparison, showing the quadratic height dependence inherited from the gradually increasing cone radius and the index step due to the truncated tip. In this work, we show that the reflection from a glass substrate with a nanocone array can be explained by both frameworks. Each has a regime of application depending on the nanocone dimensions and the relative wavelength scale. The length scale regime studied here focuses on truncated cone diameters and heights that are on the order of a wavelength. It is subtly different from cones and cylinders that are either much smaller than[63] or much greater than the wavelength in either height or maximum diameter of the cone.[23, 198] Cylindrical waveguide theory describes the behavior due to the shape of the cone structures, while diffraction and effective medium theories complete the description of the reflection behavior. These principles come together to more fully describe the phenomenon of near-perfect dielectric nanocone anti-reflection performance.

In experimental demonstration, nanocone arrays were then printed onto glass substrates via NIL to demonstrate that a inherently scalable and inexpensive fabrication method could be used to realized the highly effective reflection reduction of nanocone arrays on glass substrates. Specifically, this approach is highly valuable to solar PV cells. A 20% power conversion efficient PV cell or module would gain about 1% absolute power conversion efficiency when encapsulation glass reflection is near-zero. Exposure to outdoor elements should not be significantly problematic for sol-gel printed cones, as the oxide differs from the native glass substrate only in density. Other applications could include photo-detectors and perfect transmission applications. The principles outlined in this work are non-specific to glass or sol-gel, but any non-absorbing materials. These low-reflection substrates were coupled to both a smooth photo-detector and a commercial PV solar cell showing reflection could be essentially removed from the system.

5.2 Simulations of Nanocone Parameter Space

The open-source Rigorous Coupled Wave Analysis (RCWA) S^4 RCWA code was used to investigate the ability of truncated cones to drastically increase the transmission of light into low index substrates.[101] RCWA allows efficient exploration the parameter space and allows facile parsing of different diffraction orders present.

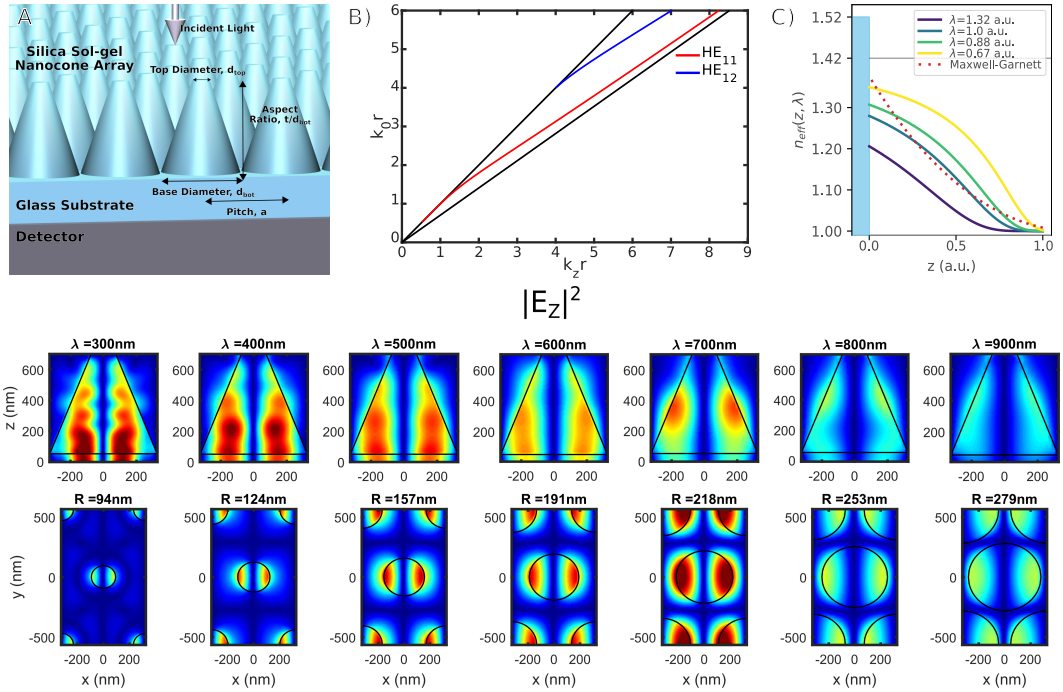

Figure 5.1: A) A schematic depiction of sol-gel nanocones (n=1.42) on a glass substrate(n=1.52), used as a cover glass for some detector such as a solar cell or photodiode. B) The dispersion relation of the first and second order HE_{1m} cylindrical waveguide modes bounded by the free-space light line and substrate light line for a cylinder with refractive index $n = 1.42$. C) The effective/mode index for the HE_{11} mode as a function of position for different wavelengths compared to a Maxwell-Garnett effective medium function for a truncated cone. The functions are normalized to the cone height. Bottom: Characteristic field profiles of the $|E_z|^2$ depicting the HE_{11} waveguide mode coupling in cones at different wavelengths showing coupling strengthens as the diameter relative to the wavelength increases.

Results were confirmed with a commercial-grade simulator based on the finite-difference time-domain (FDTD)[74]. These nanostructures compare favorably to complex anti-reflection (AR) coatings such as graded index layers at normal and grazing incidence for both TE and TM polarizations.

Non-dispersive materials are assumed in order to leverage normalized units, where the base diameter d_{bot} of the cone is 1 μm, and larger or smaller cone arrays can be described by applying a scaling factor to the structure and incident wavelengths.[79, 101] The normalized free space propagation constant is related to the frequency in these units by $\vec{k}_0 = \frac{2\pi}{\lambda} = 2\pi/\omega$. The truncated nanocone parameter space is defined in terms of the base diameter by the aspect ratio (height t/d_{bot}), the top-bottom diameter ratio (d_{top}/d_{bot}), and the relative pitch of a hexagonal array (a/d_{bot}), such that a close packed lattice has unit length basis vectors. These structure parameters are seen in Figure 5.1A). Parameter sweeps were performed

with equal k_0 spacing between k_0=0.275 and k_0=3, covering the visible and NIR wavelengths from λ=3.36 µm to λ=0.333 µm for a canonical cone of a d_{bot}=1 µm, d_{top}=0.7 µm, height t=0.9 µm in a close packed hexagonal array. In parameter sweeps, one of these parameters was changed while the others remain fixed at the canonical values. A minimum of 37 Fourier components are used for each RCWA calculation to sufficiently capture the first 6 diffractive orders of a hexagonal array on this length-scale. Convergence testing demonstrated that including more orders did not appreciably affect results since they correspond to diffractive orders only allowed for k_0 greater than 3. The small numerical differences from simulations with 100 or more Fourier components did not impact the ability to draw important conclusions. Circles with radius dependent up the z location were patterned in discrete layers of thickness 0.02 µm(roughly 15 layers for λ=0.3 µm) to give a staircase approximation to the cone structures.

In these reflection response parameter spaces, diffraction orders manifest as horizontal lines along the aspect ratio axis. Background axial modes, analogous to Fabry-Perot modes, interfere with the sharp onset of diffraction, causing Fano resonances at specific k_0 values. The spectral location of these diffraction orders is determined by the cone array's 2D lattice momentum, with unit cell vectors $|\hat{a}_{1,2}| = 2\pi/\Lambda$ where Λ is the lattice periodicity between cones. Transmitted and reflected diffraction orders of in-plane momentum $\vec{k}_{\|}$ are allowed when the one of the two Rayleigh conditions in Equation (5.1) are met, where **m** and **n** are the integer diffractive order numbers.[34]

$$\begin{aligned} Re(\vec{k}_0)n_{ambient} - Re(\mathbf{m}\hat{a}_1 + \mathbf{n}\hat{a}_2) &= -Re(\vec{k}) \\ Re(\vec{k}_0)n_{substrate} - Re(\mathbf{m}\hat{a}_1 + \mathbf{n}\hat{a}_2) &= -Re(\vec{k}) \end{aligned} \tag{5.1}$$

The perpendicular ($\mathbf{m} = 0, \mathbf{n} = 0$) zeroth order is always supported. Importantly, the transmitted diffraction orders have an explicit dependence on the substrate index, and the lowest order diffraction occurs at when the free-space momentum is equal to the shortest in-plane lattice vector, and is the unit cell lattice vector in the M direction.[79] As a relevant example, in this hexagonal geometry, the irreproducible lattice vector $M = \hat{a}_1/2 = 1/\sqrt{3}\hat{y}$, and the momentum vector at the edge of the reciprocal space unit cell is $2M = 2\hat{a}_1 = 2/\sqrt{3}\hat{y}$. At the edge of the reciprocal unit cell, a zero momentum in plane wave-vector $\vec{k}_{\|} = 0$ is equivalent to a wave vector of reciprocal unit momentum $Re(\vec{k}_{\|}) = 2|M|$ by Bloch's theorem. By momentum conservation, scattering from normal incidence into a wave with either all, or a portion of its momentum parallel to the substrate is only possible for

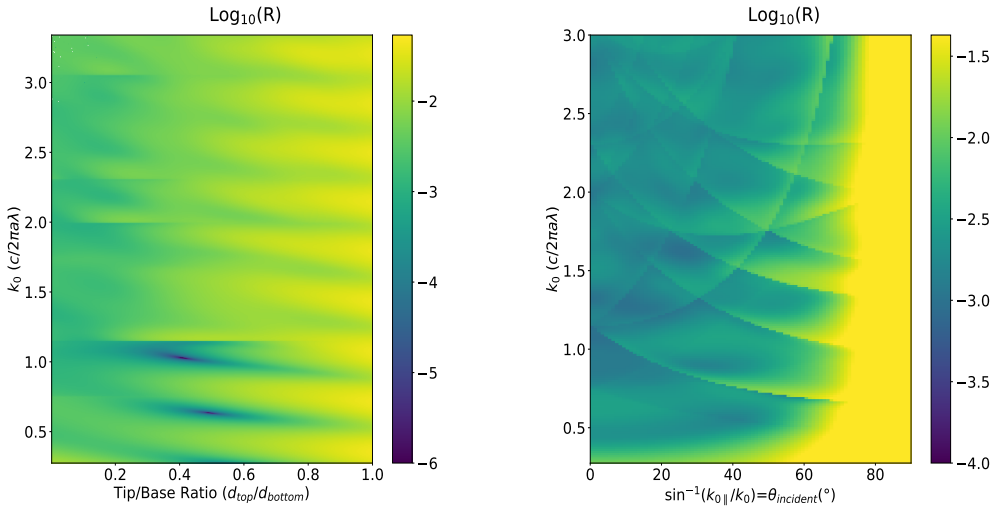

Figure 5.2: Left: The log base 10 reflection response of conical frustums with a d_{bot}=1 µm and aspect ratio of 0.9 in a close packed hexagonal array with varying d_{top} relative to d_{bot}. A tip-base ratio of 1 gives close packed cylinders, while the zero value is a perfect cone. Right: The angle of incidence (AOI) dependent reflection response of the canonical cone array.

$\vec{k}_0 > 2Mn_{substrate}$. A wave with $Re(\vec{k}_0)$ equal to $2|Mn_{substrate}|$ or other integer lattice vector that scatters into a perfectly substrate parallel wave is known as a Rayleigh-Woods anomaly, and demarcates the onset of a diffractive mode.

First explored is the effect of the diameter of the top of the truncated cone, d_{top}, versus the diameter of the base of the cone, d_{bot}, in RCWA simulations. Plane wave light is incident upon the cones that are place upon a glass substrate of refractive index 1.52. The refractive index of the cone medium approximates that of silica sol-gel and is 1.42.[170] The aspect ratio (t:d_{bot})of the cones presented in Figure 5.2 is fixed at 0.9, closely resembling what was achieved in experiment. This size regime is most of interest because the cones are similar is size to well studied Mie resonators, yet significantly shorter than other AR cone structures reported in literature.[21, 61, 63, 118, 158, 164] Additionally, cones of this height are readily realizable via the chosen fabrication method of silica sol-gel NIL, and potentially more mechanically robust than very tall cones. All figures show the TM and TM polarization averaged response, unless explicitly stated. Cone arrays display distinct spectral features are seen in the reflection response of Figure 5.2. First, for a tip to base ratio of 1, the average reflection is on the order of $10^{-1.5} \approxeq 0.968$ and oscillates with increasing frequency. These oscillatory features in the spectrum are due to axial interference modes along the cone axis, analogous to Fabry-Perot interference

of thin-films, arising from the nearly solid layer where the cylinders are packed to fill 90% of the projected area. This can be approximated as a thin film by applying effective medium theory to give a volume averaged effective index of 1.278 with equal thickness to the cone height, t. Following these features towards smaller tip-base ratios in Figure 5.2 shows broadening, decreasing reflection, and blue shifting of the peaks with increasing taper, creating a lower broadband reflection response. This change from a cylinder to cone shape gives a change from constant effective refractive index to that of a continuous effective index function matching impedance of the incident wave more smoothly for the entire spectrum. An accumulated phase of approximately π occurs along the cone axis at reflection minimums, and zero total phase accumulation at maximums giving the Fabry-Perot destructive/constructive interference fringes.[195] These phase conditions were clearly seen in examination of the Ex or Ey fields of simulation results. Last, there exists a Fano resonance which manifests as distinct horizontal lines in the plot, corresponding to the wavelengths when new diffractive modes can be coupled into from free-space. Similar shapes were seen in [20, 21, 121]. The interaction of these diffraction modes with the cylindrical waveguide and axial Fabry-Perot modes has important implications to the effective medium theory descriptions of tapered cone arrays. The deep minima in reflection seen near k_0=0.76 and k_0=1 would repeat periodically with a non-structured graded-index layer, but are disrupted in a cone array. The turn-on of reflected diffractive orders above $k_0 = 2M \approxeq 1.154$ interferes with the conditions for destructive interference in the axial modes.

The lattice period effect on reflection of the array showed that close packing is optimal. The low refractive index of the material inhibits Mie-like resonant modes in the cones from creating a large optical cross-section necessary for incoupling light into the cone. In order for the optical cross-sections overlap sufficiently cones should be close enough so that incident light will not encounter any flat substrate. This is contrasted to the behavior of high index semiconductor nanowires and nanocones, where extremely sparse arrays with areal footprint of 6% can interact with nearly the entire physical area due to large optical cross-sections. [49, 85] In these arrays, the Rayleigh condition of Equation (5.1) requires momentum matching and higher order diffraction modes will red shift to lower required free space momentum the lattice momentum vectors decrease with increasing pitch.

The polar AOI dependent reflection of nanocone arrays is appreciably insensitive. The results are shown in Figure 5.2for the canonical cone array. Results are polar-

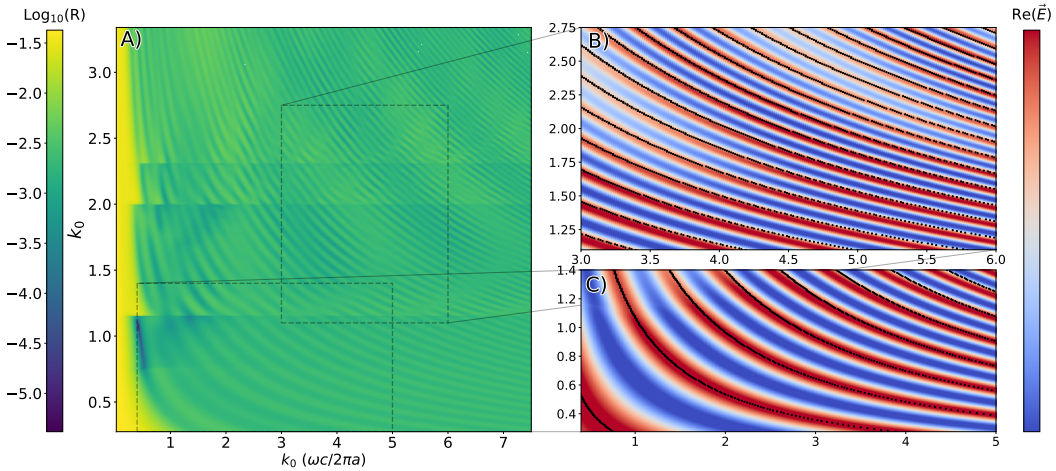

Figure 5.3: A) the log_{10} reflection response of the canonical nanocone array with varying aspect ratio (height t). Sub-plots show portions of the regions of applicability for the B) dispersive cylindrical waveguide mode index function and C) the Maxwell-Garnett effective-medium function plotted in Figure 5.1. The zeroth order electric field amplitude (a.u.) of the nanocone array recorded 1/2 wavelength into the substrate is shown for each region. The field amplitude of same zeroth order in each approximation maximum values are represented by the black-dotted overlay lines.

ization averaged, with performance of each polarization between ±2% of each other. In some regions, however, TM reflects much less than TE at angles greater than 60°. The axial interference modes are largely overcome by the many active diffraction orders for increasing angle. Transmitted diffraction modes become red-shifted due to the increased momentum vector parallel to the surface. The significantly stable response out to high angles is the result of both the radial symmetry of the modes and of the cone and is broadband, providing an attractive anti-reflection solution for applications such as solar PV.

Examining effects of cone aspect ratio, $A = t_{cone}/d_{bot}$ gives fundamental insight to the applicability of effective medium theories compared to cylindrical waveguide modes. RCWA simulations reveal a complex landscape of decreased reflection due to nanocones on glass substrates. Figure 5.3 shows the log_{10} response as a function of aspect ratio. A large number of axial, Fabry-Perot like interference features are continuous increasing height and free-space propagation constant. Expectedly, the number of these modes supported is directly proportional to the height of the cone and/or k_0 as more full wavelengths are supported.

The characteristic field profiles of Figure 5.1 show that the cylindrical waveguide modes exist in these arrays at these scales. The regime of greatest applicability for each approximation is seen by contrasting the cylindrical waveguide and Maxwell-

Garnett effective index functions of Figure 5.1, shown on the top right and bottom right, respectively, of Figure 5.3. Unique to RCWA simulations is the ability to separate the different propagating plane wave modes. The zeroth order mode purely propagates along the substrate-perpendicular, a-axis direction, and it was extracted from the simulations of cone arrays with varying aspect ratio. The zeroth order wave electric field amplitude recorded at 1/2 wavelength into the substrate is represented by the color map zoom plots for the indicated parameter sub-space. The same zeroth order field amplitudes were recorded for simulations of a graded index region, composed of finely discretized 1 nm layers with z-dependent refractive index according to the functions shown in Figure 5.1. The electric field amplitude maxima were extracted from the cone array at same z-position (dotted lines) and overlaid onto the electric field amplitude extracted from the waveguide mode and Maxwell-Garnett approximation simulations. The effective medium function matches the cone array electric fields extremely well in regions of low $\vec{k}_0$ and/or small aspect ratios, but is seen to deviate at larger $\vec{k}_0$. For either larger cones or larger $\vec{k}_0$, the cylindrical waveguide mode approximation matches the fields of the cone array zeroth order better than effective medium theory. The cylindrical waveguide includes effects of resonant coupling of larger $\vec{k}_0$ when there is enough coupling distance along the cone. The overlapping region aid in showing the transition from one approximation to the other.

This observation provides strong evidence for the greater accuracy of the waveguide mode description for nanocones, even though quantitative field magnitude agreement between cone arrays and either planar approximation is not possible due to energy also coupling into diffractive modes. A region of exception exists for $\vec{k}_0$ less than the first transmitted diffraction mode, where only the zeroth order propagates, and there is quantitative agreement between the effective medium approximation and the cone array field magnitudes. For $\vec{k}_0$ above the first transmitted diffraction order, regions of low lightness contrast are seen in Figure 5.3A, and reduced field magnitude in Figure 5.3B corresponding to decreased zeroth order power transmission into the substrate, and conversely, increased diffraction efficiency. It is in these regions where the Maxwell-Garnett approximation breaks down compared to the waveguide approximation. From the Huygens-Fresnel principle, each cone should act as wave source in the phenomenon of diffraction. When sufficient energy has been couped to these guided modes, the cone's base will be the exit into the substrate, with the majority of the energy concentrated around the cone axis. Thus when waveguide mode coupling is stronger, diffractive mode coupling should increase proportionally,

decreasing the reflection. An explanation for the oscillatory nature of these high diffraction efficiency regions remains outstanding.

5.3 Experimental Results

Methods

Electron beam lithography was used to define circles 100 nm in diameter and various pitches of d_{bot}=270nm, 325nm, and 450nm in a PMMA double layer on a silicon waver. The wafer was developed and then alumina was evaporated into the exposed holes. The resist was lifted-off and the wafer was etched using ICP-RIE at various parameters to achieve the right cone taper targeted. Details of this etching process for cone shapes in silicon can be found in other works. [185] [184]

Chapter 2 provides details of double layer XPDMS/PDMS nanoimprint stamp fabrication. Due to the large volume of the cone array that needed to be filled by silica sol-gel, not spun onto glass substrates, but drop cast. The glass substrate used was a VWR microscope slide made of Swiss Glass and average refractive index of 1.52 at a wavelength of 600 nm. A non-textured calibrated photodiode (Thorlabs FDS1010) or a high efficiency (21.6%, Neo Solar Power) textured Si solar cell was coupled to the glass slide with matching fluid of index 1.52 so that the same photo-detector could be used for all cone size samples. The glass slide was imprinted with cones of d_{bot} = 540 nm, d_{bot} = 650 nm, d_{bot} = 900 nm, a layer of sol-gel, or no patterning. The PV cell was diced into areas smaller than the printed nanocone area on the cover glass substrates. The cells were measured using the SARP full-spectrum laser characterization instrument described in Appendix A. A large spot size greater than 1 mm was used in all measurements to record an ensemble response of the array. This experimental setup is used to approximate a infinite half plane as in RCWA or FDTD simulations, where the photodiode acts as a transmission monitor, and the output current gives the relative transmission to an unmodified cover glass. The sol-gel and glass slides are lossless in the regions of measurements, so $R = 1 - T$. The relative reflection percentage is also used as a figure of merit to differentiate small changes in absolute reflection on the order of < 1%.

Angle and Polarization Dependent EQE Measurements

Planar Photodiode

The polar angle dependent reflection reduction for nanocones on a photodiode relative to a glass cover is shown in Figure 5.5 and Figure 5.6. The horizontal black

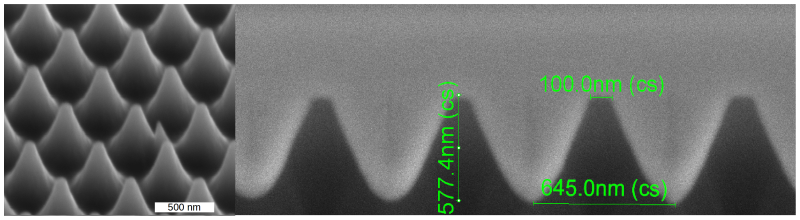

Figure 5.4: An example SEM image of the fabricated nanocone master molds. Right, a tilt angle view of the array. Left: a Focused Ion Beam milled cross-sectional image. On the right, the dark contrast areas is the nanocone array, where the light contrast is a W-capping layer deposited for sample protection and added contrast. The goal for this sample was etch to 650 nm with d_{bot} = 650 nm, but the etch did not go for enough time, and all samples were around 580 nm in height t.

dashed lines near -5.2% indicate the decrease needed for perfectly zero reflection at normal incidence. The illumination axis was approximately along the lattice vector of the hexagonal lattice unit vector corresponding to 0° azimuthal rotation. The values are normalized to the response measured for a flat glass slide without surface structuring or layers to clarify the differences created by nanocone structures. Multiple "ripples" in the data are explained as the result of high sensitivity in measurement setup, capable of detecting other minute interference mechanisms within proceeding lenses and in the photodiode itself. For TE polarized light incident upon the nanocone structured glass, normally incidence (0°) shows nearly 5% reduced reflection in the flat portions of the response curves, corresponding to near zero reflection overall. Immediately seen is the fact that many portions of the spectrum exceed this value, dipping and then decaying. This is attributed to light being trapped between the structured glass surface and the flat surface of the photodiode at high angles via diffracted orders causing multiple photon capture opportunities at the photodiode. Flat portions of the spectrum correspond to wavelengths that of weaker diffraction, and/or regions where out-coupling is possible by free-space diffraction modes. Dips rise sharply as the first order free space diffraction mode is allowed with decreasing wavelength. Reflection decrease also rise with wavelength due to weakening diffraction efficiency as the first order substrate diffraction approaches its cut-off. Below this cut-off the behavior is well described by the effective medium approximation.

Minima occur at different wavelengths as determined by the pitch, equal to d_{bot} for these close packed arrays. Dips red-shift with increasing angle as predicted by the simulations of Figure 5.2, with experiment also matching the predicted increase in reflection magnitude with angle of the diffraction orders. Because this data is expressed as a ratio to reflection of glass at the same AOI, the TE response is

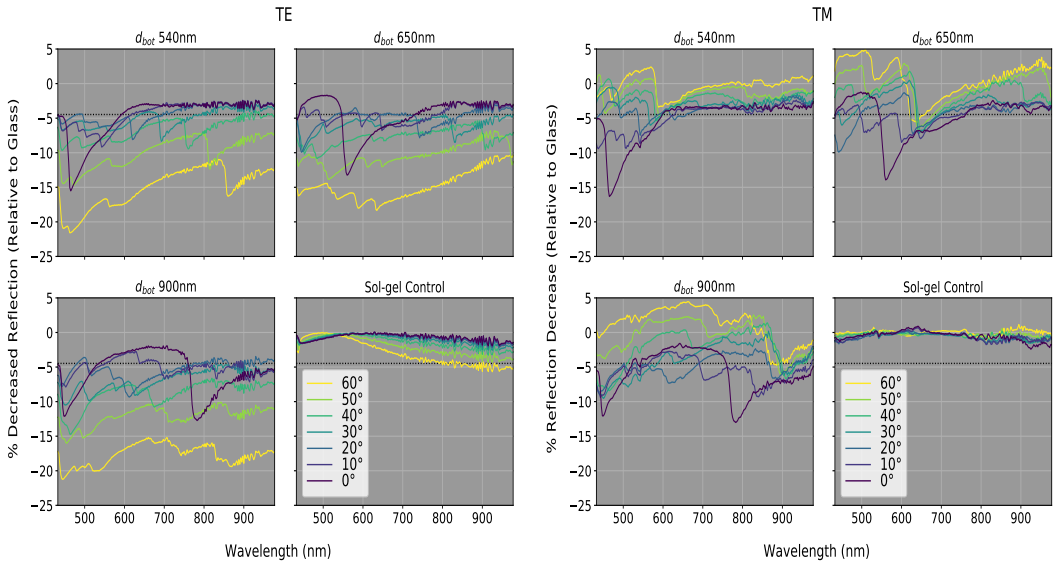

Figure 5.5: The percentage decrease of reflection with the indicated nanocone glass anti-reflection array applied to the photodiode for TE and TM polarized light. The black dashed lines indicate the response needed for perfectly zero reflection at normal incidence. Peaks correspond to light trapping of diffracted modes guided between the smooth photodiode and cover glass surface.

exaggerated due to the monotonic increase of Fresnel reflection for flat surfaces. Last, the lower right plot shows that adding an unstructured layer of sol-gel to the glass surface does show some decrease in the longer wavelength regions with increasing angle. It thus also acts as planar anti-reflection layer, but the reflection never decreases below the level of -5.2% for zero reflection, and no off-axis light-trapping effects are observed.

At an AOI of 0°, TM light reflection is reduced across the entire spectrum for all nanocone samples, displaying the same spectrum features a TE light. For TM polarized light, similar features are seen, but only the strongest diffraction peaks outperform flat glass at larger AOI. The Fresnel equations predict reduced reflection for TM polarized light for AOIs approaching the Brewster's angle near 60°. This increased transmission of planar glass with AOI means that nanocone structures under-perform relative to the planar case. Of note, the sample with d_{bot} displays the most wavelengths considered to be in the Maxwell-Garnett effective medium regime, and at wavelengths longer than 700 nm, never *under performs* flat glass, maintaining a reduction near -5%. Larger cones do under perform at the largest angles for wavelength away from the diffraction enhancement due to scattering. The sol-gel control indicates performance on par to the flat glass substrate, indicating that the nanocone arrays frustrate the Brewster's effect.

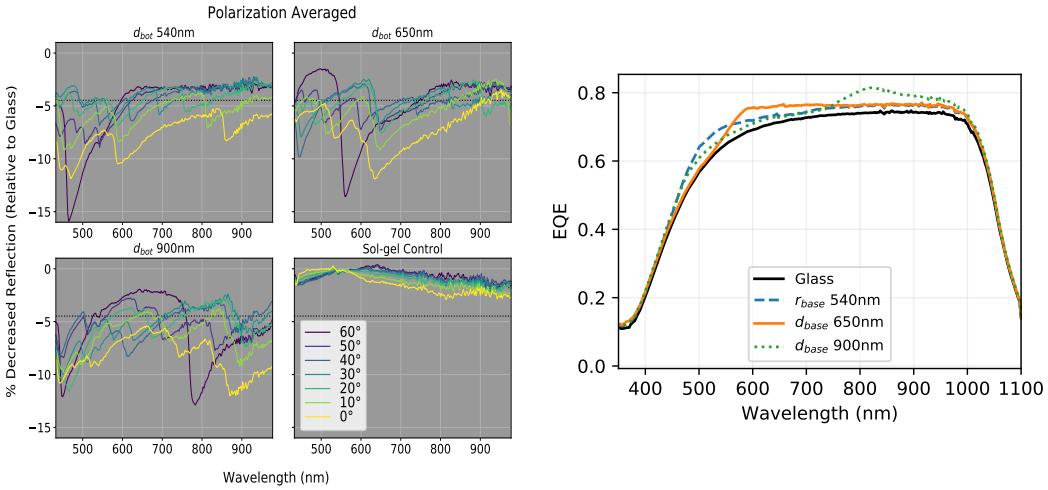

Figure 5.6: Left: The averages of Figure 5.5 are shown relative to a glass cover. The decrease at all angles for TE polarization gives an overall reflection reduction. The light trapping near the diffracted wavelengths decreases the apparent reflection to less than zero. Right: Increased EQE is seen for all samples. Each nanocone array has a particularly strong EQE enhancement in different spectral regions which is governed by the bottom diameter. At longer wavelength the EQE response is nearly identical, indicating regions where an effective medium explanation should be more appropriate.

The polarization average is shown in Figure 5.6. The overall decrease is mostly ascribed to the TE transmission decrease, with the TM response bringing up the overall average for larger AOIs. Normally incident light for all three nanocone arrays is always above this value, which indicating the light trapping occurring. This diffractive light trapping led to important questions and conclusions that were presented previously. In order to measure a true reflection value of only the glass surface, a PV cell was used as the the detector.

Figure 5.6 shows the photodiode EQE covered by non-patterned and nanocone patterned glass when measured with unpolarized, incoherent light from a Xenon lamp. Benefits to this measurement is the extended measurement range into the UV and near-infrared wavelengths, relevant to the solar industry, and the incoherent beam reduces extraneous interferences in the final signal. Increased EQE is seen throughout the spectrum, with wavelength ranges of enhancement specific to each sample. Narrower cones provide additional enhancement in the blue, while enhancement in wider cones red-shift as expected for larger periodicities. Again, rather than simply reproducing the EQE spectrum of the un-patterned glass, distinct regions of increased EQE are seen, corresponding to the diffractive light trapping. Away from these trapped wavelengths, nanocones with $d_{bot} = 540\,\text{nm}, 900\,\text{nm}$ match in the short wavelength and mid-visible spectrum, while $d_{bot} = 540\,\text{nm}, 650\,\text{nm}$ match

in the near-infrared, with near zero reflection. It is not immediately obvious why d_{bot} = 650 nm slightly under performs the others in the short wavelengths, due to the Fano resonant nature of the reflected diffraction for this aspect ratio of roughly 0.9, which can be seen in Figure 5.3A at $\vec{k}_0$=1.14. Interestingly, the sample with d_{bot}=540 nm has an aspect ratio > 1, putting its Fano resonance at wavelengths shorter than the first reflected order, perhaps just beyond the strong increase in reflection at the left hand side of Figure 5.3A. Only a few data points exist beyond the reflected diffraction order, but the normal incident cure of d_{bot}=540 nm on the left hand side of Figure 5.6 levels off sooner than the lower aspect ratio samples.

Textured Si Solar Cell

Measurements with a planar photodiode revealed the light trapping effects of diffraction and suppressed out-coupling from the glass between first diffraction order wavelengths. Silicon photovoltaic cells already employ light trapping surface texturing to randomize incident light. This texturing is leveraged here to interrupt the specular reflection of nanocone glass diffracted orders, which previously led to apparent instances of less than zero reflection. The solar cell surface reflection was measured in an integrating sphere [83] to use the wavelength dependent reflection spectrum as a calibration factor C in order when calculating the glass surface reflection; the silicon cell's average surface reflection was 2%. As a calibration factor, C resembles the internal quantum efficiency (IQE) of the cell, in that it directly relates the reflection $R_{surface}$ and EQE_{sample}. This allows us to use Equation (5.2) to find the absolute R for the different nanocone surfaces. Loss due to contact grid shadowing is relatively constant and is accounted for by measuring the EQE_{PVcell} in the same location for all samples, away from the finger grid. This is not strictly true for diffracted orders impinging at a new angle, but the effect is expected to be minimal, as scattering from the textured surface is also occurring.

$$R_{surface} = 1 - \frac{EQE_{sample}}{C} \tag{5.2}$$

Curves are smoothed with a digital lowpass filter to better separate small interference features from overall trends, since response values are close to zero, the minute interferences are amplified during the division operation of Equation (5.2). There is a spurious peak near 532 nm that is due to stray light from the monochromator of the 1064 nm supercontinuum pump wavelength; the value is some combination of the response for both wavelengths, but is dominated by the 532 nm response and can be safely disregarded as an artifact.

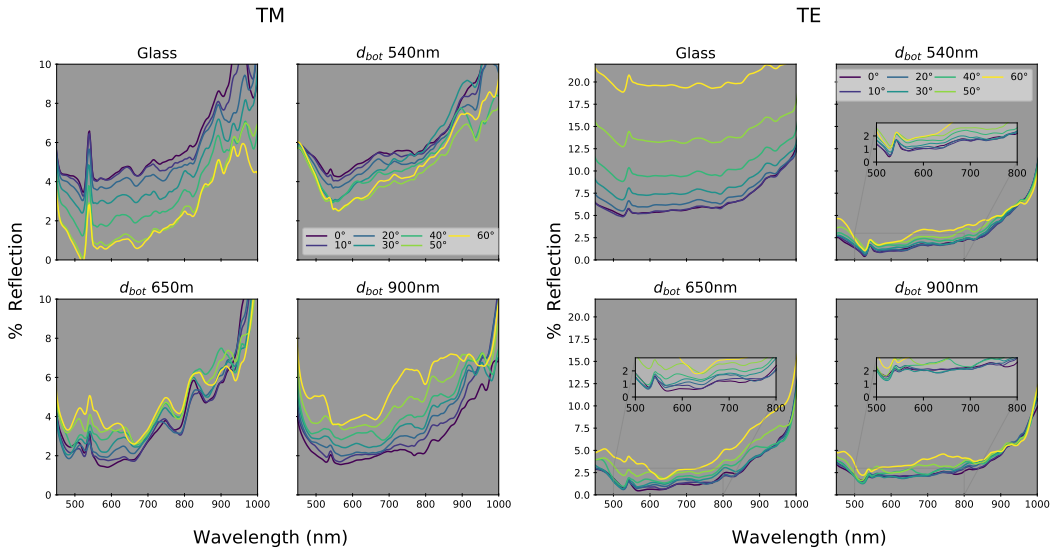

Figure 5.7: The absolute TE and TE reflection curves for glass and the nanocone patterned glass surface. The lowest value seen for TE reflection is 0.32% in d_{bot} = 540 nm nanocone surface structures. The other array minimums for d_{bot} = 650 nm and d_{bot} = 900 nm nanostructures are 0.37% and 1.8% respectively.

The trends of Figure 5.7 are similar to the measurements for the planar photodiode, but without obvious light trapping effects. For TM light, the glass shows a reflection approaching 0 when near the Brewster's angle. Nanocone arrays show slightly increasing reflection with AOI. Anomalously, the d_{bot} = 540 sample shows a response that decreases with angle. This may be the result of an inhomogeneity in the printing process for this sample, but the behavior is as expected for the other polarization. For TE light, reflection below 0.5% is seen in a decent band of the spectrum for d_{bot} = 540 nm and d_{bot} = 650 nm samples. The reflection spectra appear to "bottom out" at a particular value across the visible spectrum. Again, there are no obvious regions where light-trapping of the first diffraction mode is seen. The textured surface of the PV cell worked as hoped to disrupt this process in order to find the absolute reflection of the glass substrates with nanocones.

The polarization spectra are averaged and the results are displayed in Figure 5.8. Overall, the lowest reflection is from nanocones with d_{bot} = 650 nm. The lowest point of polarization averaged reflection is 0.88% at 572 nm. EQE measurements for these samples show that when a glass substrate is placed in from of the PV cell, the EQE drops by roughly 5% as expected from the Fresnel reflection calculation for glass of index n=1.52. Printing nanocone arrays onto this cover glass returns the EQE to the same levels as if the glass cover was not present. These results confirm the previously conclusions of reduced reflection across the visibile and near

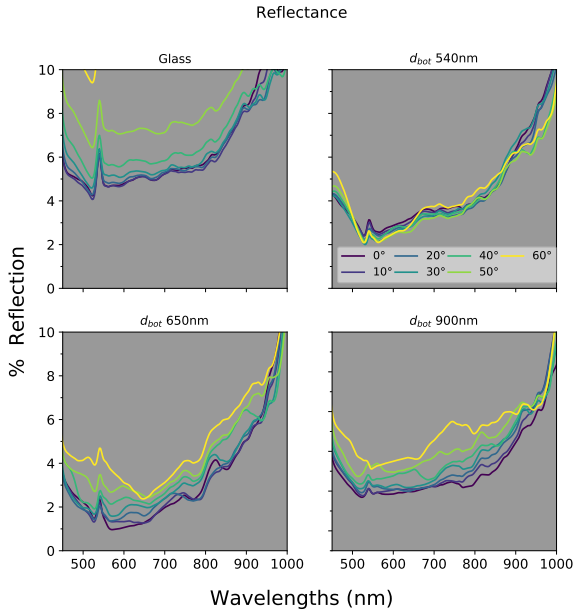

Figure 5.8: The polarization averaged reflection of a glass cover on a silicon solar cell. This is the extracted reflection from the glass interface, and not of the entire stack. Even these relatively short nanocones with aspect ratio between 0.65 and 1.08 can reduce reflection significantly out to large AOI compared to flat glass.

infrared spectrum. Unpolarized and incoherent measurements were not performed due in part to the need to isolate collection to only the patterned area of the glass and a mismatch between that instrument's larger spot size, the shape of the diced silicon cells, and nanocone array high fidelity areas making the samples impossible to properly mount.

5.4 Simulation of Observed Experimental Results

Post-experiment RCWA and FDTD simulations further clarify mechanisms seen in experiment, especially that of light trapping in the photodiode experiments. First, the monotonic drop in reflection followed by a steep increase of reflection for the different samples is explained by analyzing the photonic band structure of the nanocone array. Next, simulations of the different aspect ratios indicate that a larger range of aspect ratios would be a good future direction for deeper analysis.

FDTD simulations were used to compute the band diagram of the nanocone array, relating the free space momentum to lattice propagation constants along the Brillouin zone symmetry vectors.[48, 79] Figure 5.9 shows the modes of the system as bright bands in the band diagram. The right hand side shows the photodiode experimental spectra, normalized in k_0 to match the features and wavelengths to the band diagram units, and normalized in magnitude. It is immediately seen that the normalized

experimental results match peaks near perfectly. Overlaid are horizontal lines indicating k_0 at which a new diffractive mode is allowed. The light cone for free space, $k_0 n_{amb}/mk$ and the substrate light cone, $k_0 n_s/mk$, are plotted in blue and red dashed lines, where mk indicates an integer multiple of the relevant lattice vector. The free space and substrate dispersion lines are folded in the first zone for values up to $k_0 = 2M = 1.154$.

We trace the substrate light line from the zero momentum Γ point in the M direction, past its first fold to when it crosses back to the Γ point at a k_0 of $2M/n_{substrate} = 0.759$ marked as the blue horizontal line. Here the Rayleigh condition of Equation (5.1) is satisfied and allowing the first transmitted diffraction order. Free space light at normal incidence has enough momentum to scatter into the plane of the lattice with a new component $\vec{k}_{\|} \leq \vec{k}_0$. At this k_0, the experimental response starts to dip below the baseline value as diffractive light trapping is activated. Waves are trapped between the photodiode efficiently until the substrate light line crosses the free space light line, allowing for easier scattering back into free space. The shoulder (just below the cyan horizontal line) in the response is indicative of this scattering occurring in experiment with low efficiency. The low efficiency is likely due to difficulty coupling back into the previous scattering mode after undergoing reflection from the photodiode. The cyan line indicates the k_0 that is equivalent to the lattice momentum of $2K/n_{substrate}$, where the first order diffraction in the K direction is allowed into the substrate. This diffraction creates a second channel for diffracted light with large $\vec{k}_{\|}$ that is also trapped. The geometric lattice vector magnitude from $2M/n_{substrate}$ and $2K/n_{substrate}$ onsets is plotted and overlaid as the dark blue and cyan dashed curves up to the Γ point with $k_0 = 2M$. This matches the simulation of the complex cone structure well, indicating that the lattice momentum function and the band structure are in agreement. First order free space diffraction is allowed when the ambient light line returns to the Γ point at $k_0 = 2M$, the horizontal magenta line. Here, the first free space mode can efficiently trade momentum $|2M|$ with either of the two substrate diffraction modes. At this k_0, light that was diffracted and subsequently reflected back to the cone array can easily scatter into oblique free-space modes without a large change in momentum. The light trapping effect seen in experiment is essentially quenched up until the second order diffractive modes, as indicated by the right hand side line spectra of aspect ratio 0.65.

Last, we look at the parameter sweep of aspect ratio for the canonical cone displaying the content of diffracted light in the substrate and free-space directions in

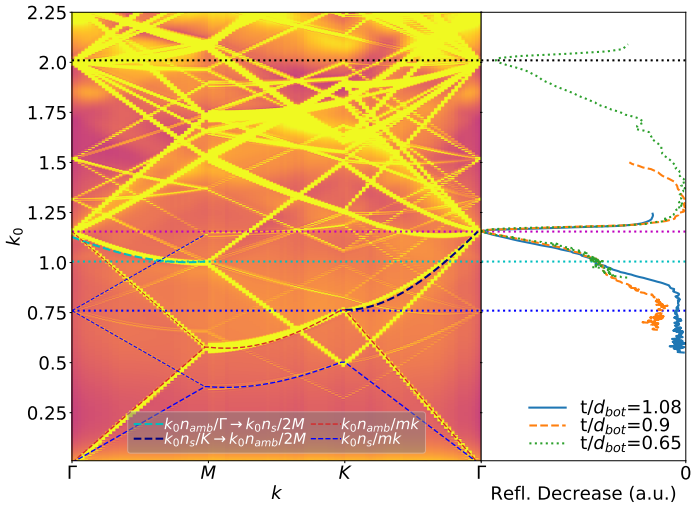

Figure 5.9: The FDTD computed band structure of the canonical cone array on glass. Overlay are lines corresponding to either the ambient or substrate dispersion or a diffracted order dispersion relation. Horizontal lines at Rayleigh points are meant to guide the eye between features of the band diagram and the normalized experimental resutls plotted on the right. Experimental results from measurements with the smooth photodiode shown by green dots, orange dashes, and solid blue represent experimental arrays of d_{bot}=900 nm, 650 nm, and 540 nm respectively.

Figure 5.10. The only difference between experimental cones and this parameter sweep is a top-bottom diameter ratio difference, which is seen in Figure 5.2 to have low influence on the response below 0.3, and the experimental range is between 0.1 and 0.18. The horizontal lines are carried over from Figure 5.9, marking the Rayleigh points. The vertical lines represent the experimental samples. Immediately seen in these plots is that no power found in diffraction modes below their allowed momentum, consistent with the already presented results and basic diffraction theory. Of immediate importance is an explanation to why the light trapping in experiment manifests with a slow onset from the first allowed substrate diffraction. In Figure 5.10A) the allowed diffraction has low efficiency starting at the first order (blue dotted line), increases more quickly after the next order is allowed (cyan dotted line) leading up to the first reflected diffraction (magenta dotted line) with a diffraction strength of about 30%. These results corroborate the conclusions drawn from analysis of the band structure diagram. At the lower k_O values, it is possible to see that the lower aspect ratio cones have more diffraction strength than the larger aspect ratio samples, which is also seen in the experimental curves of Figure 5.9. Transmitted diffraction is responsible for the majority of transmission at higher k_0.

This strength has an apparent periodic dependence with aspect ratio. The oscillatory nature of the diffraction strength requires more investigation.

Figure 5.10B) shows the reflected diffraction strength. Right after the first mode is allowed (magenta line), experimental reflection increases rapidly, much quicker than the transmitted diffraction. This provides reasonable explanation of the similar rapid change of reflection reduction in experiments. This plot also provides clues to the differences in magnitude of the experimental reflection increase after the new diffraction order is allowed. The lowest aspect ratio of 0.65 (green dotted line) sees the greatest reflection increase for k_0 above the free space diffraction, followed by the other samples. The k_0 at which the reflection begins to decrease again for each experimental curve in Figure 5.9 matches with the fraction of power that is diffracted to free space. Had it been possible to measure decreasingly small wavelengths for the array of $d_{bot} = 540\,\text{nm}$, it would be expected to display light trapping into higher k_0s since it's aspect ratio cuts through a region of high transmitted diffraction strength and between peaks in free-space diffraction strength. In fact, taking the ratio of A and B showed that an aspect ratio of 1.08 is roughly ideal for light trapping by maximizing the substrate diffraction strength while minimizing the free space diffraction strength. To target the visible to near-infrared light spectrum between 400 nm and 1000 nm, a cone with $d_{bot} \approxeq 900\,\text{nm}$, height of 972 nm, and d_{top} less than 250 nm should be ideal. Last, the periodic nature of the axial reflection modes show up in Figure 5.10B) as this mechanism competes with free space diffraction. Of note is the same periodic maxima along the aspect ratio axis appear with free space diffraction as they did with substrate diffraction, and deserve further investigation.

5.5 Conclusions

In closing, the novel description of the cylindrical waveguide modes responsible for the anti-reflection behavior of nanocone arrays builds on the concept of continuous index grading is presented. From this, we see that a fine point tip is not necessary for the anti-reflection effect, but only a large enough diameter tip to smoothly couple target wavelengths. Fabry-Perot axial modes, cylindrical waveguide modes, and effective medium approximations are shown to be the main coupling mechanisms for incident light, with each dominating different portions of the spectrum.

Short, low aspect ratio, nanocones compare favorably to commonly seen highly tapered cone structures due to diffractive light trapping between the first substrate diffraction mode and first free-space diffraction modes. These materials were chosen

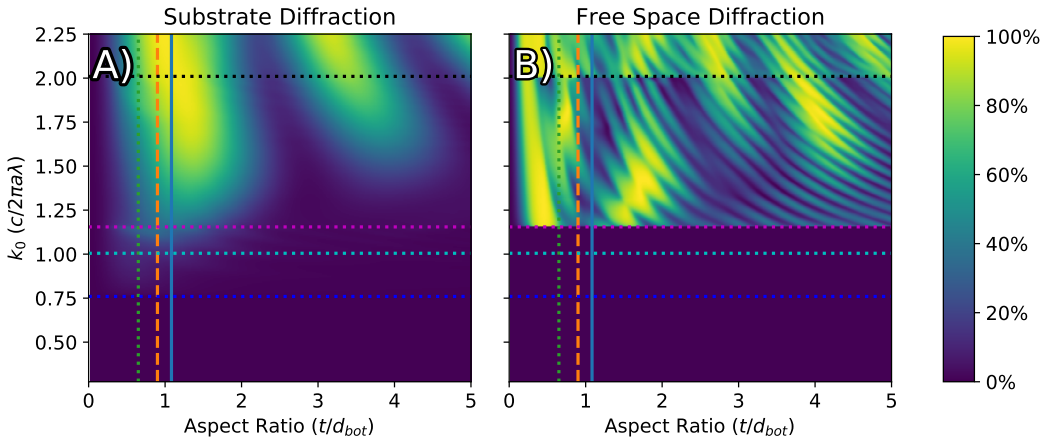

Figure 5.10: The diffraction strength as percentage of transmitted A) and reflected B) flux in a non-zero mode for the canonical cone with varying aspect ratio. Vertical lines correspond, to the experimental cone array's aspect ratio, where green dots, orange dashes, and solid blue represent experimental arrays of d_{bot}=900 nm, 650 nm, and 540 nm respectively. Horizontal lines are the same from Figure 5.9 as an eye guide for the relevant k_0s of diffraction modes.

due to their availability and relevance to applications such as solar PV. However, the results are presented can be applied to any other lossless dielectric combination. For example, materials that exactly match the substrate index to the approximate continuous index function should give yet fewer orders of magnitude reflection. Though realistic perfect combinations of materials exist, non-intuitively, the cone material would have higher index than the substrate; the optimum cone index can be calculated from the approximations discussed. Additionally, because the substrate first order is refractive index dependent, the region of light trapping can be extended by increasing the refractive index of the substrate.

Coupling incident light into the low order diffraction modes that cannot easily trade momentum with the lattice for free space scattering internally traps light between the substrate and absorber, creating multiple absorption opportunities. This manifests as sharp dip in the apparent reflection reduction of experiments with planar photodiodes. This phenomenon puts low-aspect ratio nanocone arrays into a unique category that provide broadband anti-reflection *and* light trapping for nearly all AOIs, while also being designed to target specific wavelengths to a even greater degree. One optimal nanocone aspect ratio is found to be 1.08, as it balances strength of substrate diffraction efficiency with minimized free space out-coupling. In experiments with silicon PV cells, surface texture masked effects of diffractive light trapping due to scattering, allowing for parsing of near zero glass surface reflection of less than 0.37% in the visible spectrum. Similarly low

values were seen for three different size nanocones across the visible to near infrared spectrum. These results are similar or better than other literature exploring the limits of nanocone array anti-reflection structures. [9, 23, 63, 106, 158] These nanocone arrays experimentally show minimal to no overall angle dependence. Apparent glass reflection at high AOI was reduced by as much as 21%, the product of angle independent light trapping and waveguide coupling with a smooth effective index function.

Using silica sol-gel and NIL enables promising application of these structures as an affordable and scalable augmentation of existing solar cell designs. Not studied here, but encouraging, other work has shown nanocone surface structures can be designed to have self-cleaning capabilities in addition to being environmentally inert silicon oxide, decreasing solar PV maintenance costs while increasing collected sunlight over time. Due to the redirection of light via diffraction, so called "dead space" in solar modules between cells could potentially be mitigated. Reducing the reflection of the solar cell cover glass would provide an additional 1.42 mA cm^{-2} photocurrent and could lead to power conversion efficiency gains of 1% or greater.

Chapter 6

PHOTONIC STRUCTURES TOWARDS PERFECT REFLECTION IN LUMINESCENT SOLAR CONCENTRATORS

6.1 Introduction

Much of current PV research maintains focus on decreasing the levelized cost of solar electricity solar to prices lower than coal, oil, and natural gas. Concentrating photovoltaics (CPV) devices offer a possible solution to minimizing the overall cost of PV-generated electricity. By concentrating the light that impinges upon a solar cell, the device power conversion efficiency can be increased. Additionally, by developing a concentration method that focuses the light to a smaller area, the amount of costly PV material required decreases. However, two fundamental hurdles for geometric CPV cells exist. First, the complexity and cost of optics involved in concentration sometimes outweigh the benefit of decreased device area. Second, CPV cells often require tracking hardware in order to effectively concentrate light. A LSC overcomes both of these shortcomings of traditional geometric concentrators.[**Lunardi2019**]

A schematic of the LSC is seen in Figure 6.1. The large light gray rectangle represents a slab of dielectric material, typically a coating low index polymer. Solar cells are demarcated by dark gray rectangles. In the top instance these cells are coupled at the sides to a slab of low index material, edge-lining the slab with 4 solar cells. The second instance (bottom) shows a solar cell that is in the same plane as the waveguide. Both designs have strengths and weaknesses, yet the edge-lined solar cell is more thoroughly studied than the coplanar design. The coplanar design is given careful consideration in the investigations herein. Common to both cases, sunlight is incident from the top of the polymer slab surface. Luminophores, marked as circles, are homogeneously distributed with a controllable concentration. The luminophores absorb and then re-emit light as photoluminescence (PL). Specifically, the luminophores studied here absorb high energy blue light and emit lower energy red light; the benefit of this is treated below. The particle concentration of the dots determines the amount of light absorbed in the slab, yet it also determines how much scattering and potential re-absorption of emitted light the luminophores participate in. The escape cone indicates the angles at which light can enter and leave this

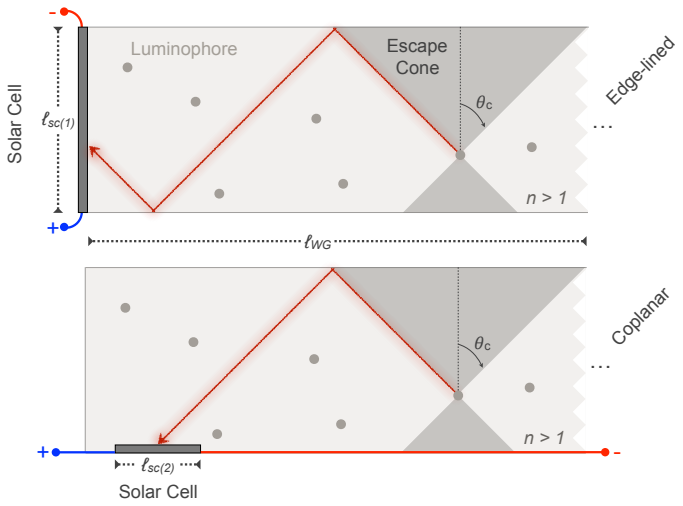

Figure 6.1: A schematic of a single junction LSC shows the solar cell placement, escape cone, luminophores, emission travel path, length L and thickness T, and solar cell width l. Bold red and blue lines indicate electrical connections to the photovoltaics. Figure courtesy of D. Needell

slab of material. Emitted light travels along the paths indicated by the red arrows, showing how rays of luminescence are guided by TIR.

The theoretical benefit of these devices is that the acceptance area can be orders of magnitude greater than the actual photovoltaic device. Using a low index polymer help to accept more diffuse light due to its low reflectance at large AOIs and absorption of luminophores is angle independent. This is contrasted by the large reflection exhibited at large AOIs for typical high refractive index semiconductor PV devices. Large materials savings could conceivable be attained by swapping a production of large area, high-cost III-V solar cells such as GaAs for a low cost, high volume production of polymers and luminophores like polylauryl-methacrylite (PLMA)and QDs. Only a fraction of the area of the high cost solar device would be needed in such a device. Additional savings come from other auxiliary costs involved in solar energy deployment such as the cost to ship and install heavier crystalline materials versus light weight polymers. Further, the absorption and visual appearance of the device by tuning the luminophore optical properties. Schemes of transparent, energy producing windows have already been demonstrated in experiment.[104] This same transparency allows LSCs are a potential mate for traditional silicon PV cells in a modular tandem design. An LSC that more efficiently converts high energy photons by guiding them to a higher voltage cell allows lower energy photons to pass through to the silicon bottom cell, outputting the combined power.[111] Here, a focus is given to these tandem devices in an exploration of how they might be

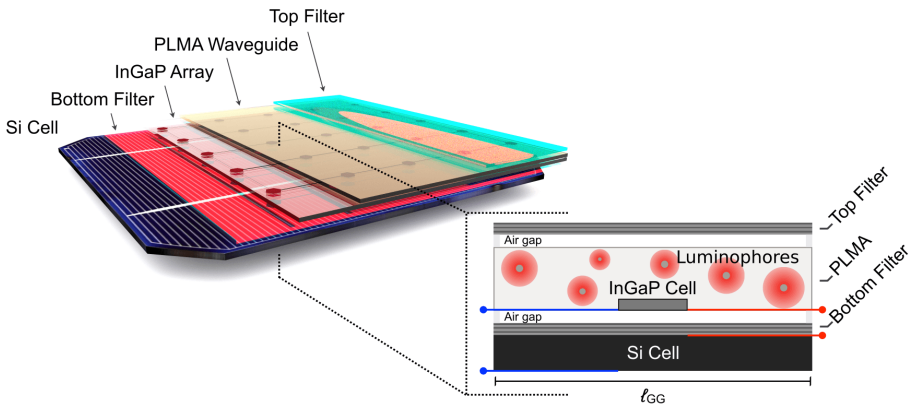

Figure 6.2: A mock-up of an InGaP LSC/Si tandem solar cell. Quantum dot luminophores are embedded in a PLMA waveguide. These absorb high energy blue wavelengths and luminesce at lower energy red wavelengths. The longer wavelengths not absorbed by the luminophore pass through to the Si bottom cell. Top and bottom filters depicted help to trap luminescence and are studied in detail. Figure courtesy of D. Needell

realized and their ultimate performance limits.

A tandem LSC device is proposed and depicted in Figure 6.2. A PLMA waveguide embeds CdSe/CdS quantum dots and a high performance InGaP micro PV cell. These micro cells are arranged in a grid along the bottom of the waveguide. The waveguide is sandwiched between two filters that have been optimized to maximize luminescence trapping and power output of the tandem design. The design follows from the methods and analysis presented in the subsequent sections. The goal of these filters is to better trap PL from the QDs that emits within the TIR escape cone. The top module is separated by an air gap from a silicon bottom cell. The higher bandgap InGaP cells are able to output more power than the lower bandgap Si cell due to less thermalization loss. They thus have a higher power conversion efficiency for blue photons. Red photons below the InGaP band gap are converted by the Si cell. The sum of the two powers exceeds that of either individual cell.

6.2 Analytical Treatment, Investigation, and Insights of LSCs

Thermodynamic Concentration Limit

The angle of TIR in Figure 6.1 is given by Snell's law, $\theta = sin^{-1}(\frac{n_2}{n_1})$. Only light that is outside this escape cone is guided to and collected by cells. Light within the escape cone is typically lost after a few bounces between the top and bottom surface. The Fresnel equations for reflection magnitude of perpendicular(s, TE) and parallel(p, TM) polarizations, are given in 6.1. TE reflection increases monotonically polarized

light, while TM reflection will reach a minimum of zero before increasing towards unity reflection. Relying on Fresnel reflection is not sufficient for concentrating photons in the waveguide slab.

$$R_{TE} = \left|\frac{\tan(\theta_i - \theta_t)}{\tan(\theta_i + \theta_t)}\right|^2, R_{TM} = \left|-\frac{\sin(\theta_i - \theta_t)}{\sin(\theta_i + \theta_t)}\right|^2 \tag{6.1}$$

The mechanism leveraged in an LSC is the absorption and consequent luminescent emission of red-shifted light. This change in energy is known as the Stokes-shift.[152, 182] When a luminophore is embedded in a dielectric slab, luminescent intensity is distributed into a full 4π steradians.[183] The slab acts as a waveguide and concentrator because a significant portion remains trapped in the index guided modes of the slab. Light intensity in the slab is maximized by accessing all available modes of the slab. Relative to free-space, this intensity is greater by a factor of $2n^2$ within the slab.[183] This process is similar to the enhancement of Figure 1.4.

Coupling a solar cell to this slab gives the trapped photons an escape route. In a lossless system every photon eventually finds the solar cell and is absorbed. In this fashion, the slab's area relative to the solar cell can be many factors greater. The same photon flux as is incident on to the slab will reach the solar cell as it travels the waveguide. The ratio two areas and is known as the geometric gain (GG). This is represented in 6.1 by the ratio of L and T in the first case and the ratio of L and l in the second case.

The theoretical power conversion efficiency, η, limit of PV cells coupled to an LSC has been shown to not be greater than, but equal to, to that of a non-concentrating PV device with an area equivalent to waveguide.[56, 124] [102] Traditional CPV concentrates by decreasing entropic loss through restricting the etendue of a solar cell; is no photon energy loss. In LSCs the down conversion of the absorbed high energy photons is analogous to a trade of energy for for the reduced entropy, that is, concentrated light intensity. There exists a fundamental thermodynamic relation between the achievable concentration in a waveguide and the magnitude of the Stokes-shift.[182] The limit of the concentration is defined as the ratio of the external brightness, B_{ext} to internal brightness B_{int}, $C = \frac{B_{ext}}{B_{int}}$, where B has units of intensity per unit area per solid angle per second. For an LSC, C is approximated by Equation 6.2 where ω_1 and ω_2 are the frequencies of absorption and emission, respectively.

$$C \leq \frac{\omega_2^2}{\omega_1^2} e^{\frac{\hbar(\omega_1-\omega_2)}{k_b T}} \tag{6.2}$$

Equation 6.2 can be re-written in terms of energy as approximately[145]:

$$C \leq \frac{E_2^3}{E_1^3} e^{\frac{(E_1-E_2)}{k_b T}} \tag{6.3}$$

Equation 6.3 can be used to calculate the maximum C achievable by a terrestrial based LSC with a luminophore that perfectly absorbs up to a certain energy E_1 and perfectly emits at a lower energy E_2. This takes into account the infinitesimal fractional photon flux at E_1 relative to the total AM1.5G solar spectrum flux $I(E)$ as δf_{E_1}. Here δf_{E_1} is the Kronecker delta function used to select only the fractional portion of the spectrum at E_1.

$$C \leq \int_0^\infty \delta_{E,E_1} f_{E_1} \frac{E_1^3}{E_2^3} e^{\frac{(E_1-E_2)}{k_b T}} dE \tag{6.4}$$

This integration accounts for the fact that there are less high energy photons in the solar spectrum. The Stoke's shift represents a band of photons that are lost. So, there must be a balance between flux concentration to the flux that is lost due to the energy gap.

Concentration values in Figure 6.3 are affected by the solar spectrum photon distribution to a degree but the exponential trend is similar. The relationship for an evenly distributed spectrum would be symmetric with energy. These values also do not necessarily imply that an LSC should exceed the efficiency of a single junction since that is thermodynamically determined by detailed balance. The optical environment for cells coupled to a waveguide inherently changes their external radiation efficiency, i.e. their radiative recombination rate.[143] Figure 6.3 highlights the importance of choosing the correct, and large Stokes-shift for a luminophore in an LSC. The largest C factors demonstrated to date are only on the order of 30x relative to specific bands of the solar spectrum.[13] Concentration factors were only on the order of 20x prior to recent use of large Stokes-shift luminophores. The power conversion efficiency of full LSC PV devices has been correspondingly small also.

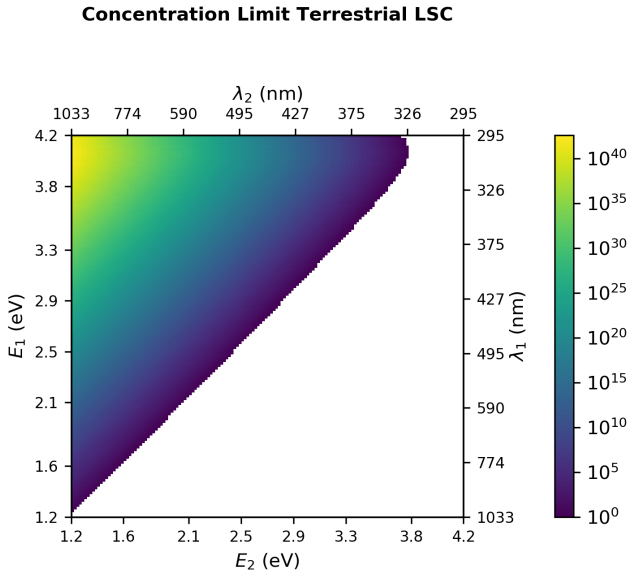

Figure 6.3: The concentration limit of luminescent solar devices given by Equation 6.4 relative to the entire solar spectrum. The concentration factor greatly exceeds the geometric concentration limit of 42,600 suns.[119]

Analytical Model of Photon Travel Path in a TIR Waveguide

The large disparity between the C factors achieved thus far and the correspondingly low efficiencies arises from a variety of loss mechanisms. Equation 6.5 give the expression for the maximum power output of a solar photovoltaic cell. The V_{OC}, J_{SC}, and FF are the device voltage at open circuit, the short circuit current density, and the fill fraction at the maximum power point, respectively. The power conversion efficiency of the overall device is given as the fraction of incident power to the output power in Equation 6.6.

$$P_{max} = V_{OC} J_{SC} FF \tag{6.5}$$

$$\eta_{device} = \frac{P_{out}}{P_{in}} = \frac{V_{OC} J_{SC} FF}{P_{in}} \tag{6.6}$$

This work focuses on increasing the J_{SC} component first, though many strategies to affect the J_{SC} can also positively affect the other two factors. The J_{SC} for a is found by the integral of the entire frequency dependent

$$J_{SC} = \int_{\omega=0}^{\infty} I(\omega) \eta_{coll}(\omega) d\omega \tag{6.7}$$

where $I(\omega)$ is the intensity and $\eta_{coll}(\omega)$ is the collection efficiency of the photo-converting device, in this case a photovoltaic cell. The collection efficiency in a typical solar cell is governed by its own properties alone. The generalized function $\eta_{coll}(\omega)$ includes consideration of other less-traditional mechanisms, such as the incorporation of targeted band rejection filters and up or down frequency shifting elements such as luminophores with a large Stokes-shift. In an LSC, luminophore α, PL, and the waveguide loss must be taken into account as in Eq. 6.8.

$$\eta_{coll}(\omega, \mu, T) = \alpha(\omega, \mu, T)\eta_{PL}(\omega)\eta_{Guide}(\omega)\eta_{EQ}(\omega) \tag{6.8}$$

In Eq. 6.8, $\alpha(\omega, \mu, T)$, $\eta_{PL}(\omega)$, $\eta_{Guide}(\omega)$, $\eta_{EQ}(\omega)$, correspond to the luminophore absorption probability, the photoluminescent quantum yield (PLQY), the waveguiding efficiency, and the photovoltaic external quantum efficiency respectively. The independent variables ω, μ, and T are the frequency, chemical potential, and temperature. Typically, the chemical potential and temperature dependence of absorption of the the quantum dots is a second order effect and it is a reasonable assumption that $\alpha(\omega, \mu, T) \rightarrow \alpha(\omega)$. However, if sufficiently large concentrations of light are achieved in an LSC, these factors, especially μ, become increasingly important. Each of these factors will depend on the optical design of an LSC to different degrees.

A novel analytical expression for the average distance a photon travels in a waveguide was developed in order to describe the loss from a slab waveguide. This is used to determine the intensity $I(\omega)$ seen by a collector in the waveguide. The aim is to fully account for the parameters and properties of real devices. Important factors include placement of solar cells, losses such a non-unity PLQY, the EQE of the solar cells. Design choices, such as the use of notch filters should also be accounted for. Optimization of an increasing number of parameters in the complex LSC system is difficult. Modeling of LSC loss mechanisms is typically done via Monte-Carlo ray tracing. This has proven to be accurate on many occasions, but is computationally expensive.[124] [12] [11] [179][123] Simplified descriptions using fundamental equations that describe the behavior of LSCs allows greater optimization opportunity. To date few others have attempted to supply such a model, and a great need is unfilled.[117] The complexity of the device encourages a modular approach when developing these types of mathematical descriptions.

The different loss mechanisms of the LSC in Figure 6.5 were considered. The closed

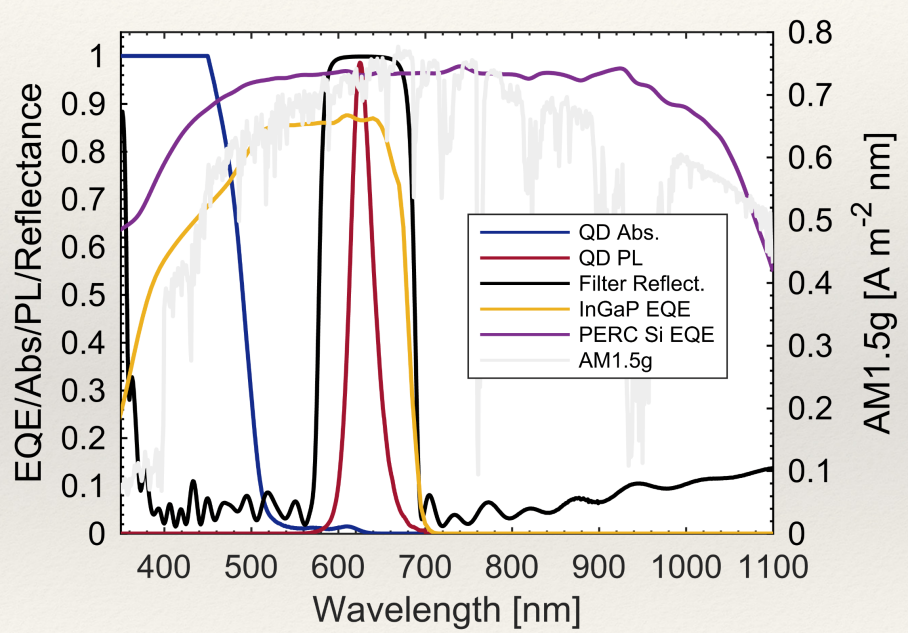

Figure 6.4: The typical EQE, Reflection, QD luminophore absorption and PLQY spectra for the components of a tandem LSC studied. The AM1.5D photocurrent spectrum is plotted in the background. The QD absorb blue light and emit PLnear 630 nm. This is matched to the InGaP EQE. The Si bottom cell EQE (purple) is most efficient in the infrared portion of the spectrum. A dielectric notch filter reflection spectrum is shown to have been designed to perfectly reflect light in the PLspectrum and have now reflection outside of this band (black). Figure Courtesy of D. Needell

form analytical model accounts for each mechanism and calculates a J_{SC} as an input to the detailed balance model of Shockley and Queisser to find the corresponding V_{OC} and FF of 6.5. [143] The intensity distribution of PL within the waveguide around the collector is defined as I_{PL}. This intensity is determined by 6.7.

Equation 6.9 defines a parameter N as the average number of reflections from the top and bottom guiding surfaces as a function of angle θ from the normal vector of the waveguide, the average scattering distance ξ, and the thickness of the waveguide T. The average scattering distance ξ is related to the scattering of waveguide imperfections, such as particulates, and the overlap of the absorption and emission probabilities of the luminophore. Thickness T is assumed to be constant through the rest of the derivation, but note here that it can be varied. Equation 6.9 derives from 2-dimensional trigonometry. It assumes each photon begins at the bottom of the waveguide, slightly overestimating the actual distance traveled. The upper limit on this error is a single integer multiple of N.

$$N(\theta, \xi, T) = \frac{\xi}{T}\cos(\theta) \tag{6.9}$$

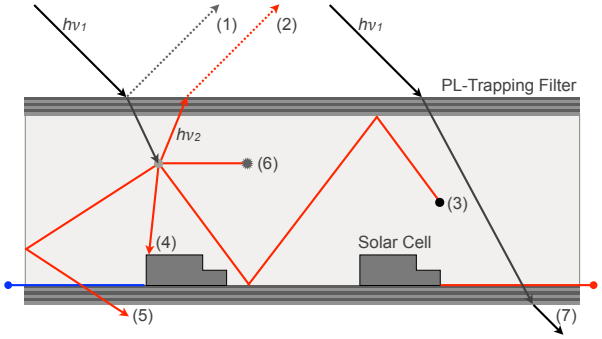

Figure 6.5: Co-planar waveguide LSC loss mechanisms are depicted:1) reflection from the front surface. 2) incomplete trapping of PL within the escape cone. 3) a luminescent photon is reabsorbed by a luminophore and thermalizes. 4) a photon is lost to non-radiative recombination in the solar cell from imperfect internal quantum efficiency η_{coll}. 5) a luminescent photon is lost to the escape cone of the bottom surface 6) parasitic loss due to non-zero absorption of the waveguide material. 7) photon is never absorbed. Figure Courtesy of D. Needell.

The spherically averaged intensity of the light after N interactions with the LSCs waveguide boundaries is given as I, calculated by integrating the angle and wavelength dependent reflectance at the boundary. The change from ω to λ by the relation $\lambda = c\omega/2\pi$ where c is the speed of light is noted. The intensity of the emission after the first PL event given by Equation 6.10:

$$I(\lambda, \xi) = \frac{\int R(\theta, \lambda)^{N(\theta,\xi)} \cos(\theta) \sin(\theta) d\theta}{\int \cos(\theta) \sin(\theta) d\theta} \tag{6.10}$$

Next, the overall photon intensity, i.e. probability of photon existence, after M steps/events through the course of travelling a distance ξ. $\mathcal{I}(M, \lambda)$ denotes this

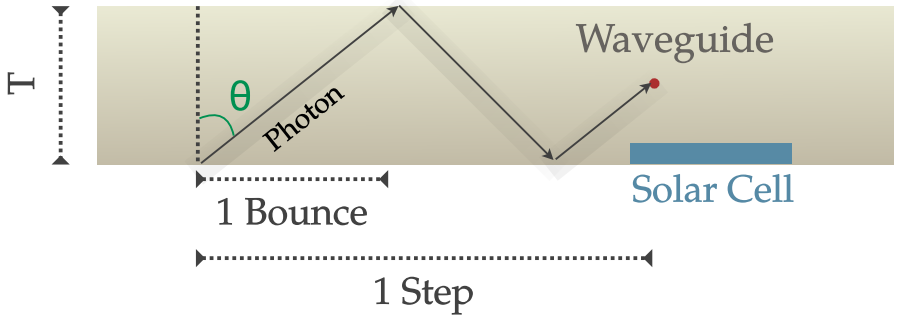

Figure 6.6: A luminescent photon travels along an average path ξ (black ray) at some angle θ from the direction normal to the waveguide. It experiences one of the loss events shown in Figure 6.5. It will be reflected by the boundaries N times for a given thickness T. Figure courtesy of D. Needell.

spherically averaged intensity of the photon after M emission/re-emission events. Each event, $m \in M$ has an intensity according to 6.11.

$$\mathcal{I}(m) = \int I_0(\lambda)\eta_{PLQY}(\lambda)Q_{PLQY}(\lambda)I(m-1,\lambda)\mathrm{d}\lambda \tag{6.11}$$

This spherical intensity distribution is adjusted by the properties of the luminophore in Equation (6.11) at each event m. These properties are wavelength dependent functions, namely the PLQY, $\eta_{PLQY}(\lambda)$, and the emission spectrum, $Q_{PLQY}(\lambda)$. These factors affect the distribution after each absorption and re-emission event. A non-unity η_{PLQY} accounts for photons can be lost to thermalization. The emission spectrum Q_{PLQY} accounts for the fact that a photon has a certain probability of emitting at a new wavelength. This is explicitly accounted for because the other parameters depend on this wavelength. This is analogous to calculating the probability that a photon for given parameters has not been extinguished after M steps, which is the product of M such intensities $\mathcal{I}(M,\lambda)$. Equation (6.12) shows the expanded form of the finally intensity after all steps M. This is compactly written by raising the integral to the power M in as in Equation 6.13.

$$\begin{aligned}\mathcal{I}(M,\lambda) = I_0(\lambda) \int I_0(\lambda_M)I_N(\lambda_M)Q(\lambda_M)\Big(\int I_0(\lambda_{M-1})I_N(\lambda_{M-1})Q(\lambda_{M-1}) \\ \ldots\Big(\int I_0(\lambda_1)I_N(\lambda_1)Q(\lambda_1)\mathrm{d}\lambda\Big)\ldots\mathrm{d}\lambda_{M-1}\Big)\mathrm{d}\lambda_M\end{aligned} \tag{6.12}$$

$$\mathcal{I}(M,\lambda,\xi) = I_0(\lambda)\Big[\int Q(\lambda)I_{\mathrm{edge}}(\lambda,\xi)\eta_{\mathrm{PLQY}}(\lambda)d\lambda\Big]^M \tag{6.13}$$

The photons are subject random walk, so to determine the overall intensity after M steps, 6.13 is reformed to depend on an expectation travel distance. A 2 dimensional random walk is appropriate due to radial symmetry.

$$\langle\vec{r}_{\mathrm{step}}\rangle = \frac{\int \xi \sin^2(\theta)\cos(\theta)\mathrm{d}\theta}{\int \sin(\theta)\cos(\theta)\mathrm{d}\theta} \tag{6.14}$$

$$\langle\vec{r}\rangle = \sqrt{M}\,\langle\vec{r}_{\mathrm{step}}\rangle \tag{6.15}$$

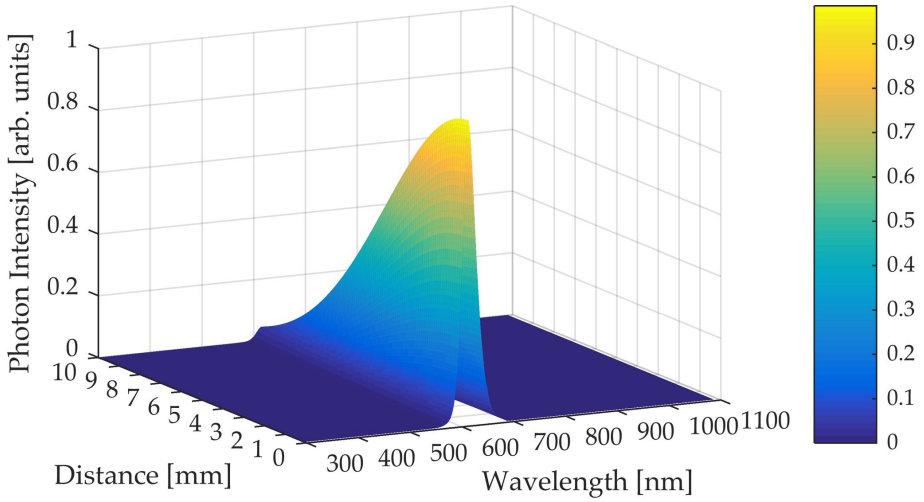

Figure 6.7: The expected intensity of photons collected from varying radial distance. Here, the reflection of the top and bottom surfaces was considered to be perfect, scattering was included, and PLQY is 99%. Figure courtesy of D. Needell.

Finally, equation 6.16 expresses the intensity distribution as a function of distance from the solar cell in the waveguide. Integrating this function over the space around a gives the total intensity seen by a co-planar solar cell.

$$I_{\mathrm{MFP}}(\langle\vec{r}\rangle, \lambda, \xi) = I_0(\lambda)\Big[\int Q_{\mathrm{PL}}(\lambda) I(\lambda, \xi)\eta_{\mathrm{PLQY}}(\lambda) d\lambda\Big]^{\langle\vec{r}\rangle^2/\langle\vec{r}_{\mathrm{step}}\rangle^2} \tag{6.16}$$

First results of this model are plotted in Figure 6.7. A characteristic probability distribution over travel distance is seen along with QD emission profile in the wavelength axis. As expected, collection near the cell is greatest. Surprisingly, in order for a photon intensity to be collected from as little as 10mm away, requires perfectly reflecting boundaries and zero scattering loss. This result stresses the need for perfect PL guiding. Future analysis is calculating the integral value of this distribution for a solar cell by discretizatizing the absorbing area is needed. To realize more rigorous results, the reflectance from the solar cell itself should be be taken into account. Additionally, the scattering length ξ should have an additional dependence on $\alpha(\lambda)$ as in 6.8. Including this $\alpha(\lambda)$ enables accounting for the position of initial absorption, which was initially assumed to be a second order effect. Work to show the impact of a photon's emission position within the waveguide as related to its ability to find the solar cell is on going.

Finally, Figure 6.5 presents experimental measurements of the photon collection by a single InGaP microcell. The experimental LSC uses a silvered mirror on the bottom of the cell to prevent loss mechanisms 5) and 7) in Figure 6.5. This modification

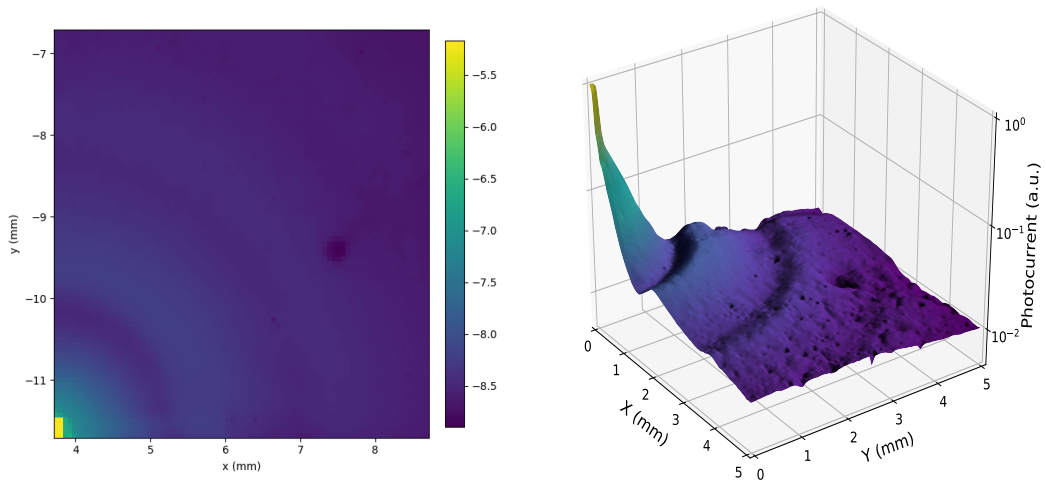

Figure 6.8: Left, the $log10$ laser beam induced Current response of a InGaP microcell embedded in a 30 µm thick PLMA waveguide in Amperes. The sample was illuminated with a 20 µm spot at 490 nm. The photocurrent is measured over an area 5 mmx5 mm from a corner of the microcell. Right, the same waveguide with a top-side dielectric notch filter.

amounts to mechanism 5) being equivalent to mechanism 2) by reflection. Photons subject to mechanism 2) traverse the waveguide thickness at most twice. Last, there are no restrictions on photons being lost from the 4 vertical sides of the waveguide. Photons that arrive at these sides escape unimpeded. We see the expected collection distribution as a function of radial position, but with key differences that would not normally be predicted.

The collection was orders of magnitude less than expected. The peak response was about 10^{-5}, while 0.5 mm away the response had dropped by three orders of magnitude to between 100 nA and 10 nA. Compared to the analytical model, this is explained above by a multitude of factors. The initial PLQY of the QD luminophores was 99%+. However, it has been shown that PLQY is subject to decrease to as low as 60% when incorporated in PLMA waveguide.[13] Next, a loss due to the microcell's non-unity EQE was not considered in the calculations of Figure 6.7. Thus Figure 6.7 is only equivalent to the collected photocurrent for unity InGaP EQE. The EQE of the cell in Figure 6.8 at the PLwavelength of 635 nm is around 80%. The right hand side plot of 6.8 compared to the left hand plot does show increased collection of luminescent photons across the same area. Both show an equal collection over an initial distance of 1 mm. They also show and the same distribution of collection out to about 4 mm with a level of around 100 nA.

There are distinct periodic rings in the response plots. This is best explained as an

effect of the TIR cone creating areas which the cell will collect best from that are a distance of $d = \tan(\theta)2t$ for θ_{TIR} and thickness of the waveguide t. This distance in this particular case for an angle $\theta_{TIR} = 44.76$ and the thickness t= 30 μm is d=60 μm. This value does not match these sets of measurements where the rings are located at multiples of 1.2 mm. The Ag mirror used as a reflector has an offset of about 1 mm due to it's acrylic encasing. When using this value to as t the radius, a value on the same order of magnitude is calculated, $d = 2.4$. The mirror is seen to help trap more photons in these troughs compared to the case without mirrors. This implies that photons not collected in the troughs are photons lost to the escape cone, and supports the theory above. A rigorous measurement of the thickness of the mirrored surface relative to the waveguide along with deeper analysis still needs to be done.

Conclusions

This section has highlighted the importance and sensitivity of the LSC performance to the waveguide efficiency η_{WG} and to other loss mechanisms. An analytical model to facilitate understanding of these different losses in an LSC was developed. This model attempts to find the mean travel distance of a luminescent photon. A specific focus on optimizing luminescent photon trapping designs is presented next. Collaborative efforts utilizing a Monte Carlo model that expand on this work can be found in the Published Content and Contributions.

6.3 1-D Bragg Stack Notch Filter Design for Tandem LSCs

Quarter wavelength Bragg Filters

Design of the top and bottom filters in Figure 6.2 are discussed in detail here. The design goal is to create perfect reflectance in PL band while minimizing reflection outside this band. Losses are minimized when this reflection is maximized at all angles for the PL wavelengths. The Monte-Carlo modeling results of Figure 6.9 show the sensitivity of a tandem device to filter performance is extreme. The model takes accepts inputs of top and bottom cell EQEs, QD luminophore absorption, and PL spectra such as those shown in Figure 6.4. It then calculated the J_{SC} by Equation (6.7) . Finally, empirical values for V_{OC} and FF were used to calculate the power conversion efficiency by Equation (6.6). The model made the simplifying assumption that the reflection spectrum is angle independent.

The tandem device power conversion efficiency decreases drastically for imperfect filter reflection. A peak of 27.5% power conversion efficiency is found for perfect reflectance in the rejection-band and perfect transmission in the pass-bands. This

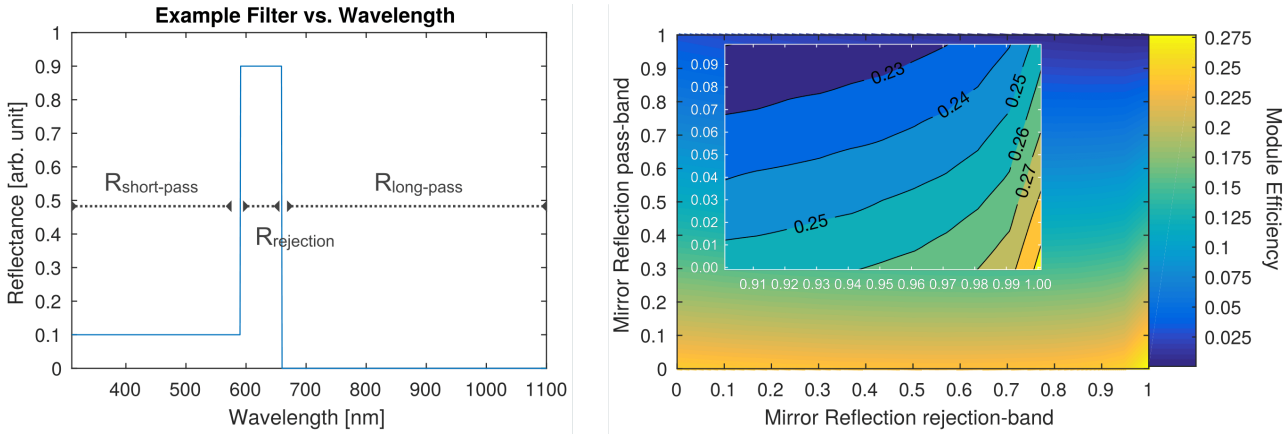

Figure 6.9: Left: The shape of a top-hat notch filter reflection spectrum. Right: Monte-Carlo ray tracing simulations of parametrically varied rejection-band and pass-band reflection and tandem the resulting module power conversion efficiency. The overall device efficiency is highly sensitive to the notch-filter reflection. Figure components courtesy of D. Needell

falls to 26% for 95% rejection-band reflection while maintaining perfect transmission in the pass-bands. A further decrease to 24% was seen for 95% reflection in the rejection-band, but 8% reflection in the pass-bands. Reflection of 95% and 8% are considered typical values for un-optimized filters.

It is possible, yet difficult, to meet these near perfect criteria. The open source software *OpenFilters* was used to create 1D Bragg stack dielectric filters by varying the periodicity of low and high refractive index dielectric materials.[96] Considering only two materials, large reflection results from multiple destructive interferences in the alternating layers of high and low refractive index. Creating filters with high rejection-band reflection, low pass-band reflection, *and* omni-directional rejection-band reflection is facilitated by adding more than two materials. Optimization tools were needed to achieve these desired results when increasing the number of refractive index possibilities. A needle optimization was used to realize perfect reflection in the rejection band minimized reflection in the pass-bands.[96]

In the simplest implementation, a 1 dimensional dielectric Bragg stack consists of alternating $\frac{1}{4}\lambda$ layers where λ is the center wavelength of the notch filter. The alternating layers create destructive interference of the electric field amplitude, disallowing propagation through the length of the stack; in real applications this mechanism is near perfect for a reasonable amount of layers and normal incident light.

The angular response of these Bragg stacks is known to blue shift. Considering this

as a problem of Bloch periodicity helps simplify the mechanism: the modes of this optical system do not allow certain wave vectors $\vec{k}$ (see Section 1.2). At normal incidence, the stack periodicity is matched to wave vectors at the edge of the first Brillouin zone, and lie in a photonic band gap, between $\vec{k}_{0,Gap0}$, and $\vec{k}_{0,Gap1}$.

$$\vec{k}_{0,Gap0} < \vec{k}_0 < \vec{k}_{0,Gap1} \tag{6.17}$$

As AOI increases, the component of the incident wave-vector along the periodicity axis shrinks. On a band diagram of $\vec{k}_0$ and $\vec{k}_{\|}$, the component of $\vec{k}$ in the direction $\vec{k}_{\|}$ decreases with AOI until its value fall outside the photonic band-gap. The same decrease in $\vec{k}_{\|}$ moves modes from above the band-gap into that band gap. Center of the rejection-band depends on angle according to a cosine function, $\lambda_{RejectionCenter}\ \cos(\theta)\lambda$. This arises from the dot product of the periodicity normal vector and incoming wave-vector.

$$\begin{aligned} \vec{k}_{\|} &= \hat{n} \cdot \vec{k}_0 \\ \vec{k}_{\|} &= \cos(\theta)\vec{k}_0 \\ \vec{k}_{\|}(\theta = 0) &= \vec{k}_0 \\ \vec{k}_{\|,Gap0}(\theta_1 \geq 0) &\leq \vec{k}_{0,Gap0} \\ \vec{k}_{\|,Gap1}(\theta_1 \geq 0) &\leq \vec{k}_{0,Gap1} \end{aligned} \tag{6.18}$$

The wave-vector for light of $\vec{k}_0$ in this photonic bandgap are complex, and the wave function is evanescent in the direction of the periodicity. In the infinite limit, they will not traverse the entire periodic structure, but be rejected.[79] In the finite scenario, they will be reduced in value significantly due to the imaginary part of the wave-vector.

Figure 6.10 gives an example of a simple quarter wave Bragg filter described above to show the blue shifting of the rejection band and the oscillatory reflection outside the band for wavelengths that are $\frac{1}{4n}$ harmonics. The left and right plots represent the reflection response into and out of a PLMA waveguide respectively as a function of AOI and wavelength across the usable solar spectrum. The angle and wavelength averaged reflection in a band of of 30nm around the PL wavelength is 78.4% and 90.8% into and out of the waveguide respectively. The out of band transmission is 73.5% and 41% into/out of the PLMA waveguide. These values are far from the acceptable range of the Monte Carlo top-hat shaped simulations of mirror responses in Figure 6.9.

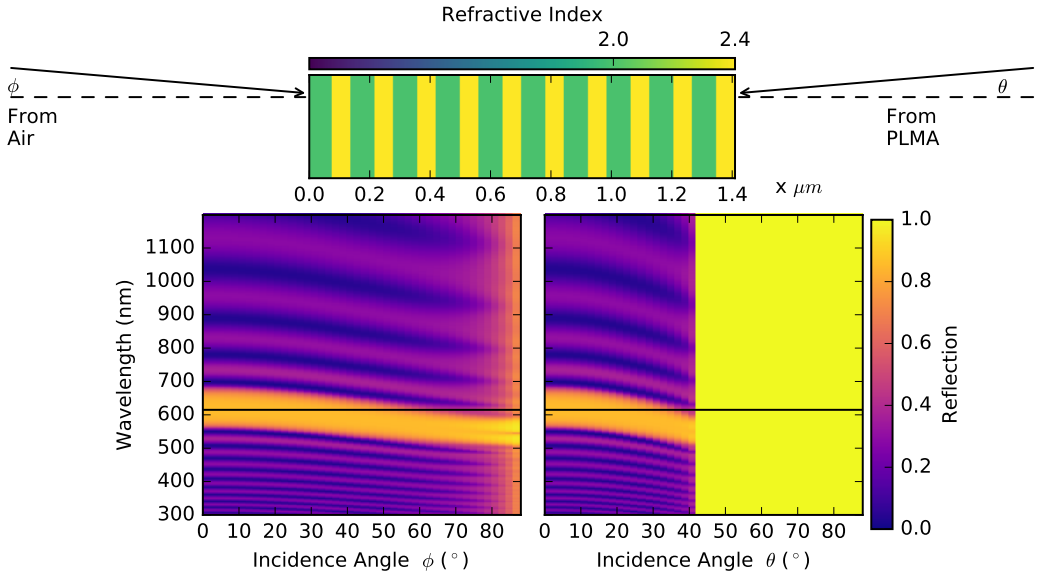

Figure 6.10: The unpolarized reflection response of the a $\frac{\lambda}{4}$ Bragg stack filter targeting a QD luminophore with PL at 615nm. Layer refractive indexes alternate between 2.0 and 2.4. These indexes correspond to high quality TiO_2 and another lossless dielectric such as ZnS. The filter is directly coupled to a PLMA waveguide of n 1.42 – there is no air gap as in Figure 6.2. The left plot shows the angle and wavelength dependent reflection response of the stack filter from incidence in air; the right plot is incident from the waveguide. The large yellow rectangle marks the angles of TIR in the waveguide.

Optimization of Non-binary Index Aperiodic 1D Notch Filters

Optimization through OpenFilters' Needle optimization tool were utilized to create a-periodic filter designs using multiple restrictions on the indexes of refraction in the stack. The figure of merit FOM is zero reflection in the pass-bands and perfect reflection in the rejection-band. This FOM is input directly into the software on a per-wavelength basis. Two classes of result were given: first, a restriction to discrete indexes of refraction of known materials, and second, freely allowing the optimization to use and mix refractive indexes from 1.4 to 2.5, corresponding to the lower and upper limits of known lossless dielectrics. Example materials with refractive indexes between these values include high and low index silica glasses, intermediate oxides such as alumina, high index materials such as titania, zinc-sulphide, and zinc-selenide. Co-deposition of different high and low compounds can create an intermediary effective refractive index. [64]

In many cases the reflection out of band was improved upon the Needle-optimizes results by the manually adding single layer on the free space side of the filter. A $\frac{3\lambda}{4n}$ low index layer where $\lambda \approx 400\,\text{nm}$ is targeted to reduce the blue wavelength pass-band, since this is where the QD luminophores absorb. This pass band was

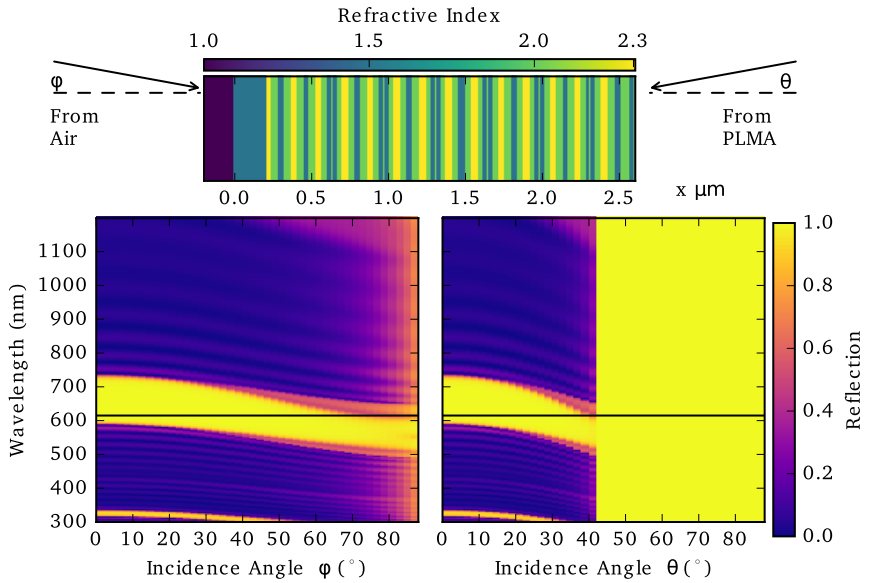

Figure 6.11: The same plot layout as in Figure 6.10 depicting a nearly periodic stack of refractive indexes 1.5, 2.0 and 2.3. The top most layer on the air side utilizes a $\frac{3\lambda}{4}$ layer targeting the blue and near infrared portions of the spectrum to reduce the pass band reflection. This is seen as reduced reflection near 400 nm and 1050 nm. The angle average rejection band reflection into/out of the waveguide is 95.7% and 98.4% respectively. The pass bands show into/out of waveguide reflection of 80.2% and 44.9%.

chosen over the long wavelength pass band because modeling showed that the tandem module efficiency was limited by the top cell rather than the bottom cell. The notch filter in Figure 6.11 utilizes this $\frac{3\lambda}{4} \approx 1100$ nm to create an anti-reflection effect seen at both 400 nm and 1050 nm due to the zeroth and first harmonics of the constructive interference. The angle average rejection band reflection into/out of the waveguide was 95.7% and 98.4% respectively and the pass band into/out of waveguide reflection is 80.2% and 44.9% respectively.

The stack in Figure 6.11 approaches the design goals indicated by Figure 6.9 in terms of the rejection band angle averaged reflectance but falls short in the pass band. The LSC tandem design must accept a maximum number of photons in the pass-bands as a trade-off for the photons rejected by the achieving PL trapping .

Improving upon the filter of Figure 6.11 required allowing the optimizer to freely vary the refractive index in addition to the position and thickness of the layers. The upper limit of the allowed refractive index is a generous 2.5. The design was mostly a periodic binary stack of refractive indexes 2 and 2.5, with intermediate refractive indexes of 1.7 and 1.8 used only on the PLMA side of the filter, as indicated by the schematic. This likely had the effect of minimizing the reflection on this side of

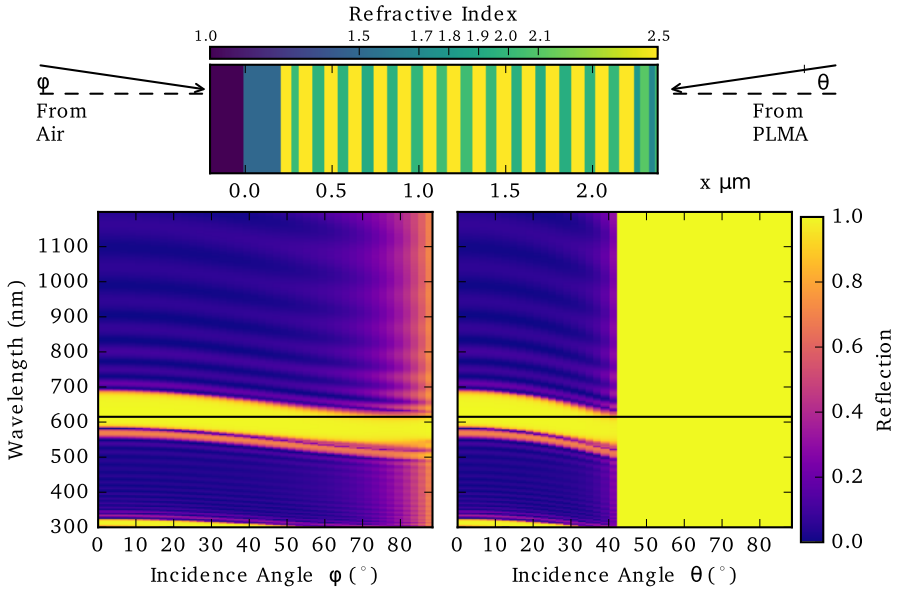

Figure 6.12: The same plot layout as in Figure 6.10 depicting an aperiodic stack of freely varied refractive indexes from 1.5 - 2.3.

the stack by allowing the refractive index of the layers to gradually decrease to that of the PLMA. The same $\frac{3}{4}$ anti-reflection layer is used. This was the best discrete index filter that was found. According to Figure 6.9, the limit of efficiency for a tandem module of such a filter should around 22.5%. However, the Monte-Carlo model predicts a power conversion efficiency of 16.2% and 13.5% for a geometric gain of 5 and 100, respectively. The assumption in the top-hat model of Figure 6.9 of angle independent reflection response did not hold when using real Bragg stack notch filters.

Last, there was an effort to reduce the potential cost of these Bragg filters by reducing complexity. The manufacturing of these filters requires vacuum deposition of materials, and a corresponding deposition time. Reducing thickness reduces this time per unit, which can translate to appreciable cost savings in a high volume manufacturing situation. The thickness of the filters presented thus far averaged 2.5 µm. Bragg filters under 1 µm in thickness were explored as a potential route to lowering future hypothetical production costs. The sub-micron design depicted in 6.13 came close to the best performing filter of Figure 6.12 for the angle averaged reflection in the rejection band, but did not compare favorably in the pass bands. The filter reaches 96.5% and 98.6% for rejection band reflection into/out of the waveguide respectively. The pass bands average into/out of waveguide reflection of 72.7% and 32.0%, which is higher than desirable. The Monte-Carlo simulations

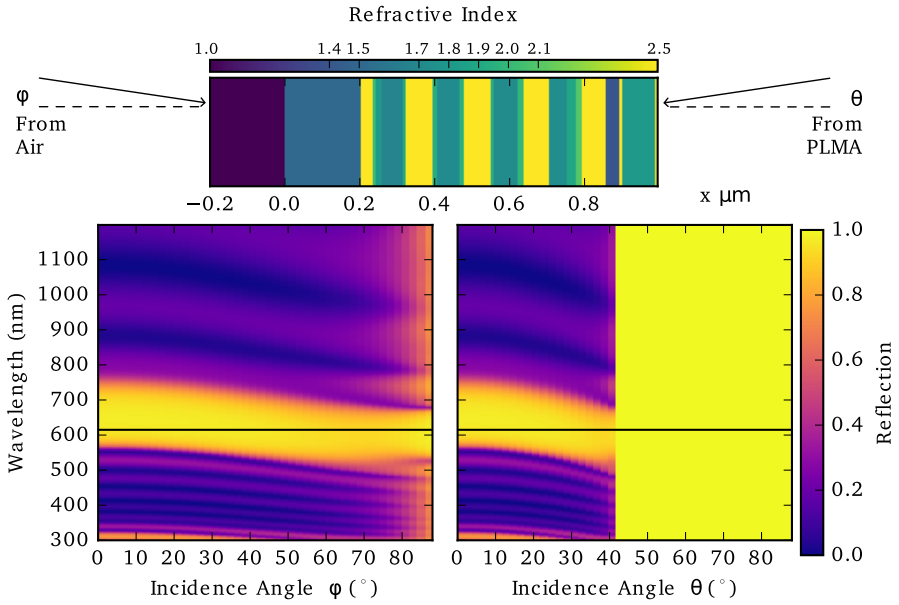

Figure 6.13: The same plot layout as in Figure 6.10 depicting an aperiodic stack of freely varied refractive indexes from 1.5 - 2.3. The aim was to find a Bragg stack filter that has a thickness below 1.5 µm while maximizing its reflection performance in the rejection and pass bands.

predicted an overall tandem module power conversion efficiency of 11.9% and 9.1% for a geometric gain (GG) of 5 and 100, respectively. The rejection band was nearly double in width, limiting the transmission and thus power conversion efficiency. An investigation into the trade-off between manufacturing costs savings and overall LCOE using a non-optimal, but still relatively high performance, Bragg filter should be undertaken to determine the overall best strategy.

Ultimately, the fabrication of the Bragg stack filters wsa outsourced to Evaporated Coatings, Inc. The optimized filter calculated approximately matched the performance of the purchased Bragg filters. Unfortunately, the custom layered design and materials are proprietary, and thus a detailed materials and layer stack comparison cannot be made.

High Precision Measurements of Bragg Stack Filters

Polymer Filters

A serendipitous discovery of a low cost, off-the-shelf multi-layered polymer film was also examined for viability as a LSC filter. Transmission was measured for varying AOI using a custom built high precision laser beamline, here referred to as SARP (Appendix A). The beamline is capable of reproducibly measuring values to

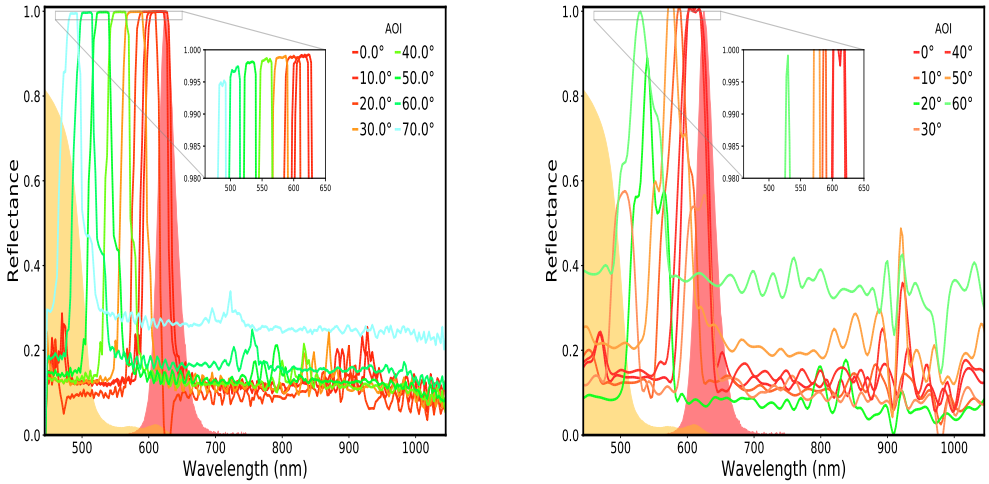

Figure 6.14: Reflection measurements of a commercial periodically layered polymer filter. Left, reflection was measured with a custom monochromatic laser line from 0° AOI to 70°. Right, reflection of the same sample was measured from 0° to 60° with a J.A. Woollam ellipsometer in transmission mode.

3 decimal places across visible and near-infrared wavelengths. Figure 6.14 plots reflection of polymer filters, calculated by as $R = 1 - T$, along with previously measured spectra of the QD absorption and PL for direct comparison.

Two plots of the same sample are shown in order to highlight the capabilities of SARP and the stringent requirements of measurement tools for near perfectly performant samples. The curves are colored according to their spectra's CIE value, mimicking what the eye sees at each angle. The left plot shows the data as taken by SARP and the right-hand plot as taken by the ellipsometer. Noted differences between each is the contrasted ability to resolve narrow bandwidth interference modes across the spectra, the expected linear trend of peak reflection wavelength, and the precision of the SARP measurement for near perfect reflection. The industrial grade ellipsometer did not have the resolution or precision when characterizing these filters to the needed degree. The ellipsometer shows anomalous behavior such as a red-shift in the reflectance peak wavelength between between the change of AOI from 20° to 30°, peak values greater than unity, unresolved interferences and smoothed rejection bands.

The dependence of high reflection across a narrow band on alternating high and low refractive index values was previously discussed in Section 6.3. Reflection spectra displayed on the left plot of Figure 6.14 show that a large number of alternating low

index polymer materials also approach near-perfect performance in terms of peak reflection. They showed with a steep, well defined rejection bandwidth. Here the thickness of the polymer mirror was approximately 100 µm. Multitudes of Fabry-Perot thin film interference modes manifest as short oscillating peaks through the entire spectrum. The large quantity of interference features confirmed the suspected large number of thin-film layers included in this polymer filter. This is contrasted with the relatively thin 2 µm Bragg filters of Section 6.3 in which only a few of these features were seen. These peaks are even detected along the flat portion of peak reflectance, and were seen blue-shifting with the reflection peak in the left-hand side plot of Figure 6.14 as predicted by theory in Equation (6.18). The complex wave-vector in polymer mirrors is expected to have a small imaginary term due to low refractive index constrast. The evanescent wave therefore extends much deeper into the periodic medium film, and so a much greater thickness is required for such high reflection values. Reflection in the pass bands is unfortunately an issue when considering this material as a top filter. As previously presented, Monte Carlo modeling showed that pass band reflection values should be on the order of 5% or less.

These polymer mirrors show great promise as a high volume, low-cost alternative to vacuum style depositions of high index dielectric materials. However, their performance needs to be adjusted to the specific requirements of the tandem LSC module.

6.4 Conclusions

A new analytic description of luminescent photon travel in a waveguide was presented. This expression matched experiment qualitatively in its shape with respect to increasing radius from a microcell. Experiments were subject to many different losses that were not taken into account in the analytical equations. These losses can and should be incorporated for more accurate predictions. Such an analytical analysis tool will be of great use in the optimization of LSC devices.

Bragg stack filters were designed and analyzed as a potential solution to the loss of PL by the escape cone of a polymer waveguide slab. Simulation optimized filters showed promise, with a final Monte-Carlo model prediction of 16.2% power conversion efficiency. However, these designs required additional improvement to reach the maximum possible power conversion efficiency of near 29%. A potential low-cost polymer Bragg stack filter was successfully characterized to a high degree

of precision during its consideration for use in the tandem LSC design. It showed peak reflection up to 99.9%. Measurements withs this precision were made possible by the significant efforts to create the SARP beamline of Appendix A.

Chapter 7

COUPLED LUMINOPHORE NANOPHOTONIC STRUCTURES FOR DIRECTIONAL EMISSION

A main flaw in the strategy of using a dielectric slab as a waveguide is the loss of PL through the escape cone. In a wave-vector paradigm, this is due to the fact that all emission wave-vectors have an equivalent density of optical states, meaning, an unpolarized dipole will have equal probability to emit into the escape cone as it will to emit into guided TIR modes. Nanophotonic principles applied to solar cells have shown that the LDOS within a material can be significantly modified and tailored to frequencies such that light occupies these high LDOS locations. [15–17, 108, 124, 172, 176, 180] Nanophotonic emission control is a widely studied strategy to increase the extraction and direction of emitted light in LED devices.[39, 41, 77, 174, 177, 193, 196] The opposite strategy has been given less attention. With the exception of Bragg stack filters, nanophotonic principles not as often been applied to trapping PL in a periodic waveguide for directional PL for LSC applications. [10, 36, 55, 59, 65, 66, 128]

The benefits of moving to a 2 dimensional periodic structure are many. An immediate benefit is that the complexity of the problem is reshaped from requiring tens to hundreds of layers in a Bragg stack, to just as little as one successfully patterned layer. Patterning via a scalable process, such as NIL, has been proven in the context of LED light emission.[77, 174, 190] Next, patterning allows control of the allowable k-vectors in the photonic environment, mitigating the chance that a photon will be emitted into free-space and lost. The structure could be designed to preferentially emit into the TIR of a slab, or as is studied here, in the place of the 2D nanophotonic structure, perpendicular to incident light. Additionally, the preference to emit into chosen wave vectors is directly proportional to the PLQY. This is because the radiative recombination is directly related to the increase in the spontaneous emission rate of modified optical environments. [27, 45, 88, 129, 163] This is quantified by measuring the Purcell factor (P_f), which is the ratio of emitted power in one optical environment compared to another for a dipole of a given polarization. This opens the possibility of utilizing less than perfect QDs in a nanophotonic waveguide. Higher performance QDs, coupled with lower waveguide loss should combine to achieve an overall greater power efficiency. An auxiliary

benefit to devices such as the tandem LSC described in Figure 6.2 is enhanced in-coupling of sunlight for both the top and bottom cells. Periodic structures were shown in Chapter 5 to decrease the initial reflection loss in PV devices, which has been shown for other periodic structures as well.[151, 164] Last, related to the second and third benefits, theory has shown that the thermodynamic limit of light trapping can be exceeded for specific wavelength in which the LDOS has been increased. This suggests that it may be possible to fabricate an LSC that in fact does outperform its traditional non-concentrating PV counterpart.[191, 192]

7.1 Proposed Systems

A first step in a scalable nanophotonic design for coupling dipole emission from luminophores, such as Cd/Se QDs, organic dyes, rare earth metal doped materials, and chalcogenide 2D materials, is presented. The incorporation of a nanophotonic waveguide design involves an abundance of tunable parameters and allows for many derivative designs and schemes that follow directly from the simplified approaches given here as first examples.

First, a thin film on the order of micrometers, is deposited upon a low refractive index substrate required mechanical support. This substrate here was a glass or polymer substrate with a refractive index of 1.42. The thin-film should be of a refractive index greater than that of the surrounding dielectric environment in order to provide optical contrast. The high index layer would ideally be a lossless dielectric or large bandgap semiconductor. Within these required materials properties there exists a wide range of refractive indexes, ranging from the substrate index, (polymers, glasses, and oxides) to high index semiconductors with indexes of refraction approaching $n = 4$ or more in the visible frequency spectrum. Other viable materials systems include wet-chemistry based oxide sol-gels and polymers, wherein the luminiphore could conceivably be directly incorporated into the material itself as a dispersion with varying luminophore particulate concentrations. Typically, the surrounding dielectric is air, with a refractive index taken to be unity. Dispersive materials and low bandgap semiconductors have the highest refractive indexes, which presents challenges and trade-offs when used in nanophotonic waveguide designs. Conversely, lossless dielectrics will have lower refractive indexes, increasing the design challenge of creating strongly guided modes within a slab waveguide.

The targeted periodic index guiding nanostructure can be fabricated by typical integrated circuit fabrication techniques including photo-lithography, and EBL, resist

development, depositions of an etch mask or selective etch promoter, It can also be made via wet and/or dry etching to realize a final nanostructure. Other routes to achieve large scale fabrication on the order needed by the photovoltaic industry and worldwide power demands include nanoimprint lithography, continuous UV photo-lithography, gravure printing, holographic lithography, and other highly parallelized nano-fabrication methods.[151]

The material for the nanophotonic slab structures studied here are abstract such that the refractive index can be chosen as required. The maximum allowed refractive index is 2.2, representing the approximate index of lossless TiO_2 sol-gel. TiO_2 is studied first because it is one of the most likely candidates for future working devices. It has a high enough index such that moderate to significant modification of the photonic environment seen by a QD luminophore is possible. Additionally, TiO_2 sol-gel imprint lithography has been demonstrated in literature, making it a amenable to low-cost and large scale NIL production.[5, 86, 188] Alternatively, a lower refractive index of 1.8, Al_2O_3 is another potential dielectric for nanoimprint based structuring, as explored in Chapter 2, and has been demonstrated as a successful luminophore embedding material previously. [125, 175] Other candidates for a high index, lossless dielectric with index above 2 include ZnS, ZnSe, ZnTe. These can be be deposited with the required optical quality at large scale when only a thin film is needed. This evidenced by the current ability of the solar manufacturing industry to produces such thin-films on a large scale. An interesting regime not explicitly studied here, but falling within the purview of the concepts, include amorphous materials such as a-SiC:H, and materials such as transparent conducting oxides. These can offer dynamic modulation of optical properties prospects in nanostructures.[70]

The first design goal is to maximize the coupling of dipole emission into photonic crystal (PC) slab guided modes in a two dimensional periodic dielectric environment, confining the electromagnetic energy to a few micrometers or less in the z-dimension. Relaxing this constraint is the consideration that emission into the substrate is not detrimental as long as it is outside of the substrate escape cone, but trapped by TIR. The light emitted to free space should be minimized as much as possible. Consideration of the P_f to increase the PLQY of QDs is discussed but not co-designed. One potential design mock-up is presented in Figure 7.1.

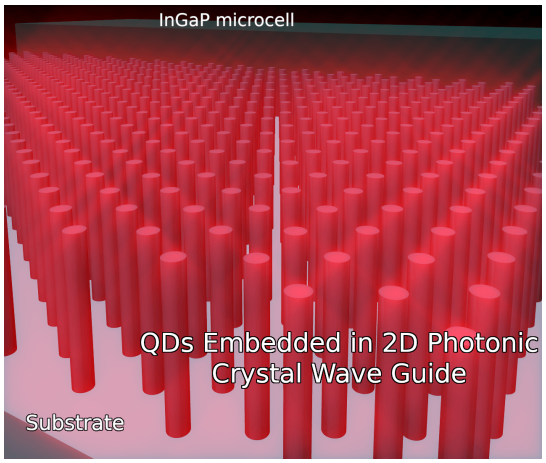

Figure 7.1: One mock-up of a PC based wave guide. QDs or other luminophore are embedded into a high index periodic or otherwise structured material on a substrate. The discrete guided modes carry PL energy in the plane of the waveguide toward a photo-collector elsewhere. Here, an InGaP micro-solar cell is seen in the background the where the PL is collected. Not shown: PL is also diffracted into the substrate at high angles into TIR modes of the substrate and can impinge upon the photo-collecter from the substrate-side.

7.2 Nanophotonic LSC Waveguide Theory

The wave vector conditions for guided modes are given in Section 1.2. The key result is restated here:

$$\begin{aligned} n^2\vec{k_0}^2 &< \vec{k_{mz}}^2 \\ n^2\vec{k_0}^2 - \vec{k_{mz}}^2 &< \vec{k}^2_{m\|} \end{aligned} \tag{7.1}$$

Both TIR modes and photonic slab propagating modes can satisfy the criteria given in Equation (7.1) where enough wave momentum is in-plane such that the wave cannot propagate into free-space. It is worth acknowledging that these formulations apply to plane waves, and here we endeavor to work with QDs which are approximately incoherent dipoles. However, over long distances proportional to the GG of a LSC, dipole emission will approach that of plane waves, increasing the value of the analysis.

Returning to Equation (1.21) can foster greater insight to the possible behavior of dipoles in a modified optical environment. This relationship can be further generalized to explicitly include the group velocity of a wave

$$\omega(\vec{k_m})c = \frac{d\omega}{d\vec{k_m}}\vec{k_m} \tag{7.2}$$

which gives the dispersion relationship of a wave vector in an arbitrary dielectric environment, periodically structured or not. In the case of a homogeneous material,

this group velocity is the material's refractive index, which, alternatively is the slope of its dispersion relation on a momentum-frequency, $\vec{k}_{\parallel}$ - ω, plot, commonly referred to a band-structure diagram, an example of which is shown in Figure 7.3.

The group velocity of Equation (7.2) is approximately directly related to the LDOS, consequently controlling the emission behavior of a dipole emitter. For modes $\vec{k}_m$ approximately confined in two dimensions of planar waveguides, (indicating a minimized $\vec{k}_{mz}$), such as in our system, the optical states per area per frequency can be expressed as:

$$\rho_m = \frac{1}{2\pi} \vec{k_{m\parallel}} \frac{d\omega}{d\vec{k_{m\parallel}}} \tag{7.3}$$

where m is the mode index of a given wave-vector.[17, 153] This directs designs towards periodic structures with a high number of available $\vec{k}_{\parallel}$s per frequency and/or large $\vec{k}_{\parallel}$. These targets are in-line with the conditions imposed by Equation (7.1), and further specifies the "types" of desired modes are slow-light modes, rather than just any mode that will satisfy Equation (7.1).

Last, P_f enhancement is shown to increase the PLQY of emitters compared to their PLQY in free-space, giving proportional enhancement in a nanophotonic waveguide relative to a PLMA slab waveguide.[78] The PLQY is the ratio of fractional radiative recombination rate to total recombination rate, which is equivalent to the radiative power to the input power of a dipole:

$$\mathrm{PLQY} = f_{rad} = \frac{\dot{k}_{rad}}{\dot{k}_{rad} + \dot{k}_{non-rad}} = \frac{\dot{k}_{rad}}{\dot{k}} = \frac{P_{rad}}{P} \tag{7.4}$$

The P_f is equal to the radiative recombination rate of a luminophore in a modified optical environment compared to that of a luminophore in free-space.

$$\begin{aligned} f_{rad} = f_{Purcell} &= \frac{\dot{k}_{1rad}}{\dot{k}_{0rad}} \\ \dot{k}_{1rad} &= f_{Purcell} \dot{k}_{0rad} \end{aligned} \tag{7.5}$$

Assuming the non-radiative recombination rate is power independent and there are no other losses, the fraction of non-radiative recombination in the new environment is equal to its value in free-space

$$f_{1non-rad} = f_{0non-rad} = 1 - f_{0rad}. \tag{7.6}$$

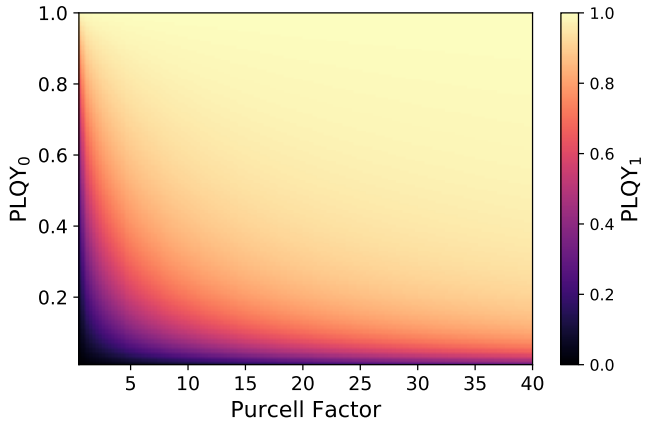

Figure 7.2: The results of applying Equation (7.7) to QDs of various original PLQY_0 in and environment with increasing P_f. The largest single wavelength P_f seen in simulation was 50 for a z-polarized dipole centered in a square lattice of rods with index of 2.2, normalized radius of 0.4, and normalized thickness of 4.6 in the lowest order TM mode.

Combined with Equation (7.5) the new PLQY in the modified optical environment is calculated by Equation (7.7).

$$\begin{aligned}\mathrm{PLQY}_1 &= \frac{\dot{k}_{1rad}}{\dot{k}_1} \\ &= \frac{\dot{k}_{1rad}}{\dot{k}_{1rad} + \dot{k}_{1non-rad}} \\ &= \frac{\dot{k}_{1rad}}{\dot{k}_{1rad} + \dot{k}_0(f_{non-rad})} \\ &= \frac{\dot{k}_{1rad}}{\dot{k}_{1rad} + \dot{k}_0(1 - \mathrm{PLQY}_0\,)}\end{aligned} \tag{7.7a}$$

$$\mathrm{PLQY}_1 = \frac{f_{Purcell}\dot{k}_{0rad}}{f_{Purcell}\dot{k}_{0rad} + \dot{k}_0(1 - \mathrm{PLQY}_0\,)} \tag{7.7b}$$

$$\mathrm{PLQY}_1 = \frac{f_{Purcell}\mathrm{PLQY}_0\dot{k}_0}{f_{Purcell}\mathrm{PLQY}_1\dot{k}_0 + \dot{k}_0(1 - \mathrm{PLQY}_0\,)} \tag{7.7c}$$

$$\mathrm{PLQY}_1 = \frac{f_{Purcell}\mathrm{PLQY}_0}{f_{Purcell}\mathrm{PLQY}_0 + (1 - \mathrm{PLQY}_0\,)} \tag{7.7d}$$

Figure 7.2 applies Equation (7.7)d and shows the exciting potential to raise the PLQY of non-optimum QDs to that of higher performance QDs with moderate to large P_f enhancement. Currently, it is difficult to synthesis QDs with PLQY greater than 0.80-0.09, found typically potentially toxic CdSe/CdS core shell dots or low Stokes-shift organic dyes.[13, 65, 137] Alternate materials systems, such as Cu based chacogenide luminophores, reach between 0.40-0.60 PLQY. [30, 105, 138, 142] Coupling to nanophotonic environments that show P_f on the order of 10-20 can

lift these PLQYs to greater than 0.90, while already high performance luminophores become near perfect for P_f between 5-10. Figure 7.2 shows a maximum P_f of 50, which was the largest seen for single wavelengths in simulations. More often, values of P_f were between 2-7 were seen.

From Eqn 2 of Reference [38], we can find that the proportionality factor of the P_f in two lossless, homogenous optical environments is the inverse of their refractive indexes. Equation (7.8) allows calculation of the results of the P_f relative to an embedding material such as PLMA. Converting simulations results from free-space enhancement to enhancement over a polymer used in LSC waveguides, such as PLMA, was not undertaken in this work, but should be in future study.

$$\frac{f_{1Purcell}}{f_{0Purcell}} = \frac{n_0}{n_1} \tag{7.8}$$

Slab Photonic Crystal Coupled Emission

Bandstructure Simulation

Two simulation strategies represent a large first step to understanding the potential to trap PL in nanostructures. Four fundamental geometries were examined first due to their high symmetry and are well studied: hexagonal and square lattices of high index rods or holes in a high index layer. Results are reported in units normalized to the period of structure, and can be scaled by an appropriate factor to the desired wavelength or frequency. First, computation with the Plane Wave Expansion method via the MPB software was used to characterize the trapped modes.[80] Normalized units enabled the second simulation strategy of exploration with broadband techniques such as FDTD. FDTD was able to estimate overall performance metrics of percent luminescence trapped and P_f enhancement. Only the highest performing structures for hexagonal and rod lattices are presented and analyzed in depth.

In Figure 7.3 the band diagram of hexagonal and square index 2.2 rods on a substrate of index 1.42 are shown. The dimensions for the hexagonal array of rods is a vertical height of 4.6, a radius of 0.25, and a pitch of 1. Dimensions of the square differ with a radius of 0.35. Only the few lowest order modes are displayed since they are the only fully guided modes in the plane of the structure. Of note was the high sloped $\frac{d\vec{k}_{\parallel}}{d\omega}$ TM-like and TE-like bands at the Brillouin zone edges. These modes had the highest LDOS and correspondingly largest P_fs, matching the results of subsequent FDTD simulation results. Additionally, these diagrams show that there is a continuum of modes that exist in the substrate, denoted by the gray shaded

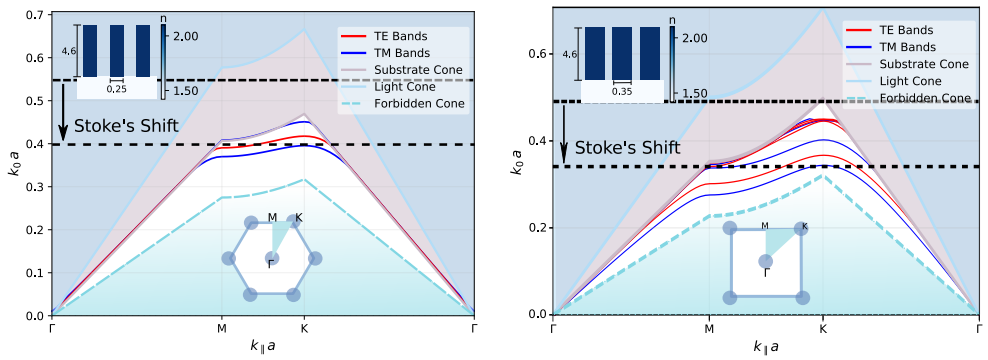

Figure 7.3: Folded band diagrams, calculated in 3D, of a high performing PC slab waveguides made from lattices of rods with index 2.2 on substrate of 1.42. The insets shows a profile view of the structure in the top left, and a schematic of the irreproducible Brillouin zone vectors in the center bottom. Bands below the substrate cone are guided laterally in the photonic crystal. The Stoke's for CdS/CdSe QDs is also depicted

area. These modes are TIR modes, and can work in cooperation with the photonic crystal slab to guide PL in the lateral direction. Diffraction from the lattice imparts a large enough lateral momentum for PL to enter into these TIR modes should they not originally coupled to the PC waveguide modes. Free-space incident light is absorbed above the blue light cone, and a frequency down-shift due to the Stoke's-shift allows a free-space photon to become a trapped photon as the frequency crosses the light cone, allowing PL into a new high magnitude $\vec{k}_{||}$ vector, as depicted. It is also worth mentioning that, in the absence of the discrete bands, the same mechanism of TIR PL trapping is enabled by this crossing from the light cone to the trapped modes of the substrate cone. This is actually the mechanism of traditional LSCs. The forbidden cone represents modes that are unavailable because they have momentum greater than allowed by the high index material. These diagrams helped to narrow the range of exploration in the computationally expensive FDTD simulations to PCs with promising waveguide modes as shown.

7.3 FDTD Calculations

Calculating the power distribution in the lateral and vertical directions requires full-wave simulations with luminophoress approximated as dipole sources. Full simulation periodic boundary conditions cannot be used as in Chapter 3 due to the error of coherent dipole coupling between unit cells. A sufficiently large array is build in the CAD environment with between 12-14 unit cells for final calculations. This affords the electric and magnetic fields enough distance to spatially decay before encountering PML or absorber boundaries in all directions. This decay

minimized any coherent interactions with boundary reflections. Two groups of 7 Poynting vector monitors were arranged in rectangular prisms, excluding a field monitor on the face that is adjacent to the PC slab such that all power flux leaving the area defined by the slab is recorded right before it exits the simulation via the absorbing boundaries. This allows the free-space waves to evolve into fields suitable for analytic far-field projection calculations used to determine the spherical power distribution at a radius of 30 µm into either half-space from the dipole emitter. This distance is the thickness of waveguides used in previous LSC experiments (Chapter 6). Finally, a set of 4 Poynting vector monitors surround the edges of the slab to record the power that exits in-plane with the PC waveguide. The monitors account for 100% of the simulation radiation power input.

In these first steps, the structure symmetry was used to reduce the computational cell to only the first quadrant. This requires that the dipole source be placed directly at the xy origin to satisfy the field symmetry requirements in addition to the structure symmetry. It is noted that this limits coupling to targeted symmetric modes. Simulation results for dipoles oriented in the x, y, z give significantly different results due to the polarizations of the trapped modes, specifically, the z-oriented dipole responses dominated the average results. This dominance is the result of strong coupling and correspondingly high P_f.

Figure 7.4A) shows the behavior of a Z-oriented dipole embedded in the center of the hexagonal lattice of Figure 7.3 across the entire range of trapped $\vec{k}_{||}$ at the edge of the Γ in the direction of K. The stacked color spectrum shows the portions of the normalized power that travel into 4 different directions. Red indicates loss to free-space, the two shades of blue represent emission into the substrate, and finally the yellow is emission in the plane of the PC slab waveguide. PL into the substrate is subdivided by whether or not it enters at angles outside the TIR escape cone. Light outside the escape cone will be trapped at the opposite substrate interface. Plotted on the right axis is the P_f in green. Finally, the bright orange qualitatively indicates the PL of CdS/CdSe QDs when weighted by the P_f spectrum. To be quantitatively rigorous, a future detailed-balance photon accounting needs to be completed. The black dashed line indicates the wavelength for which Figure 7.4B)-D) correspond, and is the peak of combined in-plane and TIR PL containment (the sum of the yellow and light blue areas).

The yellow segment of Figure 7.4 A) shows that near a certain frequency, the portion of the light that is coupled into directions with large $\vec{k}_{||}$ increases drastically; this

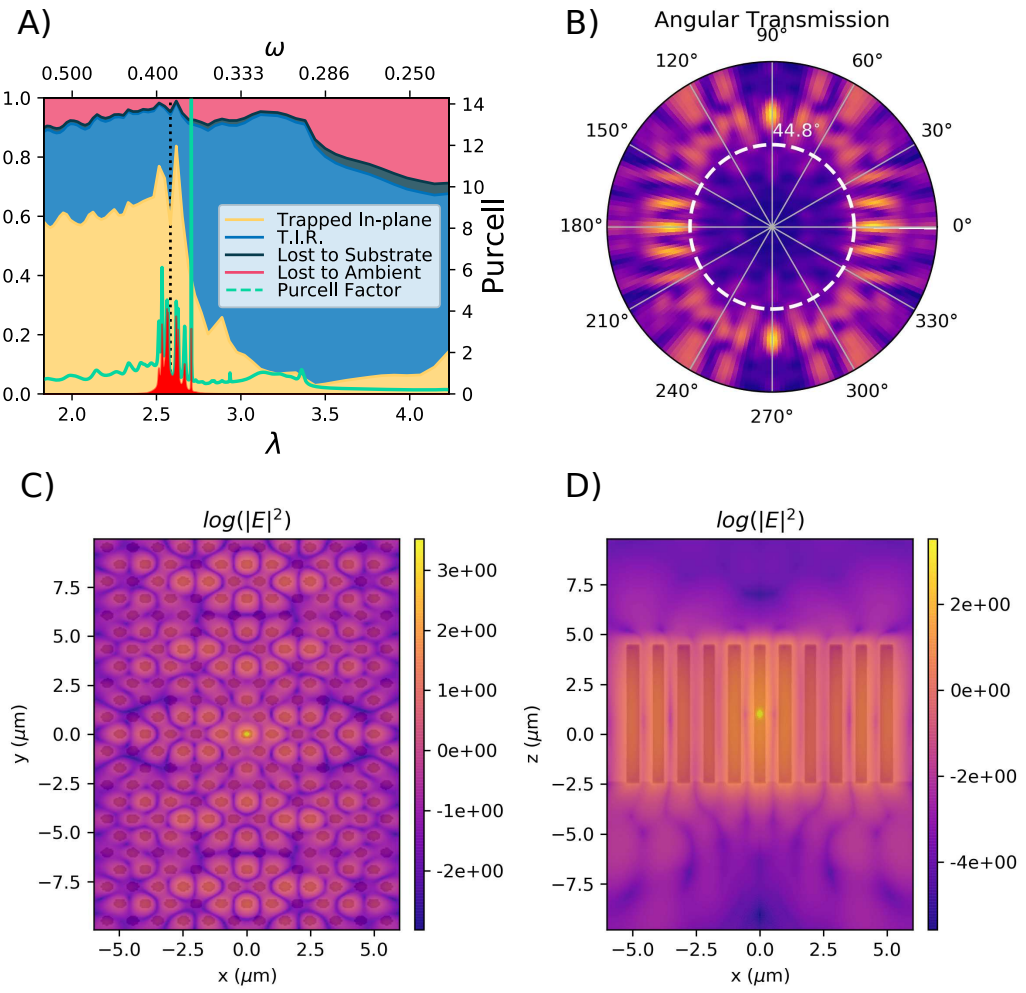

Figure 7.4: Results from a Z-oriented dipole centered in the hexagonal PC slab waveguide from Figure 7.3 A) The spectrum is parsed into the possible directions power can exit the simulation from its source in the center. The P_f spectrum and the weighted PL emission peak of the QDs previously presented in Chapter 6 are overlaid. The PL spectrum is not a rigorously quantitative representation. B) A polar plot of the emission into the substrate, where the white dashed line denotes the TIR angle outside of which PL is trapped. C) and D) show the log of electric field magnitude in XY and XZ cross-sections at the wavelength indicated by the black dashed line of A). The field is concentrated into the rods in both planes. In D) the high-angled emission into the substrate is clearly visible.

frequency is about 0.36, which from Figure 7.3A) it is seen to be the frequency where the first TM band begins to flatten as it approaches the Brillouin zone edge. A remarkably large P_f spike occurs as predicted by theory for this frequency. At a slightly larger frequency, the fraction of in-plane flux peaks and slowly begins to decline again towards higher frequencies due to the continuum of available $\vec{k}$s creating weaker preferential coupling. At lower frequencies the in-plane flux falls precipitously because there are no modes other than the linearly dispersive modes of the substrate. The fraction of totally internally reflected PL falls monotonically to the nominal value of a planar slab, 74%. Figure 7.4 B) shows the angle dependent distribution of power into the glass substrate, with the angle of TIR boundary given by the white dashed circle. The majority of the power is seen at angles greater than 44.8 deg, indicating successful coupling to large wave vectors, $\vec{k}_{\|}$. The peak value of maximum transmission for this dipole orientation, location, and geometry is 98.8%, far greater that the TIR value of 74%. This demonstrates the promise of this coupled dipole approach to directional PL emission.

Figure 7.4 C) and D) show log-scale plots of the electric field magnitude in the XY plane and the XZ plane. Figure 7.4 C) shows that the field energy takes on the periodicity of a combination of the lowest order modes at the peak trapping frequency. Figure 7.4 D) further confirms that the energy is confined to the PC waveguide with some fraction being emitted at high angles into the substrate. Some loss at high angles into the positive Z direction is seen. This is seen as power directly above the slab. The power to the left and right of the center is likely evanescently bound to the waveguide.

This is only an example of a very specific favorable situation, in which the emitter was purposefully located at a high symmetry point and oriented properly to excite TM modes. The same simulation was completed with dipoles in the X and Y orientations and averaged to obtain an incoherent emitter representation. The result is a weighted average of the emission pathways, weighted by the spectrally dependent P_f. The maximum fraction trapped for an incoherent emitter was found to be a respectably high 96.4%. In this instance, the Z-orientation dominated the average because of its high P_f, while the emission is suppressed from X and Y oriented dipoles. P_f was between 1 to as low as 0.18 for both X and Y.

The relative Z position of the emitter was also symmetrically optimized. A sensitivity to Z-placement is shown in Figure 7.5 for the weighted average maximum trapping fraction. Surprisingly, the simulated PL is not strongly scattered into free-

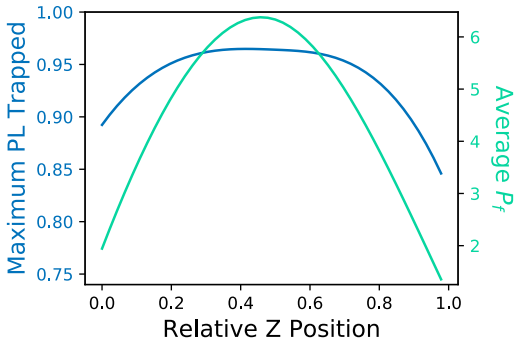

Figure 7.5: Smoothed maximum of orientation averaged trapped fraction and P_f from dipole placements along the thickness of the PC waveguide from Figure 7.3A). The Z position of 0.5 corresponds to the middle and position of peak value.

space or into the substrate escape cone even when an emitter was precisely at the Z limits of the PC waveguide. Weighted average P_f also has a dependence on the Z position, indicating that the majority of the in-plane trapped light comes from the center, and the extremities are less influenced by the PC structure, approaching homogeneous values of P_f 1.

7.4 Conclusions and Future works

The potential for nanophotonic LSCs was briefly explored and showed great promise. Maximum values greatly exceeded that of TIR and are potentially simpler than Bragg filters to fabricate, as they do not require long vacuum deposition times. Alternatively, these kinds of structures can be co-optimized with Bragg filters by controlling the angle of PL emission as demonstrated by Figure 7.4B). This design tact would relax the performance requirements on both optical components. The PLQY enhancement of lower quality QDs further motivates this study in order to broaden the potential luminophore candidates. Figure 7.4A) shows that appropriately large bandwidths can be positively modified to increase the trapping across the entire PL emission spectrum. Finally Figure 7.5 provides insight to the optimum emitter locations; emitter placement was found to be more robust than expected. The high maximal trapping fractions approached those needed for high-performance LSC devices.

Future work includes further refined simulation-based investigation with more rigorous optimization. Emitters placed off of the Z-symmetry axis should be parametrically studied at XY-symmetry points to gain a larger picture of other potential guided or lossy modes. Multiple dipoles each with random placement, orientation, and phase could be used for overall ensemble performance metrics by statistical

averaging. Investigation of the effect on the PC slab thickness and refractive index should provide further direction moving towards experimental demonstrations.

The higher frequency absorption at the different dipole locations carries equal weight as the probability of emission at those same locations. For example, Figure 7.5 indicates that absorption near the top or bottom of the PC waveguide could be detrimental if the average P_f is reduced below 1. This is of especially high importance considering the leading edge of the waveguide will likely absorb more. Strategies for modeling the absorption of an ensemble of luminophores still needs development. This should be followed by simulating the system's interaction with free-space plane waves for various AOI. In addition to this, there is non-zero non-radiative recombination in real luminophores which is not considered. Concentration of the field energy at the same locations as the luminophore equally increases the probability of re-absorption. It is hypothesized that this will be offset by increases in the radiative recombination rates, i.e. PLQY enhancement. If the assumptions of a constant non-radiative recombination rate in Equation (7.7) hold, then the radiative recombination rate should dominate in locations of high P_f. Additionally, the structure could be optimized to favor emission into the substrate TIR modes, as exemplified by Figure 7.4B).

Potential routes to control the dipole placement could involve alternating layers of materials that either do or do not have emitters embedded in them. These layers would be subsequently patterned with a process such as ICP-RIE and/or NIL. These types of PC slabs with "sandwiches" of materials have been shown to preserve their modal structures better than when directly located on a substrate and offer more control over dipole placement. Many different 2D lattices other than the four explicitly mentioned here exist as super-cell lattices, such as the honeycomb lattice, and could provide further exciting results.

Chapter 8

FUTURE DIRECTIONS AND PERSPECTIVES

Research in nanophotonic solar energy over the past two decades has reached a critical point in the laboratory and is ready for greater commercial development efforts. Scalable methods such as nanoimprint are currently being adopted in the large format electronics display industry. This learning curve will drive industrial expertise and lower costs. Just as the solar industry has benefited from integrated circuit process development, nanoimprint will find its way to solar panel production at scale. Soon the best route increased solar power conversion efficiency per unit cost will be through the advanced nanophotonic strategies like those presented here. As power conversion efficiencies approach their limits, every photon matters Previously "minimal" losses will need to be targeted for future PV improvements. The pursuit of conversion efficiency is well founded in the need to all but eliminate carbon producing energy sources by providing abundant of low cost alternatives.

To this end, direct structuring of thin film photovoltaics shows great promise. The thin-film segment of the solar industry has been relatively sidelined by a precipitous drop in cost of silicon modules. Only a handful of manufacturers retain a strong position in the market, including First Solar, Solibro, and Alta Devices. Others such as TMSC and Solar Frontier have recently shut down thin-film cell production. New optics based strategies should be pursued and adopted when possible to provide the power conversion efficiency improvements necessary to compete with low cost silicon.

The dielectric spacer layers of Chapter 4 can be applied to a wide variety of thin-film technologies and still offer a profoundly simple route to sizable conversion efficiency gains. Experimental demonstration in CdSe PV could be one promising avenue. Variations of either ordered structuring or passivating oxide layers have been shown in experiment, but this work shows the best performance will be realized by combining the two. Other locations in CIGS cells have yet to be explored, including front side patterning and front contact passivation. Thin film devices like CIGS, undoubtedly have head room for growth, and are deserving of further research. Their unique advantages such as flexible substrates provide a wider deployment opportunity compared to silicon. For example, transit energy requirements remain

a large obstacle in a new energy economy, and niche thin-film usage could play a role in the solution.

Another exciting prospect for thin-film have come in the form of perovskite solar cells, a material with astoundingly rapid progress. It is the first liquid phase cast-able solar material to ever approach the efficiencies of vacuum deposited or otherwise synthesized semiconductor devices. It's high band gap makes it a great match for silicon cells in a tandem configuration. There will be many future opportunities to apply nanophotonic light management in this material. I look forward to seeing how perovskite's challenges are overcome and to its eventual commercial deployment.

A special prospect exists for light management strategies such as printed cover glass anti-reflection nanocones of Chapter 5 and the Effectively Transparent Contacts [134]. These strategies attack previously tolerated losses in solar device designs Today, some of the least expensive silicon solar cells are at power conversion efficiency levels that were world record laboratory efforts just two decades ago. Record cells are only 2% away from the maximum silicon power conversion efficiency of 28%. Anti-reflection measures from these printed structures can provide 1% of that final stretch, without fundamentally changing cell the manufacturing processes responsible for such high performance. As a last-step in assembly, this style of scalable anti-reflection offers minimal intrusion and ideally can be integrated into the encapsulation material and module glass components bought by cell manufacturers. Printed nanocone anti-reflection could presumably even be applied retroactively. By offering angle and wavelength insensitive anti-reflection, more power per day becomes a value proposition for nanocones and ETCs.

As recommendations for future directions in for nanocone anti-reflection, designs should attempt to exploit diffractive near total internal reflection trapping. Perhaps non-intuitively, initial simulations show the bandwidth of minimum reflection can be expanded using higher index cover glasses. A hypothesis founded in the $4n^2$ mechanisms points to increased trapping within higher indexes as well. The nanocones need not always be printed, but can be etched as well. Thus, thoughts have led to questions of using mechanically harder materials such as alumina, silicon nitride, or even laboratory diamond to increase the robustness of solar modules. Inorganic oxides like silica sol gel, are environmentally inert, and their location on the module exterior should create no more concern than current protocol to avoid harming encapsulation glass.

Finally, LSCs have been an exciting topic in this thesis work. The unique strategy of

capturing down-shifted luminescence sets these devices apart from other solar cells. Yet, fundamentally, the same concepts apply. Similar to a near perfect external radiative efficiency GaAs cell, the goal of LSCs is to trap and recycle photons in a slab of material. Distinct challenges come from increased travel distance to be absorbed, requiring extremely efficient recycling for sufficient photon lifetime. Analytically describing and predicting this travel process and the numerous loss opportunities remains an open question deserving of deeper thought. Future work towards a complete fundamental thermodynamic description of the photon's journey to completely replace Monte-Carlo methods is scientifically valuable.

Another key difference from pure semiconductor solar cells is the large escape cone of low-index waveguides. This requires perfect notch filter over a wide range of angles. This first known presentation of a photonic crystal slab luminescent waveguide for solar concentration provides a completely new solution. The design addresses two critical non-idealities simultaneously. Leveraging photon wave-mechanics leads not only to nearly perfect light trapping, but increases luminescence quantum yield and concentrates light into a smaller volume that could lower cost (also, confining the photon gas in volume should raise chemical potential). Future work undoubtedly involves experimental demonstration of the concept, whether in an optimum optical system, or not. Demonstration of light guiding over a large area and subsequent collection at a photodetector is a high priority. The main challenge is properly embedding luminophores into volumes with high local density of optical states. The target mode volumes must sufficiently overlap with emission profiles to couple. A nanoimprinted quantum dot/ Titania sol gel dispersion is suggested. Alternatively, quantum-well III-V nanowire arrays could provide a route forward in this direction. Perfect light trapping will require high pattern fidelity over length scales orders of magnitude greater than the unit cell. First proof-of-concepts may need to consider using integrated circuit patterning.

Ultimately, the creative solutions offered by combining nanophotonic physics with photovoltaic devices are plenty and powerful. Fabrication methods exist to bridge the gap between the nanoscale and the kilometer scale. Continuing this research and applying these findings and the findings of numerous skilled colleagues in this field will yield technologies that leave a lasting positive impact at a crucial point in time.

BIBLIOGRAPHY

Abràmoff, Michael D., Paulo J. Magalhães, and Sunanda J. Ram (2004). *Image processing with imageJ*. DOI: 10.1117/1.3589100. arXiv: 1081-8693. URL: http://biomedicaloptics.spiedigitallibrary.org/article.aspx?doi=10.1117/1.3589100.

Abujetas, Diego R., Ramón Paniagua-Domínguez, and José A. Sánchez-Gil (2015). "Unraveling the Janus Role of Mie Resonances and Leaky/Guided Modes in Semiconductor Nanowire Absorption for Enhanced Light Harvesting". In: *ACS Photonics* 2.7, pp. 921–929. DOI: 10.1021/acsphotonics.5b00112. URL: http://pubs.acs.org/doi/abs/10.1021/acsphotonics.5b00112.

Alonso, M.I. et al. (2002). "Optical functions of chalcopyrite CuGa x In 1-x Se 2 alloys". In: *Applied Physics A: Materials Science & Processing* 74.5, pp. 659–664. DOI: 10.1007/s003390100931. URL: http://link.springer.com/10.1007/s003390100931.

Anderegg, William R. L. et al. (2010). "Expert credibility in climate change". In: *Proceedings of the National Academy of Sciences* 107.27, pp. 12107–12109. DOI: 10.1073/pnas.1003187107. eprint: https://www.pnas.org/content/107/27/12107.full.pdf. URL: https://www.pnas.org/content/107/27/12107.

Barbé, Jérémy et al. (2012). "Nanoimprinted Tio 2 sol-gel passivating diffraction gratings for solar cell applications". In: *Progress in Photovoltaics: Research and Applications* 20.2, pp. 143–148. DOI: 10.1002/pip.1131. URL: http://onlinelibrary.wiley.com/doi/10.1002/pip.1131/full%20http://doi.wiley.com/10.1002/pip.1131.

Barthel, Michael (2018). *Trends and Facts on Newspapers | State of the News Media*. URL: http://www.journalism.org/fact-sheet/newspapers/.

Battaglia, Corsin et al. (2011). "Nanoimprint lithography for high-efficiency thin-film silicon solar cells". In: *Nano Letters* 11.2, pp. 661–665. DOI: 10.1021/nl1037787.

Battaglia, Corsin et al. (2012). "Light trapping in solar cells: can periodic beat random?" In: *ACS nano* 6.3, pp. 2790–7. DOI: 10.1021/nn300287j. URL: http://www.ncbi.nlm.nih.gov/pubmed/22375932.

Bessonov, Aleksander et al. (2011). "Nanoimprint patterning for tunable light trapping in large-area silicon solar cells". In: *Solar Energy Materials and Solar Cells* 95.10, pp. 2886–2892. DOI: 10.1016/j.solmat.2011.06.007. URL: http://linkinghub.elsevier.com/retrieve/pii/S0927024811003461.

Boer, Dick K. G. de et al. (2016). "Directional sideward emission from luminescent plasmonic nanostructures". In: *Optics Express* 24.2, A388. DOI: 10.1364/OE.24.00A388. URL: https://www.osapublishing.org/abstract.cfm?URI=oe-24-2-A388.

Bronstein, Noah Dylan (2015). "Material and Optical Design Rules for High Performance Luminescent Solar Concentrators". Thesis. University of California, Berkeley.

Bronstein, Noah D. et al. (2014). "Luminescent solar concentration with semiconductor nanorods and transfer-printed micro-silicon solar cells". In: *ACS Nano* 8.1. DOI: 10.1021/nn404418h.

Bronstein, Noah D. et al. (2015). "Quantum Dot Luminescent Concentrator Cavity Exhibiting 30-fold Concentration". In: *ACS Photonics* 2.11, pp. 1576–1583. DOI: 10.1021/acsphotonics.5b00334. URL: http://pubs.acs.org/doi/10.1021/acsphotonics.5b00334.

Buehlmann, P. et al. (2007). "In situ silicon oxide based intermediate reflector for thin-film silicon micromorph solar cells". In: *Applied Physics Letters* 9.143505, pp. 1–3. URL: http://scitation.aip.org/content/aip/journal/apl/91/14/10.1063/1.2794423.

Busch, K et al. (2007). *Periodic nanostructures for photonics*. DOI: 10.1016/j.physrep.2007.02.011. arXiv: NIHMS150003.

Callahan, DM, KAW Horowitz, and HA Atwater (2013). "Light trapping in ultrathin silicon photonic crystal superlattices with randomly-textured dielectric incouplers". In: *Optics Express* 21.25, pp. 4239–4245. DOI: 10.1364/OE.21.030315. URL: http://www.opticsinfobase.org/oe/fulltext.cfm?uri=oe-21-25-30315.

Callahan, DM, JN Munday, and HA Atwater (2012). "Solar cell light trapping beyond the ray optic limit". In: *Nano letters*. URL: http://pubs.acs.org/doi/abs/10.1021/nl203351k.

Campbell, Patrick and Martin a. Green (1987). "Light trapping properties of pyramidally textured surfaces". In: *Journal of Applied Physics* 62.1, p. 243. DOI: 10.1063/1.339189. URL: http://scitation.aip.org/content/aip/journal/jap/62/1/10.1063/1.339189.

Carlson, David E. and Christopher R. Wronski (2005). "Amorphous silicon solar cells". In: *Solar Cells* 671.August, pp. 217–251. DOI: 10.1016/B978-185617457-2/50010-X.

Chadha, Arvinder Singh, Weidong Zhou, and Eric D. Cline (2012). "Design criteria to optimize the near perfect anti-reflection coating". In: *Conference Record of the IEEE Photovoltaic Specialists Conference*, pp. 2521–2523. DOI: 10.1109/PVSC.2012.6318107.

Chattopadhyay, S. et al. (2010). "Anti-reflecting and photonic nanostructures". In: *Materials Science and Engineering R: Reports* 69.1-3, pp. 1–35. DOI: 10.1016/j.mser.2010.04.001. URL: http://dx.doi.org/10.1016/j.mser.2010.04.001.

Chen, J.Y. et al. (2011). "Biomimetic nanostructured antireflection coating and its application on crystalline silicon solar cells". In: *Optics Express* 19.15, p. 14411. DOI: 10.1364/OE.19.014411. URL: https://www.osapublishing.org/oe/abstract.cfm?uri=oe-19-15-14411.

Choi, Kiwoon et al. (2017). "Super-Antireflective Structure Films with Precisely Controlled Refractive Index Profile". In: *Advanced Optical Materials* 5.3. DOI: 10.1002/adom.201600616.

Colin, Clément et al. (2013). "Broadband light-trapping in ultra-thin nano-structured solar cells". In: ed. by Alexandre Freundlich and Jean-Francois Guillemoles. Vol. 8620, p. 86200C. DOI: 10.1117/12.2004269. URL: http://proceedings.spiedigitallibrary.org/proceeding.aspx?doi=10.1117/12.2004269.

Collins, R. W. and A. S. Ferlauto (2012). *Celebrating Employee Spotlight*.

Contreras, Miguel a. et al. (2002). "Optimization of CBD CdS process in high-efficiency Cu(In,Ga)Se2-based solar cells". In: *Thin Solid Films*. Vol. 403-404, pp. 204–211. DOI: 10.1016/S0040-6090(01)01538-3.

Curto, Alberto G et al. (2010). "Unidirectional emission of a quantum dot coupled to a nanoantenna." In: *Science (New York, N.Y.)* 329.5994, pp. 930–3. DOI: 10.1126/science.1191922. URL: http://www.ncbi.nlm.nih.gov/pubmed/20724630.

Dahan, N. et al. (2012). "Optical approaches to improve the photocurrent generation in Cu(In,Ga)Se2 solar cells with absorber thicknesses down to 0.5 μm". In: *Journal of Applied Physics* 112.9, p. 094902. DOI: 10.1063/1.4762004. URL: http://scitation.aip.org/content/aip/journal/jap/112/9/10.1063/1.4762004.

Dahiya, Ravinder, Gloria Gottardi, and Nadhira Laidani (2015). "PDMS residues-free micro/macrostructures on flexible substrates". In: *Microelectronic Engineering* 136, pp. 57–62. DOI: 10.1016/j.mee.2015.04.037. URL: https://www.sciencedirect.com/science/article/pii/S0167931715002488.

Debije, Michael G. and Paul P. C. Verbunt (2012). "Thirty Years of Luminescent Solar Concentrator Research: Solar Energy for the Built Environment". In: *Advanced Energy Materials* 2.1, pp. 12–35. DOI: 10.1002/aenm.201100554. URL: http://doi.wiley.com/10.1002/aenm.201100554.

Deceglie, Michael G et al. (2012). "Supplemental Information: Design of Nanostructured Solar Cells Using Coupled Optical and Electrical Modeling". In: *Nano Letters* 12.6, pp. 2894–2900. DOI: 10.1021/nl300483y. URL: http://www.ncbi.nlm.nih.gov/pubmed/22574816%20http://pubs.acs.org/doi/abs/10.1021/nl300483y.

Deceglie, Michael G. et al. (2013). "Accounting for Localized Defects in the Optoelectronic Design of Thin-Film Solar Cells". In: *IEEE Journal of Photovoltaics* 3.2, pp. 599–604. DOI: 10.1109/JPHOTOV.2013.2240764. URL: http://ieeexplore.ieee.org/lpdocs/epic03/wrapper.htm?arnumber=6450024.

Deckman, H. W. et al. (1983). "Optically enhanced amorphous silicon solar cells". In: *Applied Physics Letters* 42.11, pp. 968–970. DOI: 10.1063/1.93817.

Ding, Y and R Magnusson (2007). "Band gaps and leaky-wave effects in resonant photonic-crystal waveguides". In: *Optics Express* 15.2, p. 680. DOI: https://doi.10.1364/OE.15.000680. URL: https://www.osapublishing.org/oe/abstract.cfm?uri=oe-15-2-680.

Du, Qing Guo et al. (2011). "Enhanced optical absorption in nanopatterned silicon thin films with a nano-cone-hole structure for photovoltaic applications". In: *Optics Letters* 36.9, p. 1713. DOI: 10.1364/OL.36.001713. URL: https://www.osapublishing.org/ol/abstract.cfm?uri=ol-36-9-1713.

Edelenbosch, Oreane Y et al. (2013). "Luminescent solar concentrators with fiber geometry." In: *Optics express* 21 Suppl 3.May, A503–14. DOI: 10.1364/OE.21.00A503. URL: http://www.ncbi.nlm.nih.gov/pubmed/24104439.

Fader, R. et al. (2012). "Novel organic polymer for UV-enhanced substrate conformal imprint lithography". In: *Microelectronic Engineering* 98, pp. 238–241. DOI: 10.1016/j.mee.2012.07.010. URL: http://linkinghub.elsevier.com/retrieve/pii/S0167931712002924.

Faraon, Andrei et al. (2011). "Resonant enhancement of the zero-phonon emission from a colour centre in a diamond cavity". In: *Nature Photonics* 5.5, pp. 301–305. DOI: 10.1038/nphoton.2011.52. URL: http://www.nature.com/articles/nphoton.2011.52.

Fehrembach, Anne-Laure, Stefan Enoch, and Anne Sentenac (2001). "Highly directive light sources using two-dimensional photonic crystal slabs". In: *Applied Physics Letters* 79.26, pp. 4280–4282. DOI: 10.1063/1.1427423. URL: http://aip.scitation.org/doi/10.1063/1.1427423.

Ferlauto, a. S. et al. (2002). "Analytical model for the optical functions of amorphous semiconductors from the near-infrared to ultraviolet: Applications in thin film photovoltaics". In: *Journal of Applied Physics* 92.5, p. 2424. DOI: 10.1063/1.1497462. URL: http://scitation.aip.org/content/aip/journal/jap/92/5/10.1063/1.1497462.

Ferraro, Antonio et al. (2018). "Directional Emission of Fluorescent Dye-Doped Dielectric Nanogratings for Lighting Applications". In: *ACS Applied Materials and Interfaces* 10.29, pp. 24750–24757. DOI: 10.1021/acsami.8b08971.

Ferry, Vivian E (2011). "Light trapping in plasmonic solar cells". PhD thesis. California Institute of Technology. URL: http://www.ncbi.nlm.nih.gov/pubmed/20588593.

Ferry, Vivian E, Albert Polman, and Harry a Atwater (2011). "Modeling Light Trapping in Nanostructured Solar Cells". In: *ACS Nano* 5.12, pp. 10055–10064. DOI: 10.1021/nn203906t. URL: http://www.ncbi.nlm.nih.gov/pubmed/22082201%20http://pubs.acs.org/doi/abs/10.1021/nn203906t.

Fleischman, Dagny et al. (2019). "High Spectral Resolution Plasmonic Color Filters with Subwavelength Dimensions". In: DOI: http://dx.doi.org/10.1021/acsphotonics.8b01634.

Fontana, Yannik et al. (2012). "Mapping the directional emission of quasi-two-dimensional photonic crystals of semiconductor nanowires using Fourier microscopy". In: *Physical Review B* 86.24, p. 245303. DOI: 10.1103/PhysRevB.86.245303. URL: http://link.aps.org/doi/10.1103/PhysRevB.86.245303%20http://journals.aps.org/prb/abstract/10.1103/PhysRevB.86.245303.

Fountaine, Katherine T. and Harry a. Atwater (2014). "Mesoscale modeling of photoelectrochemical devices: light absorption and carrier collection in monolithic, tandem, Si|WO_3 microwires". In: *Optics Express* 22.S6, A1453. DOI: 10.1364/OE.22.0A1453. URL: http://www.opticsinfobase.org/abstract.cfm?URI=oe-22-S6-A1453%20https://www.osapublishing.org/oe/abstract.cfm?uri=oe-22-S6-A1453.

Fountaine, Katherine T., Christian G. Kendall, and Harry A. Atwater (2014). "Near-unity broadband absorption designs for semiconducting nanowire arrays via localized radial mode excitation". In: *Optics Express* 22.S3, A930. DOI: 10.1364/OE.22.00A930. URL: https://www.osapublishing.org/oe/abstract.cfm?uri=oe-22-S3-A930.

Fountaine, Katherine T., William S. Whitney, and Harry A. Atwater (2014). "Resonant absorption in semiconductor nanowires and nanowire arrays: Relating leaky waveguide modes to Bloch photonic crystal modes". In: *Journal of Applied Physics* 116.15, p. 153106. DOI: 10.1063/1.4898758. URL: http://dx.doi.org/10.1063/1.4898758%20http://aip.scitation.org/doi/10.1063/1.4898758.

Fountaine, Katherine T. et al. (2016). "Near-Unity Unselective Absorption in Sparse InP Nanowire Arrays". In: *ACS Photonics* 3.10, pp. 1826–1832. DOI: 10.1021/acsphotonics.6b00341.

Fritzsche, H. (1971). "Optical and electrical energy gaps in amorphous semiconductors". In: *Journal of Non-Crystalline Solids* 6.1, pp. 49–71. DOI: 10.1016/0022-3093(71)90015-9. URL: http://linkinghub.elsevier.com/retrieve/pii/0022309371900159.

Ganapati, Vidya, Myles A Steiner, and Eli Yablonovitch (2016). "The Voltage Boost Enabled by Luminescence Extraction in Solar Cells". In: *IEEE Journal of Photovoltaics* 99.4, pp. 1–9. DOI: 10.1109/JPHOTOV.2016.2547580. URL: http:

//ieeexplore.ieee.org/lpdocs/epic03/wrapper.htm?arnumber=7454706.

Gaponenko, Sergey V. (2010). *Introduction to Nanophotonics*. Cambridge University Press. DOI: https://doi.org/10.1017/CBO9780511750502.

Garcia, Damien (2011). "A fast all-in-one method for automated post-processing of PIV data". In: *Experiments in Fluids* 50.5, pp. 1247–1259. DOI: 10.1007/s00348-010-0985-y.

Gates, Byron D. and George M. Whitesides (2003). "Replication of Vertical Features Smaller than 2 nm by Soft Lithography". In: *Journal of the American Chemical Society* 125.49, pp. 14986–14987. DOI: 10.1021/ja0367647. URL: https://pubs.acs.org/doi/abs/10.1021/ja0367647.

Giebink, Noel C., Gary P. Wiederrecht, and Michael R. Wasielewski (2011). "Resonance-shifting to circumvent reabsorption loss in luminescent solar concentrators". In: *Nature Photonics* 5.11, pp. 694–701. DOI: 10.1038/nphoton.2011.236. URL: http://www.nature.com/doifinder/10.1038/nphoton.2011.236.

Glaeser, Gerda C and Uwe Rau (2006). "Collection and conversion properties of photovoltaic fluorescent collectors with photonic band stop filters". In: *Proceedings of SPIE* 6197, pp. 61970L–61970L–11. DOI: 10.1117/12.669638.

Gloeckler, M, A L Fahrenbruch, and J R Sites (2003). "Numerical modeling of CIGS and CdTe solar cells: setting the baseline". In: *Proceedings of 3rd World Conference onPhotovoltaic Energy Conversion*.

Gloeckler, Markus and James R Sites (2005). "Potential of submicrometer thickness Cu(In,Ga)Se2 solar cells". In: *Journal of Applied Physics* 98.10, p. 103703. DOI: 10.1063/1.2128054. URL: http://link.aip.org/link/JAPIAU/v98/i10/p103703/s1%7B%5C&%7DAgg=doi%20http://scitation.aip.org/content/aip/journal/jap/98/10/10.1063/1.2128054.

Goldschmidt, J C et al. (2010). "Increasing fluorescent concentrator light collection efficiency by restricting the angular emission characteristic of the incorporated luminescent material: the 'Nano-Fluko' concept". In: *Proceedings of SPIE* 7725.October, 77250S. DOI: 10.1117/12.854278. URL: http://link.aip.org/link/?PSI/7725/77250S/1.

Grandidier, Jonathan et al. (2013). "Solar cell efficiency enhancement via light trapping in printable resonant dielectric nanosphere arrays". In: *Physica Status Solidi (a)* 210.2, pp. 255–260. DOI: 10.1002/pssa.201228690. URL: http://doi.wiley.com/10.1002/pssa.201228690.

Grann, Eric B, M. G. Varga, and Drew A Pommet (1995). "Optimal design for antireflective tapered two-dimensional subwavelength grating structures". In: *Journal of the Optical Society of America A* 12.2, p. 333. DOI: 10.1364/JOSAA.12.000333.

Green, Martin A. (2007). "Thin-film solar cells: Review of materials, technologies and commercial status". In: *Journal of Materials Science: Materials in Electronics* 18.SUPPL. 1, pp. 15–19. DOI: 10.1007/s10854-007-9177-9.

Groep, Jorik van de, Pierpaolo Spinelli, and Albert Polman (2015). "Single-Step Soft-Imprinted Large-Area Nanopatterned Antireflection Coating". In: *Nano Letters* 15.6, pp. 4223–4228. DOI: 10.1021/acs.nanolett.5b01623. URL: http://pubs.acs.org/doi/abs/10.1021/acs.nanolett.5b01623.

Gunning, William J. et al. (1989). "Codeposition of continuous composition rugate filters". In: *Applied Optics* 28.14, p. 2945. DOI: 10.1364/AO.28.002945. URL: https://www.osapublishing.org/abstract.cfm?URI=ao-28-14-2945.

Gutmann, Johannes et al. (2011). "Towards photonic luminescent solar concentrators". In: *SPIE Solar Energy + Technology* 8111, 81110K–81110K–9. DOI: 10.1117/12.893104. URL: http://proceedings.spiedigitallibrary.org/proceeding.aspx?articleid=1272910.

Gutmann, Johannes et al. (2012). "Emission of Rhodamine B in PMMA opals for luminescent solar concentrators". In: *Proceedings of SPIE* 8438.October 2015, 84381O–84381O–7. DOI: 10.1117/12.922681. URL: https://proceedings.spiedigitallibrary.org/proceeding.aspx?doi=10.1117/12.922681.

Hsu, Hung Jung et al. (2014a). "Improved light management in a-Si:H/a-Si1-xGex:H tandem cells by employing multi-functional n-type microcrystalline silicon oxide". In: *Japanese Journal of Applied Physics*. Vol. 53, pp. 1–4. DOI: 10.7567/JJAP.53.05FV09.

Hsu, Hung-Jung (2016). "Development and Optimization of Hydrogenated Amorphous Silicon Germanium Thin-Film Solar Cells for Multi-junction Cell Applications". PhD thesis, p. 139.

Hsu, Hung-Jung et al. (2014b). "Optimization of a-Si 1– x Ge x :H single-junction and a-Si:H/a-Si 1– x Ge x :H tandem solar cells with enhanced optical management 1". In: *Canadian Journal of Physics* 92.November 2013, pp. 936–939. DOI: 10.1139/cjp-2013-0682. URL: http://www.nrcresearchpress.com/doi/abs/10.1139/cjp-2013-0682.

Huang, Yao-Wei et al. (2016). "Gate-Tunable Conducting Oxide Metasurfaces". In: *Nano Letters* 16.9, pp. 5319–5325. DOI: 10.1021/acs.nanolett.6b00555.

Hyun Lee, Sang et al. (2011). "Light confinement-induced antireflection of ZnO nanocones". In: *Applied Physics Letters* 99.15, p. 153113. DOI: 10.1063/1.3651751. URL: http://link.aip.org/link/APPLAB/v99/i15/p153113/s1%7B%5C&%7DAgg=doi%20http://aip.scitation.org/doi/10.1063/1.3651751.

IEA (2018). "World Energy Outlook 2018: Electricity". In: *Iea*. URL: https://www.iea.org/weo2018/electricity/.

Inc, Lumerical. *Absorption per unit volume: Advanced method*. URL: https://kb.lumerical.com/layout_analysis_pabs_adv.html.

– *Knowledge Base*. URL: https://lumerical.com/products/fdtd-solutions.

J. Griffiths, David (2014). *Introduction to Electrodynamics David J. Griffiths Fourth Edition*. Pearson. arXiv: arXiv:1011.1669v3.

Ji, Liming, Wook Jun Nam, and Stephen Fonash (2013). "Highly ordered nano-cone back reflector arrays for ultra-thin high performance CIGS cells". In: *Conference Record of the IEEE Photovoltaic Specialists Conference*. IEEE, pp. 1977–1979. DOI: 10.1109/PVSC.2013.6744858. URL: http://ieeexplore.ieee.org/lpdocs/epic03/wrapper.htm?arnumber=6744858.

Ji, Ran et al. (2010). "UV enhanced substrate conformal imprint lithography (UV-SCIL) technique for photonic crystals patterning in LED manufacturing". In: *Microelectronic Engineering* 87.5-8, pp. 963–967. DOI: 10.1016/j.mee.2009.11.134. URL: http://linkinghub.elsevier.com/retrieve/pii/S0167931709007990.

Jiao, Xiaojin and Steve Blair (2012). "Optical antenna design for fluorescence enhancement in the ultraviolet". In: *Optics Express* 20.28, p. 29909. DOI: 10.1364/OE.20.029909. URL: https://www.osapublishing.org/oe/abstract.cfm?uri=oe-20-28-29909.

Joannopoulos, John D. et al. (2008). *Photonic Crystals: Molding the Flow of Light - Second Edition*. REV - Revi. Princeton University Press. URL: http://ab-initio.mit.edu/book/.

Johnson, Steven G. and J. D. Joannopoulos (2001). "Block-iterative frequency-domain methods for Maxwell's equations in a planewave basis". In: *Opt. Express* 8.3, pp. 173–190. DOI: 10.1364/OE.8.000173. URL: http://www.opticsexpress.org/abstract.cfm?URI=oe-8-3-173.

Johnson, Steven G., Ardavan Oskooi, and Allen Taflove (2013). *Advances in FDTD Computational Electrodynamics: Photonics and Nanotechnology*. Norwood, MA: Artech House. URL: https://us.artechhouse.com/Advances-in-FDTD-Computational-Electrodynamics-P1567.aspx.

Kane Yee (1966). "Numerical solution of initial boundary value problems involving maxwell's equations in isotropic media". In: *IEEE Transactions on Antennas and Propagation* 14.3, pp. 302–307. DOI: 10.1109/TAP.1966.1138693. URL: http://ieeexplore.ieee.org/document/1138693/.

Kelzenberg, Michael D (2010a). "Silicon Microwire Photovoltaics". PhD thesis. California Institute of Technology. URL: https://thesis.library.caltech.edu/5938/.

Kelzenberg, Michael David (2010b). "Appendix B: Silicon Microwire Photovoltaics". PhD thesis. California Institute of Technology.

Kelzenberg, Michael D et al. (2010). "Enhanced absorption and carrier collection in Si wire arrays for photovoltaic applications". In: *Nature Materials* 9.4, pp. 368–368. DOI: 10.1038/nmat2727. URL: http://dx.doi.org/10.1038/nmat2635%20http://www.nature.com/doifinder/10.1038/nmat2727.

Kim, Seok-Soon et al. (2006). "Well-ordered TiO2 nanostructures fabricated using surface relief gratings on polymer films". In: *Journal of Materials Chemistry* 16.4, p. 370. DOI: 10.1039/b512104c. URL: http://xlink.rsc.org/?DOI=b512104c.

Kleiman, Maya, Keun Ah Ryu, and Aaron P. Esser-Kahn (2016). "Determination of Factors Influencing the Wet Etching of Polydimethylsiloxane Using Tetra-n-butylammonium Fluoride". In: *Macromolecular Chemistry and Physics* 217.2, pp. 284–291. DOI: 10.1002/macp.201500225.

Koenderink, A. Femius et al. (2006). "Spontaneous emission rates of dipoles in photonic crystal membranes". In: *Journal of the Optical Society of America B* 23.6, p. 1196. DOI: 10.1364/JOSAB.23.001196. arXiv: 0512120 [cond-mat]. URL: https://www.osapublishing.org/abstract.cfm?URI=josab-23-6-1196.

Kotipalli, R. et al. (2015). "Investigating the electronic properties of Al2O3/Cu(In,Ga)Se2 interface". In: *AIP Advances* 5.10, p. 107101. DOI: 10.1063/1.4932512. URL: http://scitation.aip.org/content/aip/journal/adva/5/10/10.1063/1.4932512%20http://dx.doi.org/10.1063/1.4932512.

Kumar, A. et al. (2011). "Direct metal nano-imprinting using an embossed solid electrolyte stamp". In: *Nanotechnology* 22.15. DOI: 10.1088/0957-4484/22/15/155302. arXiv: 1102.1945.

Lambertz, a., T. Grundler, and F. Finger (2011). "Hydrogenated amorphous silicon oxide containing a microcrystalline silicon phase and usage as an intermediate reflector in thin-film silicon solar cells". In: *Journal of Applied Physics* 109.11, p. 113109. DOI: 10.1063/1.3592208. URL: http://link.aip.org/link/JAPIAU/v109/i11/p113109/s1%7B%5C&%7DAgg=doi.

Lare, Claire van et al. (2015a). "Dielectric Scattering Patterns for Efficient Light Trapping in Thin-Film Solar Cells". In: *Nano Letters*, p. 150630085420008. DOI: 10.1021/nl5045583. URL: http://pubs.acs.org/doi/abs/10.1021/nl5045583.

Lare, Claire van et al. (2015b). "Light Coupling and Trapping in Ultrathin Cu(In,Ga)Se 2 Solar Cells Using Dielectric Scattering Patterns". In: *ACS Nano*. DOI: 10.1021/acsnano.5b04091. URL: http://pubs.acs.org/doi/10.1021/acsnano.5b04091.

Lare, M. van, F Lenzmann, and A Polman (2013). "Dielectric back scattering patterns for light trapping in thin-film Si solar cells". In: *Optics Express* 21.18, p. 20738. DOI: 10.1364/OE.21.020738. URL: http://www.opticsinfobase.org/abstract.cfm?uri=oe-21-18-20738.

Lare, M.-Claire van and Albert Polman (2015). "Optimized Scattering Power Spectral Density of Photovoltaic Light-Trapping Patterns". In: *ACS Photonics*, p. 150626105810001. DOI: 10.1021/ph500449v. URL: http://pubs.acs.org/doi/abs/10.1021/ph500449v.

Larouche, Stéphane and Ludvik Martinu (2008). "OpenFilters: open-source software for the design, optimization, and synthesis of optical filters." In: *Applied optics* 47.13, pp. C219–C230. DOI: 10.1364/AO.47.00C219.

Le Tarnec, Louis and Damien Garcia (2012). "Erratum: Robust smoothing of gridded data in one and higher dimensions with missing values (Computational Statistics and Data Analysis (2010) 54 1167-1178)". In: *Computational Statistics and Data Analysis* 56.6, p. 2182. DOI: 10.1016/j.csda.2011.12.001.

Lee, Jessamine Ng, Cheolmin Park, and George M. Whitesides (2003a). "Solvent Compatibility of Poly(dimethylsiloxane)-Based Microfluidic Devices". In: *Analytical Chemistry* 75.23, pp. 6544–6554. DOI: 10.1021/ac0346712. arXiv: arXiv:1011.1669v3. URL: https://pubs.acs.org/doi/full/10.1021/ac0346712?src=recsys.

– (2003b). "Solvent Compatibility of Poly(dimethylsiloxane)-Based Microfluidic Devices". In: *Analytical Chemistry* 75.23, pp. 6544–6554. DOI: 10.1021/ac0346712. arXiv: arXiv:1011.1669v3.

Li, Xiaofeng et al. (2011). "Bridging electromagnetic and carrier transport calculations for three-dimensional modelling of plasmonic solar cells." In: *Optics express* 19 Suppl 4.May, A888–A896. DOI: 10.1364/OE.19.00A888.

Liu, Victor and Shanhui Fan (2012). "S4: A free electromagnetic solver for layered periodic structures". In: *Computer Physics Communications* 183.10, pp. 2233–2244. DOI: 10.1016/j.cpc.2012.04.026. URL: http://dx.doi.org/10.1016/j.cpc.2012.04.026.

Markvart, T. (2006). "Detailed balance method for ideal single-stage fluorescent collectors". In: *Journal of Applied Physics* 99.2, p. 026101. DOI: 10.1063/1.2160710. URL: http://aip.scitation.org/doi/10.1063/1.2160710.

Masson-Delmotte V., et. al. and T. Waterfield (eds.) (2018). "2018 Summary for Policymakers in Global Warming of 1.5°C. An IPCC Special Report". In: p. 32. URL: https://www.ipcc.ch/sr15/chapter/summary-for-policy-makers/.

Meinardi, Francesco et al. (2014). "Large-area luminescent solar concentrators based on /'Stokes-shift-engineered/' nanocrystals in a mass-polymerized PMMA matrix". In: *Nat Photon* 8.5, pp. 392–399. DOI: 10.1038/nphoton.2014.54\rhttp://www.nature.com/nphoton/journal/v8/n5/abs/nphoton.2014.54.html#supplementary-information. URL: http://dx.doi.org/10.1038/nphoton.2014.54.

Meinardi, Francesco et al. (2015). "Highly efficient large-area colourless luminescent solar concentrators using heavy-metal-free colloidal quantum dots". In: *Nature Nanotechnology* 10.10, pp. 878–885. DOI: 10.1038/nnano.2015.178. URL: http://www.nature.com/doifinder/10.1038/nnano.2015.178.

Min, Wei-Lun, Bin Jiang, and Peng Jiang (2008). "Bioinspired Self-Cleaning Antireflection Coatings". In: *Advanced Materials* 20.20, pp. 3914–3918. DOI: 10.1002/adma.200800791. URL: http://doi.wiley.com/10.1002/adma.200800791.

Müller, Joachim et al. (2004). "TCO and light trapping in silicon thin film solar cells". In: *Solar Energy* 77.6, pp. 917–930. DOI: 10.1016/j.solener.2004.03.015. URL: http://linkinghub.elsevier.com/retrieve/pii/S0038092X04000647.

Munday, Jeremy N. (2012). "The effect of photonic bandgap materials on the Shockley-Queisser limit". In: *Journal of Applied Physics* 112.6, p. 064501. DOI: 10.1063/1.4742983. URL: http://scitation.aip.org/content/aip/journal/jap/112/6/10.1063/1.4742983.

Naghavi, N. et al. (2010). "Buffer layers and transparent conducting oxides for chalcopyrite Cu(In,Ga)(S,Se)2 based thin film photovoltaics: Present status and current developments". In: *Progress in Photovoltaics: Research and Applications* 18.6, pp. 411–433. DOI: 10.1002/pip.955.

Nakagawa, Yasuhiko, Mitsuhiro Gunzi, and Shouzi Kakio (1998). "Related content Fabrication and Characterization of Diffraction Gratings Using Photosensitive Al2O3 Gel Films". In: *Japanese Journal of Applied Physics* 37.4R, p. 1842. URL: http://iopscience.iop.org/article/10.1143/JJAP.37.1842/meta.

Needell, David R. et al. (2018). "Design Criteria for Micro-Optical Tandem Luminescent Solar Concentrators". In: *IEEE Journal of Photovoltaics* 8.6, pp. 1560–1567. DOI: 10.1109/JPHOTOV.2018.2861751. arXiv: 1710.00034. URL: https://ieeexplore.ieee.org/document/8432067/.

Nikolaev, Ivan S., Willem L. Vos, and a. Femius Koenderink (2009). "Accurate calculation of the local density of optical states in inverse-opal photonic crystals". In: *Journal of the Optical Society of America B* 26.5, p. 987. DOI: 10.1364/JOSAB.26.000987. URL: http://www.opticsinfobase.org/abstract.cfm?URI=josab-26-5-987.

Novotny, Lukas and Bert Hecht (2006). *Principles of Nano-Optics*. Cambridge University Press. DOI: https://doi.org/10.1017/CBO9780511813535.

Oreskes, Naomi (2004). "The Scientific Consensus on Climate Change". In: *Science* 306.5702, pp. 1686–1686. DOI: 10.1126/science.1103618. eprint: https://science.sciencemag.org/content/306/5702/1686.full.pdf. URL: https://science.sciencemag.org/content/306/5702/1686.

Orgassa, K., H.W. Schock, and J.H. Werner (2003). "Alternative back contact materials for thin film Cu(In,Ga)Se2 solar cells". In: *Thin Solid Films* 431-432.03, pp. 387–391. DOI: 10.1016/S0040-6090(03)00257-8. URL: http://linkinghub.elsevier.com/retrieve/pii/S0040609003002578.

Oskooi, Ardavan et al. (2012). "Partially disordered photonic-crystal thin films for enhanced and robust photovoltaics". In: *Applied Physics Letters* 100.18, p. 181110. DOI: 10.1063/1.4711144. URL: http://link.aip.org/link/APPLAB/v100/i18/p181110/s1%7B%5C&%7DAgg=doi.

Papakonstantinou, Ioannis and Clemens Tummeltshammer (2015). "Fundamental limits of concentration in luminescent solar concentrators revised: the effect of reabsorption and nonunity quantum yield". In: *Optica* 2.10, p. 841. DOI: 10.1364/OPTICA.2.000841. URL: http://www.osapublishing.org/viewmedia.cfm?uri=optica-2-10-841%7B%5C&%7Dseq=0%7B%5C&%7Dhtml=true.

Peter Amalathas, Amalraj and Maan M. Alkaisi (2017). "Efficient light trapping nanopyramid structures for solar cells patterned using UV nanoimprint lithography". In: *Materials Science in Semiconductor Processing* 57.January, pp. 54–58. DOI: 10.1016/j.mssp.2016.09.032. URL: http://dx.doi.org/10.1016/j.mssp.2016.09.032.

Peters, Marius, Jan Christoph Goldschmidt, and Benedikt Bl??si (2010). "Angular confinement and concentration in photovoltaic converters". In: *Solar Energy Materials and Solar Cells* 94.8, pp. 1393–1398. DOI: 10.1016/j.solmat.2010.04.009.

Petrol, British (2018). *67th BP Statistical Review of World Energy*. Tech. rep., pp. 1–56.

Poitras, Daniel and J a Dobrowolski (2004). "Toward perfect antireflection coatings. 2. Theory." In: *Applied optics* 43.6, pp. 1286–1295. DOI: 10.1364/AO.43.001286.

Radha, Boya et al. (2013). "Metal hierarchical patterning by direct nanoimprint lithography." In: *Scientific reports* 3, p. 1078. DOI: 10.1038/srep01078. URL: http://www.pubmedcentral.nih.gov/articlerender.fcgi?artid=3584315%7B%5C&%7Dtool=pmcentrez%7B%5C&%7Drendertype=abstract.

Rau, Uwe, Florian Einsele, and Gerda C. Glaeser (2005). "Efficiency limits of photovoltaic fluorescent collectors". In: *Applied Physics Letters* 87.17, pp. 1–3. DOI: 10.1063/1.2112196.

Rau, Uwe, Ulrich W. Paetzold, and Thomas Kirchartz (2014). "Thermodynamics of light management in photovoltaic devices". In: *Physical Review B* 90.3, p. 035211. DOI: 10.1103/PhysRevB.90.035211. URL: http://link.aps.org/doi/10.1103/PhysRevB.90.035211.

Reisfeld, R (2001). "Prospects of sol ± gel technology towards luminescent materials". In: *Optical Materials* 16, pp. 1–7.

Repins, Ingrid et al. (2009). "Required Material Properties for High-Efficiency CIGS Modules". In: ed. by Alan E. Delahoy and Louay A. Eldada. July, pp. 74090M–74090M–14. DOI: 10.1117/12.828365. URL: http://proceedings.spiedigitallibrary.org/proceeding.aspx?articleid=1340399.

Rosenzweig, Cynthia et al. (2008). "Attributing physical and biological impacts to anthropogenic climate change". In: *Nature* 453.7193, pp. 353–357. DOI: 10.1038/nature06937. URL: http://www.nature.com/articles/nature06937.

Rousseau, I. and V. Wood (2013). "Nanophotonic luminescent solar concentrators". In: *Applied Physics Letters* 103.13, p. 131113. DOI: 10.1063/1.4823538. URL: http://scitation.aip.org/content/aip/journal/apl/103/13/10.1063/1.4823538.

Russell, KJ et al. (2012). "Large spontaneous emission enhancement in plasmonic nanocavities". In: *Nature Photonics* 6.July. DOI: 10.1038/NPHOTON.2012.112. URL: http://www.nature.com/nphoton/journal/v6/n7/abs/nphoton.2012.112.html.

Saive, Rebecca, Colton R. Bukowsky, and Harry A. Atwater (2017). "Three-dimensional nanoimprint lithography using two-photon lithography master samples". In: pp. 1–4. arXiv: 1702.04012. URL: http://arxiv.org/abs/1702.04012.

Saive, Rebecca et al. (2016a). "Effectively Transparent Front Contacts for Optoelectronic Devices". In: *Advanced Optical Materials*, pp. 1470–1474. DOI: 10.1002/adom.201600252.

– (2016b). "Effectively Transparent Front Contacts for Optoelectronic Devices". In: *Advanced Optical Materials* 4.10, pp. 1470–1474. DOI: 10.1002/adom.201600252.

Saive, Rebecca et al. (2017a). "Silicon heterojunction solar cells with effectively transparent front contacts". In: *Sustainable Energy & Fuels* 1.3, pp. 593–598. DOI: http://dx.doi.org/10.1039/C7SE00096K.

– (2017b). "Silicon heterojunction solar cells with effectively transparent front contacts". In: *Sustainable Energy & Fuels* 1.3, pp. 593–598. DOI: 10.1039/C7SE00096K. URL: http://xlink.rsc.org/?DOI=C7SE00096K.

Saive, Rebecca et al. (2018). "Effectively transparent contacts (ETCs) for solar cells". In: *2017 IEEE 44th Photovoltaic Specialist Conference, PVSC 2017* 2016-Novem, pp. 1–4. DOI: 10.1109/PVSC.2017.8366859.

Sang, Boasheng et al. (2014). *Nanostructured CIGS Absorber Surface for Enhanced Light Trapping*. URL: https://patentscope.wipo.int/search/en/WO2014028542.

Sark, Wilfried G J H M van et al. (2008a). "Luminescent Solar Concentrators–a review of recent results." In: *Optics express* 16.26, pp. 21773–21792. DOI: 10.1364/OE.16.021773.

Sark, Wilfried G.J.H.M. van et al. (2008b). "Luminescent Solar Concentrators - A review of recent results". In: *Optics Express* 16.26, p. 21773. DOI: 10.1364/OE.16.021773. URL: http://www.osapublishing.org/viewmedia.cfm?uri=oe-16-26-21773%7B%5C&%7Dseq=0%7B%5C&%7Dhtml=true.

Schropp, R. E I et al. (2009). "Nanostructured thin films for multibandgap silicon triple junction solar cells". In: *Solar Energy Materials and Solar Cells* 93.6-7, pp. 1129–1133. DOI: 10.1016/j.solmat.2009.02.010.

Shah, Arvind (2010). *Thin-Film Silicon Solar Cells*. Ed. by Arvind Shah. EPFL Press. DOI: 10.1201/b16327. URL: https://www.taylorfrancis.com/books/9781439808108.

Sharma, K. K. (2006). *Optics: Principles and Applications*. Elsevier Academic Press.

Sharma, Manoj et al. (2017). "Near-Unity Emitting Copper-Doped Colloidal Semiconductor Quantum Wells for Luminescent Solar Concentrators". In: *Advanced Materials* 29.30, p. 1700821. DOI: 10.1002/adma.201700821. arXiv: 1606.06523. URL: http://doi.wiley.com/10.1002/adma.201700821.

Shockley, William and Hans J. Queisser (1961a). "Detailed Balance Limit of Efficiency of p−n Junction Solar Cells". In: *Journal of Applied Physics* 32.3, pp. 510–519. DOI: 10.1063/1.1736034. URL: http://aip.scitation.org/doi/10.1063/1.1736034.

– (1961b). "Detailed Balance Limit of Efficiency of p-n Junction Solar Cells". In: *Journal of Applied Physics* 32.3, p. 510. DOI: 10.1063/1.1736034. URL: http://scitation.aip.org/content/aip/journal/jap/32/3/10.1063/1.1736034.

Smestad, G. et al. (1990). "The thermodynamic limits of light concentrators". In: *Solar Energy Materials* 21.2-3, pp. 99–111. DOI: 10.1016/0165-1633(90)90047-5. URL: http://www.sciencedirect.com/science/article/pii/0165163390900475.

Solano, Manuel et al. (2013). "Optimization of the absorption efficiency of an amorphous-silicon thin-film tandem solar cell backed by a metallic surface-relief grating." In: *Applied optics* 52.5, pp. 966–79. URL: http://www.ncbi.nlm.nih.gov/pubmed/23400058.

Sopra Materials Database. URL: http://www.filmetrics.com/refractive-index-database/Mo/Molybdenum.

Staebler, D. L. and C. R. Wronski (1977). "Reversible conductivity changes in discharge−produced amorphous Si". In: *Applied Physics Letters* 31.4, pp. 292–294. DOI: 10.1063/1.89674. arXiv: arXiv:1410.7495. URL: http://aip.scitation.org/doi/10.1063/1.89674.

Stanbery, Billy J. (2002). “Copper Indium Selenides and Related Materials for Photovoltaic Devices”. In: *Critical Reviews in Solid State and Materials Sciences* 27.2, pp. 73–117. DOI: 10.1080/20014091104215. URL: http://www.tandfonline.com/doi/abs/10.1080/20014091104215.

Statement, Joint (2001). “The Science of Climate Change”. In: *Science* 292.5520, pp. 1261–1261. DOI: 10.1126/science.292.5520.1261. eprint: https://science.sciencemag.org/content. URL: https://science.sciencemag.org/content/292/5520/1261.

Steltenpool, M. et al. (2012). “PERIODIC TEXTURED SUBSTRATE BY NANO-IMPRINT TECHNOLOGY WITH THIN TCO LAYER FOR INCREASED LIGHT-TRAPPING IN THIN-FILM SILICON SOLAR CELLS”. In: *Proceedings of 27th European Photovoltaic Solar Energy Conference and Exhibition*, pp. 2123–2128.

Stokes, G. G. (1853). “On the Change of Refrangibility of Light. No. II”. In: *Philosophical Transactions of the Royal Society of London* 143.June 1848, pp. 385–396. DOI: 10.1098/rstl.1853.0016. arXiv: arXiv:1011.1669v3. URL: https://royalsocietypublishing.org/doi/pdf/10.1098/rstl.1852.0022%20http://www.royalsocietypublishing.org/doi/10.1098/rstl.1852.0022%20http://rstl.royalsocietypublishing.org/cgi/doi/10.1098/rstl.1853.0016.

Stuart, HR and DG Hall (1997). “Thermodynamic limit to light trapping in thin planar structures”. In: *JOSA A* 14.11, pp. 3001–3008. URL: http://www.opticsinfobase.org/abstract.cfm?uri=josaa-14-11-3001.

Stuckelberger, Michael et al. (2017). “Review: Progress in solar cells from hydrogenated amorphous silicon”. In: *Renewable and Sustainable Energy Reviews* 76.June 2016, pp. 1497–1523. DOI: 10.1016/j.rser.2016.11.190. URL: http://dx.doi.org/10.1016/j.rser.2016.11.190.

Sze, S.M. and K.K. Ng (2006). *Physics of Semiconductor Devices*. Wiley. URL: https://books.google.com/books?id=o4unkmHBHb8C.

Tadanaga, K. et al. (1995). “Microstructure of Al2O3 xerogels and aerogels from aluminium-tri-sec-butoxide modified with ethylacetoacetate”. In: *Journal of the Ceramic Society of Japan* 103.6, pp. 582–585. DOI: 10.2109/jcersj.103.582. URL: http://cat.inist.fr/?aModele=afficheN%7B%5C&%7Dcpsidt=3633372.

Takayama, Shuichi et al. (2001). “Topographical micropatterning of poly(dimethylsiloxane) using laminar flows of liquids in capillaries”. In: *Advanced Materials* 13.8, pp. 570–574. DOI: 10.1002/1521-4095(200104)13:8<570::AID-ADMA570>3.0.CO;2-B.

Tang, Yu-Hsiang et al. (2012). “Fabrication of Nanocone Subwavelength Antireflection Structures on Quartz Substrates”. In: *Japanese Journal of Applied Physics*

51, 06FF06. DOI: 10.1143/JJAP.51.06FF06. URL: http://stacks.iop.org/1347-4065/51/06FF06.

Tauc, J. (1974). *Amorphous and Liquid Semiconductors*. Ed. by J Tauc. Boston, MA: Springer US, p. 176. DOI: 10.1007/978-1-4615-8705-7. URL: http://link.springer.com/10.1007/978-1-4615-8705-7.

Tavakoli, Mohammad Mahdi et al. (2015). "Highly Efficient Flexible Perovskite Solar Cells with Antireflection and Self-Cleaning Nanostructures". In: *ACS Nano* 9.10, pp. 10287–10295. DOI: 10.1021/acsnano.5b04284. URL: http://pubs.acs.org/doi/10.1021/acsnano.5b04284.

Tiedje, T and E Yablonovitch (1984). "Limiting efficiency of silicon solar cells". In: *Electron Devices, IEEE ...* 5, pp. 711–716. URL: http://ieeexplore.ieee.org/xpls/abs%7B%5C_%7Dall.jsp?arnumber=1483879.

Treharne, R E et al. (2011). "Optical Design and Fabrication of Fully Sputtered CdTe/CdS Solar Cells". In: *Journal of Physics: Conference Series* 286, p. 012038. DOI: 10.1088/1742-6596/286/1/012038. URL: http://stacks.iop.org/1742-6596/286/i=1/a=012038?key=crossref.f72fda0fcf5aa2cd75968988273f5ce4.

Tsakmakidis, Kosmas L et al. (2016). "Large spontaneous-emission enhancements in metallic nanostructures: towards LEDs faster than lasers". In: *Opt Express* 24.16, pp. 17916–17927. DOI: 10.1364/oe.24.017916. URL: http://www.opticsexpress.org/abstract.cfm?URI=oe-24-16-17916%7B%5C%%7D5Cnhttps://www.osapublishing.org/DirectPDFAccess/68BC48BB-081C-C550-54AA078C6EE31E0C%7B%5C_%7D348138/oe-24-16-17916.pdf?da=1%7B%5C&%7Did=348138%7B%5C&%7Dseq=0%7B%5C&%7Dmobile=no.

Tsui, Kwong-Hoi et al. (2014). "Low-Cost, Flexible, and Self-Cleaning 3D Nanocone Anti-Reflection Films for High-Efficiency Photovoltaics". In: *Advanced Materials* 26.18, pp. 2805–2811. DOI: 10.1002/adma.201304938. URL: http://doi.wiley.com/10.1002/adma.201304938.

Vermang, Bart et al. (2013). "Development of rear surface passivated Cu(In,Ga)Se2 thin film solar cells with nano-sized local rear point contacts". In: *Solar Energy Materials and Solar Cells* 117, pp. 505–511. DOI: 10.1016/j.solmat.2013.07.025. URL: http://linkinghub.elsevier.com/retrieve/pii/S0927024813003711.

Vermang, Bart et al. (2014a). "Employing Si solar cell technology to increase efficiency of ultra-thin Cu(In,Ga)Se 2 solar cells". In: *Progress in Photovoltaics: Research and Applications* 22.10, pp. 1023–1029. DOI: 10.1002/pip.2527. URL: http://dx.doi.org/10.1002/pip.1160%20http://doi.wiley.com/10.1002/pip.2527.

Vermang, Bart et al. (2014b). "Introduction of Si PERC rear contacting design to boost efficiency of Cu(In,Ga)Se2solar cells". In: *IEEE Journal of Photovoltaics* 4.6, pp. 1644–1649. DOI: 10.1109/JPHOTOV.2014.2350696.

Vermang, Bart et al. (2015). "Highly reflective rear surface passivation design for ultra-thin Cu(In,Ga)Se2 solar cells". In: *Thin Solid Films* 582, pp. 300–303. DOI: 10.1016/j.tsf.2014.10.050. URL: http://linkinghub.elsevier.com/retrieve/pii/S0040609014010116.

Verschuuren, M and HV Sprang (2007). "3D photonic structures by sol-gel imprint lithography". In: *MRS Proceedings* 1002.mailstop 12, pp. 1–6. URL: http://journals.cambridge.org/abstract%7B%5C_%7DS1946427400596456.

Verschuuren, Marcus Antonius (2010). "Substrate Conformal Imprint Lithography for Nanophotonics". Doctorate. Utrecht University.

Wang, Ken Xingze et al. (2012). "Absorption Enhancement in Ultrathin Crystalline Silicon Solar Cells with Antireflection and Light-Trapping Nanocone Gratings". In: *Nano Letters* 12.3, pp. 1616–1619. DOI: 10.1021/nl204550q. URL: http://www.ncbi.nlm.nih.gov/pubmed/22356436%20http://pubs.acs.org/doi/10.1021/nl204550q.

Wang, Ken Xingze et al. (2014). "Light trapping in photonic crystals". In: *Energy & Environmental Science* 7.8, p. 2725. DOI: 10.1039/C4EE00839A. URL: http://xlink.rsc.org/?DOI=C4EE00839A.

Wang, Peng and Rajesh Menon (2013). "Optimization of periodic nanostructures for enhanced light-trapping in ultra-thin photovoltaics". In: *Optics Express* 21.5, p. 6274. DOI: 10.1364/OE.21.006274. URL: http://www.ncbi.nlm.nih.gov/pubmed/23482196%20https://www.osapublishing.org/oe/abstract.cfm?uri=oe-21-5-6274.

Wang, Shujie et al. (2018). "Enhanced light out-coupling efficiency of quantum dot light emitting diodes by nanoimprint lithography". In: *Nanoscale* 10.24, pp. 11651–11656. DOI: 10.1039/C8NR02082E. URL: http://xlink.rsc.org/?DOI=C8NR02082E.

Wang, X.J. and M.K. Lei (2005). "Preparation and photoluminescence of Er3+-doped Al2O3 films by sol–gel method". In: *Thin Solid Films* 476.1, pp. 41–45. DOI: 10.1016/j.tsf.2004.08.169. URL: http://linkinghub.elsevier.com/retrieve/pii/S0040609004013215.

Whitesell, Kelsey a., Dennis M. Callahan, and Harry Atwater (2013). "Silicon solar cell light-trapping using defect mode photonic crystals". In: *IEEE Proceedings of PVSC*. Ed. by Alexandre Freundlich and Jean-Francois Guillemoles. Vol. 8620, p. 86200D. DOI: 10.1117/12.2005450. URL: http://proceedings.spiedigitallibrary.org/proceeding.aspx?doi=10.1117/12.2005450.

Wu, Qiang et al. (2018). "Directional emission of plastic luminescent films using photonic crystals fabricated by soft-X-ray interference lithography and reactive ion etching". In: *Scientific Reports* 8.1, p. 9254. DOI: 10.1038/s41598-018-27593-w. URL: http://www.nature.com/articles/s41598-018-27593-w.

Würfel, P. and U. Würfel (2016). *Physics of Solar Cells: From Basic Principles to Advanced Concepts*. Wiley. URL: https://books.google.com/books?id=009hDAAAQBAJ.

Xu, Lu et al. (2016). "Enhanced Photon Collection in Luminescent Solar Concentrators with Distributed Bragg Reflectors". In: *ACS Photonics* 3.2, pp. 278–285. DOI: 10.1021/acsphotonics.5b00630.

Xu, Yunlu, Tao Gong, and Jeremy N. Munday (2015). "The generalized Shockley-Queisser limit for nanostructured solar cells". In: *Scientific Reports* 5, p. 13536. DOI: 10.1038/srep13536. URL: http://www.nature.com/doifinder/10.1038/srep13536%20http://www.nature.com/articles/srep13536.

Yablonovitch, E. and G.D. Cody (1982). "Intensity enhancement in textured optical sheets for solar cells". In: *IEEE Transactions on Electron Devices* 29.2, pp. 300–305. DOI: 10.1109/T-ED.1982.20700. URL: http://ieeexplore.ieee.org/document/1482197/.

Yablonovitch, Eli (1980). "Thermodynamics of the fluorescent planar concentrator". In: *Journal of the Optical Society of America* 70.11, p. 1362. DOI: 10.1364/JOSA.70.001362.

– (1982). "Statistical ray optics". In: *Journal of the Optical Society of America* 72.7, p. 899. DOI: 10.1364/JOSA.72.000899. URL: http://www.opticsinfobase.org/abstract.cfm?URI=josa-72-7-899%20http://www.opticsinfobase.org/abstract.cfm?uri=josa-72-7-899%20https://www.osapublishing.org/abstract.cfm?URI=josa-72-7-899.

Yalamanchili, Sisir et al. (2016). "Enhanced Absorption and less than 1% Spectrum-and-Angle-Averaged Reflection in Tapered Microwire Arrays". In: *ACS Photonics* 3.10, pp. 1854–1861. DOI: 10.1021/acsphotonics.6b00370.

Yalamanchili, Sisir et al. (2018). "Highly absorbing and high lifetime tapered silicon microwire arrays as an alternative for thin film crystalline silicon solar cells". In: *2017 IEEE 44th Photovoltaic Specialist Conference, PVSC 2017*. IEEE, pp. 1–5. DOI: 10.1109/PVSC.2017.8366710. URL: http://ieeexplore.ieee.org/document/7750213/.

Yang, Chongyin et al. (2011). "Intrinsic ZnO films fabricated by DC sputtering from oxygen-def icient targets for Cu (In, Ga) Se2 solar cell application". In: *Chinese Optics Letters* 9.10, pp. 2–5. DOI: 10.3788/COL201109.103102.High. URL: http://www.opticsinfobase.org/abstract.cfm?uri=col-9-10-103102.

Yang, L et al. (2013). "Optimal design of ultra−broadband, omnidirectional, and polarization−insensitive amorphous silicon solar cells with a core−shell nanograting structure". In: *Progress in Photovoltaics: . . .* April 2012, pp. 1077–1086. DOI: 10.1002/pip. URL: http://onlinelibrary.wiley.com/doi/10.1002/pip.2206/full.

Yoon, Kyung min, Ki yeon Yang, and Heon Lee (2009). "Fabrication of polycrystalline TiO2 nanopatterns by TiO2 sol base imprint lithography". In: *Thin Solid Films* 518.1, pp. 126–129. DOI: 10.1016/j.tsf.2009.07.056.

Yu, Chen Chieh and Hsuen Li Chen (2015). "Nanoimprint technology for patterning functional materials and its applications". In: *Microelectronic Engineering* 132, pp. 98–119. DOI: 10.1016/j.mee.2014.10.015. URL: http://dx.doi.org/10.1016/j.mee.2014.10.015.

Yu, Chen-chieh and Hsuen-li Chen (2014). "Nanoimprint technology for patterning functional materials and its applications". In: *Microelectronic Engineering* 132, pp. 98–119. DOI: 10.1016/j.mee.2014.10.015. URL: http://linkinghub.elsevier.com/retrieve/pii/S016793171400447X.

Yu, Zongfu, Aaswath Raman, and Shanhui Fan (2010). "Limit of nanophotonic light-trapping in solar cells". In: *Conference Record of the IEEE Photovoltaic Specialists Conference* 18.September, pp. 76–78. DOI: 10.1109/PVSC.2010.5614248. arXiv: 1004.2902.

Yu, Zongfu, Sunil Sandhu, and Shanhui Fan (2014). "Efficiency above the Shockley–Queisser Limit by Using Nanophotonic Effects To Create Multiple Effective Bandgaps With a Single Semiconductor". In: *Nano Letters* 14.1, pp. 66–70. DOI: 10.1021/nl403653j. URL: http://pubs.acs.org/doi/abs/10.1021/nl403653j.

Yue, Qingyang et al. (2014). "Analysis on the light-extraction efficiency of GaN-based light-emitting diodes with deep-hole amorphous photonic crystals structures". In: *IEEE/OSA Journal of Display Technology* 10.12, pp. 1070–1077. DOI: 10.1109/JDT.2014.2342272. arXiv: AP.53.012301.

Zangwill, Andrew (2012). *Modern Electrodynamics*. First. Cambridge University Press. DOI: 10.1017/CBO9781139034777. URL: https://www.cambridge.org/core/product/identifier/9781139034777/type/book.

– (2013). *Modern electrodynamics*. Cambridge: Cambridge Univ. Press.

Zelsmann, M. et al. (2003). "Seventy-fold enhancement of light extraction from a defectless photonic crystal made on silicon-on-insulator". In: *Applied Physics Letters* 83.13, pp. 2542–2544. DOI: 10.1063/1.1614832.

Zhao, G and N Tohge (1995). "Patterning Films of Al2O3 Chemically Gaoyang Thin Modified Films by the Photolysis of Gel with Benzoylacetone". In: *Journal of the Ceramic Society of Japan* 1296.103, pp. 1293–1296. DOI: doi.org/10.2109/jcersj.103.1293.

Zhu, Jia et al. (2010). "Nanodome solar cells with efficient light management and self-cleaning." In: *Nano letters* 10.6, pp. 1979–84. DOI: 10.1021/nl9034237. URL: http://www.ncbi.nlm.nih.gov/pubmed/19891462.

Appendices

Appendix A

SPATIAL & ANGLE RESOLVED CONFOCAL SPECTRAL LASER MICROSCOPY (SARP OR SARCSLM)

A.1 Standard Beam Configuration

An NKT SuperK Extreme 20 W white laser is aligned parallel to an optical table surface and then focused on the slit of a Oriel 77770 1/4 m monochromator with an achromatic doublet f_l = 40 mm planoconvex lens after passing through an optical chopper wheel (variable frequency from 50 Hz - 10 kHz depending on installed wheel). The white light is expanded after passing the slit, redirected, and collimated via an elliptic mirror. The light see a ruled diffraction grating with either 2400 lines/mm, 1200 lines/mm, or 600 lines/mm and is dispersed onto a second elliptic lens. Each wavelength forms an image of the entrance slit on a second exit slit. The wavelength is selected from the diffracted rays by controlling the width of the exit slit from 30 µm to 2000 µm, determining the bandpass width. The monochromator minimum bandpass is a function of the leading optics alignment and aberrations; it is estimated to be less than 1nm. Finally, an automated filter wheel (not shown) is used to pass only the first order grating diffractions beyond 750 nm. A polarizing wire grid filter can be placed immediately after the exit slit and filter wheel (not shown). A reference diode is placed at the exit slit, using a glass slide to sample 5% of the photocurrent output. This allows adjustment of measured responses over time, acting as a calibration factor. The polarizer placement before the reference diode helps to reduce noise by better equalizing the fraction of sampled power to power that reaches the sample, rather than including a large fraction that will not see the sample. In general the best placement for the reference diode would

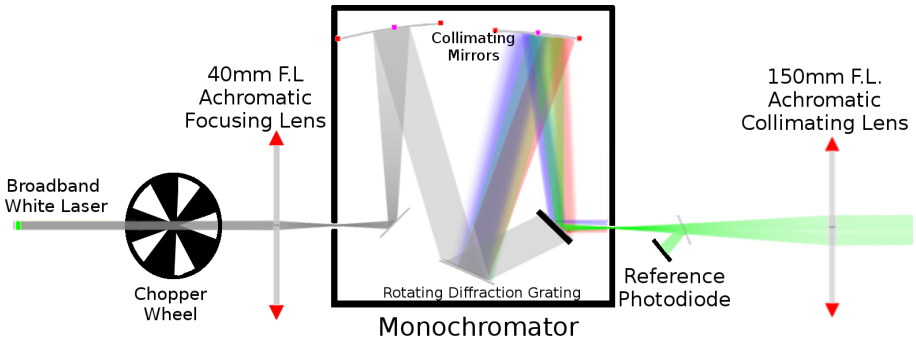

Figure A.1: The initial laser path common to all measurement configurations.

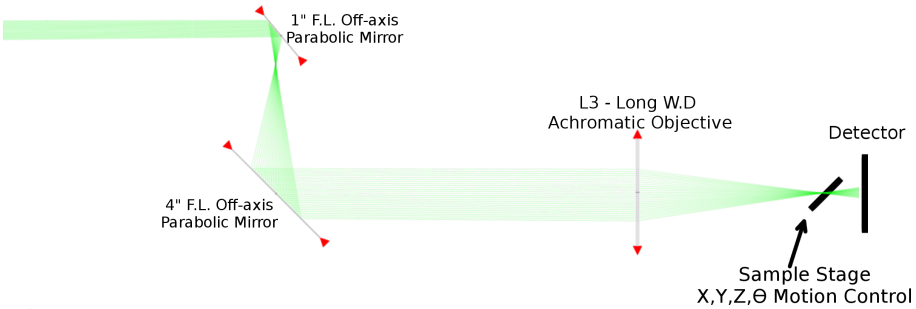

Figure A.2: The standard beam path for spatial, angle, and spectrally resolved laser microscopy measurements.

be just prior to the sample, however, due to the priority of beam line flexibility, it is placed early in the beam line. A 2 inch achromatic doublet lens of $f_l = 150\,\text{mm}$ is mounted on a flip-mount, allowing it to be used as an option for more power down the beam path. This lens was aligned to collimate light over a length greater than 1 m, approaching 2 m. This was determined by measuring the spot size just after and at the end of the beam path, both being roughy 4 mm.

The monochromatic beam (collimated or expanding) impinges upon a $\frac{1}{2}$ inch diameter off-axis parabolic mirror, sampling the least divergent center of the beam, focusing it 90° off the initial axis to a point 1 inch away. The beam expands over the next 4 inches before striking a second off-axis parabolic mirror, 2 inches in diameter, $f_l = 4^{"}$. After expansion, the beam is extremely collimated, enabling near diffraction limited measurements. Again, an number of optional optical components (not shown) can be inserted at this point including neutral density filters, beam splitters for white light sample illumination, apertures, and a beam splitter enabling camera (IDS UI-1460SE) viewing of the sample an laser down the beamline. This monochromatic beam can be used as is for illumination of large area samples. The beamline was designed and collimated for long working distance objective lenses to be placed before a sample. A detector can be placed behind a sample for transmission measurements, in front of the sample with the use of a beam splitter for normal incidence reflection measurements, or the sample itself can be the detector, common for many devices measured such as micro solar cells.

The objective holder is mounted on 2 computer controlled micro positioning stages (Newport M-VP-25XA) with a minimum step of 100 nm, allowing 25 mm translation of the objective in along the axis along the beamline (Z1) and perpendicular to the beamline, parallel to the table surface (X1). The sample is mounted on a second set of four micro positioning stages: an axis normal to the plane of the table (Y1), a

rotational axis around the table normal direction θ, a second axis perpendicular to the beamline and parallel to the table (X2), and a second axis to translate the sample along the beamline (Z2) (Newport M-VP-25XA, Newport URS75BCC, Newport M-VP-25XA, micro positioning stage with Thorlabs Z825B 25 actuator stages, respectively). The first two motion controllers, Z1 and X1, allow for calibration and correction of chromatic and mechanical aberrations at the back-focal plane of the objective on a sub-micron scale. The Y1 stage allows for both translation and aberration correction along its axis. The θ rotational axis allows for sample rotation about a eucentric axis intersecting the beam line, enabling a feature uncommon in many optical microscopes. Finally, the redundant X2 and Z2 axes allow for sample translation over long distances giving greater range of sample and scan sizes. This allows the aberration correcting stages to not force the objective to focus different portions of the laser spot reaching the back focal plane, which can cause astigmatism when large movements are required. The long working distance objectives available include 2x, 5x, 10x and 50x (Mitutoyo Plan Apo models). Other short working distance objective can be used with a thread adapter (the mount is SM1 threading).

Measurements

Alignment

1. Mount the sample.

    1.1. A magnetic mount base should be installed to the motion controller stage. The complimentary magnetic sample mount should be attached to the preferred sample holder. Most typical is a dual tilt stage with a square flat glass installed with double sided tape, giving a flat surface to then use double sided tape on the sample as well. When measuring transmission, the sample and glass mounting slide should rise above the holder by at least 1 cm to allow clearance for the photodetector place behind it later.

    1.2. Magnetically install a(the) reflective sample without any objectives installed in the path.

    1.3. Set the monochromator to a visible wavelength such as 525 nm or 550 nm. Set laser to a low enough power, for safety, to minimally see scattered light from the spot when an alignment card is place in the beam line.

1.4. Adjust position of the area of interest on the sample to be roughly where the focal point of the first objective will be (This would be unknown upon first use, but can be found by removing the sample, installing the objective, and using an alignment card to find roughly the z-position with the smallest spot. The objective's working distance can also be looked-up.).

1.5. The proper tilt can be found by using an adjustable iris up-beam line from the sample. Light reflected from the sample should return through this iris when it is near fully closed. Fully open the iris afterward.

2. Move the objective stage's X1 position to the center of the beam path, roughly -6.25 mm. It is best that this axis is not used for moving the spot across the sample, but only for beam spot corrections. This ensures consistency across different portions of the sample, that the same portion of the incident beam was used at the sample, and any lens-flaws or other non-idealities are normalized out.
3. Place the objective in front of the sample. The objective should already be properly aligned to the beam path. Align according to one of the procedures below:

   Method 1 – Free Space Optics (Advanced, Assured)

   3.1. Ensure no obstructions, filters, or redirecting optics are in the beam path. Do not remove lenses or parabolic mirrors.

   3.2. Translating the sample in-out of the objective axis will show a back-reflected spot on the monochromator exit slit that grows or contracts with the z-position of the objective relative to the sample.

   3.3. The focus plane is attained when the reflected light spot can be seen on the monochromator slit-door, at its smallest diameter.

   3.4. Make sure the laser is at a low alignment power and care is taken to not directly view any direct beams or intense scattered light. Observing the back reflected spot at the monochromator slit door *does not* involve looking into the monochromator, only at the scattered back-reflected spot. Scattered light from the monochromator exit usually is the brightest light source at the exit slit, so small tweaks to the sample tilt or rotation will show a moving spot that can be centered onto the slit, which is the

reflected spot. The sample will likely not be perfectly rotated/tilted after the iris alignment alone.

3.5. If the back-reflected spot shows an elliptical shape, the focus is astigmatic and the focal plane "of least confusion" will be the most circular back reflected spot. Sample tilt and rotation are the most common causes of astigmatism.

- If the collimating lens is not in place, a magnified image of the sample will be projected back to the monochromator, and, between us dear reader, is something fascinating to see. Due to the objective's infinity correction, when this image is in focus, the sample is also in focus.
- If the sample or other optical component is, to a high degree of certainty, not the cause of astigmatism, the objective motion stage will need re-alignment. Mounting a silver mirror firmly into the threaded mount should suffice as a reflection source to ensure the beam travels back to the monochromator through the lenses and mirrors, indicating the mount is orthogonal to the beam. Aligning this mount, or any motion stage, is risky. There are many degrees of freedom and constraints determined by the range of motion on the motion controllers. Alignment of the objective needs to ultimately consider that the focal spot of *all* the objectives should be near the center of each of these ranges, especially nearest orthogonal axis of rotation.

3.6. Iterate until the back-projected spot is circular (or rectangular, see below), at its smallest, and nearly returns through the monochromator slit. Mark the z-position of focus.

3.7. The laser, objective, and sample are now in focus at the sample surface with near diffraction limited spot. These results should be seen in the camera after installing the beam splitters to view the sample surface. The spot should be at its smallest when the z-position is tweaked back and forth.

- Due to the 150 mm focal length collimating lens, the objective is actually imaging the monochromator slit onto the sample, and it will appear rectangular. The collimating lens can be removed and still achieve a near-diffraction limited spot, but with lower power.

The spot size without the collimating lens was verified via beam spot analysis. A 50x objective with NA of 0.55 gives a spot on the order of less than 2 μm FWHM. Without the collimating lens, the objective is still sampling a small portion near the center of the beam, and is nearly collimated. Due to the long distance between the two, largely divergent rays will not make it past the double parabolic mirror beam expander. The beamline was most often used in this fashion to great effect.

- With white light illumination, the sample may appear out of focus in the camera *but the spot is not*. This often causes confusion, but is a result of the non-collimated white light making the sample appear out of focus. When the camera lens is properly focused at infinity, both the spot and the image should be in focus enough for finding an are of interest and minor focal readjustments with stage translation.

Method 2 – Camera Based (Easiest, results not guaranteed)

3.1. Place the camera beam splitter into the beam path to view the sample surface and beam spot. Ensure the camera is focused at infinity. Use neutral density filters, laser power, or the camera exposure settings until the sensor is not saturated with the laser spot such that it appears dim.

3.2. Translate the objective until the spot size is at its smallest.

- Multiple "spots" can appear in the camera when the objective is far from focus, and the laser spot may not always be centered in the camera image. These spots can be from the beam splitters or other optics. The laser spot is typically the brightest. If the sample is in the superstrate configuration, a "false" focus at that first interface is sometimes found. The sample focus will be further along the z-axis, so often translating through both spots and returning to the brighter one ensures the proper focus is found.

3.3. Turn on the white light source to verify the sample is visible in the camera along with the focused spot. This white light camera can be used during the focusing process, but if the camera is out of focus, it will lead to confusion. Turning the camera on second removes an extra degree of uncertainty.

- If the camera and spot are not in focus at the same point, the *sample* needs to be translated on its Z2 motion axis, along with the objective in the same direction, by the same amount until everything is in focus through the camera. These focal planes may not be exactly equivalent due to the non-collimated white light source, in which case the focused beam spot is considered the focus position.

3.4. Place the camera beam splitter into the beam path to view the sample surface and beam spot. Ensure the camera is focused at infinity. Use neutral density filters, laser power, or the camera exposure settings until the sensor is not saturated with the laser spot such that it appears dim.

3.5. Translate the objective until the spot size is at its smallest. If it appears rectangular, remove the collimating lens if desired, but power will be lower.

- Multiple "spots" can appear in the camera when the objective is far from focus, and the laser spot may not always be centered in the camera image. These spots can be from the beam splitters or other optics. The laser spot is typically the brightest. If the sample is in the superstrate configuration, a "false" focus at that first interface is sometimes found. The sample focus will be further along the z-axis, so often translating through both spots and returning to the brighter one ensures the proper focus is found.

3.6. Turn on the white light source to verify the sample is visible in the camera along with the focused spot. This white light camera can be used during the focusing process, but if the camera is out of focus, it will lead to confusion. Turning the camera on second removes an extra degree of uncertainty.

4. If the camera and spot are not in focus at the same point, the *sample* needs to be translated on its Z2 motion axis, along with the objective in the same direction, by the same amount until everything is in focus through the camera. These focal planes may not be exactly equivalent due to the non-collimated white light source, in which case the focused beam spot is considered the focus position.
5. Note that the white light beam splitter and the camera beam splitter can and do shift the spot location by up to a few μm. The first can be accounted for by making note of the spot location shift in the live image when when installing

and removing the white light splitter. The second can be accounted for by either leaving it in place, or taking an initial spatial XY scan to locate the exact position of the sample.

6. **Eucentric Axis Alignment**

   This alignment can be done visually when not using a microscope objective or with the aid of the software written for this purpose. These measurements are not recommended for large magnifications and large angles. At large magnifications, the focal depth is narrow, and minute changes in angle can bring parts of the sample out of focus to extremes, and the spot spreads rapidly. In this situation, the sample area sees completely different wave vectors and angular content from the focused beam, so the response is actually a convolution of many incident angles, rather than a single angle of incidence. For accurate results, this situation should be checked.

   There are multiple approaches to this. Perhaps the simplest, given low magnification and a large field of view with multiple distinguisable features. The eucentric axis will be the portion of the area that does not go out of focus when the sample is increasingly rotated. However this is not always seen with the limited field of view offered by the microscope objective combined with a sample that was initially place far from the eucentric axis. However, by taking care to initially place the sample near the center the rotation axis, simple adjustments in the sample stage's X2 and Z2 axes are all that is needed to bring a feature that remains in focus to the laser spot. *The X1 objective position should not be adjusted. If this has not moved from it's default position, it should already be aligned to the eucentric axis.* Ideally, both should be in focus at the camera under any rotation at the eucentric axis. The laser focal spot should be positioned in Z1 an X1 at this point.

   6.1. Focus the laser spot onto a large, distinguishable scattering portion of the sample such as a unique defect or alignment marker. If not using an objective simply move the spot to this area.

   6.2. Use the alignment program to rotate the sample a small amount, between 5° - 15°. The spot should not have shifted drastically from the initial position.

   6.3. Follow the instructions given by the alignment program.

   6.4. Use the alignment program to bring the sample back to zero rotation.

The sample will likely be slightly out of focus. Adjust the Z2 to bring the sample back into focus. The focal spot will be moved closer to the eucentric axis. The sample will need to be adjusted in X2 so that the feature is returned to the spot size.

6.5. Iterate this alignment through larger and larger angles until the maximum desired is well aligned. Check that an angle half of the maximum is still well aligned.

Measurement

With the sample aligned properly, measurements can be taken in multiple fashions. A calibrated photodiode can be placed in the path of a transmitted or reflected beam, or the sample itself can be measured if it produces a photo-response current.

1. Ensure that desired any filters and polarizers are placed in the beam line before each measurement. The white light beam splitter should be removed before measurements for maximized signal to noise ratio, but can be left in.
2. Normal Incidence Reflection

   The off-normal incidence reflection measurement requires a two-theta stage setup which is not currently installed, but not impossible to add in the future.

   2.1. Ensure the camera beam splitter is in place.

   2.2. Mount the calibrated photodiode (Newport ST818-UV) in the beam path between the camera and splitter.

   Make note of the attenuator position, as it is usually not used. Observe the reflected light as it hits the detector to ensure it is properly hitting the detector area, just slightly under filling it if possible. The beam line iris's can be used to adjust this area.

   2.3. A baseline scan should be done with a calibrated mirror or other reference in order to normalize the measurement results. This allows the beamline optical response to be normalize from the final measurement.

3. Transmission

   3.1. The camera beam splitter can be in or out of the beam line according to sample power requirements.

3.2. Mount the calibrated photodiode (Newport ST818-UV) in the beam path behind the sample such that it is close enough to capture the main transmitted beam, but as little scattered light as possible to reduce noise.

Scattered light can result from the sample, or from reflection between the photodiode and the sample. This positioning depends on the user's goals and how much the sample scatters. A reasonable method is to only capture light scattered into the main transmitted cone, such that specular transmission and specular reflection measurements can be more directly compared. In this case, the transmitted "circle" should just underfill the detector area with and without the sample.

3.3. A baseline scan should be done with the sample removed.

4. Photocurrent

4.1. The camera beam splitter can be in or out of the beam line according to sample power requirements. Typically, the beam splitters were removed because of signal to noise considerations.

4.2. Attach sample leads to a BNC cable adapter through alligator clips or otherwise. The vertical mounting of the sample and

5. Make sure the photodetector/sample is connected to the sample transimpedence amplifier through the coaxial cable.
6. Ideally, set the transimpedence amplifier to the highest gain possible to get a signal just under the 1 V limit for the wavelength with the weakest response.

- This requires some before-hand knowledge of the beam's spectral content and photodiode/sample response, which changes with each configuration. One or two trials might be necessary to ensure the lock-in amplifiers do not overload during the spectrum scan and learn more about the sample's response. If signal to noise is not an issue, lower or minimum amplification can be used decrease the likelihood of a lock-in overload during an unattended scan.
- The lock-in amplifier system should filter out amplified noise if setup properly.

7. Place the photodiode where the sample should be to take a baseline response. For reflection, make sure the sample is replaced with a known mirror specimen. Record the photocurrent spectrum for the configuration so that sample

measurements can be normalized to this spectrum. *A baseline needs to be taken whenever the beam line or laser power changes*. Any of these changes will change the incident photocurrent spectrum an invalidate previous baseline measurements.

8. Replace the sample in the magnetic mount. The spot position relative should not have moved, but should be double checked.

Notes and Tips

- A well designed sample mount for a specific use cases is something to consider. Other than small chips, the tilt mount and double sided tape are often not enough to hold the sample in place, or can be damaging.

- The vertical mount scheme can place a lot of stress and strain on sample leads, leading to samples dismounting, falling off, disconnected leads, or getting pulled out of position when doing automated rotation. Design samples and sample holders where this stress can be moved away from the sample. Taping lead wires to the stage such that they do not move the sample is a good basic strategy. Ideally, a rigid sample holder, compatible with the stage and magnetic mounting, with fixed contact locations or BNC output should be designed.

- The large degree of permutations give great measurement flexibility, but can lead to missed details. A couple of trial runs showing expected response are a good idea before setting a full automated sample scan.

- Including the beam splitters in measurements will heavily polarize the incident spectrum.

- Normalized data R_{norm} should be calculated from the recorded photocurrent PC of the sample and baseline, but also include a normalization to the reference diode photocurrent Ref from both the baseline and sample spectra according to:

$$R_{norm} = \frac{PC_{sample}}{PC_{baseline}} \frac{Ref_{baseline}}{Ref_{sample}} \tag{A.1}$$

  and the EQE calculated by:

$$EQE_{sample} = \frac{PC_{sample}}{PC_{baseline}} \frac{Ref_{baseline}}{Ref_{sample}} EQE_{photodiode} \tag{A.2}$$

This helps to account for any fluctuations of the laser between runs, since laser sources are not known to be stable over the course of hours. The calculation is not perfect however, and noise should be avoided in the first place.

Maximized Beam Intensity Configuration

The collimating lens is typically not used because it creates an image of the monochromator slit on the sample, biasing the resolution in one direction. For measuring features near the diffraction limit, it is often removed. The light bundle near the center of the beam travels nearly 1.5 m and is collimated enough to create a near diffraction limited spot. However, some samples have a small signal-to-noise ratio in this configuration and require more power. The collimating lens assures more power is sent to the beam expander at the cost of resolution.

Furthermore, the beam expansion mirrors can be by-passed entirely using redirection mirrors. The spot size out of the collimating lens through this beam path is approximately the same size as the objective entrance pupil. Combined with the 20W laser at maximum output, this configuration maximizes the power at the sample, but sacrifices μm resolution. In this work, samples from Chapter 5 uses this configuration, without the objective lens for a large sampling spot size and maximized power. Measurements from Chapter 3 utilized the setup without the collimating lens and a low magnification 2x objective. The beam line was re-designed with this kind of flexibility in mind.

A.2 Integrating Sphere Configuration

An integrating sphere path previously existed prior to upgrading the beam line to include further measurment capabilities, and is described in full detail in Reference [83] so modifying the beam line required movement and realignment of this setup. The modified path includes the 150 mm focal length collimating lens to account for. A removable 125 mm focal length is placed after the collimating lens to focus the beam through a view port at the sample in the center. The addition of an adjustable iris before the collimating beam helps ensure the spot size is small enough to fit through the smaller of the available view ports. Apertured collimated light alone could not be reasonably used to detect a signal due to the low throughput after the loss in the integrating sphere.

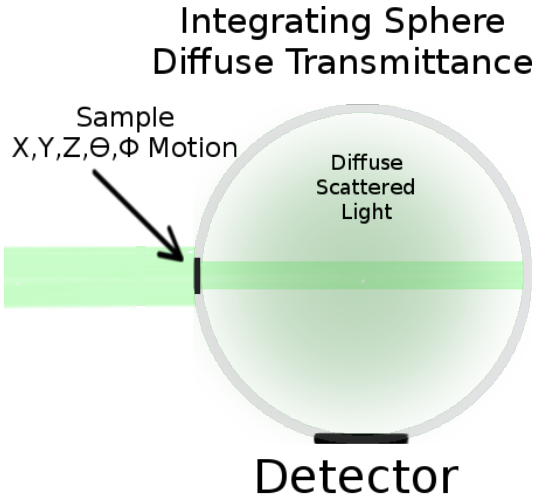

Figure A.3: An integrating sphere can be inserted after the monochromator of Figure A.1 to capture diffuse scattered light from transmission (sample mounted on front of sphere) or reflection (sample mounted in middle of sphere).

A.3 Confocal Microscopy Configuration

For measuring transmission of samples that are extremely sensitive to noise or very low signals compared to a background signal, or just to gain resolution when the spot size is exponential decay is problematic, a transmission confocal microscopy setup was created. The same monochromatic and collimated beam is redirected 180° via mirrors to hit the sample from "behind". A flip mount mirror allows for the re-directed beam and typical beam path to be readily switched between. The second arm of the beamline was aligned such that the laser beam light can be sent in a circuit back to this flip mirror. The sample is focused with the forward beam first in the camera as described above. Next, the redirection mirror is flipped back into place. For samples with some thickness, the focal point in reflection may differ from the transmission focal point. The now backward incident light should form an image of the transmissive micro scale object. In fact, due to the size of the beam in this configuration, some samples are much easier to focus purely in transmission mode. A second objective positioned "behind" the sample and is focused onto the back surface onto the same feature. Ideally, this objective should be identical to the first for full resolution, though depending on the application this may not be necessary. An objective with enough working distance for the sample was used to illuminate the same focal volume as the first objective, meaning alignment was done in 5 dimensions – the three spatial and two angular dimensions. A sample with a "window" is best for this alignment, so that light can visually seen from both sides. Alignment assumes that the front half of the beam line and objective are properly

aligned. The procedure for the rear objective alignment is as follows: This assumes that the 100 mm focal length lens and an imaging lens (75 mm was used) is placed properly at the "detector" position so that the camera can view the image formed at the pin-hole aperture.

1. Ensure that the sample is in focus, and is perpendicular to the beam by carefully noting its back reflection of the beam. Use the camera to monitor the feature in focus. Turn on the white light to illuminate the window from the front such that white light can be seen from behind the sample, if possible. If not aligning to a sample with a window, the flip mirror can be utilized to visually re-acquire the focal point of the front objective relative to the rear objective.

2. Place the second objective in the beam path. Adjust its height XY position such that it's back pupil is filled with the laser beam is nearly level and straight with the beam line. This is a iterative process. The video camera image will at some point show illumination from the back. The white light source and the redirecting mirror will need to be swapped in an out while the rear objective is placed, such that the window is illuminated from the front (to be aligned to) and such that the camera can see the rear illumination (to confirm light is entering the window.)

3. The Z focus of the rear objective was manipulated once the X, Y and rotation degrees of freedom were fixed. The objective was mounted on a flip mount, on a micro-manipulator stage for this fine tuning. The objective was moved to an approximately correct focus as determined by the distance that gave a small visual focal point on the sample surface.

4. Remove the sample and its magnetic mount holder. The laser beam should not be seen to hit the front objective outside of its acceptance lens. The light exiting the front mount should appear in a nice, round, collimated even intensity shape.

    - If the beam is round, but grows/shrinks dramatically when the alignment card is moved in the Z direction, the rear objective should be translated in its Z direction with the micromanipulator.
    - An ellipical lens can mean mis-alignment in any of the other 4 dimensions. Mis alignment in the X or Y are easier to deal with, the elliptical

shape is a result of the beam being cut-off before entering the front objective lens. Angle mis-alignment is more difficult to remedy.

- If the collimating lens is in place, an image of the slit door should be formed through the two objectives, and will have a very sharp outline for at least some distance. Ideally the image would be projected to infinity. This should also be viewable in the camera.

After these two objectives are aligned to the same focal volume, light is re-directed by a 45-degree mirror through an image forming lens to an image plane where a pin-hole detector can be placed. The position of the 100 mm lens is not critical because the beam is collimated after the second objective, but the pin-hole position is. (Pin hold is a 50 µm from ThorLabs or other. Starting large and moving progressively smaller is recommended.) The pin-hole was mounted in a quick release holder (Thorlabs SM1QA and) inside in a locking-lens tube with position control. Turning the tube with the pin hole attached translates the pin-hole along the beam axis. The camera is used to determine when the pin-hole was in the image plane, because the pin hole should have a sharply defined outline at the image plane. The pinhole is defining the portion of the image through which light can pass, which is what provides the increased resolution in confocal microscopy, and the ability to select the light from which Z plane is being detected. A blurred or otherwise outline indicates that light with angular content is impinging the pin-hole. Either scattered light or light from a plane either in front or behind the objective focal plane. Once the pinhole is in place, the low noise, low dark current photodiode (Thorlabs SM05PD3A) can be installed with the quick locking mechanism. The detector should be aligned to the pinhole and give a steady signal read out on the lock-in amplifier.

Using this optical setup sub percentage transmission was detectable with a 5 to 10 signal to background noise ratio, in situations where the background noise was from either scattered light or from the larger format photodiode.

A.4 High Precision Measurements and Noise Abatement

High precision measurements to 0.001 were required for the measurements of near perfect transmission and near perfect reflection samples in Chapter 5 and Chapter 6 in addition to collaborative work with other students, such as the work with transmission confocal microscopy. These measurements required consideration of every component in the system and its contribution to the overall noise. While developing this procedure, sources of noise were found in unexpected components, components

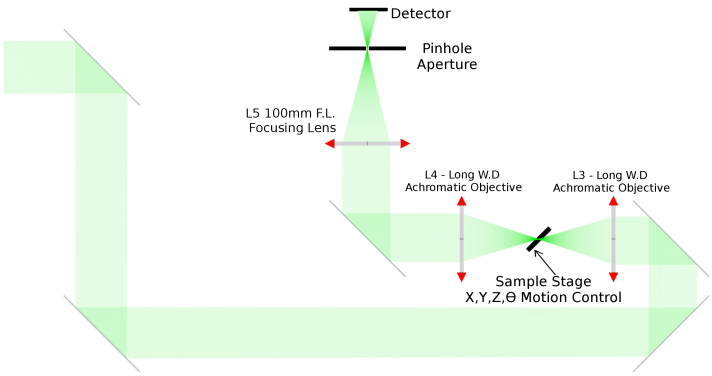

Figure A.4

that were designed to have lower noise, and were remedied. Leveraging the capabilities of lock-in amplifiers is key to this end, and a deeper understanding of the origins of noise is required. A great resource is the Stanford Research Systems 830 Lock-in Amplifier product manual or similar. This discussion can serve as a topic primer. The actual electronics setup of the lock-in circuit is described in Reference [83] Appendix B.

Often, a superstition or myth was spread about picking a chopper reference frequency: *Use a prime number.* The reasoning behind this is that there would be no lower harmonics as a source of noise else where in the system. While true, the wisdom of this advice stops there. Noise can come from anywhere at any frequency, and thus the best strategy is to know the system being measured.

Start with knowing the sample. A first question is "What is the time constant of the response?" The time constant is defined as the time the signal takes to reach 63.2% of its final value in response to a step function stimulus/excitation. So, a signal that takes 0.1s to reach 63.2% its final value, will need roughly $t\tau$=0.5s to be within 1% its final value assuming naturally exponential rates. As a first heuristic, chopping rates should be at a frequency lower than the required multiples of τ to reach the desired level of precision. Fortunately, photodiode time constants are in the nanoseconds range, but if an a signal is the product of heat transfer or a chemical reaction, this will likely not be the case. The lock-in also has a time constant, and that time constant setting should be greater than the time the sample requires to reach its final desired value, or ideally more than it. As an example $\tau_{LIA} > 5\tau_{sample}$ should give greater than 99% of the final value and a roughly 1% precision.

This time constant determines the required filter bandwidth you will need to get an

arbitrarily precise signal from a lock-in amplifier. Lock-ins equivalent function in frequency space is to act as a notch-pass filter, passing only the signal at the reference frequency through to processing, and ideally would be perfect. However, due to the discrete nature of the measurement, there is some band-width to this filtering. The time constant is related to the minimum modulation frequency according to $f = 1/(2\pi\tau)$. This gives the maximum frequency of chopping to get a desired level of precision from the lock-in amplifier. Likely, this will be in the kHz range, but it is good to be aware that chopping at higher frequencies is an option, because often strong noise sources can come from low frequencies. This is especially true of "$1/f$" noise, which is the name for a naturally occurring spectrum of noise that decays from 0Hz with a slow slope of inverse cut-off frequency. Each system has its own $1/f$ noise spectrum and its own cut-off frequency for this type of noise. So, this paradigm of time constant gives an upper limit, and it is more likely that longer time constants and slower frequencies will be needed.

Picking a Reference Frequency

1. Start with connecting the signal amplifier output, in this instrument the transimpedence amplifiers, to a spectrum analyzer or oscilloscope.

2. Set the amplifier to intended or the maximum amplification anticipate to encounter, this should ideally create a high level of white noise on the analyzer read out. Taking the FFT in the scope should show an even power distribution across the frequencies near the frequency given by the previously determined lock-in time constant; there should not be a 1/f slope in that portion of the noise spectrum, or else another amplifier should probably be used.

3. Connect the response device to the scope, which is usually a photodiode for reflection/transmission measurements, but it could also be a custom fabricated photo-responsive device or a potentiostat. Look for the same white noise spectrum from this circuit, in the dark. Next look for the same noise spectrum in the steady state, such as constant illumination. There should be an equal magnitude spectrum of white noise.

4. Component by component, build the measurement circuit and examine its noise spectra in this fashion, with and without a steady-state stimulus. If any component introduces 1/f noise close to where you need to modulate, replace it.

5. With all components connected, pick a reference frequency from the flat, constant background, white noise portion. Ideally a portion of the spectrum will have a flat background under both dark and illuminated (laser incident onto sample) conditions, but priority can be given to the illuminated state. Find a part of the spectrum with only white noise in a range of ±bandwidth (the bandwidth is the $f = 1/(2\pi\tau)$ determined by your precision level). The lock-in amplifier should only pass through signal at that band to the signal processor. As long as it is flat, and the sample signal is higher than the background, the lock-in should be able to reliably read-out the signal magnitude.

6. Start the response modulation (the chopper) with the scope and FFT read out connect still by using a BNC Tee connector. The signal should be the largest peak at that signal. There will be harmonics from the square wave signal, but they should be much smaller or outside the determined bandwidth.

   If there are two signals with comparable magnitude in the desired bandwidth, another reference frequency should be tried. Alternatively, increasing the sample signal by increasing illumination power or otherwise can be a solution.

   A common source of equal magnitude noise near the reference frequency in mechanically chopped signals such as this is phase jitter. The mechanical nature of the chopper wheel means that it can sometimes have trouble maintaining a steady frequency due to defects, bends, wear and tear from years of lab use and other non-idealities that create instabilities. A change in frequency can sometimes help mitigate these effects.

7. At this point, a measurement can be taken to characterize the overall level of noise. The time constant of the lock-in, in practice, should be long enough to experience at least a few if not tens of signal cycles. The lock-in becomes more precise with the number of samples input. An important nuance: the final value reported by the lock-in is not the steady state value of the sample, it is the magnitude of the input frequency. So, a more precise magnitude will come from multiple samplings of the photodiodes "stead-state" value. A helpful thought is to consider the discrete nature of the signal seen by the lock-in and how accurately one can determine a frequency without an infinite time sampling – the longer the time sample, the better resolved the frequency becomes.

An example of some frequencies that are good to avoid are 50/60Hz and harmonics there-of coming from supply lines. The power in harmonics of 50/60Hz decay with increasing frequency, so eventually they won't be above the background level if one needs to chop at these higher harmonic frequencies. Shorter time constant samples should be modulated at higher frequencies because of the correspondingly larger pass bandwidths, thus a larger white noise band is required.

There are additional filters on the lock-in output signal which add more time required for the signal output to reach its steady state voltage read-out, i.e. the signal measured in this system. The Stanford Research Systems 830 user's manual gives 99% final values require settling times as follows: 6dB filter $\rightarrow 6\tau$, 12dB $\rightarrow 7\tau$, 18dB $\rightarrow 9\tau$, 24dB $\rightarrow 10\tau$. In experiment, a noisy signal typically required a 24dB filter and a settling time (time for lock-in to reach steady state after a change in the system, such as a change in wavelength) of $12\tau_{lock-in}$ or more to achieve the highest precision.